Iron and Cobalt Pyridonate Complexes: Synthesis and Catalysis

Dissertation

Zur Erlangung des Doktorandengrades der Naturwissenschaften

Dr. rer. Nat.

Am Institut für Anorganische und Angewandte Chemie

der Universität Hamburg

Vorgelegt von

Andrey Fedulin

Aus Moskau (Russland)

Hamburg, February 2023

The experimental part of this work was performed from October 2019 to December 2022 at the Institute of Inorganic and Applied Chemistry, University of Hamburg. This work was supervised by Prof. Dr. Axel Jacobi von Wangelin.

Date of thesis submission:	08.02.2023
Board of examiners:	1) Prof. Dr. Axel Jacobi von Wangelin
	2) Prof. Dr. Gerrit A. Luinstra
Date of thesis defence:	24.03.2023
Board of examiners:	1) Prof. Dr. Axel Jacobi von Wangelin
	2) Prof. Dr. Wolfgang Maison
	3) Dr. Thomas Hackl

“To understand the world at all, sometimes you could only focus on a tiny bit of it, look very hard at what was close to hand and make it stand in for the whole…”

Donna Tartt

Table of Contents

1. Abstract and Zusammenfassung

1.1. Abstract

The aim of this thesis is the investigation of 3d transition metal complexes supported by *N,O* and *N,N* ligands (pyridonates and diamides) and their application in catalysis. 2-Pyridonates is a modular ligand platform capable of varied and multifaceted coordination chemistry. To date, catalytically relevant pyridonate complexes were mostly based on noble metals. Therefore, the main goal of this work is to expand the chemical space for 3d transition metal pyridonate complexes, explore their reactivities and find new catalytic applications.

The first part of this thesis (**Chapter 2**) introduces the key features of the 2-pyridonate ligand, highlights its enzymatic role and gives a literature overview of the first-row transition metal pyridonate complexes with an emphasis on catalysis. Characteristic features of 2-pyridonate ligands such as flexible binding modes, hemilability, tunability and proton responsive character are discussed.

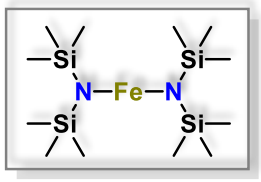

Chapter 3 reviews the properties and reactivities of the convenient iron (II) precursor bis[bis(trimethylsilyl)amido]iron(II), that was utilized for synthesis of polynuclear pyridonate clusters (**Chapter 4**). These topologically unprecedented Fe_4 and Fe_5 clusters, supported by simple 2-pyridonate ligands, were studied by XRD, Mossbauer spectroscopy and SQUID magnetometry.

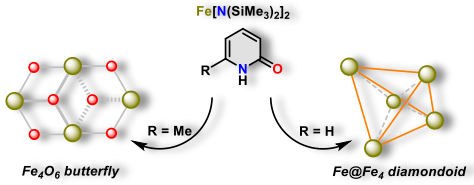

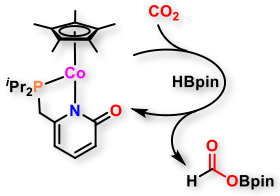

In **Chapter 5,** the modified pyridonate ligand, bearing additional phosphine donor group, was used for the synthesis of Co(II) half-sandwich complex. This complex demonstrated high catalytic activity and selectivity in the CO_2 hydroboration to borylformate. Mechanistic studies reveal the formation of Co^{III}-H intermediates as a possible active species.

As a side project, heteroleptic triamido ferrate (II) complex, supported by tetraphenylethylene diamide and $N(SiMe_3)_2$ ligands, was prepared and applied for catalytic alkene hydrosilylations (**Chapter 6**). Mechanistic studies suggest the substitution of the silamide group and formation of catalytically relevant iron hydride species.

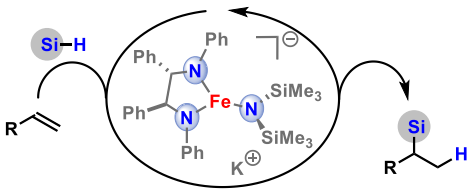

1.2. Zusammenfassung

Das Ziel dieser Arbeit ist die Erforschung von 3d-Übergangsmetallkomplexen mit *N,O*- und *N,N*-Liganden (Pyridonate und Diamide) und deren Anwendung in der Katalyse. 2-Pyridonate bilden eine modulare Ligandenplattform, die vielfältige und facettenreiche Koordinationschemie ermöglicht. Die meisten bekannten, katalytisch relevanten Pyridonat Komplexe basieren auf Edelmetallen. Daher ist das Hauptziel dieser Arbeit die Erforschung neuer 3d-Übergangsmetall-Pyridonat Komplexe, sowie die Untersuchung von deren Reaktivität und neuen katalytischen Anwendungen.

Der erste Teil dieser Arbeit (**Kapitel 2**) stellt die Haupteigenschaften des 2-Pyridonat Liganden vor, beschreibt seine Rolle in Enzymen und gibt einen Überblick über 3d-Übergangsmetall-Pyridonat-Komplexe mit Fokus auf Anwendungen in der Katalyse. Wichtige Merkmale des 2-Pyridonat Liganden wie flexible Bindungsmodi, Hemilabilität, Abstimmbarkeit und der proton-responsive Charakter werden diskutiert.

Kapitel 3 beschreibt die Eigenschaften und Reaktivitäten des nützlichen Eisen(II) Vorläufers Bis[bis(trimethylsilyl)amido]eisen(II), der zur Synthese von polynuklearen Pyridonat Clustern genutzt wurde (**Kapitel 4**). Diese topologisch beispiellosen Fe_4 and Fe_5 Cluster, verbrückt durch 2-Pyridonat Liganden, wurden mittels XRD, Mößbauer Spektroskopie and SQUID Magnetometrie.

In **Kapitel 5** wurde ein modifizierter Pyridonat Ligand, funktionalisiert mit einer zusätzlichen Phosphingruppe, für die Synthese eines Co(II) Halbsandwichkomplexes genutzt. Dieser Komplex zeigte hohe katalytische Aktivität und Selektivität in der Hydroborierung von CO_2 zu Borylformiat. Mechanistische Experimente deuten auf die Bildung von Co^{III}-H Intermediaten als mögliche aktive Spezies hin.

Als Nebenprojekt wurde ein heteroleptischer Triamidoferrat(II) Komplex mit Tetraphenylethylendiamid und $N(SiMe_3)_2$ Liganden synthetisiert und in der katalytischen Hydrosilylierung von Alkenen eingesetzt (**Kapitel 6**). Mechanistische Studien weisen auf die Substitution der Silamid-Gruppe und Bildung von katalytisch relevanten Eisenhydrid-Spezies hin.

2. 3d Transition Metal Pyridonate Complexes

2.1. Overview and the Key Features of the Pyridonate Ligand Platform

Rational ligand design unlocking new properties and reactivities of metal complexes is one of the key challenges in modern synthetic coordination chemistry.[1] Since Alfred Werner (Nobel Prize 1913) conceptualized the main aspects of coordination chemistry, the ability of a plethora of organic- and main group-based ligands to generate new metal complexes was increasingly studied.[2] The systematic variation of the nature of the ligand backbone and donor atoms (steric and electronic effects), number of donor atoms (denticity), charge and other parameters enable control over structure, physical properties and reactivity of the derived metal complexes. Therefore, an ever-growing number of ligand frameworks are designed to support molecular metal complexes leading to tunable magnetic and optical properties as well as catalytic activities.

Among the broad variety of ligands used in coordination chemistry, modular N,O-ligands 2-pyridonates exhibit an especially versatile set of properties. As a neutral molecule, 2-pyridone is an N-heterocycle that is found in tautomeric equilibrium with 2-pyridinol (or 2-hydroxypyridine) both in solution and solid state (Scheme 2.1a).[3–5] The solution state equilibrium depends on solvent polarity and ring substituent effects with polar solvents and electron-withdrawing substituents in the 6-position favoring the pyridone form. The 2-Pyridone tautomer belongs to the class of cyclic amides (lactams) with a hydrogen atom attached to nitrogen and the adjacent C=O bond possessing significant double bond character. In contrast, the 2-pyridinol tautomer could be described as an aromatic pyridine ring with a hydroxy group in the *ortho*- position to the nitrogen. Deprotonation of 2-pyridone leads to the formation of anionic 2-pyridonate with the negative charge delocalized between nitrogen and oxygen atoms (Scheme 2.1a). Both neutral tautomers and the deprotonated form of 2-pyridone could act as ligands upon coordination to the transition metal of the main group element.

Anionic 2-pyridonates belong to the class of 1,3-N,O heterobidentate ligands and are characterized as LX-type donors (Scheme 2.1b).[6] Hard oxygen/nitrogen set of donor atoms enables both σ- and π-donor properties. The anionic charge is distributed in a range between N-centered amido- and O-centered aryloxy resonance forms (Scheme 2.1b). The predominant character of bonding depends on the coordinated metal, substituent effects and also could be influenced with the choice of the solvent. Fixation of the nitrogen in the six-membered ring results in high conformational rigidity of the NCO motif and a tight bite angle upon chelation. Pyridonate scaffolds contain four possible positions for functionalization. The nature of the introduced substituent allows a modulation of the bonding situation, stability and reactivity of resulting metal complexes.

It is noteworthy that metal-pyridinol motif was found in the active site of [Fe]-hydrogenase metalloenzyme (Scheme 2.1c).[7] Therefore, natural occurrence of pyridone-based systems and their mechanistic role in biocatalysis serve as a great inspiration for the development of biomimetic models and related metal complexes.

An important characteristic feature of 2-pyridonate ligands is a high diversity of binding modes (Scheme 2.1d).[8,9] Depending on the nature of the metal, ligand substituent

and crystallization conditions, 2-pyridonate can adopt monometallic κ^1-N or κ^1-O coordination mode, chelating mode (κ^2-N,O) and one of bridging modes (μ_2, μ_3-N,O) or their combination, linking together two or three metal ions. Such diverse array of binding modes leads to the rich coordination chemistry spanning from mononuclear complexes to high-nuclearity clusters and coordination polymers.

Dynamic interconversion between coordination modes in solution leads to another important feature of pyridonates - *hemilability*. A hemilabile ligand is a chelating ligand that readily undergoes decoordination of one of the donor groups leaving another part of chelate still bound to the metal.[10] As a result, vacant coordination site is generated leading to possible follow up substrate activation and catalysis. For pyridonates hemilability is described usually as a change in bonding modes between κ^2-N,O to either κ^1-N or κ^1-O (Scheme 2.1e).[11]

Apart from the use as a supporting platform controlling metal-centered reactivity, pyridonates may also be engaged in bond breaking/forming events working in concert with metal ion. Such synergetic bond activation is described in modern literature as metal-ligand cooperation (MLC) and constitutes an important attribute relevant to catalysis.[12,13] A metal-bound (κ^2-N,O) or pendent (κ^1-N) oxygen donor of a 2-pyridonate complex may act as a Lewis base, cleaving a substrate E–H bond in cooperation with a metal center (Scheme 2.1f). Depending on the polarity of an E-H bond, three distinct pathways are possible. (a) E-H is an acidic molecule and it undergoes deprotonation by the internal pyridonate-2-O, forming hydroxy group attached to ligand (pyridinol tautomer) and nucleophilic E-group bound to the metal. Such ligand-protonated metal complex could participate further to metal centered reactivity and act as a proton shuttle. (b) E-H is nonpolar hydrogen (H_2) that is cleaved heterolytically to result in metal hydride supported by pyridinol ligand. This species could further transfer hydrogen to the substrate with C=O, C=N bond or release hydrogen leading to numerous (de)hydrogenation/transfer hydrogenation/hydrogen borrowing catalytic transformations. (c) E-H is a hydridic molecule (for example borane or silane) and the bond cleavage results in hydride transfer to the metal center accompanied by binding of electrophilic E-group to oxygen. Formed metal-hydride complexes may act as active catalytic species in hydroelementation catalysis. Importantly, change in bonding modes during cooperative action is also accompanied by aromatization/dearomatization of the cyclic ligand backbone.[14] That is especially evident for κ^1-N complexes where N-ligated pyridonate with pendent C=O group can restore aromaticity through a MLC event.

In conclusion, variable κ and μ binding modes make pyridonates attractive linkers for the synthesis of polynuclear clusters and materials, while electronic and steric modularity, hemilabilily, proton-responsive character, cooperative reactivity and second coordination sphere effects drive its application in homogeneous catalysis.

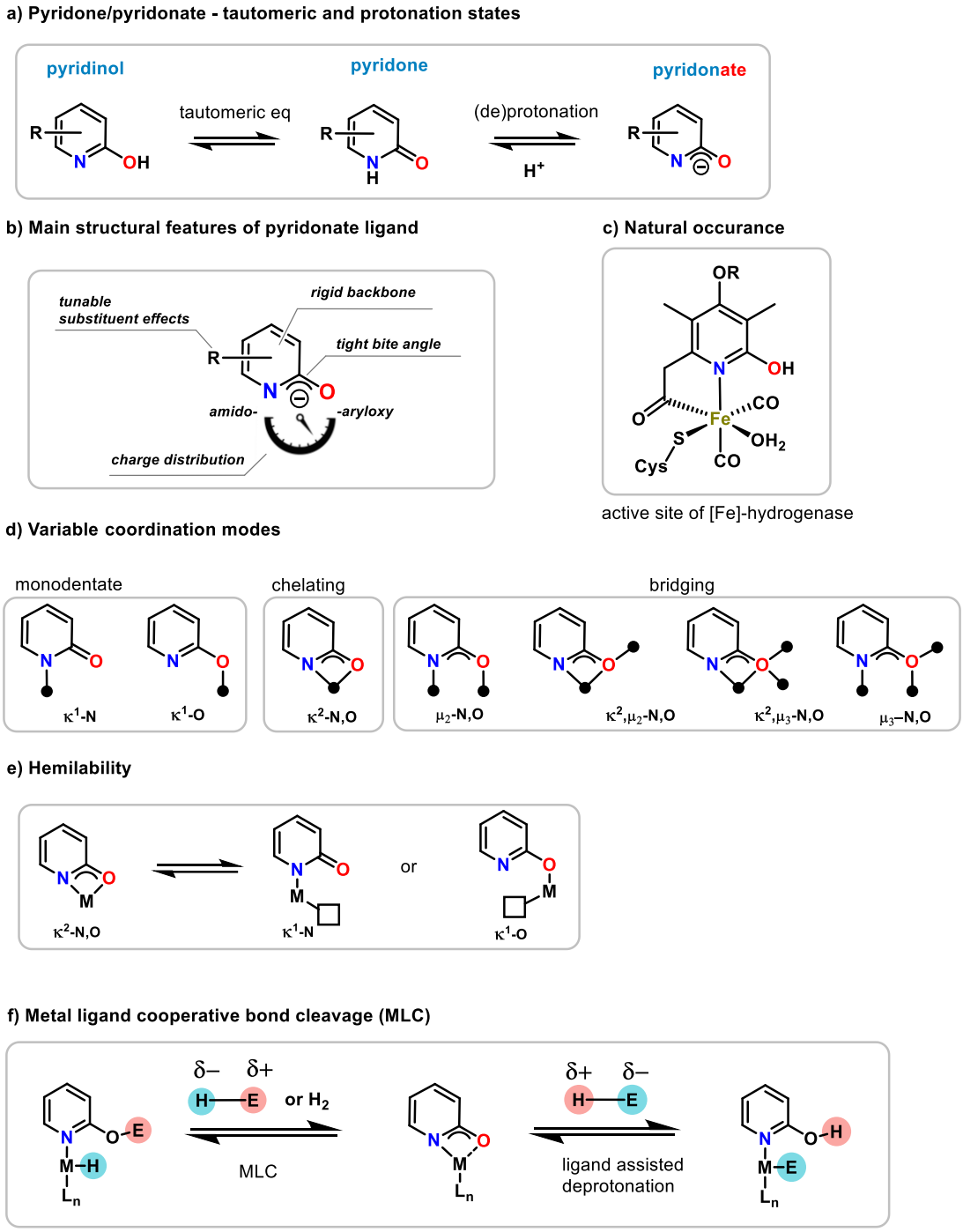

Scheme 2.1. Overview of 2-pyridone/pyridonate ligand platform.

2.2. Iron Hydrogenase and Related Bioinspired Models

2.2.1. Iron Hydrogenase Structure and Catalytic Mechanism

Hydrogenases are class of metalloenzymes that can catalyze hydrogen splitting or generation.[15] The three types of hydrogenases are known as [NiFe]-, [FeFe]- and [Fe]-hydrogenases. Unlike bi-metallic [NiFe]-, [FeFe]- hydrogenases, [Fe]-hydrogenase contains only one redox-inactive metal center and lacks additional iron-sulfur cluster unit.[16]

[Fe]-hydrogenase was isolated from the methanogenic archaea *Methanobacter marburgensis* grown under nickel-limited conditions.[17] This metalloenzyme was first crystallographically characterized in 2008 and revisited in 2009 by *Shima* and coworkers.[18] Recently, the atomic-resolution crystal structure of the activated [Fe]-hydrogenase at 1.08 Å was resolved.[19] The active site of [Fe]-hydrogenase (iron-guanylylpyridinol cofactor, FeGP) consists of a low-spin octahedral Fe(II) center, ligated by two CO ligands, cysteine, water, acyl-carbon and a guanylyl-pyridonol moiety (Scheme 2.2a). The pyridinol unit coordinates to Fe in a bidentate fashion through acyl linkage as well as through nitrogen atom with the pendent OH group uncoordinated to the metal center. The guanosine monophosphate (GMP) group is attached at the para-position of the pyridinol ring.

[Fe]-hydrogenase is involved in the catalytic methanogenesis pathway converting CO_2 and H_2 to CH_4 (Scheme 2.2b). It enables the reversible heterolytic cleavage of H_2 to H^+ and H^- pair followed by the stereoselective hydride transfer to the C1 carrier molecule methenyl-tetrahydromethanopterin ($CH\text{-}H_4MPT^+$) to form methylene-H_4MPT ($CH_2\text{-}H_4$MPT) that further undergoes reduction to methane.

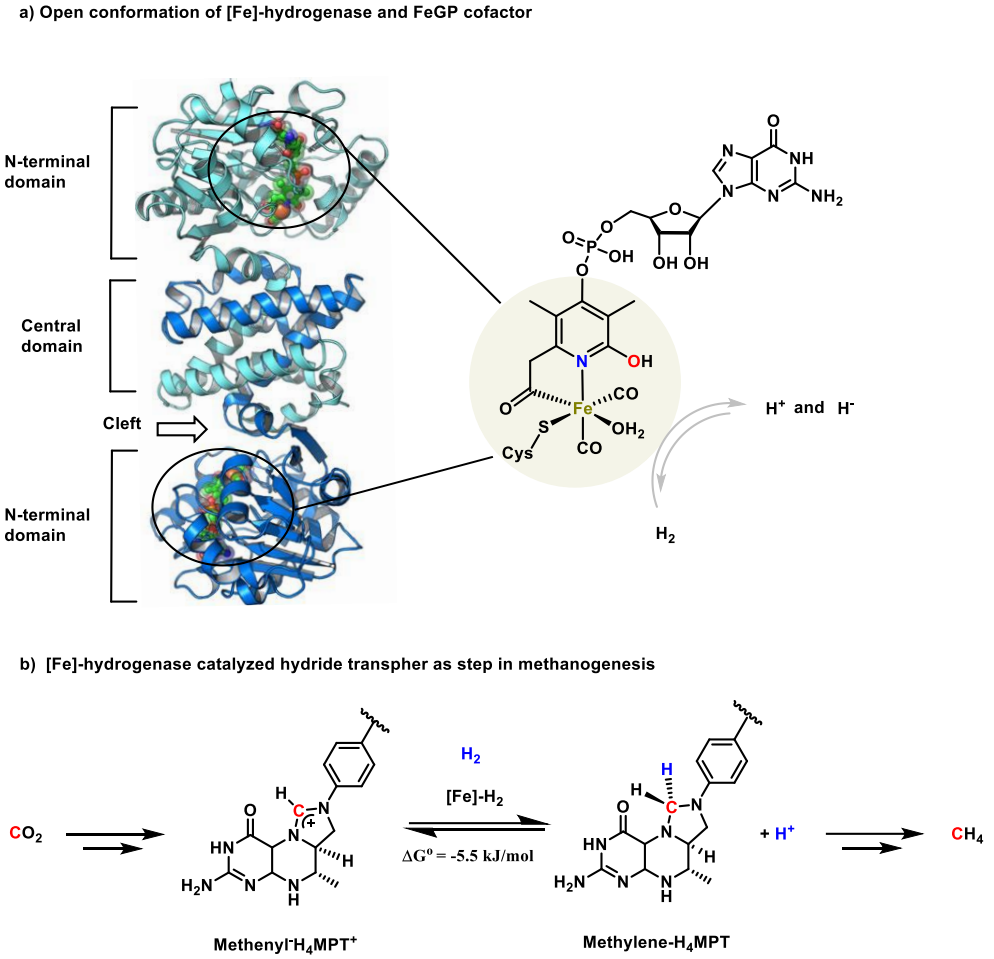

Scheme 2.2. Structure of [Fe]-hydrogenase metalloenzyme, FeGP cofactor and its catalytic role in methanogenesis.

From a structural point of view, the [Fe]-hydrogenase metalloenzyme is built from two N-terminal domains and one central domain that form two substrate accessible active-site clefts (Scheme 2.2a). The catalytic clefts can adopt open and closed conformations along with movements of adjacent domains. The change in conformation was proposed to be an essential step for the hydride transfer to the substrate. Based on obtained crystal structures and performed quantum chemical calculations, the following mechanism was suggested (Scheme 2.3). [19] The open form of the metalloenzyme binds the substrate CH-MPT$^+$, initiating the closure of the catalytic cleft along with the dissociation of a labile water ligand (**I** → **II**). The pentacoordinate intermediate **II** gets deprotonated at the 2-OH position of pyridinol to form intermediate **III** bearing 2-O$^-$ basic functionality. Then, H_2 diffuses through the short protein gas channel towards the Fe vacant coordination space (intermediate **IV**). Coordinated dihydrogen then undergoes heterolytic splitting assisted by proximate 2-O$^-$ base, thereby producing Fe-H with protonated ligand periphery (compound **V**). After that the hydride transfer to the carbon atom of CH-H_4MPT$^+$ takes place. The opening of catalytic clefts results in the release of the reduced substrate CH_2-H_4MPT and the hexacoordinate complex **I** is regenerated through the binding of the water molecule.

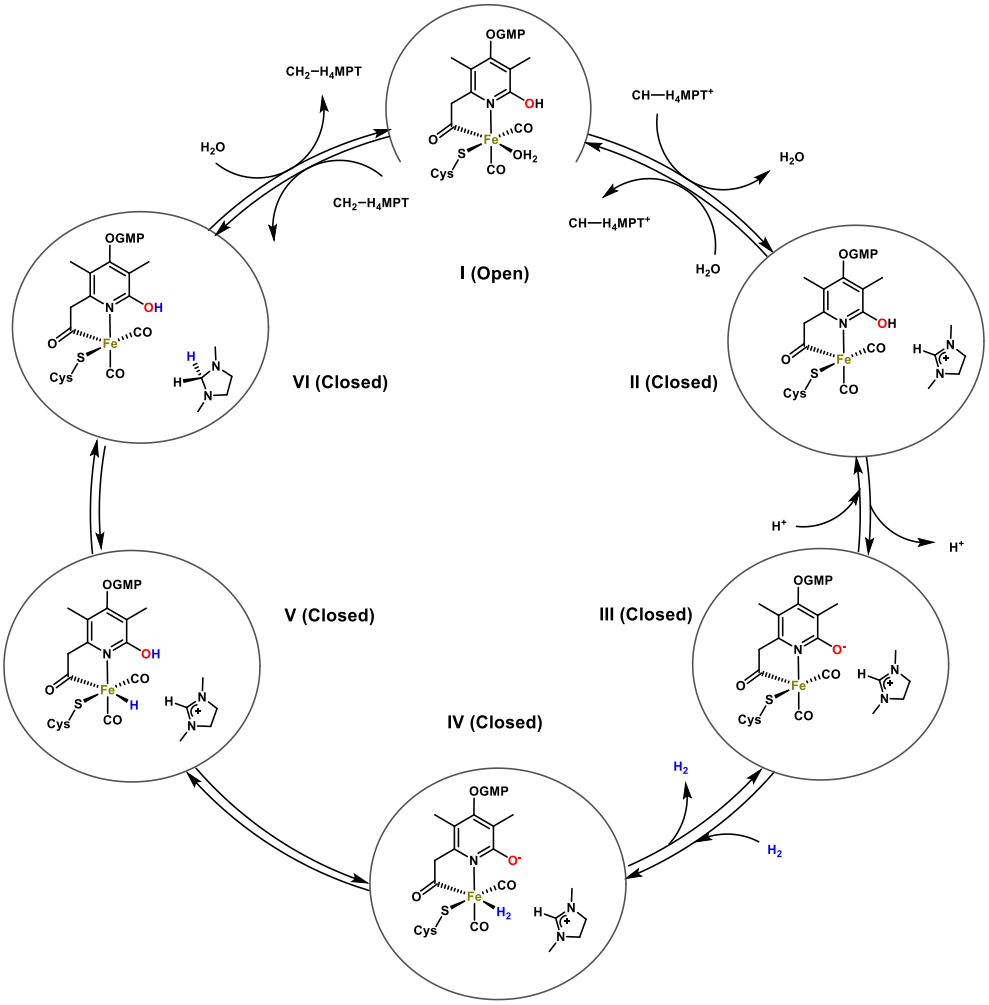

Scheme 2.3. The proposed catalytic cycle for the [Fe]-hydrogenase

The relative structural simplicity of [Fe]-hydrogenase active site, its capability of operating under low hydrogen pressure in aqueous media and the intriguing second sphere effects of the pyridinol unit taken together make FeGP an attractive blueprint for the development of synthetic biomimetic models (Scheme 2.4a). Over the last thirty years numerous structural and functional models were developed. Also, the utilization of 2-pyridone as a design element for synthetic hydrogenation catalysis was often inspired by its enzymatic role.[7]

While many models are designed to emulate the specific *fac*-C,N,S coordination environment using different (not containing 2-pyridone) ligand architectures[20–22], series of model complexes featuring pyridonate/pyridinol motifs were developed by *Hu* and *Song* groups (Scheme 2.4b).

2.2.2. Synthetic Models of [Fe]-Hydrogenase

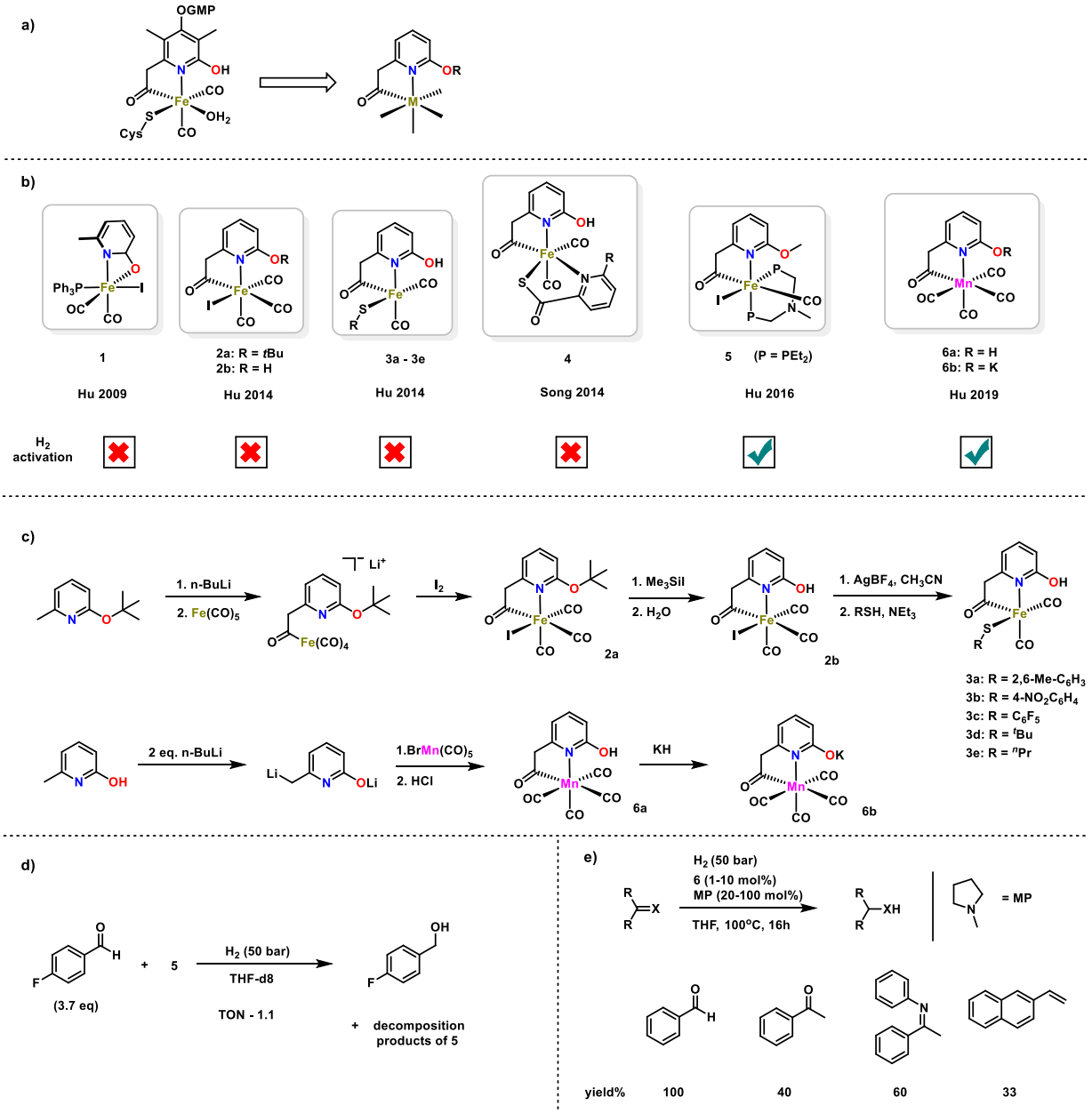

Scheme 2.4. a) Design strategy towards [Fe]-hydrogenase synthetic model b) Representative examples of FeGP synthetic models reported by *Hu* and *Song* c) Synthesis routes towards complexes **2**, **3** and **6**. d) Aldehyde hydrogenation by complex **5** e) Catalytic hydrogenation using **6** as catalyst.

In the same year of the first crystallographic elucidation of FeGP, the first model complex **1** containing 2-pyridone motif by was published by *Hu* and coworkers.[23] It was obtained by the reaction between sodium 6-methyl-2-pyridonate with $Fe(CO)_3(PPh_3)I_2$. The x-ray structure of **1** reveals an Fe(II) ion in pseudo-octahedral geometry with unfunctionalized 6-methyl-pyrionate ligand bound to the Fe(II) complex via κ^2-N,O mode, two carbonyl groups, phosphine and iodine ligands. Iodide could be exchanged by bulky thiolates but the resulting iron pyridonate thiolate complexes were found to undergo rapid decomposition at room temperature in solution.[24]

The first synthetic models **2a** and **2b** containing [Fe]-hydrogenase-related acylmethylpyrdinol ligand were also reported in 2014 by *Hu* and coworkers.[25] According to their report, acyl coordination was introduced by nucleophilic attack of lithiated 2-*tert*-butoxy-6-methylpyridine on the carbonyl group of $Fe(CO)_5$ (Scheme 2.4c). Then, *in situ* formed metalate intermediate was oxidized by iodine to give pentacoordinated complex **2a.** Removal of the ^{t}Bu protecting group enabled the isolation and structural characterization (XRD) of the complex **2b** featuring the pyridinol-2-OH group. Iodine abstraction by $AgBF_4$ followed by treatment with various aryl and alkyl thiolates lead to the formation of pyridonate thiolate complexes **3a-e**. Despite the fact that complexes **3a-e** constitute the most structurally faithful models known to date, their further application and reactivity studies were hampered by their high instability in solution. Interestingly, incorporation of 2-pyridinol-containing model complex **2b** into [Fe]-hydrogenase apoenzyme (enzyme lacking metal cofactor) imparted the reconstructed semi-synthetic hydrogenase with enzymatic activity, while its analogue with OMe group instead of OH was inactive.[26] These findings support the hypothesis of the essential role of 2-hydroxy group in the second coordination sphere in heterolytic H_2 cleavage (see Scheme 2.3).

In 2014, *Song* reported the synthesis of another model complex featuring acylmethylpyridinol in combination with S,N-chelating co-ligand.[27]

Despite the high degree of structural resemblance to the native FeGP cofactor coordination sphere, none of the model complexes **1**-**4** are capable of H_2 cleavage or catalytic hydrogenation. The lack of activity for complexes **2b** and **3** is explained by their susceptibility to decomposition in the presence of base (Scheme 2.3). In order to achieve higher stability, *Hu* and coworkers introduced PNP ligand $Et_2PCH_2NMeCH_2PEt_2$ serving as pendent intermolecular base rather than the pyridinol-2-OH to afford complex **5**.[28] In contrast to previous models, complex **5** displayed activity in H_2 heterolysis which was demonstrated by H_2/D_2 exchange experiments giving HD as scrambling product. Furthermore, **5** was capable of hydrogenating 4-fluorobenzaldehyde (50 bar, 4 h, rt), even though the rapid decomposition of the complex led to very low turnover numbers (Scheme 2.4e).

Next steps toward a functional FeGP model shifted their focus from the native Fe(II) ion to the isoelectronic Mn(I) ion. The first Mn(I) complex **6a** was obtained by reaction of 6-methyl-2-pyridone with two equivalents *n*BuLi followed by addition of $BrMn(CO)_5$ and acidic work-up (Scheme 2.4c).[29]

X-ray analysis of **6a** revealed octahedral coordination geometry with acylmethylpyridinol coordinated via C,N chelation and four CO ligands completing the coordination sphere. The pendent 2-OH group could be deprotonated using one equivalent of KH to give the corresponding 2-OK derivative **2b** (characterized by X-ray as 18-crown-6 adduct). Importantly, both complexes **6a** and **6b** were competent in hydrogen heterolysis as proven by H_2/D_2 assay. Complex **6a** required stoichiometric amount of external base (2-methylpyrrolidine, Et_3N) while complex **6b** was able to

produce HD in absence of external base. These findings support the hypothesis of the key role of pendent 2-O^- base in H_2 activation.

Moreover, complexes **6a/6b** were shown to act as hydrogenation catalyst (Scheme 2.4e). Under optimized conditions (1 mol% **6a**, 20 mol% 2-methylpyrrolidine, 50 bar H_2, THF, 80 °C) quantitative yield of benzaldehyde was achieved. Other substrates such as ketones, imines and styrenes could also be hydrogenated in moderate to good yields under similar conditions (Scheme 2.4e). Deprotonated complex **6b** was also catalytically active and did not require basic additives but showed a lower reaction rate with aldehyde. Although the catalytic activity were relatively poor in comparison with state-of-the-art Mn(I) complexes[30], compounds **6a**/**6b** gave the best performance as a functional models of [Fe]-hydrogenase. Noteworthily, reconstruction of the [Fe]-hydrogenase apoenzyme with **6a** model complex replacing native cofactor leads to semi-synthetic [Mn]-hydrogenase for which the molar activity is higher than its semi-synthetic Fe analogue.[26]

In conclusion, FeGP cofactor of [Fe]-hydrogenase was proven to be responsible for H_2 heterolysis and hydride transfer within the biological methanogenesis pathway. Mechanism of the H_2 splitting and hydride transfer was elucidated and the cooperative role of the pyridinol ligand was highlighted. First examples of Fe(II) based models of FeGP demonstrated high levels of structural resemblance to natural systems but showed no (or very poor) activity in H_2 cleavage and related hydrogenations. However, the use of non-native Mn(I) leads to the development of catalytically active models capable of H_2 heterolysis and hydrogenations.

2.3. Pyridonate Complexes of 3d Transition Metals

Coordination chemistry of 3d transition metal pyridonates are mostly represented by di-nuclear complexes (paddle-wheel) and polynuclear coordination clusters[9] while mononuclear complexes are more rare. Here, the recent advances in molecular pyridonates with the focus on catalysis are shortly reviewed.

2.3.1. Examples of Noble Metal 2-Pyridionol/Pyridonate Complexes

Historically, molecular pyridonate complexes were first investigated for noble metals such as Ir, Rh, Ru, Pd. The latter advances in 3d transition metal pyridonates (including catalysis) were often inspired by their heavier homologous. Therefore, prior to describing the 3d transition metal pyridonates it would be useful to highlight several representative examples of such noble metal complexes and their related catalytic performances (Scheme 2.5).

One of the milestone compounds, half-sandwich Ir(III) complex **7** with simple 2-pyridone ligand was reported by *Yamaguchi* in 2007 and complex **7** demonstrates high catalytic performance in alcohol dehydrogenation[31,32] (TONs up to 700) and reversible

(de)hydrogenation of N-heterocycles[33]. Related iridium complex **8** supported by chelating bipyridonate ligand was active in CO_2 hydrogenation to formate[34], formic acid[35] and methanol[36]. *Szymczak* presented ruthenium complex **9** with hydroxypyridine incorporated into the chelating bis(2′-hydroxy-6′-iminopyridyl)isoindoline framework which was active in nitrile hydroboration.[37] Very recently, Rh-NHC complex **10** containing anionic 2-pyridonate ligand was reported to be capable of alkyne dimerization.[38] The Pd(II) system **11** containing CF_3 functionalized 2-pyridonate was active in undirected C-H activation of alkynes.[39]

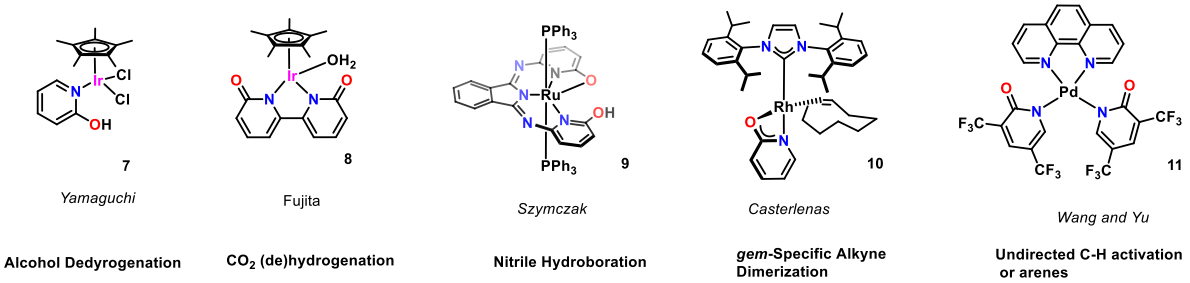

Scheme 2.5. Selected examples of noble metal pyridonate complexes

Mechanistically for all these systems the presence of proximate 2-OH/2-O^- group was found to be essential for high catalytic performance.

2.3.2. Titanium

Among other 1,3-N,O- and 1,3-N,N-chelating ligands, pyridonates were exploited by *Schafer* and coworkers for the stabilization of electrophilic early-transition metals. Titanium complex **12** (Scheme 2.6a) was synthesized by reacting $Ti(NMe_2)_4$ with two equivalents of 3-phenyl-pyridone and adopts octahedral coordination geometry with two pyridonate ligands bound in κ^2-binding mode.[40]

Complex **12** displays activity in intermolecular hydroaminoalkylation (HAA) of primary aminoalkenes (Scheme 2.6a). High chemoselectivity of challenging hydroaminoalkylation (HAA) over more common hydroamination (HA) was achieved. For comparison, $Ti(NMe_2)_4$ in absence of ligands favored hydroamination (HAA:HA = 17:83).[40] Authors proposed that titanium pyridonate **12** favors formation of bridging imido-complex **12.1** over terminal imido species **12.2** (Scheme 2.6b). Dimer **12.1** undergoes α-CH activation to give bridging metalloaziridine **12.3** that leads to formation of the hydroaminoalkylation product.[41,42] In contrast, terminal imido species **12.3** undergoes intermolecular [2+2] cycloaddition resulting in hydroamination. The authors postulated that pyridonate is acting as a bridging ligand to stabilize dimeric intermediate species **12.1** and **12.2.** thus determining hydroaminoalkylation selectivity.

Moreover, similar titanium pyridonates were applied as initiators for ring opening polymerizations.[41,42]

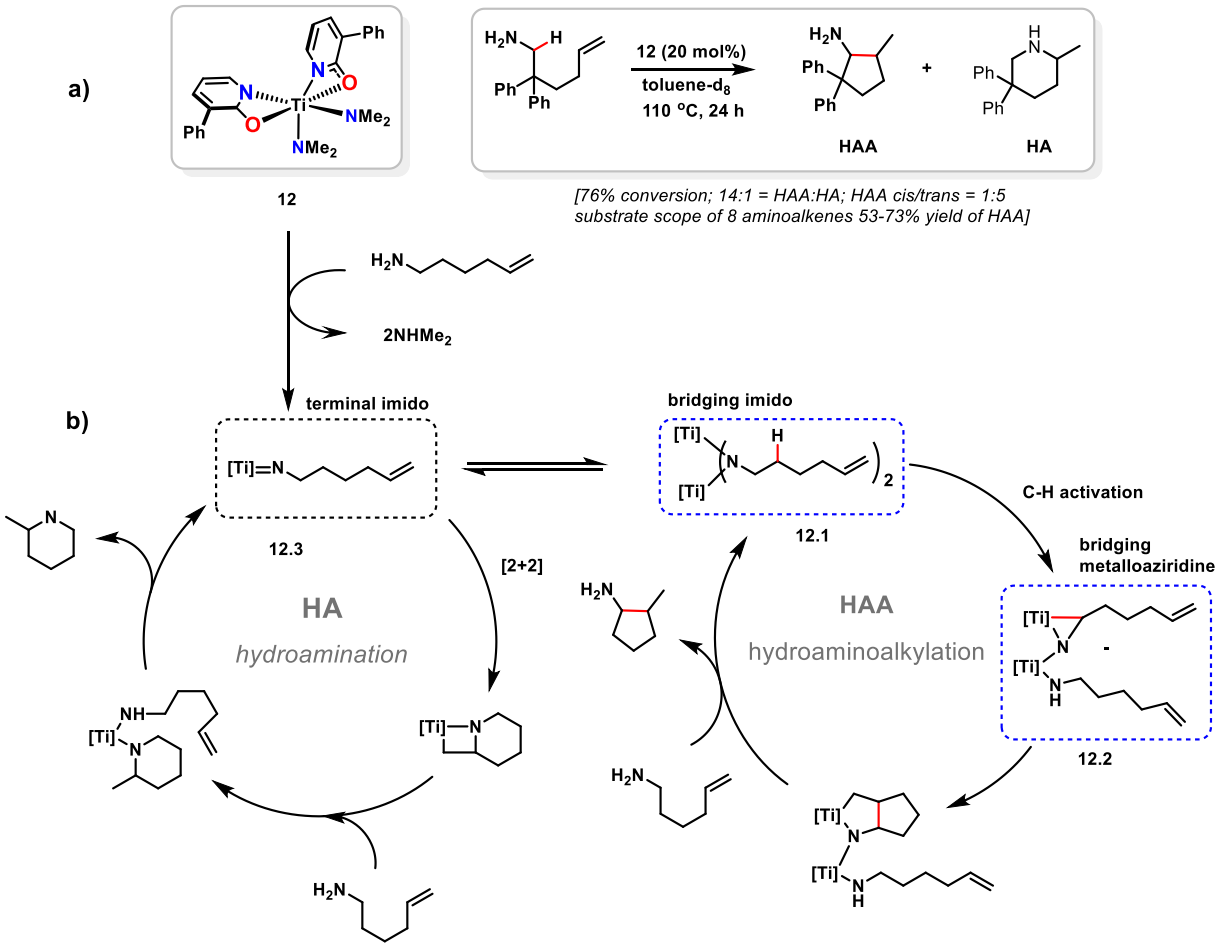

Scheme 2.6. a) Titanium pyridonate complex **12** and its catalytic activity in hydroaminoalkylation; b) proposed catalytic cycles for hydroamination and hydroaminoalkylation.

2.3.3. Vanadium

Very recently, *Schafer et al.* reported the synthesis and reactivity of vanadium (III) pyridonates.[43,44] Complex **13** could be accessed from V(III) precursor (THF)V(Mes)$_3$[44] or V(IV) V(NMe$_2$)$_4$[43] via reacting with three equivalents of 6-methyl-pyridone (Scheme 2.7a). The former pathway is redox-neutral protolytic ligand exchange and the latter combines protonolysis and reduction of metal precursor (*in situ* generated HNMe$_2$ acting as reductant). Vanadium pyridonate **13** is a *C2* symmetric dimer adopting ligands in κ^2-N,O and μ_2-O binding modes. Dimeric structure **13** could be broken to form monomer **13.1** by coordinating with the strong donor 4-dimethylaminopyridine (DMAP) (Scheme 2.7a).[43]

Complex **13** showed catalytic activity in the reductive deoxygenative coupling of benzyl alcohols (Scheme 2.7b). With diphenylmethanol as a model substrate, the key catalytic intermediates (**13.2**, **13.3**) were isolated and the plausible mechanism involving V(III)/V(IV) redox cycle was proposed (Scheme 2.7b). First, interaction of diphenylmethanol (benzhydrol) with **13** afforded the monomeric alkoxide complex **13.2** through ligand assisted deprotonation of the substrate hydroxy-group. Then, homolysis

of alkoxide C-O bond occurs along with neutral pyridone dissociation giving dimeric terminal oxo-complex **13.3** and the benzhydryl radical. The benzhydryl radical undergoes homodimerization to give the coupling product 1,1,2,2-tetraphenylethane. After that, vanadium (IV) complex **13.3** is reduced by one equivalent of benzhydrol to regenerate the initial V(III) complex **13** accompanied by the formation of benzophenone as oxidized byproduct.

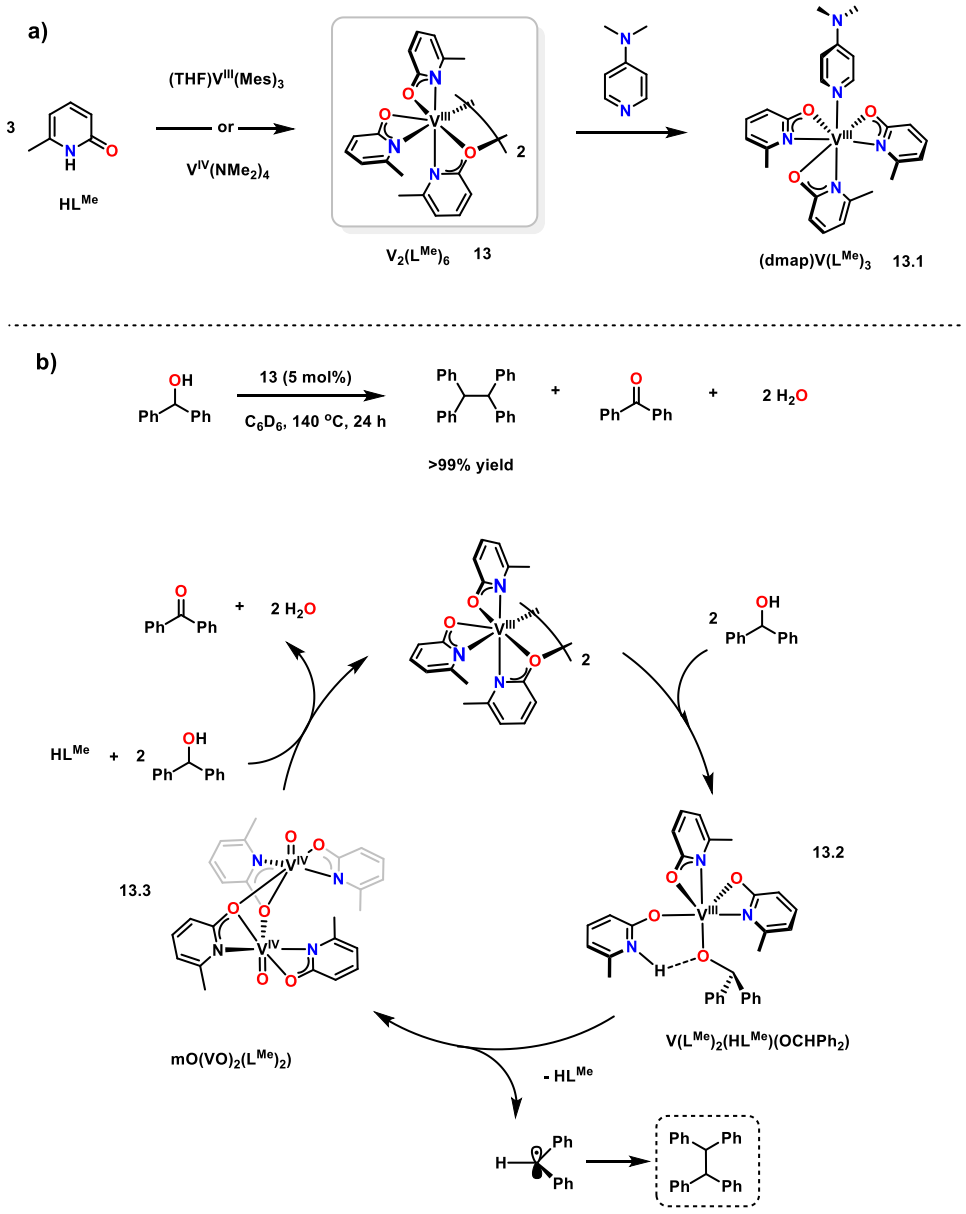

Scheme 2.7. a) Synthesis and vanadium pyridonates b) Catalytic reductive coupling of alcohols and proposed mechanism (only isolated intermediates included)

2.3.4. Manganese

Apart from the Mn-based [Fe]-hydrogenase-biomimetic complex **6a** (see paragraph 2.2, Scheme 4) a few catalytically relevant Mn(I) complexes have been reported recently (Scheme 2.8a).

In 2017 *Khusnutdinova et al.* reported the Mn(I) tricarbonyl complex **14** bearing 6,6'-dihydroxy-2,2'-bipyridine ligand.[45] This complex was found to be catalytically active for hydrogenation of carbon dioxide (0.15 mol% loading, 65 °C, MeCN, 60 bar CO_2/H_2) in the presence of DBU to give formate with turnover numbers > 6000. Moreover, in the presence of dimethylamine reduction to formamide was achieved using the same catalytic system. Two years later the same group reported complex **14** to be efficient in the transfer hydrogenation of aldehydes, ketones, imines and heterocycles.[46] In this case, co-catalytic amount of base (KO*t*Bu) was required to activate the precatalyst **14**. From the mechanistic perspective metal-ligand cooperativity was postulated as a main attribute for catalysis with complex **14**. Installation of unsubstituted or *ortho*-OMe substituted bipyridine ligand backbone leads to the loss of catalytic activity in the case of CO_2 hydrogenation as well as deteriorated performance in transfer hydrogenation. Therefore, 2-OH groups were proven to be essential element responsible for high activity. Based on DFT calculations[47] and deuterium labeling experiments[46] , the following key mechanistic steps were suggested (Scheme 2.8b): (a) deprotonation of 2-OH group by external base (DBU or KO^{t}Bu) and bromine elimination results in formation of species **14.1** featuring anionic pyridonate moiety (b) H_2 (from molecular dihydrogen or isopropanol) undergoes heterolytic splitting across manganese ion and pyridonate ligand to give monohydride complex **14.2** with protonated 2-OH moiety; (c) active species **14.2** transfers H_2 further to C=O and C=N bonds of the substrate to result at corresponding reduction product.

Another Mn(I) complex **15** containing 2-pyridiol moiety was reported recently by *Xia* and coworkers(Scheme 2.8a). [48] The ligand is coordinated in bidentate N,N fashion with the 2-OH pyridinol group and distal nitrogen from the naphthyridine fragment remaining uncoordinated. Complex **15** was active in the transfer hydrogenation of carbonyls in presence of base (0.5 mol% loading, 20 mol% KO^{t}Bu, 85 °C, 24 h, 2-propanol) and was also suitable for acceptorless dehydrogenative condensations.

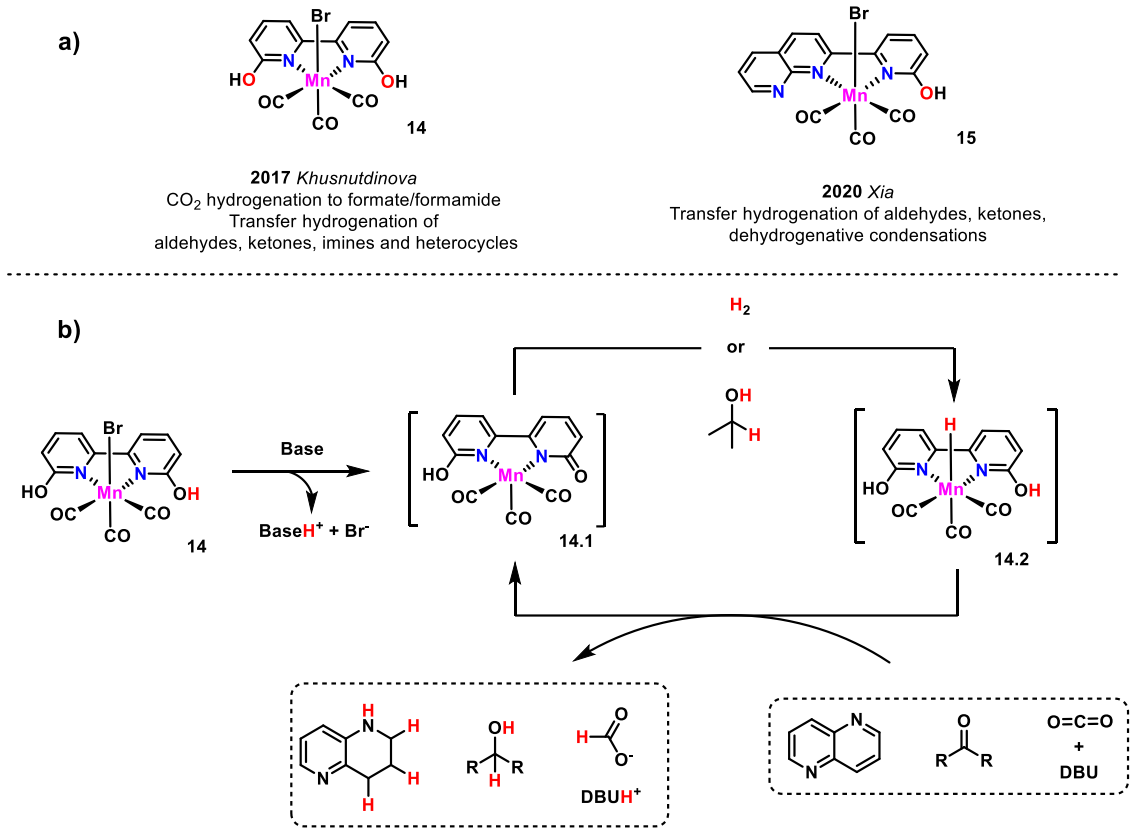

Scheme 2.8. a) Molecular structures of manganese complexes **14** and **15**; b) Simplified catalytic cycles of hydrogenation/transfer hydrogenation by complex **14**.

2.3.5. Cobalt

A series of monomeric cobalt pyridonate complexes was described by *Winpenny* in 1996.[49] As an example complex **16** bearing κ^2-N,O bounded ligands was afforded by reaction of $Co(OAc)_2$ with two equivalents of sodium 6-methyl-2-pyridonate (Scheme 2.9a).[49] Later, the solid state structure of **17** featuring the cobalt cation surrounded by tetrameric unit of hydrogen bonded 2-pyridinols and two axial aqua ligands was reported.[50] In 2013, water soluble cobalt (III) complex **18** bearing 6,6'-dihydroxy-2,2'-bipyridine ligand (analogous to **6** previously reported for Ir) was reported by *Fujita* and coworkers.[51] Complex **18** was active in CO_2 hydrogenation, although with low activity (TON 1.3) that was attributed to its thermal instability under catalytic conditions.

Half-sandwich cobalt (II) complex **19** bearing phosphinopyridonate ligand was recently reported by *Wang* group.[52] The ligand is bound to metal center through PN donors forming five-membered chelating ring, while 2-C=O remains uncoordinated. Complex **19** was applied for stereoselective sequential transformation of aryl terminal alkynes to 1,3-dienes (Scheme 2.9b). In the presence of 3 mol% **19** terminal alkynes undergoes dimerization to give (*Z*)-enynes that are further reduced by addition of ammonia-borane to yield (*E,Z*)-dienes. Based on DFT calculation and mechanistic experiments two sequential catalytic cycles were proposed. The first cycle starts with **19** reacting with alkyne through a ligand assisted metalation deprotonation step to afford cobalt alkynyl species **19.1** featuring ligand in pyridinol form that tautomerizes to pyridone form **19.2**.

Intermediate **19.2** was isolated and structurally characterized in the stoichiometric control experiment. Next, 1,2-insertion of alkyne into Co alkynyl species **19.2** gives intermediate **19.3**. Finally, intermolecular proton transfer from the ligand NH to cobalt-bound vinyl species in **19.3** results in the release of enyne and regeneration of catalyst **19**. The second cycle initiates with the coordination of BH_3 to the pyridoate 2-oxygen atom (**19.4**) and metal-ligand cooperative B-H bond cleavage leads to formation of Co-H species **19.5.** Insertion of previously formed (*E*)-1,3-enyne into Co-H bond and proton transfer from coordinated ammonia (**19.6**) closes the catalytic cycle giving (*E,Z*)-diene and species **19**.

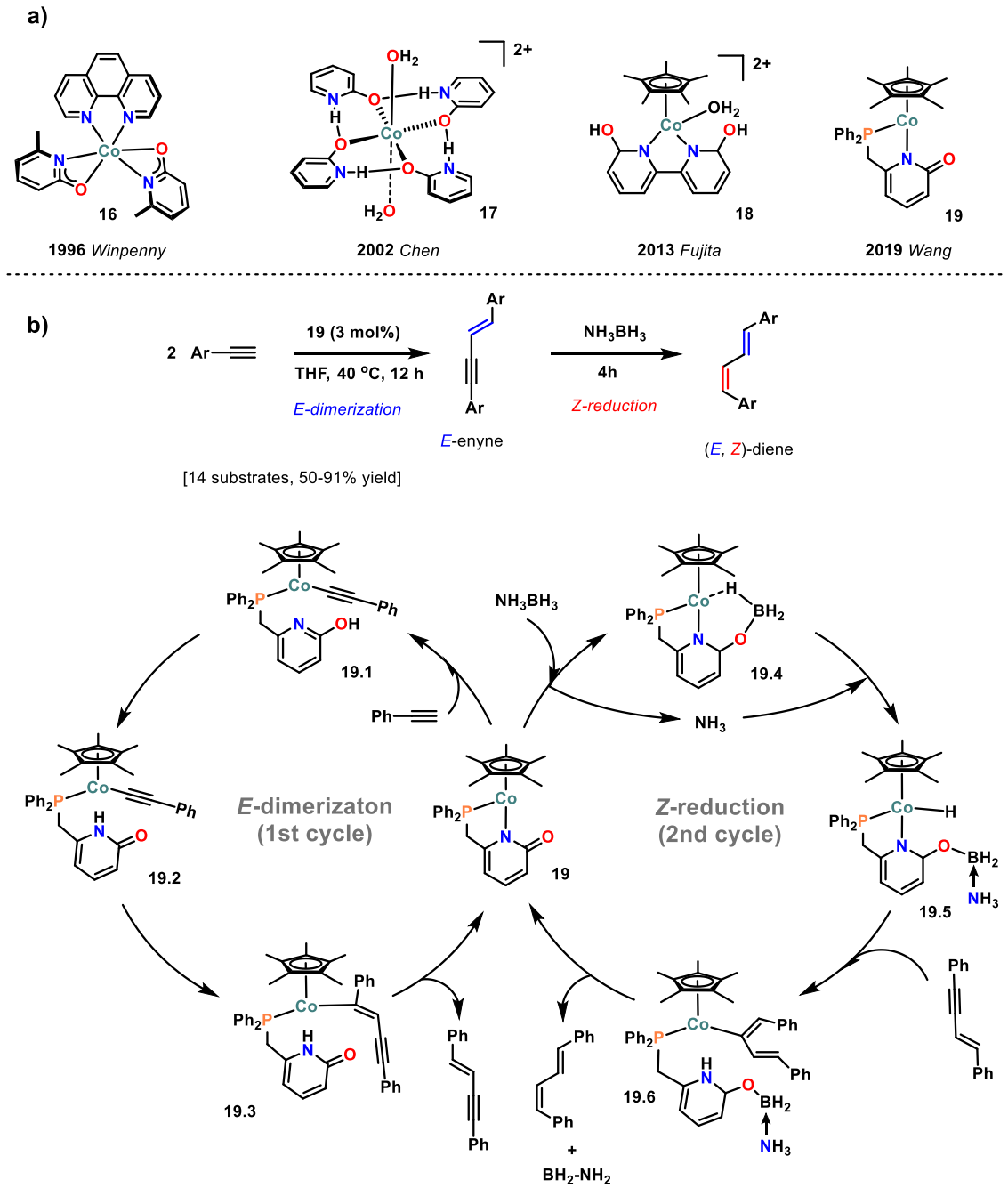

Scheme 2.9. a) Selected examples of molecular Co pyridonate complexes; b) Catalytic sequential dimerization-semireduction with **19** and proposed catalytic cycle.

2.3.6. Nickel

The first example of mononuclear nickel pyridonate **20** was structurally characterized in 1998 by López *et al*. (Scheme 2.10a).[53] This distorted square pyramidal cationic complex includes tripodal NNN co-ligand (2,4,4,9-tetramethyl-1,5,9-triazacyclododec-1-ene) and chelated 2-pyridonate.

In 2015, *Jonas et al.* reported the synthesis of related 1,3-N,O quinolinate complex **21** supported by tris(3,5-dimethylpyrazolylborate) ligand that showed catalytic activity in acceptorless dehydrogenation of alcohols (Scheme 2.10a).[54] In a series of control experiment the authors proved the essential role of the 2-OH moiety for catalysis. The authors proposed that concerted dehydrogenation of alcohol by **20** through MLC results in transient nickel hydride **21.1** that release H_2 (Scheme 2.10b).

In 2020, *Rose* and coworkers showed that N,S functionalized pyridone ligand $\mathbf{HL^{N,S}}$ in combination with the nickel (II) metal salt can form a diverse set of mono- and dinuclear structures (Scheme 2.10a).[55] Simple reaction of $Ni(Og)_2$ with slight excess of ligand and subsequent crystallization afforded nickel complexes **23** (crystallization by slow diffusion of Et_2O into MeOH) and **24** (crystallization by slow evaporation of MeCN). X-ray analysis revealed that in both complexes the ligand is coordinated in bidentate N,N fashion, while terminal N and O atoms remain uncoordinated. In **23** both pyridonate moieties are anionic and exhibit relatively long C-O distance consistent with the rare pyridinolate (2-O^-) resonance form. In contrast, in one of two NNS ligands in **24** is characterized as neutral 2-hydroxypyridine with positive charge compensated by acetate anion bound to nickel. Interestingly, the UV-Vis studies and the high-resolution mass spectroscopy probe suggested that the predominant species in solution are square-planar bis-pyridonate complex **22**. Overall, this work nicely illustrates the divergent behavior of pyridonate complexes in solution and solid-state.

Very recently the group of *Rose* described the first example of anionic Ni(0) complex **25** supported by bidentate NHC-pyridone ligand.[56] Strong donor ability of NHC-carbon favored C,N-chelation.

This complex was afforded by reaction of deprotonated NHC-armed pyridonate with $Ni(COD)_2$ in presence of 18-crown-6. X-ray structure of **25** revealed C,N chelated pyridonate and one cyclooctadiene molecule coordinated to the formally anionic nickel center. Counter cation K(18-crown-6)$^+$ forms a contact ion pair with the ligand 2-O atom. Interestingly, complex **25** showed catalytic activity in Markovnikov-selective styrene hydroboration with pinacolborane (HBpin).

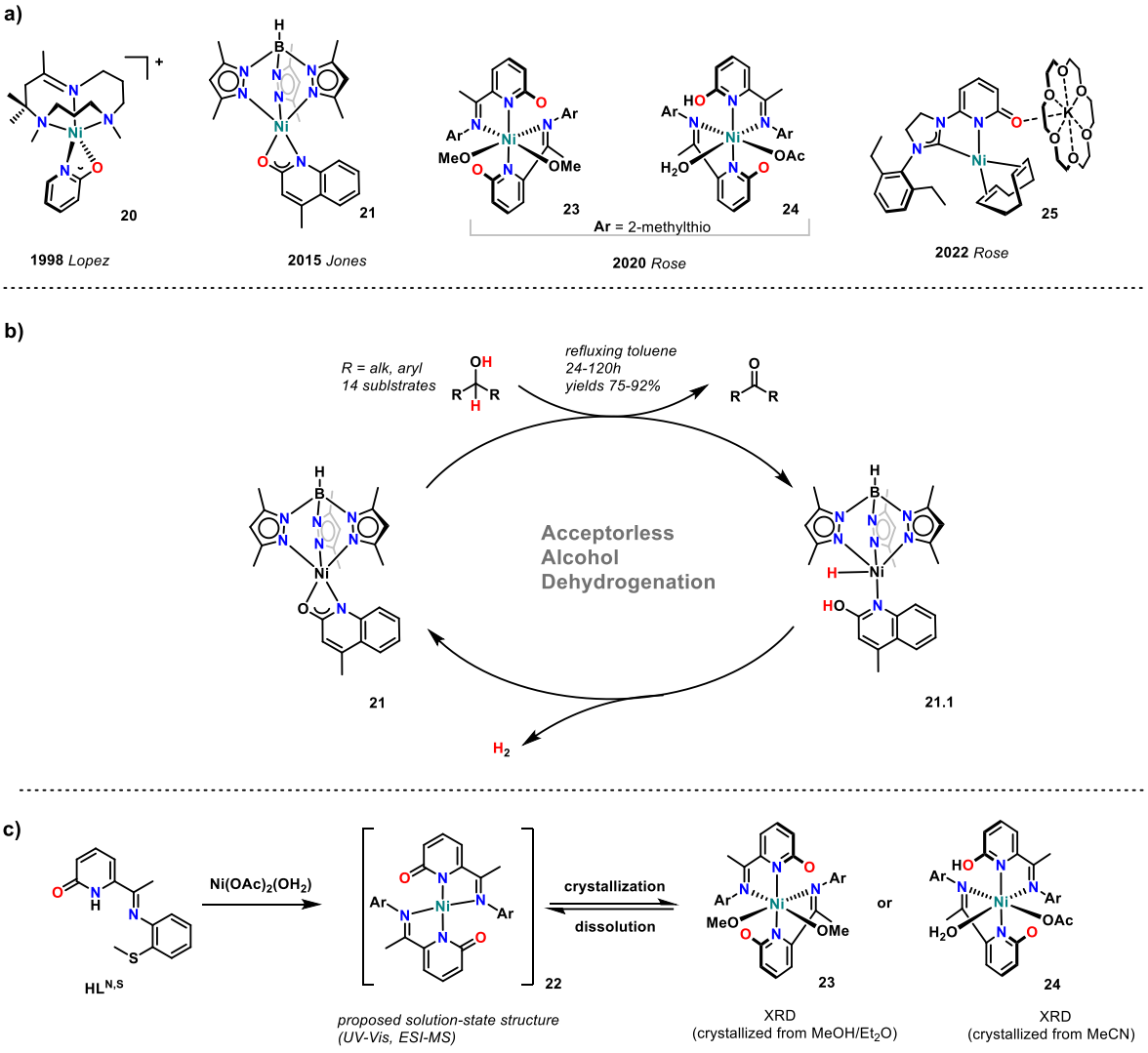

Scheme 2.10. a) Selected examples of molecular nickel pyridonate complexes; b) Proposed catalytic cycle for acceptorless alcohols dehydrogenation mediated by **21** c) Synthesis and divergence between solution and solid-state structures for nickel complexes **22** – **24**.

2.3.7. Copper

Copper complex **26a** bearing the 6,6′-dihydroxybipyridine ligand and its double deprotonated analogue **26b** were structurally characterized by *Papish* and coworkers in 2014 (Scheme 2.11a).[57] Complex **26a** displayed moderate activity in electrocatalytic water oxidation at relatively low overpotential of 477 mV. Once again, presence of OH group in *ortho* positions of pyridonate rings was proved to be essential to for catalytic activity. Since complex **26a** showed activity in basic media (pH **≥** 12.6) the fully deprotonated aqua coordinated complex **26c** was suggested to be the catalytically competent species (not confirmed by XRD analysis but assigned from EPR and HYSCORE). Moreover, the authors proposed that intermolecular hydrogen bonding between copper-coordinated water and proximal pyridonate oxygen atoms in

26c (or related species) may stabilize the key intermediates and facilitate proton coupled electron transfer (PCET) during catalysis.

A series of copper complexes with tripodal ligand tris(6-hydroxypyrid-2-ylmethyl)amine (H_3thpa) were presented by *Szymzak* and coworkers (Scheme 2.11b).[58–60] In the cationic copper(II) complex **27**, metal-bound fluoride is additionally engaged into hydrogen bonding interactions with the pendent OH group of 2-pyridinol moiety.[59] Upon one electron reduction, the unique Cu(I) fluoride adduct **28** was isolated and elucidated structurally. Complex **28** is best described as tetracoordinated by H_3thpa copper (I) center with dissociated fluoride anion "captured" in the second coordination sphere via involvement into hydrogen bonding. Moreover, complex **28** was capable of stoichiometric reduction of nitrite $Ph_3Si(ONO)$ to NO producing Cu(II) species **29**.[60]

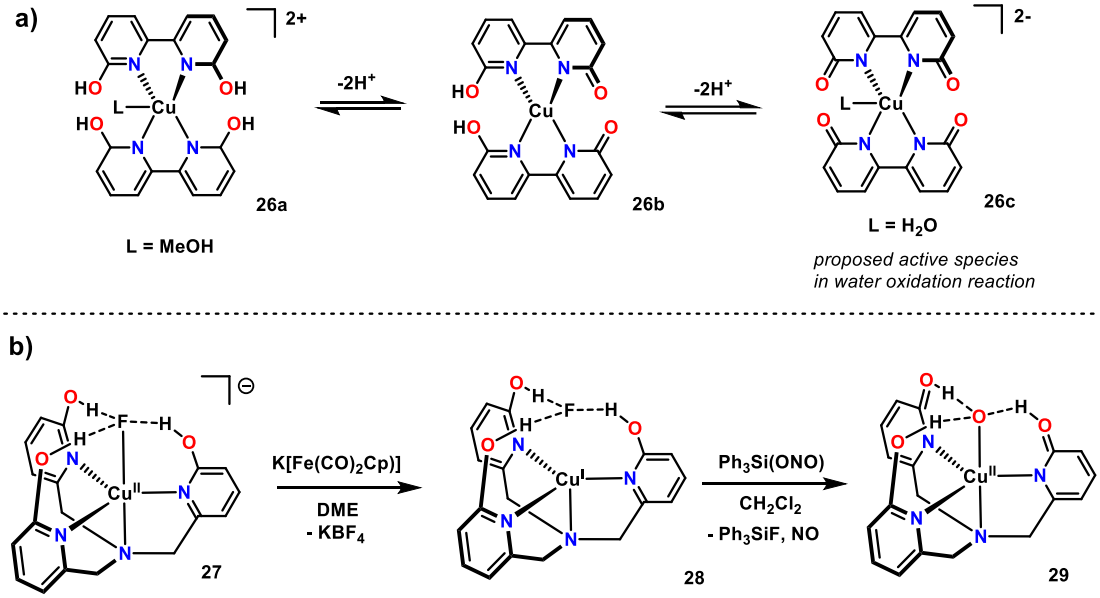

Scheme 2.11. a) Copper complexes featuring the 6,6′-dihydroxybipyridine ligand at different protonation states; b) Reactivity of copper complexes **27**, **28.**

2.4. Summary and Conclusions

2-Pyridone/2-Pyridonate ligand platform demonstrate very diverse coordination chemistry. Pyridonates can provide access to polynuclear compounds (μ_n coordination) as well as support mononuclear metal complexes (κ^1, κ^2 coordination). Metal pyridonate complexes are therefore characterized by unique set of properties including, hemilabilty, metal-ligand cooperativity and proton responsivity. Moreover, the metal-pyridinol motif plays a key role in hydrogen activation within in the active site of [Fe]-hydrogenase metalloenzyme.

Pyridonates are a very attractive ligand class for the development of metal complexes with catalytic applications. In contrast to the conventional ligands used in industry and academia, (e.g., phosphines, carbenes), pyridonates does not contain heavy atoms and are cheap to synthesize.

To date, most examples of catalytically relevant pyridonate complexes are noble metal based (Ir, Ru, Pd). However, over the last decades the interest in 3d transition metal pyridonates and their applications in catalysis has grown.

Early transition metal pyridonates (Ti, V) showed catalytic activity in carbon-nitrogen (hydroaminoalkylation) and carbon-carbon (deoxygenative coupling) forming reactions as well as polymerizations. Interestingly, no literature precedents of mononuclear chromium pyridonates are known to date. Later 3d transition metal pyridonates (Mn - Cu) demonstrated activity in different reductive transformations including hydrogenation, hydroboration as well as electrocatalytic water oxidation. Also, series of Fe and Mn biomimetic models of [Fe]-hydrogenase were developed. In many cases the essential role of the 2-O/2-OH group in the pyridonate during catalysis was proven. Metal ligand cooperativity and/or hemilabilty was often postulated to be main attribute responsible for catalytic performance.

In terms of ligand functionalization, the most common strategies are (a) to incorporate additional donor group such as phosphine, imine or NHC (complexes **19**, **23**, **24**, **25**) into the 6-position of pyridone ring; and (b) to link two pyridonate fragments, forming 6,6´- bipyridone scaffolds (**14**, **15**, **18**, **26**). In these ways, additional chelation favors stabilization of mononuclear complexes and induces κ^1-N bonding motif in pyridonate with pendent, uncoordinated oxygen atom. Pyridonates in κ^1-N bonding mode resemble motif in [Fe]-hydrogenase and demonstrate cooperative bond-activation patterns (as representative examples see Schemes 2.8, 2.9).

Consequently, pyridonate ligands appear as valuable addition to the “coordination chemist´s toolbox”. Therefore, the synthetic diversification of pyridonate ligand platform, the design of the new pyidonate coomplexes and their broad applications as catalysis are anticipated.

2.5. References

[1] R. J. Lundgren, M. Stradiotto, *Ligand Design in Metal Chemistry: Reactivity and Catalysis* **2016**, 1–14.

[2] E. C. Constable, C. E. Housecroft, *Chem. Soc. Rev.* **2013**, *42*, 1429–1439.

[3] R. H. Cox, A. A. Bothner-By, *J. Phys. Chem.* **1969**, *73*, 2465–2468.

[4] J. Frank, A. R. Katritzky, *J. Chem. Soc., Perkin Trans. 2,* **1976**, 1428–1431.

[5] M. J. Cook, A. R. Katritzky, L. G. Hepler, T. Matsui, *Tetrahedron Lett.* **1976**, *17*, 2685–2688.

[6] S. A. Ryken, P. R. Payne, L. L. Schafer, in *Ligand Design in Metal Chemistry: Reactivity and Catalysis*, **2016**, pp. 364–405.

[7] C. M. Moore, E. W. Dahl, N. K. Szymczak, *Curr. Opin. Chem. Biol.* **2015**, *25*, 9–17.

[8] M. W. Drover, J. A. Love, L. L. Schafer, *Chem. Soc. Rev.* **2017**, *46*, 2913–2940.

[9] J. M. Rawson, R. E. P. Winpenny, *Coord. Chem. Rev.* **1995**, *139*, 313–374.

[10] J. C. Jeffrey, T. B. Rauchfuss, *Inorg. Chem.* **1979**, *18*, 2658–2666.

[11] J. M. Clarkson, L. L. Schafer, *Inorg. Chem.* **2017**, *56*, 5553–5566.

[12] J. R. Khusnutdinova, D. Milstein, *Angew. Chem. Int. Ed.* **2015**, *54*, 12236–12273.

[13] M. R. Elsby, R. T. Baker, *Chem. Soc. Rev.* **2020**, *49*, 8933–8987.

[14] T. P. Gonçalves, I. Dutta, K. W. Huang, *Chem. Commun.* **2021**, *57*, 3070–3082.

[15] C. Wang, Z. Lai, G. Huang, H.-J. Pan, *Chem. Eur. J.* **2022**, *28*, e202201499.

[16] S. Shima, U. Ermler, *Eur. J. Inorg. Chem.* **2011**, 963–972.

[17] R. K. Thauer, *Microbiology* **1998**, *144*, 2377–2406.

[18] S. Shima, O. Pilak, S. Vogt, M. Schick, M. S. Stagni, W. Meyer-Klaucke, E. Warkentin, R. K. Thauer, U. Ermler, *Science.* **2008**, *321*, 572–575.

[19] G. Huang, T. Wagner, M. D. Wodrich, K. Ataka, E. Bill, U. Ermler, X. Hu, S. Shima, *Nat. Catal.* **2019**, *2*, 537–543.

[20] S. A. Kerns, M. J. Rose, *Acc. Chem. Res.* **2020**, *53*, 1637–1647.

[21] P. J. Turrell, J. A. Wright, J. N. T. Peck, V. S. Oganesyan, C. J. Pickett, *Angew. Chem. Int. Ed.* **2010**, *49*, 7508–7511.

[22] P. J. Turrell, A. D. Hill, S. K. Ibrahim, J. A. Wright, C. J. Pickett, *Dalton Trans.* **2013**, *42*, 8140–8146.

[23] B. V. Obrist, D. Chen, A. Ahrens, V. Schünemann, R. Scopelliti, X. Hu, *Inorg. Chem.* **2009**, *48*, 3514–3516.

[24] D. Chen, A. Ahrens-Botzong, V. Schünemann, R. Scopelliti, X. Hu, *Inorg. Chem.* **2011**, *50*, 5249–5257.

[25] B. Hu, D. Chen, X. Hu, *Chem. A Eur. J.* **2014**, *20*, 1677–1682.

[26] S. Shima, D. Chen, T. Xu, M. D. Wodrich, T. Fujishiro, K. M. Schultz, J. Kahnt, K. Ataka, X. Hu, *Nat. Chem.* **2015**, *7*, 995–1002.

[27] L. C. Song, F. Q. Hu, G. Y. Zhao, J. W. Zhang, W. W. Zhang, *Organometallics* **2014**, *33*, 6614–6622.

[28] T. Xu, C. J. M. Yin, M. D. Wodrich, S. Mazza, K. M. Schultz, R. Scopelliti, X. Hu, *J. Am. Chem. Soc.* **2016**, *138*, 3270–3273.

[29] H. J. Pan, G. Huang, M. D. Wodrich, F. F. Tirani, K. Ataka, S. Shima, X. Hu, *Nat. Chem.* **2019**, *11*, 669–675.

[30] P. W. Schlichter Christophe, *Synthesis (Stuttg).* **2021**, *54*, 517–534.

[31] K. I. Fujita, N. Tanino, R. Yamaguchi, *Org. Lett.* **2007**, *9*, 109–111.

[32] A. M. Royer, T. B. Rauchfuss, D. L. Gray, *Organometallics* **2010**, *29*, 6763–6768.

[33] R. Yamaguchi, C. Ikeda, Y. Takahashi, K. I. Fujita, *J. Am. Chem. Soc.* **2009**, *131*, 8410–8412.

[34] W. H. Wang, J. F. Hull, J. T. Muckerman, E. Fujita, Y. Himeda, *Energy Environ. Sci.* **2012**, *5*, 7923–7926.

[35] M. Iguchi, H. Zhong, Y. Himeda, H. Kawanami, *Chem. Eur. J.* **2017**, *23*, 17788–17793.

[36] K. I. Fujita, R. Kawahara, T. Aikawa, R. Yamaguchi, *Angew. Chem. Int. Ed.* **2015**, *54*, 9057–9060.

[37] J. B. Geri, N. K. Szymczak, *J. Am. Chem. Soc.* **2015**, *137*, 12808–12814.

[38] M. Galiana-Cameo, A. Urriolabeitia, E. Barrenas, V. Passarelli, J. J. Pérez-Torrente, A. Di Giuseppe, V. Polo, R. Castarlenas, *ACS Catal.* **2021**, *11*, 7553–7567.

[39] P. Wang, P. Verma, G. Xia, J. Shi, J. X. Qiao, S. Tao, P. T. W. Cheng, M. A. Poss, M. E. Farmer, K. S. Yeung, J. Q. Yu, *Nature* **2017**, *551*, 489–493.

[40] E. Chong, L. L. Schafer, *Org. Lett.* **2013**, *15*, 6002–6005.

[41] J. A. Bexrud, P. Eisenberger, D. C. Leitch, P. R. Payne, L. L. Schafer, *J. Am. Chem. Soc.* **2009**, *131*, 2116–2118.

[42] S. A. Ryken, L. L. Schafer, *Acc. Chem. Res.* **2015**, *48*, 2576–2586.

[43] S. E. Griffin, O. V. Adamczyk, L. L. Schafer, *Dalton Trans.* **2022**, *51*, 14654–14663.

[44] S. E. Griffin, L. L. Schafer, *Inorg. Chem.* **2020**, *59*, 5256–5260.

[45] A. Dubey, L. Nencini, R. R. Fayzullin, C. Nervi, J. R. Khusnutdinova, *ACS Catal.* **2017**, *7*, 3864–3868.

[46] A. Dubey, S. M. W. Rahaman, R. R. Fayzullin, J. R. Khusnutdinova, *ChemCatChem* **2019**, *11*, 3844–3852.

[47] X. Yan, H. Ge, X. Yang, *Catal. Sci. Technol.* **2018**, *8*, 5735–5739.

[48] C. Zhang, B. Hu, D. Chen, H. Xia, *Organometallics* **2019**, *38*, 3218–3226.

[49] A. J. Blake, L. M. Gilby, S. Parsons, J. M. Rawson, D. Reed, G. A. Solan, R. E. P. Winpenny, *J. Chem. Soc. - Dalton Trans.* **1996**, 3575–3581.

[50] M. L. Tong, Z. J. Lin, W. Li, S. L. Zheng, X. M. Chen, *Cryst. Growth Des.* **2002**, *2*, 443–448.

[51] Y. M. Badiei, W. H. Wang, J. F. Hull, D. J. Szalda, J. T. Muckerman, Y. Himeda, E. Fujita, *Inorg. Chem.* **2013**, *52*, 12576–12586.

[52] X. Zhuang, J. Y. Chen, Z. Yang, M. Jia, C. Wu, R. Z. Liao, C. H. Tung, W. Wang, *Organometallics* **2019**, *38*, 3752–3759.

[53] M. D. Santana, G. García, A. Rufete, G. Sánchez, M. C. R. De Arellano, G. López, *Inorg. Chem. Commun.* **1998**, *1*, 267–269.

[54] S. Chakraborty, P. E. Piszel, W. W. Brennessel, W. D. Jones, *Organometallics* **2015**, *34*, 5203–5206.

[55] S. T. Goralski, T. A. Manes, S. E. A. Lumsden, V. M. Lynch, M. J. Rose, *Organometallics* **2020**, *39*, 1070–1079.

[56] M. Afandiyeva, A. A. Kadam, X. Wu, W. W. Brennessel, C. R. Kennedy, *Organometallics* **2022**, *41*, 3014–3023.

[57] aD. L. Gerlach, S. Bhagan, A. A. Cruce, D. B. Burks, I. Nieto, H. T. Truong, S. P. Kelley, C. J. Herbst-Gervasoni, K. L. Jernigan, M. K. Bowman, S. Pan, M. Zeller, E. T. Papish, *Inorg. Ch=em.* **2014**, 53, 12689–12698

[58] C. M. Moore, D. A. Quist, J. W. Kampf, N. K. Szymczak, *Inorg. Chem.* **2014**, *53*, 3278–3280.

[59] C. M. Moore, N. K. Szymczak, *Chem. Commun.* **2015**, *51*, 5490–5492.

[60] C. M. Moore, N. K. Szymczak, *Chem. Sci.* **2015**, *6*, 3373–3377.

3. Bis[bis(trimethylsilyl)amido]iron(II)

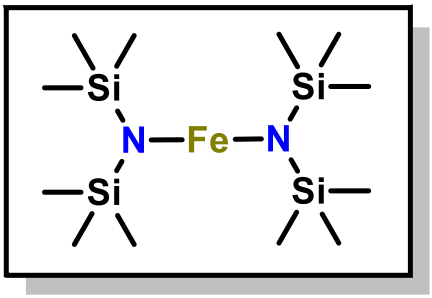

Abstract: Bis[bis(trimethylsilyl)amido]iron(II) or $Fe(hmds)_2$ is a convenient precursor of various Fe(II) complexes by virtue of its high solubility in organic solvents, the absence of halides, and the facile exchange of the sterically bulky amido ligands by protolytic ligand exchange.

[14760-22-6] $C_{12}H_{36}FeN_2Si_4$ (MW 376.62)

(main use as a halide-free, soluble precursor for low coordinate Fe(II) complexes)

[i] Reproduced from Fedulin, A.; Jacobi von Wangelin, A. Bis[bis(trimethylsilyl)amido]iron(II): Silanamine, 1,1,1-trimethyl-N-(trimethylsilyl)-, iron(2+) salt (2:1), 2019, *Encyclopedia of Reagents for Organic Synthesis*

with permission of Wiley-VCH. Schemes, tables and text may differ from published version.

[ii] Author contributions: AF manuscript preparation AJvW corresponding author, manuscript revision and correction.

3.1. General Properties

Alternate Name: iron(II) bis(1,1,1,3,3,3-hexamethyl-disilazan2-ide), $Fe(hmds)_2$

Physical Data: m.p. – 36–38 °C, bp 90–100 °C under 0.01 mmHg[1], magnetic susceptibility μ_{eff} = 3.52 μ_B (282K)[2]

Solubility: very soluble in hydrocarbon solutions, Et_2O, forms adduct with THF, reacts with protic solvents.

Form Supplied in: light green solid

Analysis of Reagent Purity: ^1H NMR (400 MHz, C_6D_6) 64,9 ppm (broad singlet)[3]

Mössbauer spectroscopy 80 K (δ = 0.59 mm/s and ΔE_Q = 1.02 mm/s)[3]

Preparative Methods:

$Fe\{N(SiMe_3)_2\}_2$ is prepared by salt metathesis between 2 equiv. $LiN(SiMe_3)_2$ and $FeBr_2(THF)_2$ in diethyl ether.[2] The THF adduct $Fe\{N(SiMe_3)_2\}_2 \cdot THF$ might form upon workup.[3] A THF-free synthesis of $Fe\{N(SiMe_3)_2\}_2$ starts from anhydrous $FeCl_2$:

Inside a N_2-filled glovebox, a Schlenk flask was charged with crushed anhydrous $FeCl_2$ beads (3.80 g, 30.0 mmol) and Et_2O (120 mL). The stirred suspension was cooled to 0 °C, after which a solution of $LiN(SiMe_3)_2$ (10.0 g, 60.0 mmol) in Et_2O (180 mL) was added dropwise (~3 drops/s). The suspension was allowed to warm slowly to ambient temperature and was stirred for 20 h. Volatile materials were removed under vacuum, and the dark-green residue was extracted with pentane (3 × 25 mL). The dark-green extracts were filtered, transferred into a round-bottom Schlenk flask, and concentrated under vacuum to a dark-green oil. The Schlenk flask was connected to a distillation apparatus, and the oil was distilled under reduced pressure (30 mTorr) to afford a pyrophoric green oil at 80−90 °C (sole fraction; oil bath temperature 105−110 °C). The product was directly transferred into a N_2-filled glovebox, and the oil solidified upon cooling to afford a light-green solid (9.9 g, 88% yield)[3].

Purification: distillation under reduced pressure[1]

Handling, Storage, and Precautions: extremely air- and moisture-sensitive compound, must be stored under a strictly inert atmosphere. Care should be taken when handling this material in large quantities as it can spontaneously combust upon exposure to air.

3.2. Introduction

$Fe\{N(SiMe_3)_2\}_2$ is monomeric in gas phase,[2] exhibits monomer-dimer equilibrium in solution (studied by variable-temperature ^{1}H-NMR, $K_{eq} = 5 \cdot 10^{-3}$ at 300 K in toluene-d_6, see eq. 1)[4] and is an amido-bridged dimer in solid state[4].

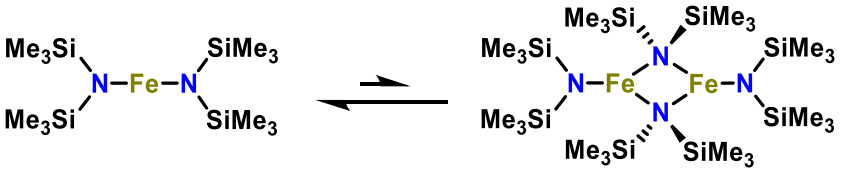

(1)

Due to the high solubility in hydrocarbon solvents and the polarity of the M-N bond, $Fe\{N(SiMe_3)_2\}_2$ can be readily used for the preparation of various low-coordinate iron complexes and catalysts.

3.3. Complexation with Lewis Bases

Due to its low coordination number and open-shell structure, $Fe(hmds)_2$ readily bind various Lewis bases. $Fe(hmds)_2$ undergoes reversible THF complexation (eq. 2).[5] The monomeric THF-adduct is a pale-blue solid[4] which partially loses THF upon distillation.[5]

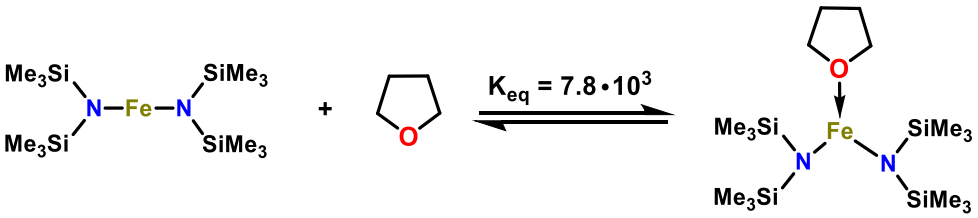

(2)

The addition of pyridine in hexane solution affords the bispyridine complex (**1**) as air-sensitive red crystals (eq. 3). After vacuum sublimation, the monopyridine complex (**2**) was isolated as green crystals.[6] Treatment of $Fe(hmds)_2$ with 4,4'-bipyridyl (4,4'-bipy) afforded polymeric adducts with zig-zag structure.[6]

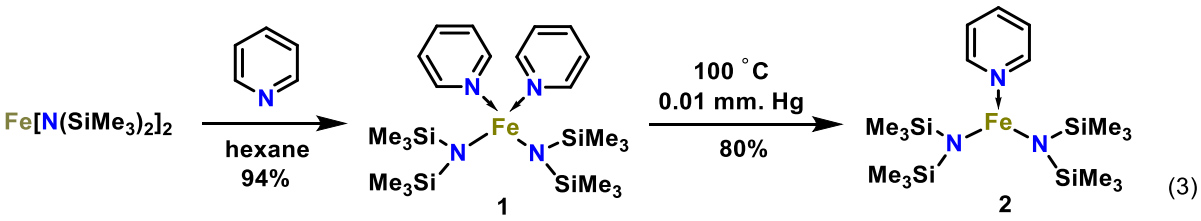

(3)

Reactions with phosphine $PCyp_3$ (Cyp = cyclopentyl) have been performed to give the adduct $Fe(hmds)_2 \cdot PCyp_3$.[7] The three-component reaction of $FeCl_2$, $KN(SiMe_3)_2$ and phosphines (PCy_3 [8], $(Et_2PCH_2)_2$ [9]) afforded corresponded phosphine complexes $Fe(hmds)_2$ PCy_3 and $Fe(hmds)_2$ $Et_2PCH_2)_2$. *N*-Heterocyclic carbenes (NHC) [10-12] and silylenes[13] also underwent facile addition to $Fe(hmds)_2$ in toluene solution to give the three-coordinate $LFe(hmds)_2$ complexes in 53-73% yields (eq. 4).

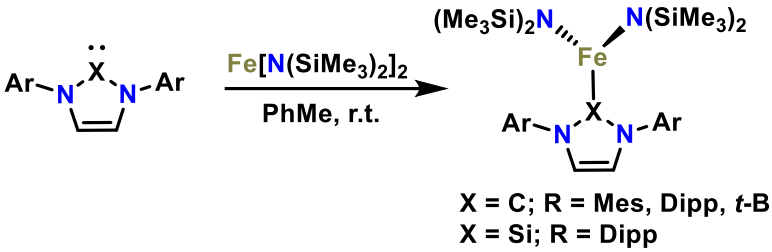

(4)

Besides coordination of neutral Lewis bases, $Fe(hmds)_2$ forms adducts with further anionic ligands (eq. 5).[14-17]

(5)

3.4. Ligand Substitution by Protonolysis

The highly polar character of the Fe-N bonds in $Fe(hmds)_2$ enable rapid protonolysis by reactions with protic reagents R_nXH. The volatile hexamethylsilazane is the only by-product. The selective substitution of one or two amido substituents can be achieved with stoichiometric amounts of the protic reagent. Amido group exchange with various other amines was effected under thermal conditions with aliphatic[18] and aromatic[19-20] amines (eq 6).

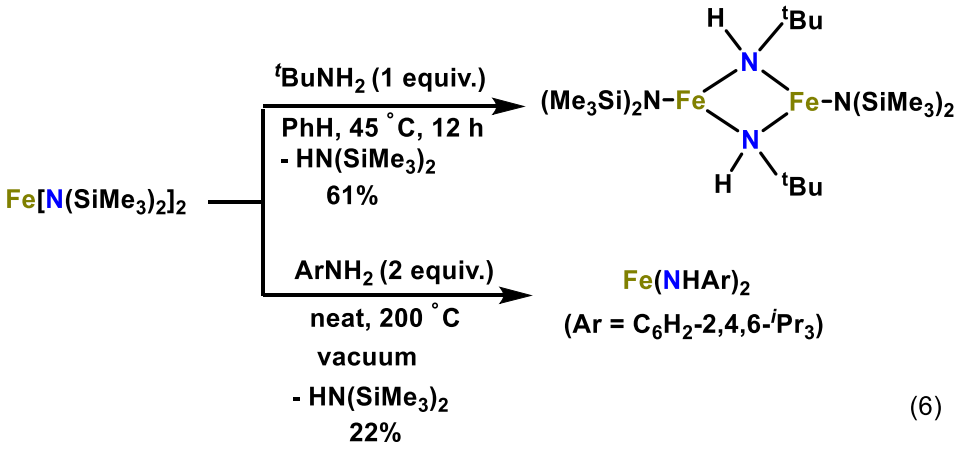

(6)

Homoleptic and heteroleptic pyridyl amide ligands have been introduced by the same route.[21-23] Tetra-coordinate pyrrole-phosphine pincer iron complexes were prepared (eq. 7).[24-25] β-Ketimines (eq. 8)[26] and formazan[27] undergo ligand substitution under similar conditions.

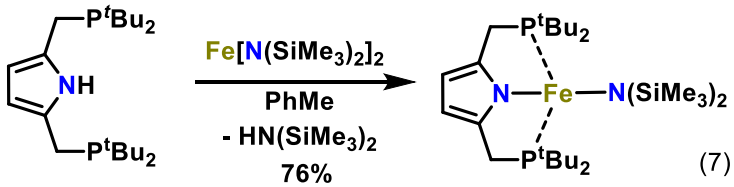

(7)

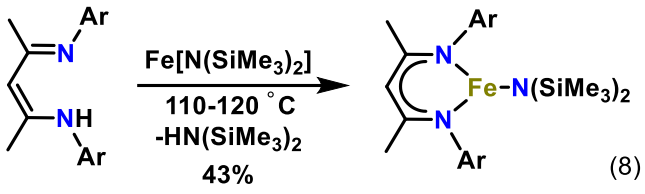

(8)

Ar =C_6H_3-2,6-*i*-Pr_2

Ligand-backbone deprotonation leads to an octahedral amidoiron complex (**3**) with the NPN-ligand shown in eq. 9.[28]

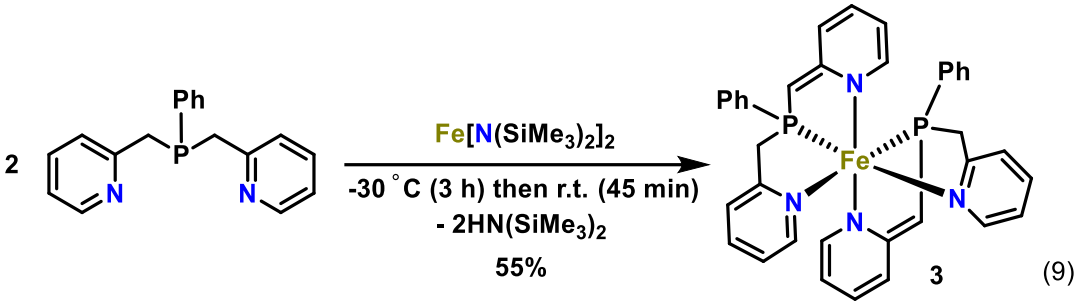

(9)

Alcohols (phenols,[29-30] catechols,[31] silanols[32-33]) give similar protolytic reactions to form alkoxide complexes (eq. 10).

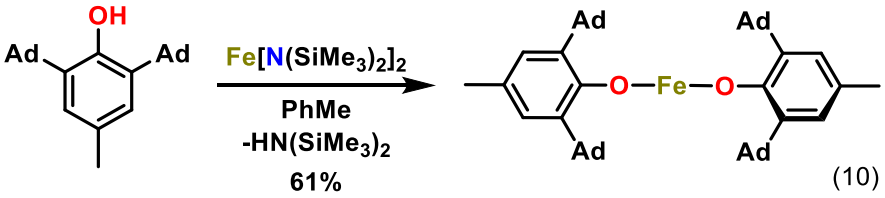

(10)

Protolytic amido group displacement was reported with phosphines ($HPMes_2$) and arsines ($HAsMes_2$).[34] Reactions of $Fe(hmds)_2$ with substituted imidazolium salts led to the formation of N-heterocyclic carbene (NHC) complexes (eq. 11).[35-36]

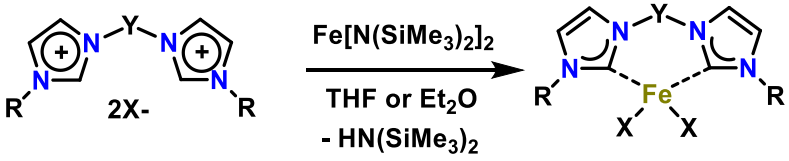

R = Me, Et, Bn, ^{t}Bu, Mes, Ad
X = Br, Cl
Y = CH_2, $(CH_2)_2$, $(CH_2)_3$, CHPh

(11)

The reaction of $Fe(hmds)_2$ with various aromatic thiols[37-42] result in the formation of iron-thiolates which have been studied as precursors to biologically relevant iron-sulfur clusters.

3.5. Preparation of Metal Complex Clusters

$Fe(hmds)_2$ was employed as starting material for the synthesis of various iron-sulfur clusters that mimic the active site of proteinogenic clusters such as the nitrogenase.[43-49] For example, sequential treatment of $Fe(hmds)_2$ with substituted thiophenols,

N,*N'*-tetramethyl thiourea, and elemental sulfur (eq. 12) resulted in the self-assembly of a Fe_8S_7 cluster complex (**4**).[47]

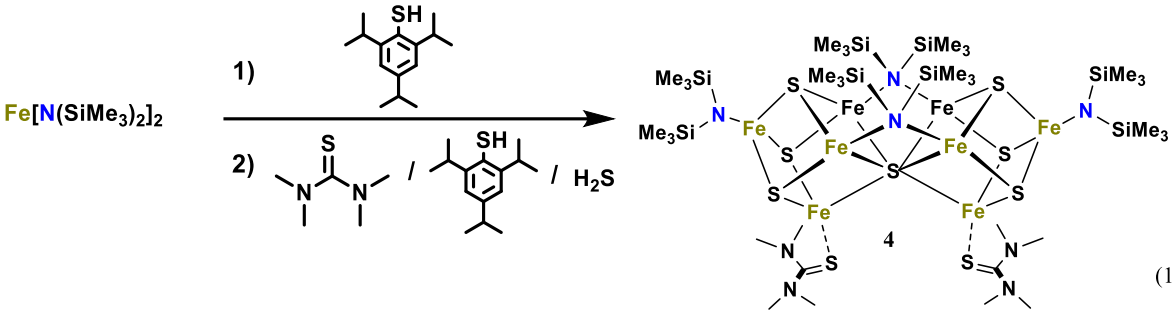

(12)

Hydrido-bridged iron amido clusters were prepared by stoichiometric ligand exchange with DIBAL-H (eq. 13)[50] or pinacolborane[51] to give planar Fe_6 (**5**) and Fe_7 (**6**) nanoclusters.

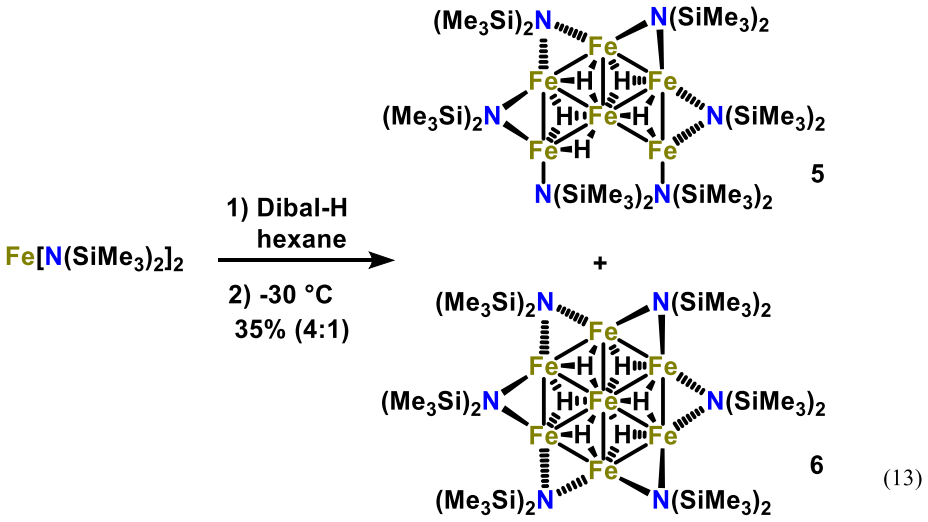

(13)

3.6. Catalytic Reactions

While $Fe(hmds)_2$ is widely used as a soluble and reactive precursor for the synthesis of various Fe(II) complexes by stoichiometric ligand exchange, there are only very few reports of the direct application of $Fe(hmds)_2$ as catalyst to organic transformations. The hydrosilyation of carbonyl compounds was reported (eq. 14).[52]

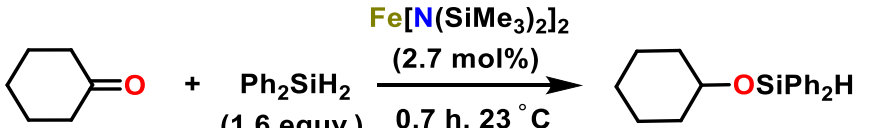

(14)

In combination with co-catalytic Dibal-H, $Fe(hmds)_2$ forms one of the most active catalyst for the hydrogenation of various alkenes and alkynes including challenging tetra-substituted alkenes (eq. 15)[50]. The reaction appears to involve conversion of intermediate clusters into catalytically active Fe(0) nanoparticles.

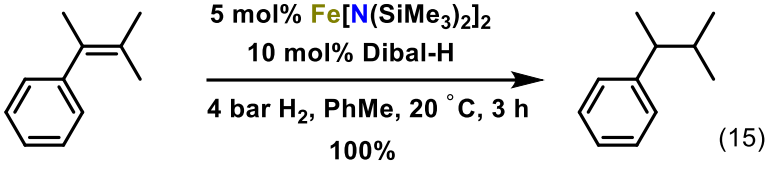

(15)

Low loadings of Fe(hmds)$_2$ were reported to catalyze the [2+2+2]-cyclotrimerization of terminal alkynes to substituted benzenes with high regioselectivity toward the 1,2,4-isomers (eq. 16).[53]

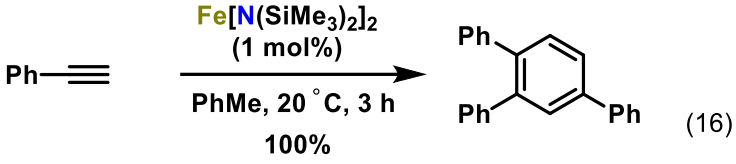

(16)

The dehydrogenative coupling between N-heterocyclic carbenes and monoarylphosphines was catalyzed by Fe(hmds)$_2$ at 80 °C (eq. 17) to give carbene–phosphinidene adducts of type **7**.[54]

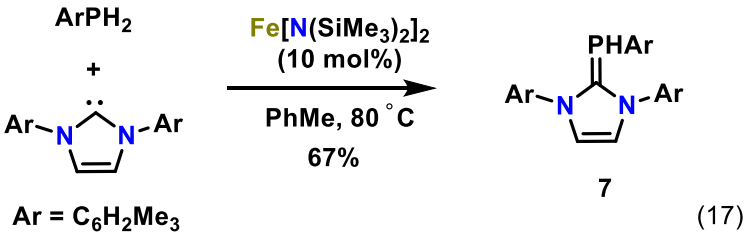

(17)

Small Fe(0) nanoparticles of <10 nm can be prepared by reaction of Fe(hmds)$_2$ with dihydrogen H_2 at elevated temperature.[55] The resultant (and similarly prepared) nanoparticles have been applied as catalysts in alkene hydrogenations.[56]

3.7. Miscellaneous Reactions

The one-electron reduction of Fe(hmds)$_2$ with KC_8 (eq. 18) was reported to give the anionic bis(hexamethyldisilazide)ferrate(I) as its potassium/crown ether salt.[57]

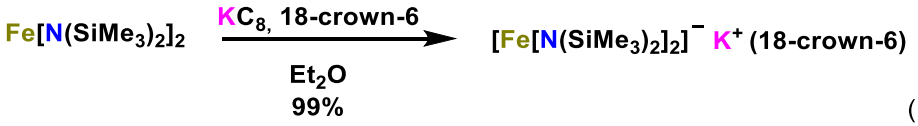

(18)

3.7. References

1. Y. Ohki, S. Ohta, K. Tatsumi, L. Davis, G. Girolami, A. Royer, T. Rauchfuss, *Inorg. Synth.* **2010**, *35*, 137-142.

2. R. A. Andersen, K. Faegri, J. C. Green, A. Haaland, M. F. Lappert, W. P. Leung, K. Rypdal, *Inorg. Chem.* **1988**, *27*, 1782.

3. D. L. Broere, I. Coric, A. Brosnahan, P. L. Holland, *Inorg. Chem.* **2017**, *56*, 3140.

4. M. M. Olmstead, P. P. Power, S. C. Shoner, *Inorg. Chem.* **1991**, *30*, 2547.

5. C.-Y. Lin, J. C. Fettinger, P. P. Power, *Inorg. Chem.* **2017**, *56*, 9892.

6. A. Panda, M. Stender, M. M. Olmstead, P. Klavins, P. P. Power, *Polyhedron* **2003**, *22*, 67.

7. C. G. Werncke, L. Vendier, S. Sabo-Etienne, J.-P. Sutter, C. Pichon, S. Bontemps, *Eur. J. Inorg. Chem.* **2017**, *2017*, 1041.

8. P.-H. Lin, N. C. Smythe, S. I. Gorelsky, S. Maguire, N. J. Henson, I. Korobkov, B. L. Scott, J. C. Gordon, R. T. Baker, M. Murugesu, *J. Am. Chem. Soc.* **2011**, *133*, 15806.

9. R. T. Baker, J. C. Gordon, C. W. Hamilton, N. J. Henson, P.-H. Lin, S. Maguire, M. Murugesu, B. L. Scott, N. C. Smythe, *J. Am. Chem. Soc.* **2012**, *134*, 5598.

10. R. A. Layfield, J. J. W. McDouall, M. Scheer, C. Schwarzmaier, F. Tuna, *Chem. Commun.* **2011**, *47*, 10623.

11. B. M. Day, T. Pugh, D. Hendriks, C. F. Guerra, D. J. Evans, F. M. Bickelhaupt, R. A. Layfield, *J. Am. Chem. Soc.* **2013**, *135*, 13338.

12. K. Pal, O. B. Hemming, B. M. Day, T. Pugh, D. J. Evans, R. A. Layfield, *Angew. Chem. Int. Ed.* **2016**, *55*, 1690.

13. M. M. Hänninen, K. Pal, B. M. Day, T. Pugh, R. A. Layfield, *Dalton Trans.* **2016**, *45*, 11301.

14. L. C. Maddock, T. Cadenbach, A. R. Kennedy, I. Borilovic, G. Aromi, E. Hevia, *Inorg. Chem.* **2015**, *54*, 9201.

15. M. A. Putzer, B. Neumüller, K. Dehnicke, J. Magull, *Chem. Ber.* **1996**, *129*, 715.

16. S. N. König, D. Schneider, C. Maichle-Mössmer, B. M. Day, R. A. Layfield, R. Anwander, *Eur. J. Inorg. Chem.* **2014**, *2014*, 4302.

17. S. A. Sulway, D. Collison, J. J. McDouall, F. Tuna, R. A. Layfield, *Inorg. Chem.* **2011**, *50*, 2521.

18. X.-D. Chen, W. Zhang, J. S. Duncan, S. C. Lee, *Inorg. Chem.* **2012**, *51*, 12891.

19. W. A. Merrill, T. A. Stich, M. Brynda, G. J. Yeagle, J. C. Fettinger, R. De Hont, W. M. Reiff, C. E. Schulz, R. D. Britt, P. P. Power, *J. Am. Chem. Soc.* **2009**, *131*, 12693.

20. A. Malassa, C. Agthe, H. Görls, M. Podewitz, L. Yu, C. Herrmann, M. Reiher, M. Westerhausen, *Eur. J. Inorg. Chem.* **2010**, *2010*, 1777.

21. A. Malassa, C. Agthe, H. Görls, M. Friedrich, M. Westerhausen, *J. Organomet. Chem.* **2010**, *695*, 1641.

22. C. Koch, A. Malassa, C. Agthe, H. Görls, R. Biedermann, H. Krautscheid, M. Westerhausen, *Z. Anorg. Allg. Chem.* **2007**, *633*, 375.

23. C. G. Werncke, M. A. Bouammali, J. Baumard, N. Suaud, C. Martins, N. Guihery, L. Vendier, J. Zheng, J. B. Sortais, C. Darcel, S. Sabo-Etienne, J. P. Sutter, S. Bontemps, C. Pichon, *Inorg. Chem.* **2016**, *55*, 10968.

24. N. Ehrlich, D. Baabe, M. Freytag, P. G. Jones, M. D. Walter, *Polyhedron* **2018**, *143*, 83.

25. H.-J. Lin, S. Lutz, C. O'Kane, M. Zeller, C.-H. Chen, T. Al Assil, W.-T. Lee, *Dalton Trans.* **2018**, *47*, 3243.

26. A. Panda, M. Stender, R. J. Wright, M. M. Olmstead, P. Klavins, P. P. Power, *Inorg. Chem.* **2002**, *41*, 3909.

27. D. L. J. Broere, B. Q. Mercado, J. T. Lukens, A. C. Vilbert, G. Banerjee, H. M. C. Lant, S. H. Lee, E. Bill, S. Sproules, K. M. Lancaster, P. L. Holland, *Chem. Eur. J.* **2018**, *24*, 9417.

28. G. Jin, L. Vendier, Y. Coppel, S. Sabo-Etienne, S. Bontemps, *Dalton Trans.* **2015**, *44*, 7500.

29. T. Hatanaka, R. Miyake, Y. Ishida, H. Kawaguchi, *J. Organomet. Chem.* **2011**, *696*, 4046.

30. R. A. Bartlett, J. J. Ellison, P. P. Power, S. C. Shoner, *Inorg. Chem.* **1991**, *30*, 2888.

31. S. C. Shoner, P. P. Power, *Inorg. Chem.* **1992**, *31*, 1001.

32. A. W. Holland, G. Li, A. M. Shahin, G. J. Long, A. T. Bell, T. D. Tilley, *J. Catal.* **2005**, *235*, 150.

33. U. N. Nehete, G. Anantharaman, V. Chandrasekhar, R. Murugavel, M. G. Walawalkar, H. W. Roesky, D. Vidovic, J. Magull, K. Samwer, B. Sass, *Angew. Chem. Int. Ed.* **2004**, *43*, 3832.

34. H. Chen, M. M. Olmstead, D. C. Pestana, P. P. Power, *Inorg. Chem.* **1991**, *30*, 1783.

35. K. Riener, S. Haslinger, A. Raba, M. P. Högerl, M. Cokoja, W. A. Herrmann, F. E. Kühn, *Chem. Rev.* **2014**, *114*, 5215.

36. V. Charra, P. de Frémont, P. Braunstein, *Coord. Chem. Rev.* **2017**, *341*, 53.

37. J. J. Ellison, K. Ruhlandt-Senge, P. P. Power, *Angew. Chem. Int. Ed.* **1994**, *33*, 1178.

38. F. M. MacDonnell, K. Ruhlandt-Senge, J. J. Ellison, R. H. Holm, P. P. Power, *Inorg. Chem.* **1995**, *34*, 1815.

39. R. Hauptmann, R. Kliß, J. Schneider, G. Henkel, *Z. Anorg. Allg. Chem.* **1998**, *624*, 1927.

40. A. K. Verma, S. C. Lee, *J. Am. Chem. Soc.* **1999**, *121*, 10838.

41. T. Komuro, H. Kawaguchi, K. Tatsumi, *Inorg. Chem.* **2002**, *41*, 5083.

42. S. Ohta, Y. Ohki, Y. Ikagawa, R. Suizu, K. Tatsumi, *J. Organomet. Chem.* **2007**, *692*, 4792.

43. Y. Ohki, Y. Sunada, M. Honda, M. Katada, K. Tatsumi, *J. Am. Chem. Soc.* **2003**, *125*, 4052.

44. Y. Ohki, Y. Sunada, K. Tatsumi, *Chem. Lett.* **2005**, *34*, 172.

45. Y. Ohki, Y. Ikagawa, K. Tatsumi, *J. Am. Chem. Soc.* **2007**, *129*, 10457.

46. R. Pryadun, R. H. Holm, *Inorg. Chem.* **2008**, *47*, 3366.

47. Y. Ohki, M. Imada, A. Murata, Y. Sunada, S. Ohta, M. Honda, T. Sasamori, N. Tokitoh, M. Katada, K. Tatsumi, *J. Am. Chem. Soc.* **2009**, *131*, 13168.

48. Y. Ohki, A. Murata, M. Imada, K. Tatsumi, *Inorg. Chem.* **2009**, *48*, 4271.

49. S. Ohta, S. Yokozawa, Y. Ohki, K. Tatsumi, *Inorg. Chem.* **2012**, *51*, 2645.

50. T. N. Gieshoff, U. Chakraborty, M. Villa, A. Jacobi von Wangelin, *Angew. Chem. Int. Ed.* **2017**, *56*, 3585.

51. R. Araake, K. Sakadani, M. Tada, Y. Sakai, Y. Ohki, *J. Am. Chem. Soc.* **2017**, *139*, 5596.

52. J. Yang, T. D. Tilley, *Angew. Chem. Int. Ed.* **2010**, *49*, 10186.

53. D. Brenna, M. Villa, T. N. Gieshoff, F. Fischer, M. Hapke, A. Jacobi von Wangelin, *Angew. Chem. Int. Ed.* **2017**, *56*, 8451.

54. K. Pal, O. B. Hemming, B. M. Day, T. Pugh, D. J. Evans, R. A. Layfield, *Angew. Chem. Int. Ed.* **2016**, *55*, 1690.

55. L.-M. Lacroix, S. Lachaize, A. Falqui, M. Respaud, B. Chaudret, *J. Am. Chem. Soc.* **2009**, *131*, 549.

56. V. Kelsen, B. Wendt, S. Werkmeister, K. Junge, M. Beller, B. Chaudret, *Chem. Commun.* **2013**, *49*, 3416.

57. C. G. Werncke, P. C. Bunting, C. Duhayon, J. R. Long, S. Bontemps, S. Sabo-Etienne, *Angew. Chem. Int. Ed.* **2015**, *54*, 245.

4. Polynuclear Iron(II) Pyridonates: Synthesis and Reactivity of Fe_4 and Fe_5 Clusters

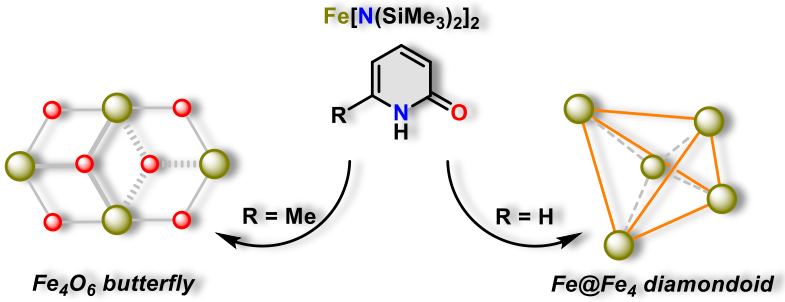

Abstract. Topologically new Fe_4 and Fe_5 clusters, $Fe_5(L^H)_6[N(SiMe_3)_2]_4$ (**1**) and $Fe_4(L^{Me})_6[N(SiMe_3)_2]_2$ (**2**), were synthesized (L^H = 2-pyridonate, L^{Me} = 6-methyl-L^H). **1** contained an unprecedented diamondoid Fe@Fe_4 tetrahedron; **2** displayed an Fe_4O_6 butterfly motif with planar Fe_4 arrangement. High-spin ferrous character (Mössbauer) and antiferromagnetic coupling across the pyridonates (SQUID) was confirmed. Complex **2** shows single-molecule magnet behavior with an effective barrier of 38.5 K. Reactivity studies documented high lability of cluster topologies and ligand coordination modes.

[i] Reproduced from Andrey Fedulin, Sandeep K. Gupta, Isabelle Rüter, Franc Meyer, and Axel Jacobi von Wangelin.Polynuclear Iron(II) Pyridonates: Synthesis and Reactivity of Fe_4 and Fe_5 Clusters. *Inorganic Chemistry* **2022**, *61*, 6149-6159. with permission of Wiley-VCH. Schemes, tables and text may differ from published version.

[ii] Author contributions: AF initiated the project, performed synthesis of clusters and analytical characterization. IR measured and analysed Mössbauer specta. SG performed SQUID measurements and data analysis. *FM* and AJvW guided the project. All authors contributed to the writing of the manuscript.

4.1. Introduction

Chelating *N*,*O*-ligands exhibit especially rich coordination chemistry with numerous applications in biology, medicine, chemical syntheses, materials, and catalysis. A large variety of such formal amino alcohol motifs are ubiquitous in nature or can be easily assembled from available and inexpensive building blocks. Among them, 1,3-*N*,*O*-ligands take a special position as they occur as the central function of amino acids, peptides, enzyme cofactors, and numerous synthetic amide moieties (carboxamides, ureas, sulfonamides, phosphoramides, etc.).[1] Strong chelation is observed with the anionic ligands that display σ- and π-bonding character to Lewis acidic metal ions. Pyridonates, the anions of 2-pyridones or 2-hydroxypyridines, are a versatile 1,3-*N*,*O*-chelating ligand platform that displays many favorable properties for rich coordination chemistry (Scheme 4.1).[2] The charge distribution between the *N*- and *O*-donor atoms shows great similarities to the ubiquitous families of carboxylate and amidate ligands. Fixation of the nitrogen in the aromatic ring results in high conformational rigidity. Diverse coordination modes with one, two, or three metal ions can be adopted, including metal chelation, metal-metal bridging, and hemilability. Pyridonates in chelating κ^2-mode are widely used as hemilabile scaffolds in catalytically active metal complexes.[3] The μ_n-bridging capacities of 2-pyridonates result in the formation of polynuclear metal complexes which have been studied for their magnetic cooperativity.[2,4]

The coordination chemistry of iron(II) ions with pyridonate ligands is rather under-explored despite the occurrence of a pyridone-iron complex in the active center of the [Fe]-hydrogenase.[5] A few related bioinspired Fe(II) model complexes have been prepared over the last decade.[6] However, the exploitation of the diverse κ- and μ-coordination modes of pyridonates for polynuclear iron complexes has not been widely explored. A single example of a ferrous pyridonate cluster was reported;[7] only very few polynuclear Fe(III)-pyridonates are known.[8] In an effort to address the knowledge gap of Fe(II) pyridonate clusters between the regimes of mononuclear and polynuclear complexes, we set out to explore ligand substitution reactions between the low-valent precursor $Fe(hmds)_2$, iron(II) bis(hexamethyldisilazide),[9] and 2-pyridone ligands. Such endeavor complemented our ongoing program of metal-hmds cluster synthesis.[10] Herein, we report the synthesis and characterization of structurally defined heteroleptic *N*,*N*,*O*-ligated Fe(II) clusters that bear pyridonates in κ^2,μ_2-coordination modes and labile amido ligands (Scheme 4.1). The isolated and fully characterized polynuclear complexes represent unprecedented examples of Fe(II) pyridonate clusters. They are easily accessible model compounds for investigations into pyridonate coordination modes, (potential) single-molecule magnets (SMM), and they can serve as pre-catalysts for organic transformations. The terminal bulky amido ligands may enable various routes of cluster derivatization such as protolytic ligand substitution with other monodentate ligands or syntheses of “higher-order” clusters, coordination polymers, or extended solids.

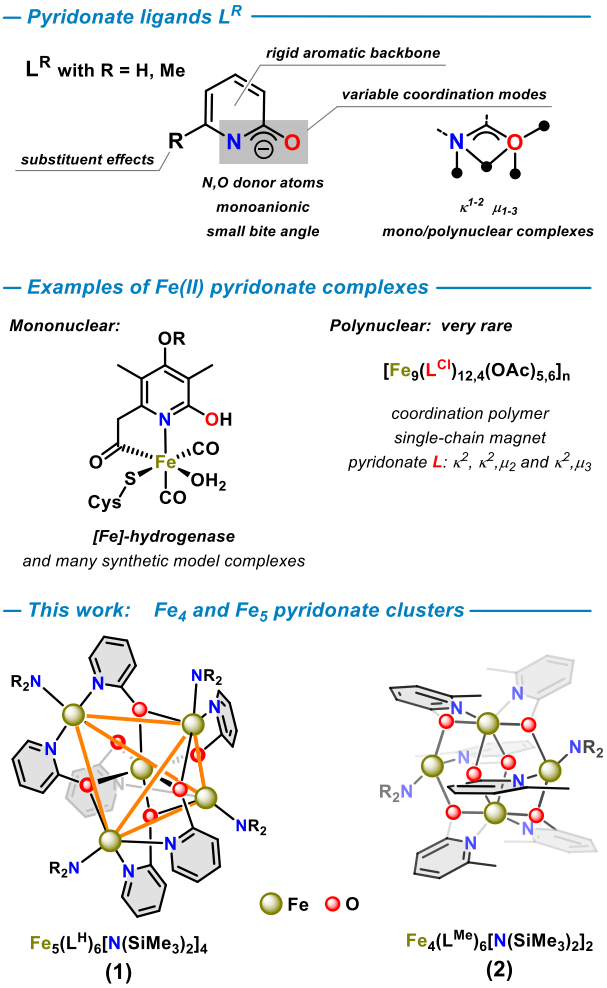

Scheme 4.1. The coordination chemistry of 2-pyridonate ligands (top). Rare applications of Fe(II) pyridonates in nature and synthesis (center). Synthesis of new Fe_5 and Fe_4 pyridonate clusters **1** and **2** (bottom).

4.2. Results and Discussion

4.2.1. Synthesis and Characterization of Fe_5 and Fe_4 Clusters

We investigated protolytic ligand substitutions of $Fe(hmds)_2$ with pyridin-2(*1H*)-one (L^HH) and 6-methylpyridin-2(*1H*)-one ($L^{Me}H$), respectively (Scheme 4.2). Both reactions cleanly afforded new polynuclear Fe(II) pyridonate clusters in high yields. Slow addition of the unsubstituted 2-pyridone (L^HH) to a solution of 1.2 equiv. of $Fe(hmds)_2$ in toluene, followed by solvent removal and washing with *n*-hexane afforded the topologically new complex $Fe_5(L^H)_6[N(SiMe_3)_2]_4$ as a yellow powder in 72% isolated yield. The complex is very sensitive to air and moisture as solid and in solution, which is evident from the rapid color change to dark brown. Small amounts of single crystals suitable for crystal structure analysis were obtained by crystallization from hexane/Et_2O (1:1) at -35 °C. Elemental analysis confirmed the cluster composition. The Evans NMR method gave a magnetic moment of μ_{eff} = 11.47 μ_B for 1 in C_6D_6 at 299 K, which is in agreement with SQUID magnetometry performed on polycrystalline interacting Fe(II), S = 2, g = 2.0, expected μ_{eff} = 10.95 μ_B) indicates orbital contributions

to the magnetic moment. The collected crystal structure data of $Fe_5(L^H)_6[N(SiMe_3)_2]_4$ (**1**) (Scheme 4.2) indicated that such pentanuclear coordination motif may be sensitive to substituents in the 6-position of the pyridonate ligand. We wondered whether a slightly bulkier ligand would deviate from this Fe@Fe_4 geometry. Consequently, 6-methyl pyridone ($L^{Me}H$) was added to 1.5 equiv. of $Fe(hmds)_2$. The resulting solid was recrystallized from hot toluene/*n*-hexane to afford the structurally different cluster $Fe_4(L^{Me})_6[N(SiMe_3)_2]_2$ (**2**) as pale-yellow microcrystals in 82% isolated yield.[11] Complex **2** is very sensitive to air and moisture as solid and in solution. The identity and purity of complex **2** were established by single-crystal structure analysis and elemental analysis (as toluene monosolvate). A magnetic moment of μ_{eff} = 10.5 B.M. at room temperature for the Fe_4 complex **2** was determined by the Evans NMR method (THF-d_8, 300 K). The slightly larger value (four isolated non-interacting Fe(II), S = 2, g = 2.0, expected μ_{eff} = 9.8 μ_B) indicates orbital contributions to the magnetic moment and is in accord with the SQUID magnetometry data for solid **2** (Figure 4.28).

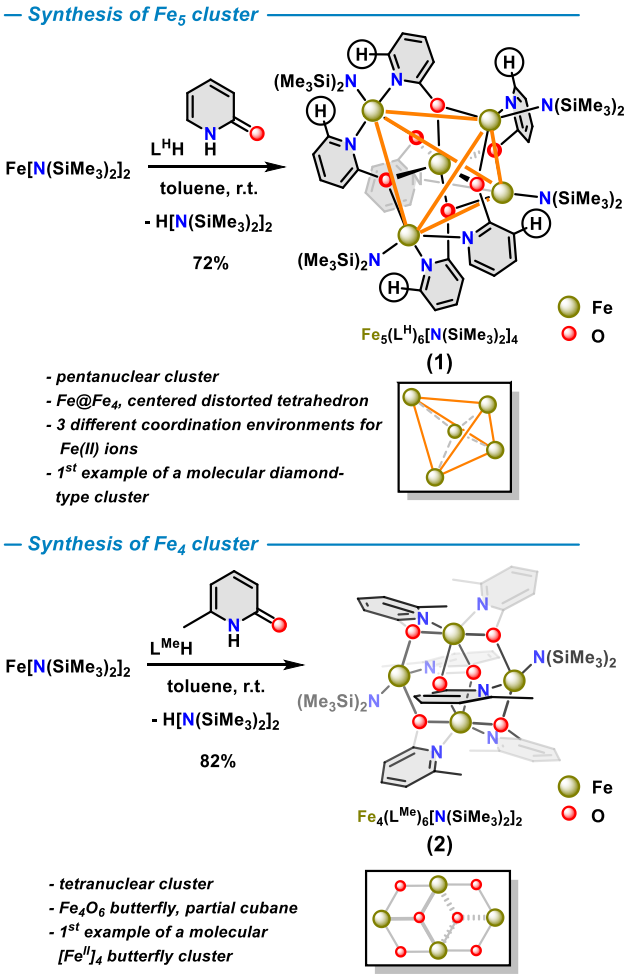

Scheme 4.2. Synthesis of pentanuclear cluster **1** and tetranuclear cluster **2**.

4.2.2. Crystal Structure Analysis

Complex **1** crystallized in the tetragonal space group $I\bar{4}$ with the asymmetric unit $Fe_2(L^H)_2$(hmds) (see Figure 4.16 for details) and comprises a Fe_4 tetrahedron stretched

along the S_4 axis (Fe-Fe distances between the vertexes are 5.1365(7) and 5.0978(7) Å) with the Fe1 inside the tetrahedral site (*i.e.* diamond-like core). The bond distance from the central Fe1 to the peripheral Fe2-Fe5 is 3.1376(5) Å. The diamondoid core is slightly distorted from ideal T_d symmetry (109.88° and 108.66°, Figure 4.19). The pyridonate ligands occupy the edges of the Fe_4 tetrahedron. The central Fe1 ion exhibits a strongly distorted octahedral O_6 coordination; each of the four surrounding Fe ions adopts a slightly distorted tetrahedral coordination from three pyridonates and one $N(SiMe_3)_2$ ligand (Figure 4.20). All pyridonate ligands coordinate in a μ_3-κ^1-N:κ^1-O:κ^1-O mode that spans three Fe ions; the amido groups bind in κ^1-N fashion. Three different Fe coordination environments are present, which are ligated by O_6 (Fe1), O_2N_2 (Fe2, Fe3) and N_3O (Fe4, Fe5) donor atoms, respectively (Scheme 4.3). According to the CCDC, complex **1** constitutes the first example of a molecular cluster featuring a diamondoid Fe(II) structure. Similar $Fe@Fe_4$ motifs are found as nodes in metal-organic framework complexes (MOFs, e.g. $Fe_3(HCO_2)_6$,[12] Fe(1,2,3-triazolate)$_2$[13]). This coordination motif resembles pentanuclear Kuratowski-type compounds of the general formula $M^cM^t_4L_6L'_4$ (central ion M^c; tetrahedral M^t; bridging ligand L (e.g. 1,2,3-triazolate); capping ligand L′ (Cl, acac, etc.)), which include Zn_5,[14a,b] Co_5 (L = 1,2,3-triazolate),[14c] Cu_5,[14d] Th_5 (L' = di(2-pyridyl ketone)[15] and several heteronuclear complexes (M^t = Zn, M^c = Fe, Co, Ni, Cu,[14d] M^c = Ru[14e]).[16] Only a limited number of such pentanuclear clusters with $M_c = M_t$ exhibit T_d symmetry with monodentate ligands L = Cl, whereas less symmetrical ligands (e.g. NO_3^-, β-diketonate) give distorted symmetry. Upon variation of the linker L', the dense metal cores of Kuratowski-type complexes can be used as building blocks for the synthesis of diverse oligomeric and polymeric compounds such as MOFs. For example, $[Co_5(btz)_6(NO_3)_4(H_2O)]$ and the radical species TCNQ (7,7,8,8-tetracyano-*p*-quinodimethane) afforded a 3D-diamondoid network structure;[17a] $[Zn_5(btz)_6(NO_3)_4(H_2O)]$ (btz = benzotriazolate) was reacted with dicarboxylate linkers to form a porous coordination framework.[17b]

The tetranuclear complex $Fe_4(L^{Me})_6[N(SiMe_3)_2]_2$ (**2**) crystallized in the space group $P\bar{1}$ with the asymmetric unit comprising half of the centrosymmetric cluster plus one toluene molecule. The Fe_4O_6 core constitutes a well-known butterfly motif, with Fe1 and Fe1′ forming the "body" and Fe2 and Fe2′ being the "wingtips". Until now, all reported examples of such Fe_4O_6 butterfly complexes contain Fe(III) ions,[18] except for a single Fe(II) coordination polymer reported by Winpenny et al. that also contains pyridonate ligands.[7] Complex **2** constitutes the first example of a molecular coordination cluster containing Fe(II) ions in a Fe_4O_6 butterfly complex. The planar Fe_4 rhomboid exhibits bond distances of 3.6218(4) Å (Fe1-Fe2) and 3.6101(4) Å (Fe2-Fe2′). Two oxygen atoms (O1 and O1′) are located 1.182 Å above and below the Fe_4 plane. The N-atoms of the terminal amido ligands are nearly coplanar with the Fe1Fe2Fe1′Fe2′ unit. The two "inner" pyridonates located above and below the Fe_4 plane adopt a μ_3-κ^1-N:κ^1-O:κ^1-O coordination. The remaining four "peripheral" pyridonates frame the Fe_4 in a mixed chelating and bridging μ-κ^2-N,O:κ^1-O coordination. The two body-Fe ions are each coordinated by O_4N_2-donor atoms in

strongly distorted octahedral geometry; the wingtip-Fe ions each form a slightly distorted tetrahedron with O_2N_2-donor atoms. Related butterfly complex structures can be found as repeating units of many extended solid-state structures, such as anhydrous $FeCl_2$ and several metal oxide monolayers (Scheme 4.3, right). In the presence of THF, the butterfly motif can be stabilized as a molecular structure in $Fe_4Cl_8(thf)_6$.[19],[20] There are several examples of such M_4O_6-containing molecular complexes with Fe(III), Mn, Co, and Ni ions[18],[21] and common ligands such as acetates, pyridine alcohols, polydentate imines, and others.

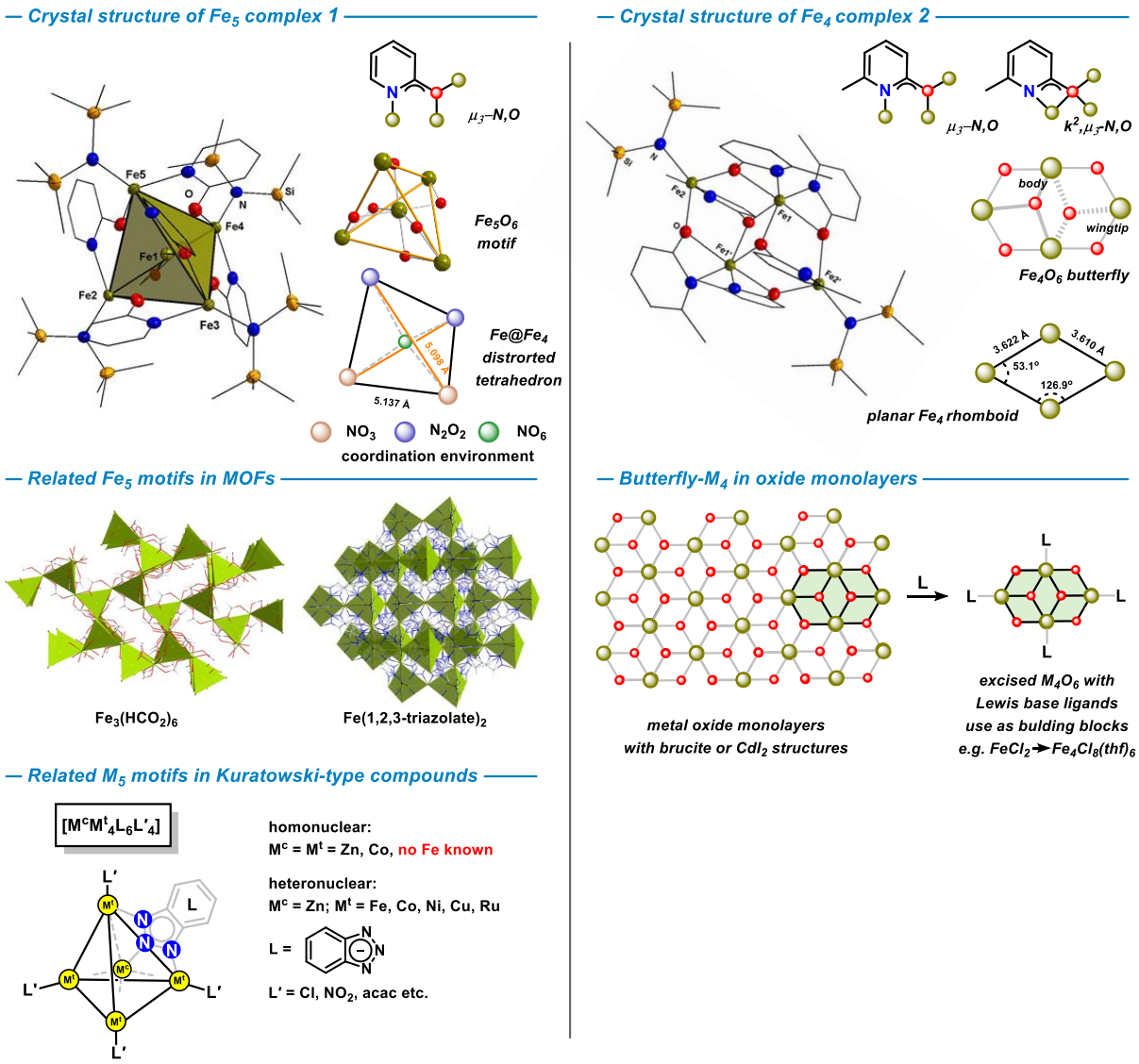

Scheme 4.3. Structural analysis of the iron(II) pyridonate clusters **1** (left) and **2** (right) and their relation to extended coordination networks.

4.2.3. Electronic and Magnetic Characterizations

The local electronic structures of **1** and **2** were analyzed using ^{57}Fe Mössbauer spectroscopy on solid samples at 80 K (Scheme 4.4). Spectral fitting and interpretation were based on observations that octahedral iron(II) high-spin compounds exhibit

higher isomer shifts than tetrahedral iron(II) species, with the latter displaying values lower than $\delta = 1$ mm s^{-1}.[22] The Fe_5 complex **1** gave three different doublets with isomer shifts/quadrupole splitting of $\delta = 0.91$ mm s^{-1}/ $\Delta E_Q = 2.11$ mm s^{-1}, $\delta = 0.93$ mm s^{-1}/$\Delta E_Q = 1.60$ mm s^{-1} and $\delta = 1.33$ mm s^{-1}/ $\Delta E_Q = 1.54$ mm s^{-1}, respectively. All parameters are in full accord with a ferrous high-spin configuration.[22] The results indicate the presence of two different pairs of tetrahedrally coordinated iron(II) ions (Fe2, Fe3 and Fe4, Fe5) with smaller isomer shifts and one octahedral iron(II) ion (Fe1) with a larger isomer shift in a ratio of 2:2:1, which is in full agreement with the molecular structure determined crystallographically. The two tetrahedral iron centers with N_3O coordination (Fe4, Fe5) likely correspond to the doublet with the lowest isomer shift ($\delta = 0.91$ mms^{-1}) because the softer N-donors provide a more covalent bond character in contrast to O-donors, leading to a decreased isomer shift compared to the N_2O_2-coordination motifs at Fe2, Fe3.[22] The Fe_4 pyridonate complex **2** gave two doublets in 1:1 ratio with isomer shifts of $\delta = 0.94$ mm s^{-1} and $\delta = 1.30$ mm s^{-1}; the former corresponding to the pair of tetrahedrally coordinated iron(II) ions (Fe2, Fe2´), and the latter to the octahedral iron(II) ions (Fe1, Fe1´). Both isomer shifts are characteristic for ferrous high-spin species. Quadrupole splittings are rather large ($\Delta E_Q = 2.74$ mm s^{-1} and $\Delta E_Q = 3.06$ mm s^{-1}) due to valence contributions and unsymmetrical ligand environments.

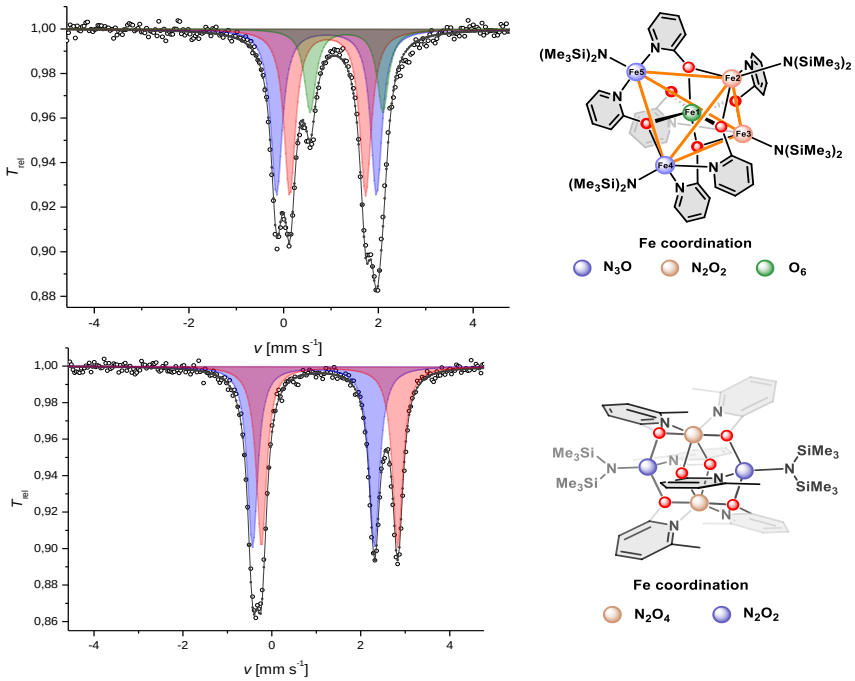

Scheme 4.4. Zero-field ^{57}Fe Mössbauer spectra of solid samples of Fe_5 (**1**, top) and Fe_4 (**2**, bottom) at 80 K.

Magnetic measurements on the pentanuclear (**1**) and tetranuclear (**2**) Fe(II) pyridonate complexes were performed on polycrystalline powder samples that were packed in a polycarbonate capsule and covered with the low-viscosity perfluoropolyether-based inert oil Fomblin Y45 to prevent any orienting of the microcrystals in the magnetic field. The magnetic susceptibility measurements were performed with an applied magnetic

field of 0.5 T between 2 K to 200 K (Scheme 4.5, top). The $\chi_M T$ value (χ_M, molar magnetic susceptibility) of 16.9 cm^3 K mol^{-1} for **1** at 200 K is larger than the expected $\chi_M T$ value (15.0 cm^3 K mol^{-1}) for five isolated non-interacting Fe(II) ions (S = 2 and g = 2.0) evidencing significant orbital contributions to the magnetic moment. Upon lowering the temperature the $\chi_M T$ product gradually decreases, indicating the presence of overriding intramolecular antiferromagnetic exchange coupling among the Fe(II) ions via the pyridonate bridges. Below 10 K the $\chi_M T$ value falls sharply to 4.37 cm^3 K mol^{-1} at 2 K. The magnetization for complex **1** rises rapidly at 2 K up to 2.0 T before showing a gradual increase to 8.54 μ_B without any complete saturation even at 7.0 T (Figure 4.29) and the reduced magnetization curves at low temperatures are non-superimposable (Figure 4.30) signifying the presence of low-lying excited states or magnetic anisotropy. This further indicates the presence of a non-zero magnetic ground state in complex **1**.

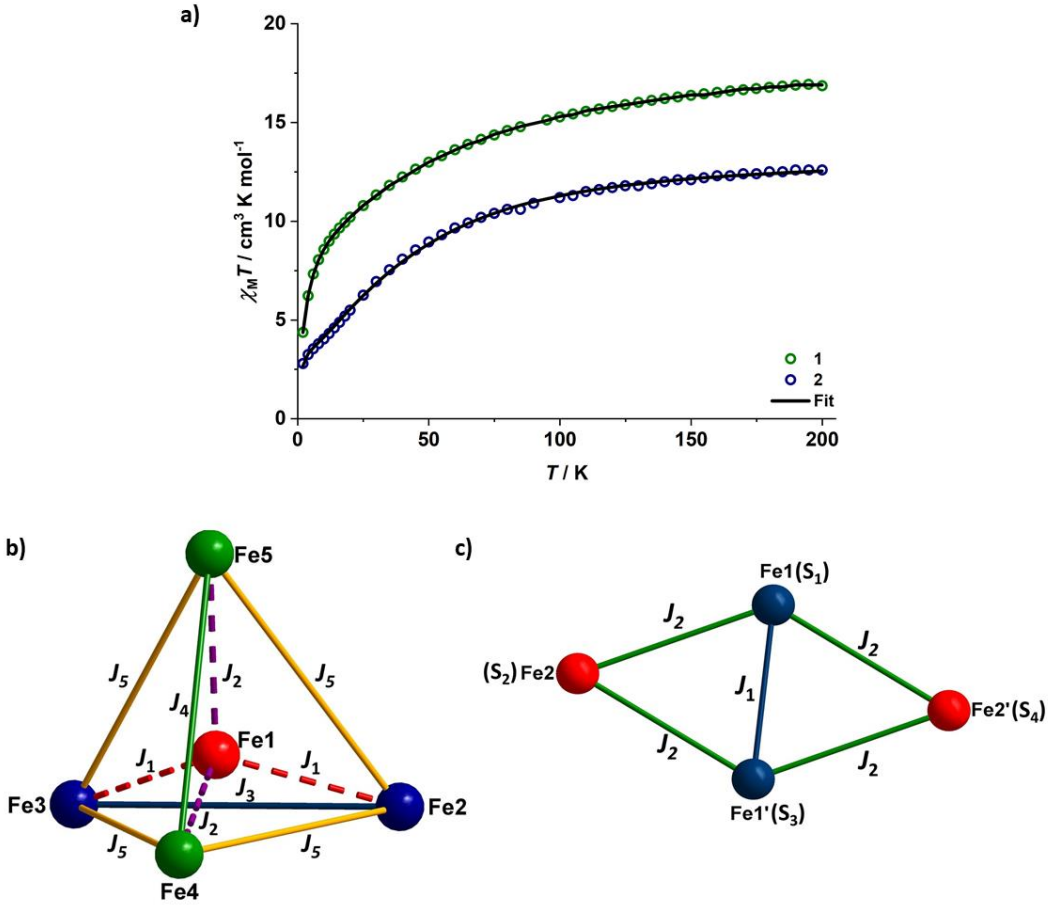

Scheme 4.5. (a) Plot of the variable temperature $\chi_M T$ for Fe(II) complexes (green (**1**), blue (**2**)). Solid black lines are the best fits. (b), (c) Magnetic exchange pathways in Fe_5 (**1**) and Fe_4 (**2**) complexes.

As evident from the molecular structure and Mössbauer spectrum of complex **1**, there are three sets of high-spin Fe(II) ions (S = 2). Hence, the experimental data for complex **1** was modelled using the magnetic exchange scheme with the following spin Hamiltonian:

$$\hat{H} = -2J_1(\hat{S}_1\hat{S}_2 + \hat{S}_1\hat{S}_3) - 2J_2(\hat{S}_1\hat{S}_4 + \hat{S}_1\hat{S}_5) - 2J_3(\hat{S}_2\hat{S}_3) - 2J_4(\hat{S}_4\hat{S}_5) - 2J_5(\hat{S}_2\hat{S}_4 + \hat{S}_2\hat{S}_5 + \hat{S}_3\hat{S}_4 + \hat{S}_3\hat{S}_5) + D_{\mathrm{Fe}}\sum_{i=1}^{5}[\hat{S}_{zi}{}^2 - \left(\frac{1}{3}\right)S_i(S_i+1)] + g\mu_B\sum_{i=1}^{5}\vec{B}\,\overrightarrow{S_i}$$

Introduction of the zero-field splitting effect (ZFS) term *D* was necessary to reproduce the data at low temperatures, but for simplification and to avoid overparameterization the Landé *g*-factor was assumed to be equal for all Fe(II) ions. The intermolecular magnetic exchange between neighbouring Fe_5 clusters was neglected. J_1, J_2, J_3, J_4, and J_5 (Scheme 4.5, bottom) represent the magnetic exchange pathways between the Fe(II) ions via the pyridonate bridges. The magnetic data was fitted with the PHI program[23] and the best fit parameters obtained were: g = 2.18, J_1 = 0.19 cm^{-1}, J_2 = 0.21 cm^{-1}, J_3 = -0.49 cm^{-1}, J_4 = -0.33 cm^{-1}, J_5 = -0.35 cm^{-1}, and D = -18.8 cm^{-1}. The fit parameters seem reasonable, however, the lack of literature reports on pyridonate bridged Fe(II) complexes hinders any comparative analysis of the exchange coupling parameters obtained. To probe the relaxation of magnetization in complex **1**, ac susceptibility measurements were performed both in zero dc field and under an applied dc field (Figures 4.31-4.34). However, no prominent out-of-phase signals (χ_M'') were obtained.

Complex **2** exhibited similar behaviour in the temperature-dependent magnetic susceptibility measurements in the higher temperature range but shows a less sharp decline in $\chi_M T$ value in the lower temperature range (Scheme 4.5, top). The $\chi_M T$ value of 12.5 cm^3 K mol^{-1} for 2 at 200 K is higher than the expected $\chi_M T$ value (12.0 cm^3 K mol^{-1}) for four non-interacting Fe(II) ions (S = 2 and g = 2.0) signifying orbital contributions to the magnetic moment. On lowering the temperature to 50 K the $\chi_M T$ product gradually decreases, indicating the presence of intramolecular antiferromagnetic exchange coupling among the Fe(II) ions. On further cooling, the $\chi_M T$ value decreases more rapidly to reach 2.68 cm^3 K mol^{-1} at 2 K. The magnetization rises linearly and sharply up to 1.0 T before showing a gradual linear increase to 4.08 μ_B without any saturation at 7.0 T (Figure 4.35). In addition, the reduced magnetization curves at low temperatures are non-superimposable (Figure 4.36) indicating the presence of low-lying excited states or magnetic anisotropy. The tetranuclear complex **2** contains two sets high-spin Fe(II) ions (S = 2) according to its Mössbauer spectrum. Hence, the experimental data for complex **2** was modelled using the magnetic exchange scheme shown in Scheme 4.5 with the following spin Hamiltonian:

$$\hat{H} = -2J_1(\hat{S}_1\hat{S}_3) - 2J_2(\hat{S}_1\hat{S}_2 + \hat{S}_1\hat{S}_4 + \hat{S}_2\hat{S}_3 + \hat{S}_3\hat{S}_4) + D_{\mathrm{Fe}}\sum_{i=1}^{4}[\hat{S}_{zi}{}^2 - \left(\frac{1}{3}\right)S_i(S_i+1)] + g\mu_B\sum_{i=1}^{4}\vec{B}\,\overrightarrow{S_i}$$

The Landé *g*-factor was assumed to be equal for the Fe(II) ions since introducing individual *g* factors did not improve the fit. As seen in the case of **1**, the introduction of the ZFS term (*D*) gave a good fit at low temperatures. J_1 and J_2 represent the magnetic exchange pathway between the equivalent Fe(II) ions and the non-equivalent Fe(II) ions via the pyridonate bridges, respectively (Scheme 4.5, bottom). The magnetic exchange interaction between Fe2(S_2) and Fe2′(S_4) was neglected due to the relatively large Fe-Fe distance. The best fit parameters obtained were: g = 2.11, J_1 = -1.0 cm^{-1}, J_2 = -0.56 cm^{-1}, and D = -12.5 cm^{-1}.

Ac susceptibility measurements were performed to probe the magnetization relaxation in complex **2**. However, no out-of-phase (χ_M'') signals were observed under zero dc field as already seen for **1** (Figures 4.38). In contrast, slow relaxation of the magnetization could be observed under an applied dc field of 1500 Oe (Figure 4.1). Clear frequency (Figure 4.1b) and temperature-dependent (Figure 4.40) maxima in χ_M'' were observed. Relaxation times were extracted by fitting the isothermal in-phase (χ_M') and out-of-phase (χ_M'') components of the ac susceptibility to a generalized Debye model yielding the α parameter in the range of 0.12–0.27 (Table 4.10.). The temperature-dependent relaxation times could be satisfactorily modelled with the following equation.

$$1/\tau = 1/\tau_{QTM} + \tau_0^{-1}\exp(-U_{eff}/k_BT),$$

where the first term corresponds to the relaxation process via quantum tunnelling and the second term corresponds to relaxation via the Orbach relaxation pathway, respectively. The best fit parameters obtained were: U_{eff} = 38.5 K, τ_0 = 1.13 x 10^{-9} s and τ_{QTM} = 0.189 s. These values compare very well to the very few literature examples of homonuclear Fe(II) cluster-based single-molecule magnets (SMMs).[24]

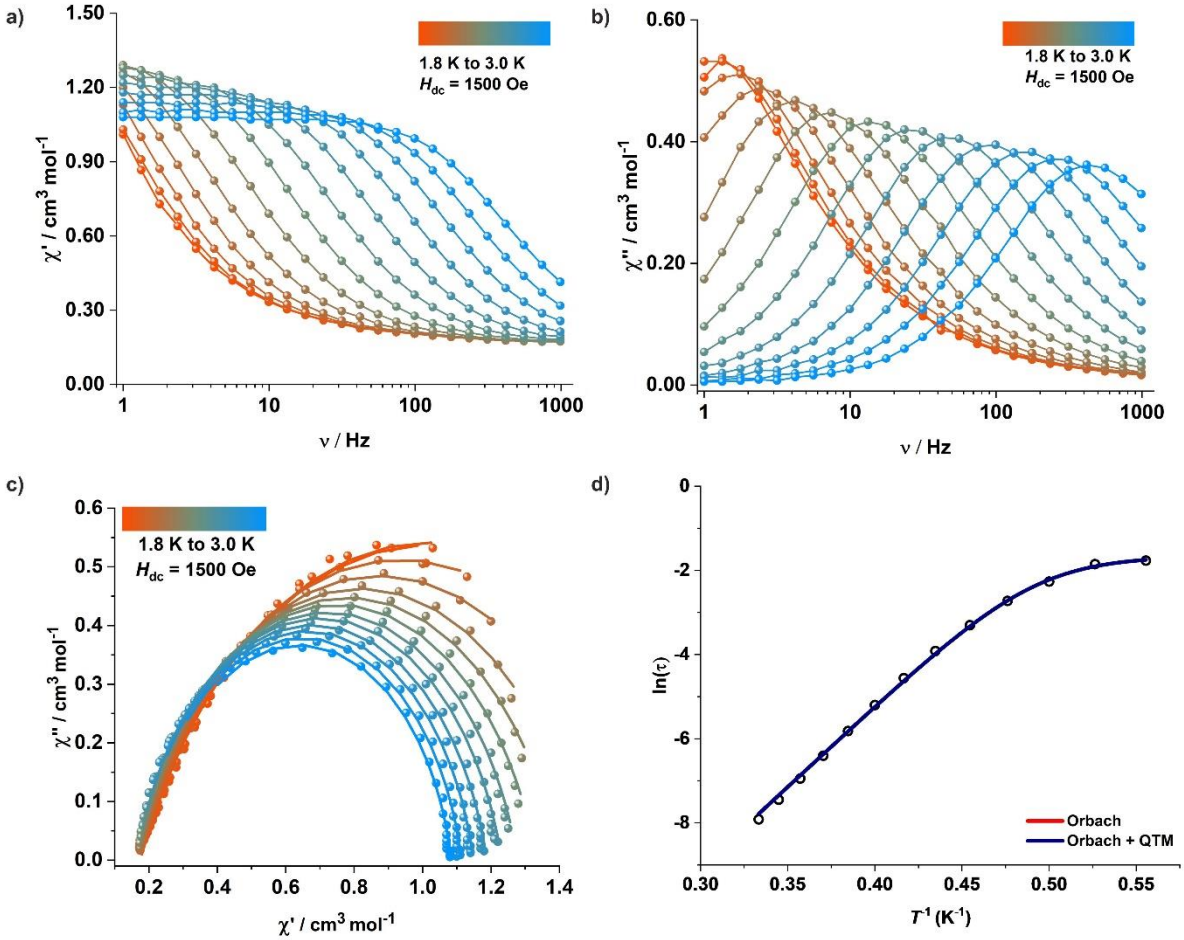

Figure 4.1. (a) In-phase (χ_M') and (b) out-of-phase (χ_M'') components of the frequency-dependent (1–1000 Hz) ac susceptibility measured in an oscillating ac field of 3.0 Oe under an applied dc field of 1500 Oe for complex **2**. (c) Cole-Cole plots for **2** under an applied dc field of 1500 Oe. (d) The plot of the relaxation time τ (logarithmic scale) *vs.* T^{-1}. The solid blue line represents the best fit to the relaxation via a combination of the Orbach pathway and QTM.

4.2.4. Reactivities

We probed the feasibility of selective ligand exchange at the well-defined Fe clusters **1** and **2**. The high basicity and monodentate binding mode of the terminal hexamethyldisilazido ligands $N(SiMe_3)_2$ may enable rapid protolytic ligand exchange. Initial attempts were directed at substitutions with alkoxides.[25] Reaction of the Fe_5 cluster **1** with 4 equiv. 2,6-di-*tert*-butyl-*p*-cresol (HOAr) led to the isolation of single crystals of the structurally different higher nuclearity μ_4-oxido-heptairon cluster $Fe_7(L^H)_9(\mu_4\text{-}O)(OAr)_3$ (**3**, Scheme 4.6, top). The central oxygen atom (probably originating from traces of water within the cresol derivative) is coordinated in the center of a Fe_4 tetrahedron; three terminal aryloxido and nine bridging pyridonate ligands build the overall $Fe_7(L^H)_9O(OAr)_3$ (see Figure 4.24 for details). An alternative pathway of amido ligand substitution was probed when the pentanuclear complex $Fe_5(L^H)_6[N(SiMe_3)_2]_4$ (**1**) was treated with 4 equiv. of $HBAr^F{}_4(OEt_2)$ in toluene upon

stirring overnight at room temperature without any observable colour change. Subsequent solvent evaporation, trituration with hexane, and crystallization by layering of the THF solution with hexane led to the isolation of minor amounts of crystals that were characterized by XRD. The reaction was accompanied by rearrangement of complex **1** to $Fe_4(L^H)_6(thf)_6(BAr^F{}_4)_2$ (**4**) that features the known Fe_4O_6 butterfly motif. The periphery of the complex is equipped with six THF molecules (Scheme 4.6, bottom).

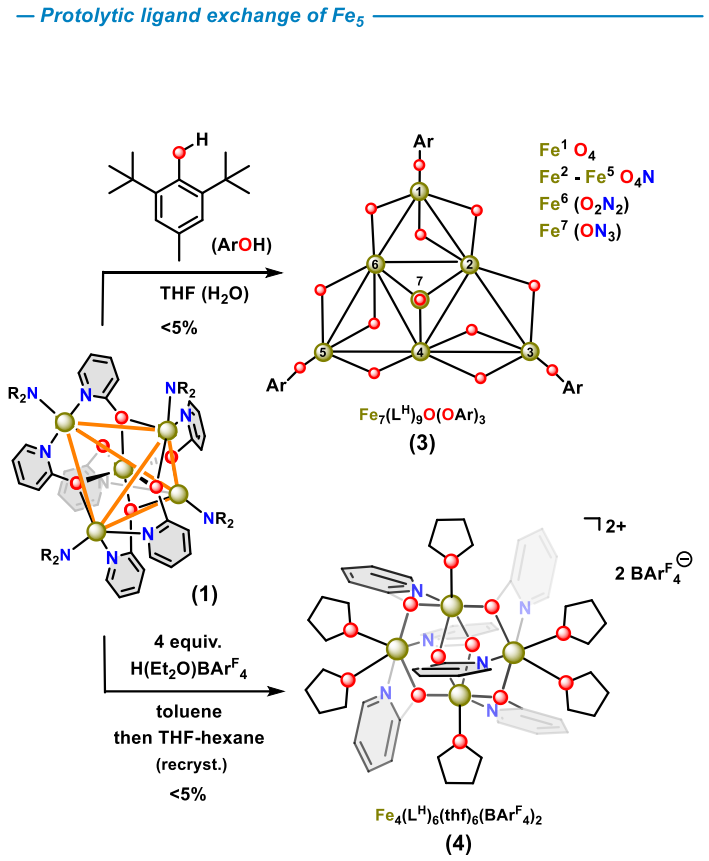

Scheme 4.6. Top: Protolytic amide substitution in cluster 1 with 2,6-di-*t*-butyl-*p*-cresol to give Fe_7 cluster **3** (for clarity reasons, only FeO coordinations are shown). Bottom: Protolytic amide elimination in 1 to give Fe_4O_6 butterfly complex **4** with peripheral THF coordination

Similar reactions with the tetranuclear complex $Fe_4(L^{Me})_6[N(SiMe_3)_2]_2$ (**2**) enabled protolytic amido ligand substitution but with preservation of the butterfly-Fe_4O_6 core. Addition of 2 equiv. 2,6-di-*tert*-butyl-*p*-cresol (HOAr) at room temperature gave no color change. Crystallization via pentane diffusion into THF solution afforded the desired complex $Fe_4(L^{Me})_6(OAr)_2$ (**5**) in which the central Fe_4O_6 butterfly and all six pyridonate binding motifs were preserved while selective substitution of two amido ligands at the termini with two cresolates ArO was achieved (Scheme 4.7, top). From a similar reaction and work-up, yellow-brown crystals of another structurally related complex $Fe_4(L^{Me})_6(OAr)_2(thf)_2$ (**6**) were obtained (Scheme 4.7, center). This complex was highly stable and exhibited no melting or decomposition up to 260 °C. The structure of **6** contains a related Fe_4O_6 butterfly motif as the precursor **5**, where the two

hexamethyldisilazido ligands at the wingtips were replaced by two phenolates. However, the coordination of two additional THF molecules to the body positions prompted a rearrangement of the two μ_2-pyridonate ligands. Two pyridonates (Scheme 4.7, highlighted in green) underwent migration from body-N-Fe to wingtip-N-Fe positions, possibly as a result of protolytic amide elimination and stabilization of the vacant coordination sites at the wingtip-Fe ions. The thf-coordinated complex **6** presumably converted to **5** upon loss of THF by drying in vacuum (68% yield after drying in vacuum; elemental analysis). The isolation of both cresolate complexes **5** and **6** may indicate equilibrating species in solution and in the presence of other suitable donor ligands. Attempts to use the parent $Fe_4(L^{Me})_6[N(SiMe_3)_2]_2$ (**2**) for bidirectional syntheses of coordination polymers in the presence of 1,ω-diol derivatives resulted in the formation of highly insoluble solids that withstood crystallization efforts (Scheme 4.7, bottom).

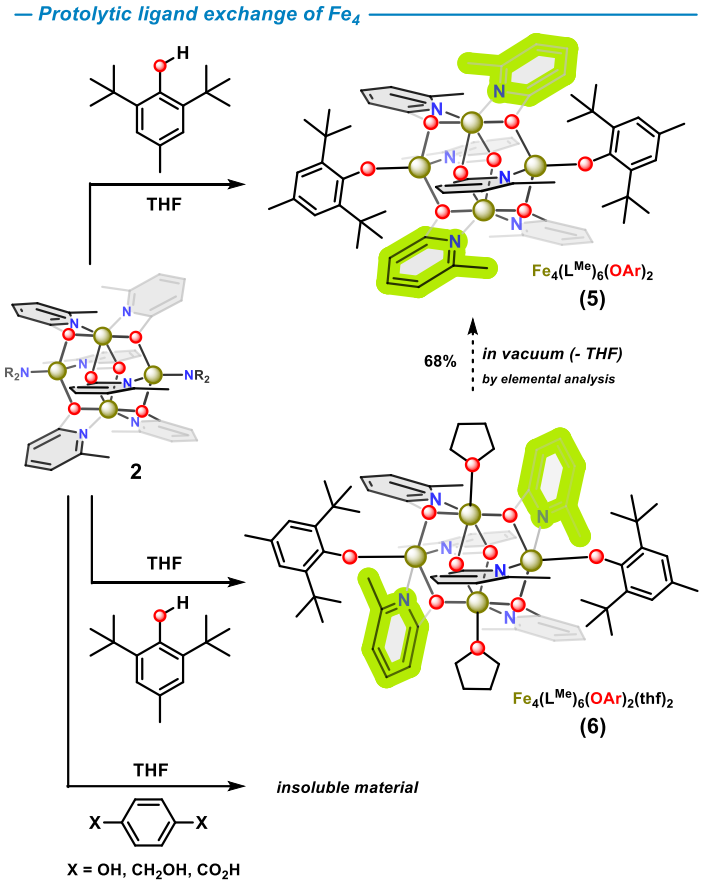

Scheme 4.7. Protolytic amide substitutions in cluster **2** with 2,6-di-*t*-butyl-*p*-cresol to give the related Fe_4O_6 butterfly clusters **5** and **6** (top, center). Attempts at syntheses of coordination polymers (bottom)

4.3. Summary and Conclusions

The high degree of flexibility and versatility of the various κ- and μ-coordination modes of pyridonate ligands wasexplored in reactions with Fe(II) precursors. The synthesis of topologically unprecedented iron(II) pyridonate clusters in high yields was achieved from reactions with the easily accessible precursor $Fe[N(SiMe_3)_2]_2$. The pentanuclear cluster $Fe_5(L^H)_6[N(SiMe_3)_2]_4$ (**1**) exhibits a very rare diamondoid structure with a centered $Fe@Fe_4$ tetrahedron core. The slightly bulkier 6-methyl-2-pyridonate afforded the tetranuclear $Fe_4(L^{Me})_6[N(SiMe_3)_2]_2$ (**2**) containing a planar butterfly Fe_4-rhomboid. Complex **1** constitutes the first example of a pentanuclear molecular iron(II) cluster. Complex **2** constitutes the first example of a tetranuclear Fe(II) molecular cluster containing the M_4O_6 butterfly motif that is mostly known from many other metal ions.[21] The high-spin configuration of Fe(II) ions in different coordination environment in **1** and **2** was evident from ^{57}Fe Mössbauer spectroscopy. The Fe(II) clusters **1** and **2** exhibit overall weak antiferromagnetic interactions. Interestingly, the Fe_4 cluster behaves as a field-induced single-molecule magnet (SMM) and thus belongs to the rare family of homonuclear Fe(II) cluster magnets.

Protolytic ligand exchange reactions with the highly labile $Fe@Fe_4$ core of the pentanuclear complex **1** afforded low yields and were accompanied by rapid cluster rearrangements into other topologies, including the Fe_4O_6 butterfly motif. The utility of the tetrairon complex **2** to serve as molecular building block was demonstrated by facile ligand exchange reactions of the terminal amido ligands under protolytic conditions. The central Fe_4O_6-pyridonate core remained intact during the peripheral ligand substitutions so that applications to the synthesis of coordination polymers or MOFs are easily foreseen.

4.4. References

(1) Ryken, S. A.; Payne, P. R.; Schafer, L. L. Tight Bite Angle N,O-Chelates. Amidates, Ureates and Beyond. In *Ligand Design in Metal Chemistry*, **2016**; pp 364-405.

(2) (a) Rawson, J. M.; Winpenny, R. E. P. The coordination chemistry of 2-pyridone and its derivatives. *Coord. Chem. Rev.* **1995**, 139, 313-374. (b) Drover, M. W.; Love, J. A.; Schafer, L. L. 1,3-N,O-Complexes of late transition metals. Ligands with flexible bonding modes and reaction profiles. *Chem. Soc. Rev.* **2017**, 46 (10), 2913-2940.

(3) (a) Fujita, K.-i.; Tanino, N.; Yamaguchi, R. Ligand-Promoted Dehydrogenation of Alcohols Catalyzed by Cp*Ir Complexes. A New Catalytic System for Oxidant-Free Oxidation of Alcohols. *Org. Lett.* **2007**, 9 (1), 109-111. (b) Clarkson, J. M.; Schafer, L. L. Bis(tert-butylimido)bis(N,O-chelate)tungsten(VI) Complexes: Probing Amidate and Pyridonate Hemilability. *Inorg. Chem.* **2017**, 56 (10), 5553-5566. (c) Griffin, S. E.; Schafer, L. L. Vanadium Pyridonate Catalysts: Isolation of Intermediates in the Reductive Coupling of Alcohols. *Inorg. Chem.* **2020**, 59 (8), 5256-5260.

(4) Parsons, S.; Winpenny, R. E. P. Structural Chemistry of Pyridonate Complexes of Late 3d-Metals. *Acc. Chem. Res*. **1997**, 30 (2), 89-95.

(5) Huang, G.; Wagner, T.; Wodrich, M. D.; Ataka, K.; Bill, E.; Ermler, U.; Hu, X.; Shima, S. The atomic-resolution crystal structure of activated [Fe]-hydrogenase. *Nat. Catal.* **2019**, 2 (6), 537-543.

(6) (a) Moore, C. M.; Dahl, E. W.; Szymczak, N. K. Beyond H2: exploiting 2-hydroxypyridine as a design element from [Fe]-hydrogenase for energy-relevant catalysis. *Curr. Opin. Chem. Biol.* **2015**, 25, 9-17. (b) Chen, D.; Ahrens-Botzong, A.; Schünemann, V.; Scopelliti, R.; Hu, X. Synthesis and Characterization of a Series of Model Complexes of the Active Site of [Fe]-Hydrogenase (Hmd). *Inorg. Chem.* **2011**, 50 (11), 5249-5257. (c) Chen, D.; Scopelliti, R.; Hu, X. [Fe]-Hydrogenase Models Featuring Acylmethylpyridinyl Ligands. *Angew. Chem. Int. Ed.* **2010**, 49 (41), 7512-7515. (d) Hu, B.; Chen, D.; Hu, X. Synthesis and Reactivity of Mononuclear Iron Models of [Fe]-Hydrogenase that Contain an Acylmethylpyridinol Ligand. *Chem. Eur. J.* **2014**, 20 (6), 1677-1682. (e) Obrist, B. V.; Chen, D.; Ahrens, A.; Schünemann, V.; Scopelliti, R.; Hu, X. An Iron Carbonyl Pyridonate Complex Related to the Active Site of the [Fe]-Hydrogenase (Hmd). *Inorg. Chem.* **2009**, 48 (8), 3514-3516. (f) Xu, T.; Yin, C.-J. M.; Wodrich, M. D.; Mazza, S.; Schultz, K. M.; Scopelliti, R.; Hu, X. A Functional Model of [Fe]-Hydrogenase. *J. Am. Chem. Soc.* **2016**, 138 (10), 3270-3273.

(7) Przybylak, S. W.; Tuna, F.; Teat, S. J.; Winpenny, R. E. P. A homospin iron(II) single chain magnet. *Chem. Commun.* **2008**, (17), 1983-1985.

(8) (a) Parsons, S.; Solan, G. A.; Winpenny, R. E. P. Synthesis, structure and preliminary magnetic studies of a heptadecanuclear iron complex. *J. Chem. Soc., Chem. Commun.* **1995**, (19), 1987-1988. (b) Blake, A. J.; Grant, C. M.; Parsons, S.; Solan, G. A.; Winpenny, R. E. P. Diiron(III) and polymeric iron(III)–sodium complexes with bridging and terminal pyridonate ligands: structures and magnetic properties. *J. Chem. Soc., Dalton Trans.* **1996**, (3), 321-327. (c) Parsons, S.; Solan, G. A.; Winpenny, R. E. P.; Benelli, C. Ferric Wheels and Cages: Decanuclear Iron Complexes with Carboxylato and Pyridonato Ligands. *Angew. Chem. Int. Ed.* **1996**, 35 (16), 1825-1828.

(9) Fedulin, A.; Jacobi von Wangelin, A. Bis[bis(trimethylsilyl)amido]iron(II): Silanamine, 1,1,1-trimethyl-N-(trimethylsilyl)-, iron(2+) salt (2:1). In *Encyclopedia of Reagents for Organic Synthesis*, pp 1-4.

(10) (a) Gieshoff, T. N.; Chakraborty, U.; Villa, M.; Jacobi von Wangelin, A. Alkene Hydrogenations by Soluble Iron Nanocluster Catalysts. *Angew. Chem. Int. Ed.* **2017**, 56 (13), 3585-3589. (b) Chakraborty, U.; Reyes-Rodriguez, E.; Demeshko, S.; Meyer, F.; Jacobi von Wangelin, A. A Manganese Nanosheet: New Cluster Topology and Catalysis. *Angew. Chem. Int. Ed.* **2018**, 57 (18), 4970-4975. (c) Chakraborty, U.; Demeshko, S.; Meyer, F.; Jacobi von Wangelin, A. Synthesis and Reactivity of an Early-Transition-Metal Alkynyl Cubane Mn4C4 Cluster. *Angew. Chem. Int. Ed.* **2019**, 58 (11), 3466-3470.

(11) Complex 2 may also be recrystallized from THF-hexane mixture to give the THF-solvate 2•$(thf)_2$.

(12) Wang, Z.-M.; Zhang, Y.-J.; Liu, T.; Kurmoo, M.; Gao, S. $[Fe_3(HCOO)_6]$: A Permanent Porous Diamond Framework Displaying H_2/N_2 Adsorption, Guest Inclusion, and Guest-Dependent Magnetism. *Adv. Funct. Mater.* **2007**, 17 (9), 1523-1536.

(13) (a) Gándara, F.; Uribe-Romo, F. J.; Britt, D. K.; Furukawa, H.; Lei, L.; Cheng, R.; Duan, X.; O'Keeffe, M.; Yaghi, O. M. Porous, Conductive Metal-Triazolates and Their Structural Elucidation by the Charge-Flipping Method. *Chem. Eur. J.* **2012**, 18 (34), 10595-10601. (b) Park, J. G.; Aubrey, M. L.; Oktawiec, J.; Chakarawet, K.; Darago, L. E.; Grandjean, F.; Long, G. J.; Long, J. R. Charge Delocalization and Bulk Electronic Conductivity in the Mixed-Valence Metal–Organic Framework Fe(1,2,3-triazolate)$_2$(BF4)$_x$. *J. Am. Chem. Soc.* **2018**, 140 (27), 8526-8534. (c) Grzywa, M.; Röß-Ohlenroth, R.; Muschielok, C.; Oberhofer, H.; Błachowski, A.; Żukrowski, J.; Vieweg, D.; von Nidda, H.-A. K.; Volkmer, D. Cooperative Large-Hysteresis Spin-Crossover Transition in the Iron(II) Triazolate $[Fe(ta)_2]$ Metal–Organic Framework. *Inorg. Chem.* **2020**, 59 (15), 10501-10511.

(14) (a) Biswas, S.; Tonigold, M.; Volkmer, D. Homo- and Heteropentanuclear Coordination Compounds with Td Symmetry – the Solid State Structures of $[MZn_4(L)_4(L')_6]$ (M = Co^{II} or Zn; L = chloride or acac; L′ = 1,2,3-benzotriazolate). *Z. Anorg. Allg. Chem.* **2008**, 634 (14), 2532-2538. (b) Bunzen, H.; Grzywa, M.; Kalytta-Mewes, A.; Volkmer, D. One-pot synthesis of ultrastable pentanuclear alkylzinc complexes. *Dalton Trans.* **2017**, 46 (8), 2618-2625. (c) Werner, T. W.; Reschke, S.; Bunzen, H.; von Nidda, H.-A. K.; Deisenhofer, J.; Loidl, A.; Volkmer, D. $[Co_5Tp^*_4(Me_2bta)_6]$: A Highly Symmetrical Pentanuclear Kuratowski Complex Featuring Tris(pyrazolyl)borate and Benzotriazolate Ligands. *Inorg. Chem.* **2016**, 55 (3), 1053-1060. (d) Cui, L.; Geng, Y.-F.; Leong, C. F.; Ma, Q.; D'Alessandro, D. M.; Deng, K.; Zeng, Q.-D.; Zuo, J.-L. Synthesis, properties and surface self-assembly of a pentanuclear cluster based on the new π-conjugated TTF-triazole ligand. *Sci. Rep.* **2016**, 6 (1), 25544. (e) Biswas, S.; Tonigold, M.; Speldrich, M.; Kögerler, P.; Weil, M.; Volkmer, D. Syntheses and Magnetostructural Investigations on Kuratowski-Type Homo- and Heteropentanuclear Coordination Compounds $[MZn_4Cl_4(L)_6]$ (M^{II} = Zn, Fe, Co, Ni, or Cu; L = 5,6-Dimethyl-1,2,3-benzotriazolate) Represented by the Nonplanar K3,3 Graph. *Inorg. Chem.* 2010, 49 (16), 7424-7434. (f) Liu, Y.-Y.; Grzywa, M.; Tonigold, M.; Sastre, G.; Schüttrigkeit, T.; Leeson, N. S.; Volkmer, D. Photophysical properties of Kuratowski-type coordination compounds $[M^{II}Zn_4Cl_4(Me_2bta)_6]$ (M^{II} = Zn or Ru) featuring long-lived excited electronic states. *Dalton Trans.* **2011**, 40 (22), 5926-5938.

(15) Tsantis, S. T.; Danelli, P.; Tzimopoulos, D. I.; Raptopoulou, C. P.; Psycharis, V.; Perlepes, S. P. Pentanuclear Thorium(IV) Coordination Cluster from the Use of Di(2-pyridyl) Ketone. *Inorg. Chem.* **2021**, 60 (16), 11888-11892.

(16) Kuratowski, C. Sur Le Problème Des Courbes Gauches en Topologie. *Fundam. Mater.* **1930**, 15, 271−283.

(17) (a) Bai, Y.-L.; Tao, J.; Huang, R.-B.; Zheng, L.-S. The Designed Assembly of Augmented Diamond Networks From Predetermined Pentanuclear Tetrahedral Units.

Angew. Chem. Int. Ed. **2008**, 47 (29), 5344-5347. (b) Wang, X.-L.; Qin, C.; Wu, S.-X.; Shao, K.-Z.; Lan, Y.-Q.; Wang, S.; Zhu, D.-X.; Su, Z.-M.; Wang, E.-B. Bottom-Up Synthesis of Porous Coordination Frameworks: Apical Substitution of a Pentanuclear Tetrahedral Precursor. *Angew. Chem. Int. Ed.* **2009**, 48 (29), 5291-5295.

(18) (a) Glaser, T.; Lügger, T. A new tetranuclear iron complex with a $[Fe_4O_6]^{6+}$ core: synthesis, structure, spectroscopic and magnetic properties. *Inorg. Chim. Acta* **2002**, 337, 103-112. (b) Murugesu, M.; Clérac, R.; Wernsdorfer, W.; Anson, C. E.; Powell, A. K. Hierarchical Assembly of {Fe13} Oxygen-Bridged Clusters into a Close-Packed Superstructure. *Angew. Chem. Int. Ed.* **2005**, 44 (41), 6678-6682. (c) Lan, Y.; Novitchi, G.; Clérac, R.; Tang, J.-K.; Madhu, N. T.; Hewitt, I. J.; Anson, C. E.; Brooker, S.; Powell, A. K. Di-, tetra- and hexanuclear iron(III), manganese(II/III) and copper(II) complexes of Schiff-base ligands derived from 6-substituted-2-formylphenols. *Dalton Trans.* **2009**, (10), 1721-1727. (d) Mulyana, Y.; Nafady, A.; Mukherjee, A.; Bircher, R.; Moubaraki, B.; Murray, K. S.; Bond, A. M.; Abrahams, B. F.; Boskovic, C. New Family of Ferric Spin Clusters Incorporating Redox-Active ortho-Dioxolene Ligands. *Inorg. Chem.* **2009**, 48 (16), 7765-7781.

(19) (a) Bel'skii, V. K.; Ishchenko, V. M.; Bulychev, B. M.; Protskii, A. N.; Soloveichik, G. L.; Ellert, O. G.; Seifulina, Z. M.; Rakitin, Y. V.; Novotortsev, V. M. Structure and magnetic properties of iron(II) chloride tetrahydrofuranate $(2FeCl_2{\cdot}3THF)_2$. *Inorg. Chim. Acta* **1985**, 96 (2), 123-127. (b) Cotton, F. A.; Luck, R. L.; Son, K.-A. New polynuclear compounds of iron(II) chloride with oxygen donor ligands Part I. $Fe_4Cl_8(THF)_6$: synthesis and a single crystal X-ray structure determination. *Inorg. Chim. Acta* **1991**, 179 (1), 11-15.

(20) Zhao, H.; Clérac, R.; Sun, J.-S.; Ouyang, X. N.; Clemente-Juan, J. M.; Gómez García, C. J.; Coronado, E.; Dunbar, K. R. A comparative structural and magnetic study of three compounds based on the cluster unit $M_4Cl_8(THF)_6$ (M = Mn, Fe, Co). *J. Solid State Chem.* **2001**, 159, 281-292.

(21) (a) Yang, E.-C.; Harden, N.; Wernsdorfer, W.; Zakharov, L.; Brechin, E. K.; Rheingold, A. L.; Christou, G.; Hendrickson, D. N. Mn4 single-molecule magnets with a planar diamond core and S=9. *Polyhedron* **2003**, 22 (14), 1857-1863. (b) Sobocińska, M.; Antkowiak, M.; Wojciechowski, M.; Kamieniarz, G.; Utko, J.; Lis, T. New tetranuclear manganese clusters with $[Mn^{II}_3Mn^{III}]$ and $[Mn^{II}_2Mn^{III}_2]$ metallic cores exhibiting low and high spin ground state. *Dalton Trans.* **2016**, 45 (17), 7303-7311. (c) Zhang, H.; Zhang, J.; Liu, R.; Li, Y.; Liu, W.; Li, W. Five Disk-Shaped $\{M^{II}_7\}$ (M = Mn, Fe, Co, Cu, Zn) Clusters and One Capsule-Like $\{Cu^{II}_6Na^{I}_2\}$ Cluster Assembled from the Same Schiff Base Ligand. *Eur. J. Inorg. Chem.* **2016**, 2016 (26), 4134-4143. (d) Bao, D.-X.; Xiang, S.; Wang, J.; Li, Y.-C.; Zhao, X.-Q. Review: Single-molecule magnets based on pyridine alcohol ligands. *J. Coord. Chem.* **2016**, 69 (21), 3131-3147. (e) Fraser, H. W. L.; Nichol, G. S.; Baldansuren, A.; McInnes, E. J. L.; Brechin, E. K. Cages on a plane: a structural matrix for molecular 'sheets'. *Dalton Trans.* **2018**, 47 (43), 15530-15537. (f) Slater-Parry, M. E.; Durrant, J. P.; Howells, J. M.; Pitak, M. B.; Horton, P. N.; Klooster, W. T.; Coles, S. J.; O'Connor, H. M.; Brechin, E. K.; Barra, A.-

L.; et al. Crowding out: ligand modifications and their structure directing effects on brucite-like {Mx(μ_3-OH)y} (M = Co(ii), Ni(ii)) core growth within polymetallic cages. *Dalton Trans.* **2019**, 48 (4), 1477-1488.

(22) Gütlich, P.; Bill, E.; Trautwein, A. X., *Mössbauer Spectroscopy and Transition Metal Chemistry: Fundamentals and Applications*, Springer-Verlag Berlin Heidelberg, **2011**.

(23) Chilton, N. F.; Anderson, R. P.; Turner, L. D.; Soncini, A.; Murray, K. S., PHI: A powerful new program for the analysis of anisotropic monomeric and exchange-coupled polynuclear d- and f-block complexes. *J. Comput. Chem.* **2013**, *34* (13), 1164-1175.

(24) (a) Nicolini, A.; Affronte, M.; SantaLucia, D. J.; Borsari, M.; Cahier, B.; Caleffi, M.; Ranieri, A.; Berry, J. F.; Cornia, A., Tetrairon(ii) extended metal atom chains as single-molecule magnets. *Dalton Trans.* **2021**, *50* (22), 7571-7589. (b) Boudalis, A. K.; Donnadieu, B.; Nastopoulos, V.; Clemente-Juan, J. M.; Mari, A.; Sanakis, Y.; Tuchagues, J.-P.; Perlepes, S. P., A Nonanuclear Iron(II) Single-Molecule Magnet. *Angew. Chem. Int. Ed.* **2004**, *43* (17), 2266-2270. (c) Hoshino, N.; Ako, A. M.; Powell, A. K.; Oshio, H., Molecular Magnets Containing Wheel Motifs. *Inorg. Chem.* **2009**, *48* (8), 3396-3407. (d) Oshio, H.; Hoshino, N.; Ito, T.; Nakano, M., Single-Molecule Magnets of Ferrous Cubes: Structurally Controlled Magnetic Anisotropy. *J. Am. Chem. Soc.* **2004**, *126* (28), 8805-8812. (e) Liu, S.; Deng, Y.-F.; Li, C. A.; Chang, X.; Zhang, Y.-Z., A linear trinuclear ferrous single molecule magnet. *Dalton Trans.* **2018**, *47* (46), 16704-16708.

(25) (a) Bartlett, R. A.; Ellison, J. J.; Power, P. P.; Shoner, S. C. Synthesis and characterization of the homoleptic aryloxides [M{O(2,4,6-*tert*-$Bu_3C_6H_2$)}$_2$]$_2$ (M = manganese, iron), the adducts [Mn(OCPh$_3$)$_2$(py)$_2$] and [Fe(OCPh$_3$)$_2$(THF)$_2$], and the mixed complex [Fe{N(SiMe$_3$)$_2$}{mu.-O(2,4,6-tert-$Bu_3C_6H_2$)}]$_2$: evidence for primarily ionic metal-oxygen bonding. *Inorg. Chem.* **1991**, *30*, 2888–2894. (b) Hatanaka, T.; Miyake, R.; Ishida, Y.; Kawaguchi, H. Synthesis of two-coordinate iron aryloxides and their reactions with organic azide: Intramolecular C-H bond amination. *J. Organomet. Chem.* **2011**, *696*, 4046– 4050. (c) Stennett, C. R.; Fettinger, J. C.; Power, P. P. Low-Coordinate Iron Chalcogenolates and Their Complexes with Diethyl Ether and Ammonia. *Inorg. Chem.* **2021**, *60*, 6712-6720.

4.5. Experimental Section

4.5.1. Materials and Methods

All experiments for air-sensitive compounds were performed under an atmosphere of dry argon, by using the standard Schlenk and glove box techniques. Solvents (Et_2O, *n*-hexane, toluene) were purified by an SPS solvent purification system under N_2; THF was distilled over sodium and benzophenone. Dry solvents were stored over molecular sieves (4 Å). Elemental analyses were determined in an inert atmosphere by the analytical department of the University of Hamburg. Melting points of the compounds were measured on a *DigiMelt SRS* instrument using a glass capillary sealed under a vacuum. $Fe(N(SiMe_3)_2)_2$ and $HBAr^F{}_4$ were prepared according to the literature procedure [1,2]. $HBAr^F{}_4$ included 2.9 Et_2O molecules per formula unit (^{1}H NMR). 2-pyridone (L^HH), 6-methyl-2-pyridone ($L^{Me}H$), 2,6-di-*tert*-butyl-*p*-cresol (ArOH) were purchased from commercial suppliers and sublimed in vacuum prior to use. Commercially available liquid substrates for catalytic screening were distilled under reduced pressure (Kugelrohr) and stored over molecular sieves (4 Å) at least 24 h prior to use. Phenylsilane was purchased from Aldrich and used as received. ^{1}NMR spectral data were collected on 300 and 400 MHz Bruker Avance spectrometers at 20 °C. Solution magnetic moment was determined by performing an NMR experiment following the procedure of Evans[3]. UV/visible absorption spectra were acquired at room temperature on an Agilent Cary 5000 UV-vis- NIR double beam spectrometer with a 10 mm quartz cuvette with a Teflon valve. UV/vis spectra of solid samples were recorded on an Agilent Cary 5000 UV/vis-NIR using a Praying MantisTM high vacuum sample cell. The samples were prepared inside a glove box with <0.1 ppm O_2 and H_2O by comminuting crystalline material of the compounds with dry KBr. FT-IR spectra were recorded on Agilent Cary 630 FTIR with ATR-device at room temperatu re inside the nitrogen filled glovebox.

^{57}Fe Mössbauer spectra were measured using a ^{57}Co source in a Rh matrix on an alternating constant acceleration Wissel Mößbauer spectrometer operated in transmission mode equipped with a Janis closed cycle helium cryostat. The isomer shifts are reported relative to iron metal at ambient temperature. Experimental data were simulated with Mfit software using Lorentzian line doublets (program developed by E. Bill, Max-Planck Institute for Chemical Energy Conversion, Mülheim/Ruhr, Germany).

4.5.2. Synthesis of Clusters

$Fe_5(L^H)_6[N(SiMe_3)_2]_4$ (**1**)

2-Pyridone L^HH (242.4 mg, 2.55 mmol) was suspended in 20 mL of toluene and the mixture was heated to 40 °C until all solid dissolved. The resulting colourless solution was added within 15 min to the stirring solution of $Fe(hmds)_2$ (800 mg, 2.12 mmol) in 10 mL of toluene. Colour changes from green through olive to yellow-orange. The solution was stirred for 16 h at room temperature followed by solvent removal in a vacuum. The solid yellow-brown residue was treated with 10 mL of hexane, then the resulting suspension was filtered through sintered glass filter and washed with additional 12 mL of hexane. Drying *in vacuo* for ca. 2 h afforded product in the form of light-yellow solid 457 mg (72%). Single crystals, suitable for X-Ray diffraction analysis, were obtained by crystallization from hexane/Et_2O (1:1) mixture at -35 °C.

Elemental analysis of bulk material calculated for $C_{55}H_{96}Fe_5N_{10}O_6Si_6$: C 43.67, H 6.51, N 9.43; found 43.67, 6.31, 9.36

Evans NMR (300 MHz, C_6D_6-C_6H_6, 299 K): μ_{eff} = 11.47 μ_B

Melting with decomposition at 212-214 °C

$Fe_4(L^{Me})_6[N(SiMe_3)_2]_2$ (**2**)

6-Methyl-2-pyridone $L^{Me}H$ (217.3 mg, 1.98 mmol) was suspended in 10 mL of toluene and the mixture was heated to 50 °C until all solid dissolved. The resulting colourless solution was added within 10 min to the stirred solution of $Fe(hmds)_2$ (500 mg, 1.33 mmol) in 10 mL of toluene. The reaction mixture was stirred overnight to give lemon-yellow suspension and shortly heated to 60 °C to dissolve formed precipitates. The solvent was removed under reduced pressure, the residue was dried for 15 minutes and then washed with 5 mL of hexane. Afforded pale yellow powder was recrystallized from a hot hexane/toluene 2:5 mixture in a pressure bottle. After storing overnight in -35 °C, gold-yellow crystalline solid was isolated (352 mg, 82%). Single crystals, suitable for X-Ray diffraction analysis, were obtained during the described crystallization procedure. Alternatively, the compound could be recrystallized by THF/hexane layering at -35 °C to give the solvate **2•2C_4H_8O.**

Elemental analysis calculated for toluene monosolvate $C_{55}H_{80}Fe_4N_8O_6Si_4$ C 51.41, H 6.28, N 8.72; found 51.67, 6.27, 8.91

Melting with decomposition at 223 °C

Evans NMR (300 MHz, THF-d_8, 300 K): μ_{eff} = 10.5 μ_B

*$Fe_7(L^H)_9(\mu_4\text{-}O)(OAr)_3$ (**3**)*

A solution of 2,6-di-tert-butyl-p-cresol ArOH (reagent grade without purification, 0.24 mmol, 53 mg, 4 eq) in 1.0 mL of toluene was added to the solution of cluster **1** (0.6 mmol, 90 mg, 1 eq) in 3.0 mL of toluene. The reaction mixture was stirred overnight at room temperature resulting in a color change from yellow to olive green. Volatiles

were removed in reduced pressure and the sticky greenish-brown solid residue was treated with 2 mL of hexane. Solid was collected by filtration, washed with 2 mL of hexane and dried in a vacuum to give 68 mg of yellow solid. Single crystals suitable for X-Ray diffraction analysis were obtained by slow evaporation of saturated Et_2O solution.

*$Fe_4(L^H)_6(thf)_6(BAr^F{}_4)_2$ (**4**)*

To the solution of cluster **2** (50 mg, 0.033 mmol, 1 eq) in toluene (2.0 ml) was added 1.0 mL of $H(Et_2O)_{2.9}BAr^F{}_4$ (145 mg, 0.134 mmol, 4 eq) solution in THF and the reaction mixture was stirred overnight at room temperature. Volatiles were removed in reduced pressure and the yellow sticky solid residue was triturated with 2.0 mL of hexane and stirred overnight. The precipitate was isolated by filtration and dried in a vacuum to give 85 mg yellow solid. In order to grow single crystals, 12 mg of obtained solid was dissolved in 0.5 mL THF, layered with 1.0 mL hexane and stored at -35 °C to give a small crop of crystals suitable for XRD diffraction studies.

*$Fe_4(L^{Me})_6(OAr)_2$ (**5**) and $Fe_4(L^{Me})_6(OAr)_2$*2THF (**6**)*

Solution of 2,6-Di-tert-butyl-p-cresol ArOH (sublimed in vacuum prior to use) in 1.0 mL of THF was added to solution of cluster **2** (40 mg, 31µmol) in 1.5 mL of THF. The solution turned yellow and stirred for overnight, the solvent was removed under reduced pressure and residue was dried *in vacuo* for 30 min. The solid residue was re-dissolved in 3.0 mL of THF and the resulting solution was filtered through the syringe filter (PTFE 0.2 µm). The obtained filtrate was subjected to vapor diffusion with pentane for 3 weeks, affording the product as yellow-brown crystals of 6 (27.6 mg, 68%), suitable for X-Ray diffraction analysis.

Elemental analysis calculated for $C_{66}H_{82}Fe_4N_6O_8$ C 60.48, H 6.31, N 6.41; found, C 60.80, H 6.44, N 6.28 (fits thf-free cluster **5**)

Melting point >260 °C

Under the same condition in another batch, crystals of **5** were isolated and analyzed by X-Ray diffraction analysis.

4.5.3. Catalytic Tests

*Hydrosilylation catalyzed by complexes **1** and **2***

Complexes **1** and **2** were employed in a series of hydrosilylations of unsaturated substrates (Table 4.1). Indeed, very high catalytic activity was observed in the hydrosilylation of acetophenone with phenylsilane, however, the parent complex $Fe[N(SiMe_3)_2]_2$ bearing two basic amido ligands showed higher activity.[4] Alternative reactions with less electrophilic ester, carboxamide, alkene, and alkyne functions gave no conversion under the same conditions.

A scintillation vial was charged with substrate (0.101 – 0.265 mmol) and 1.6 equiv. phenylsilane followed cluster **2** (0.5-2.0 mol%), **Fe(hmds)$_2$** (1.0 – 2.0 mol%) in 0.6 mL C_6D_6 or **1** cluster (0.5-2.0 mol%) in 0.6 mL C_6D_6:THF-d_8 = 5:1 mixture. The mixture was stirred at room temperature for selected time and transferred to a J. Young NMR tube. Reaction progress was monitored by ^{1}H NMR spectroscopy. Analytical characterization of acetophenone hydrosilylation products ($PhSiH_2OCH(Me)Ph$, $PhSiH(OCH(Me)Ph)_2$) matched literature data.[5]

Table 4.1. Catalytic hydrosilylations in the presence of clusters **1**, **2**, and $Fe(hmds)_2$.

entry	substrate	catalyst (mol%)	result*
1	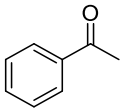	**2** (0.5)	3,5 h 98% conv 20 h – full conv
2	--	**2** (0.25)	3,5 h 90 % conv 20 h 96% conv (80% yield)
3	--	**1** (0.5)	4 h full conversion
4	--	$Fe(hmds)_2$ (1.0)	3,5 h full conv
5	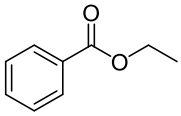	**2** (0.5) **1** (0.5)	No conversion
6	--	$Fe(hmds)_2$ (2.0)	No conversion
7	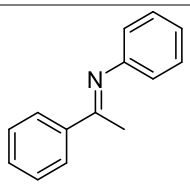	**2** (0.5) **1** (0.5)	No conversion
8	--	$Fe(hmds)_2$ (2.0)	No conversion
9	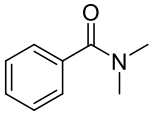	**2** (0.5) **1** (0.5)	No conversion
10	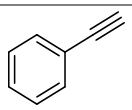	**2** (0.5) **1** (0.5)	No conversion
11	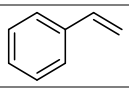	**2** (0.5) **1** (0.5)	No conversion

* ^{1}H NMR conversion is determined as a ratio between product and substrate integrals.

4.5.4. Infrared Spectroscopy

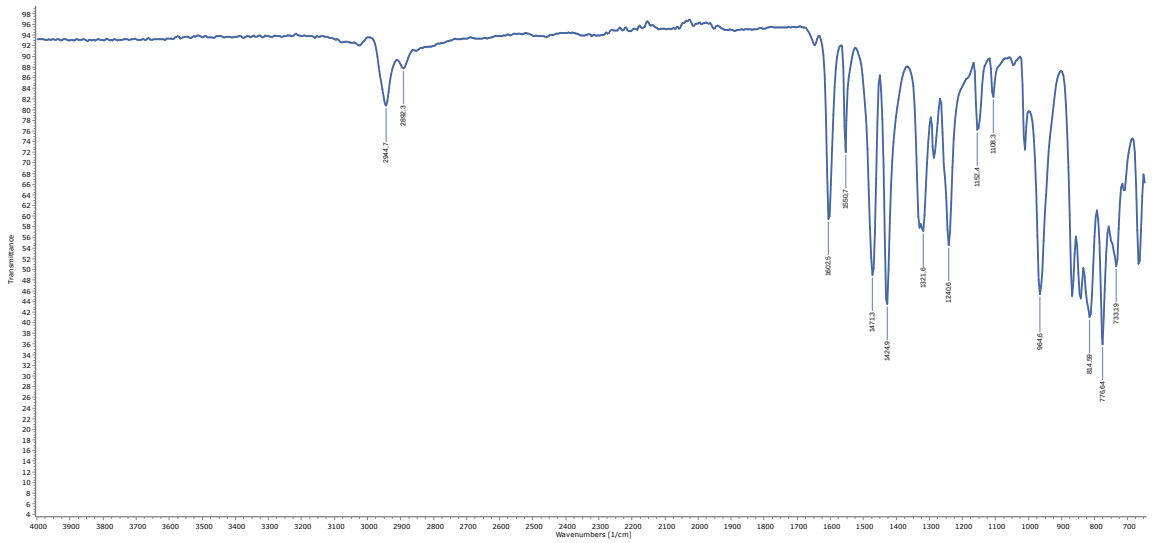

Figure 4.2. Transmission ATR spectrum of **1**.

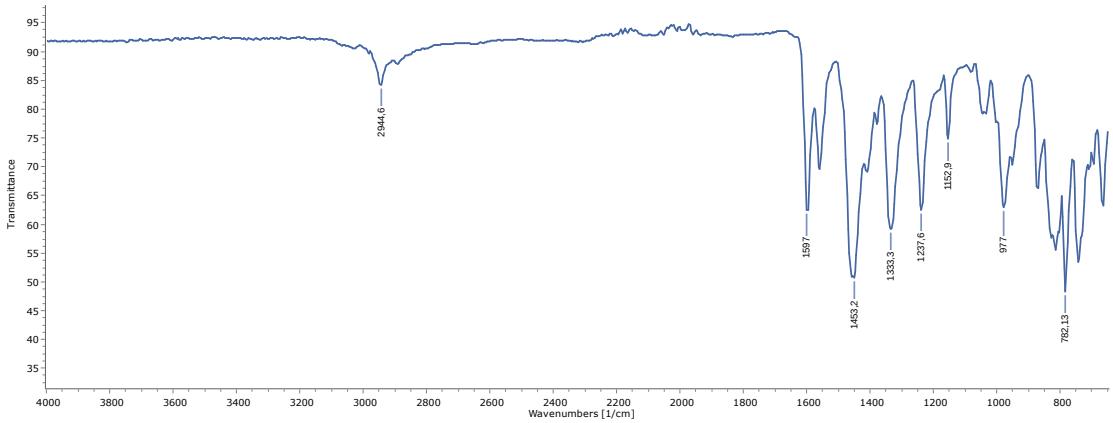

Figure 4.3. Transmission ATR spectrum of **2**.

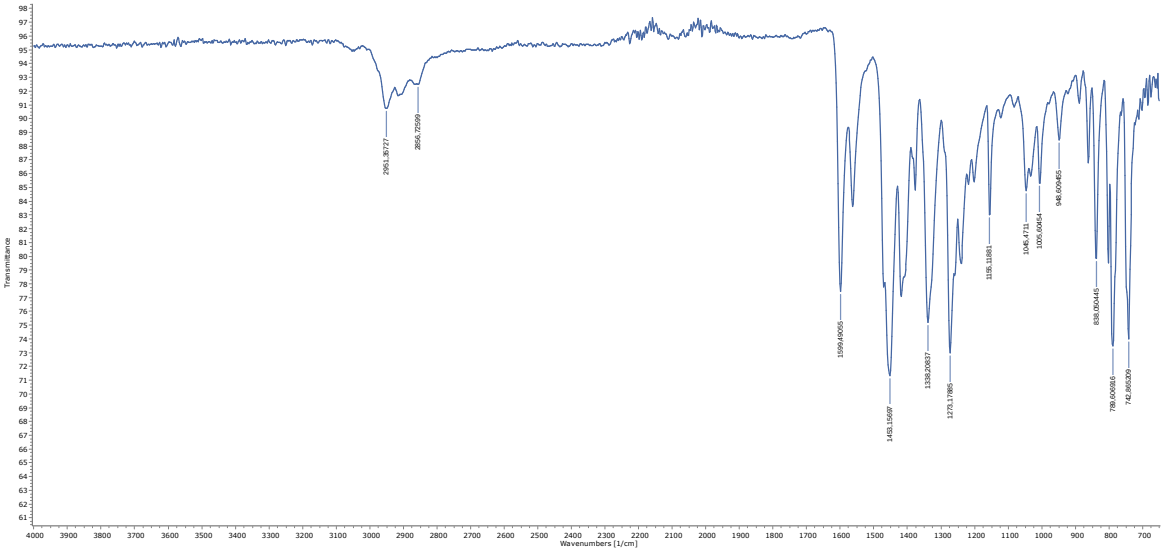

Figure 4.4. Transmission ATR spectrum of **5**.

4.5.5. UV-Visible Spectra

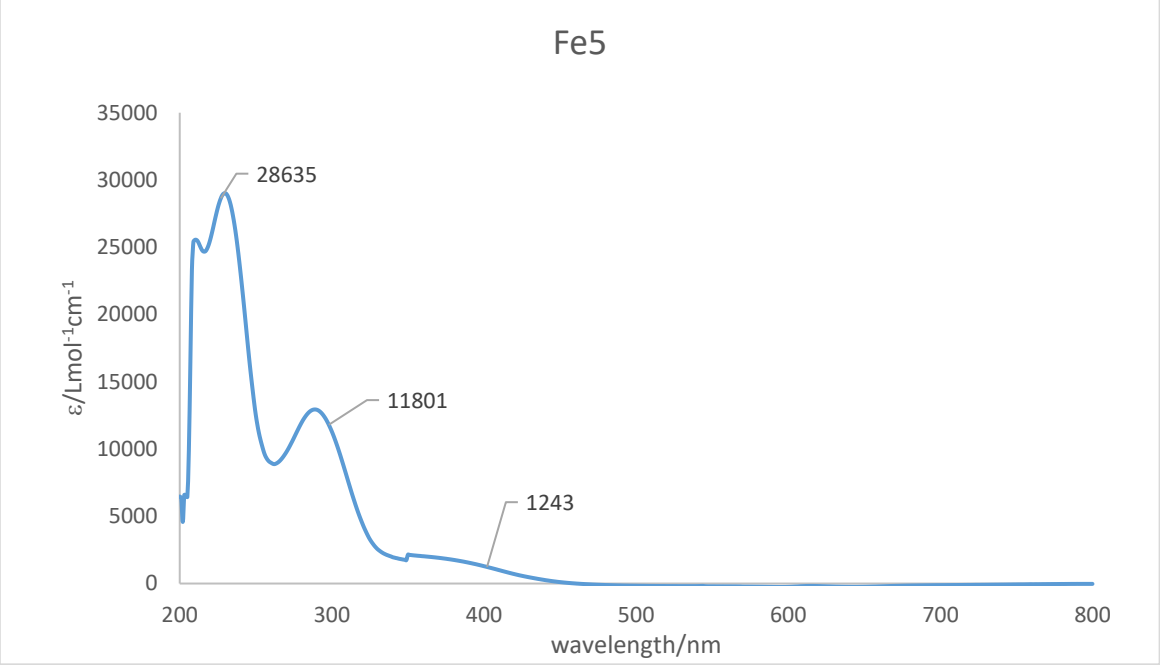

Figure 4.5. UV-Visible spectrum of **1**

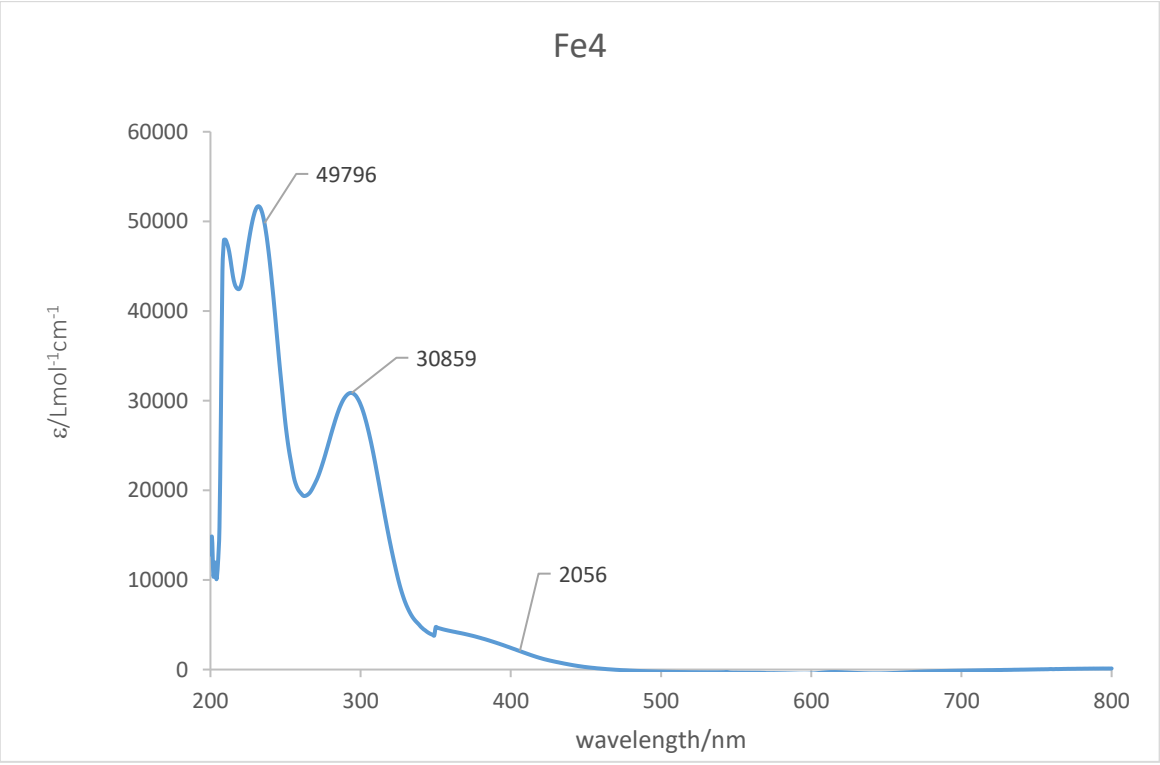

Figure 4.6. UV-Visible spectrum of **2**.

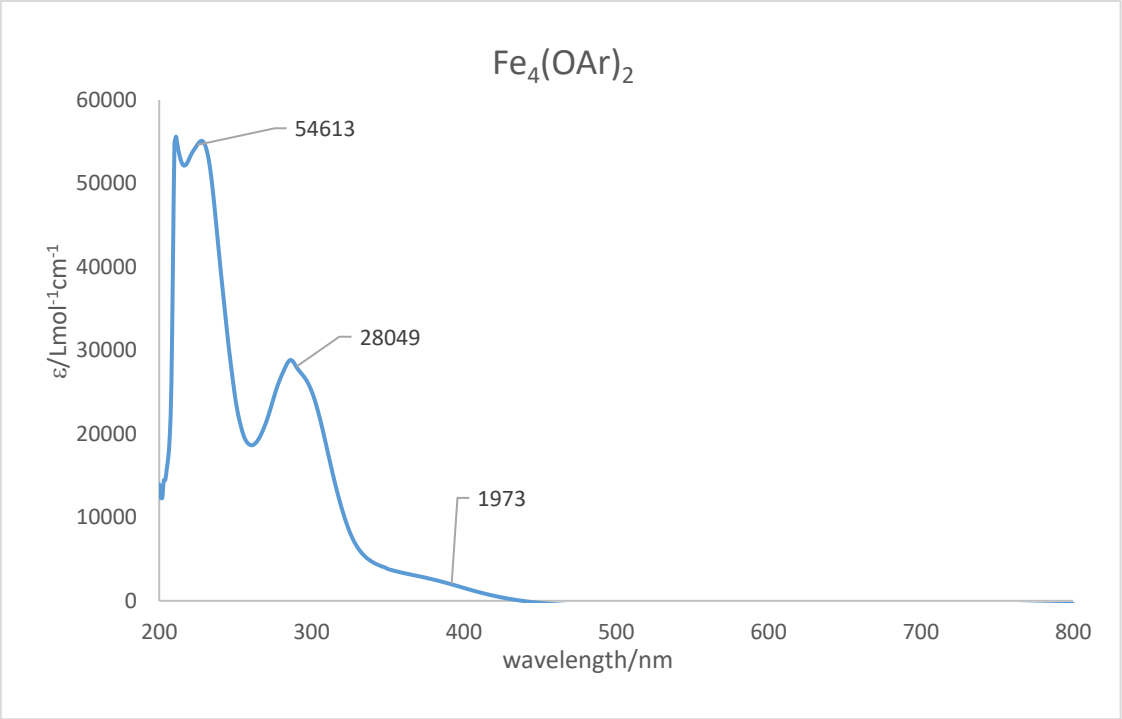

Figure 4.7. UV-Vis spectrum of **5**.

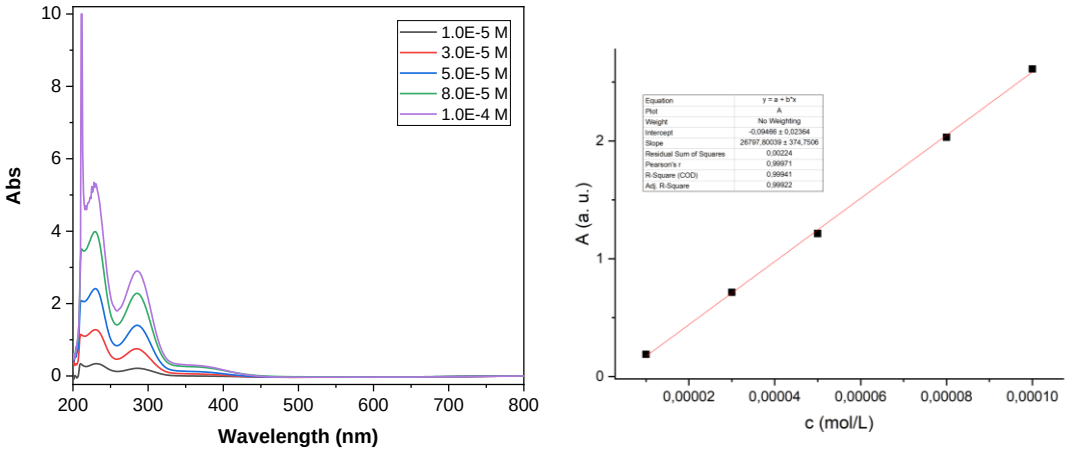

Figure 4.8. UV-Vis spectra of cluster **1** in THF in different concentrations (left); adherence to Beer's law for absorption maximum at 300 nm (right).

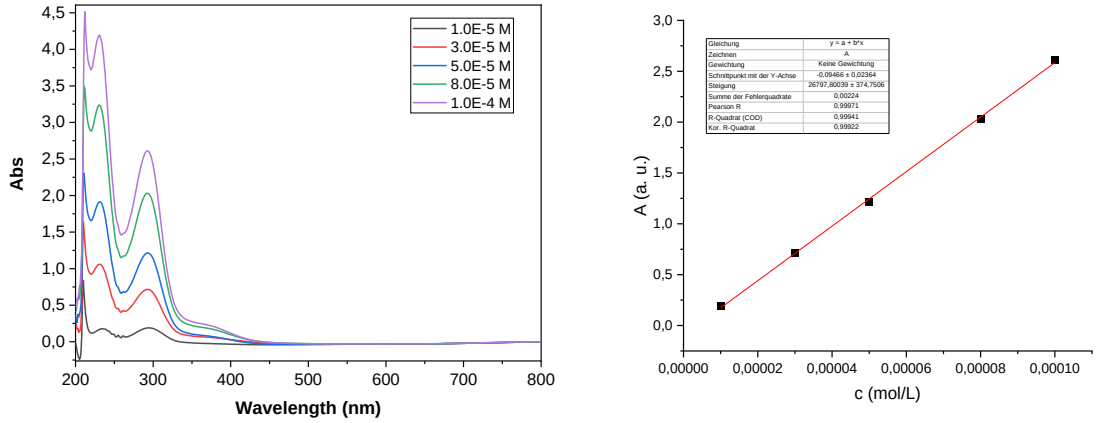

Figure 4.9. UV-Vis spectra of cluster **2** in THF in different concentrations (left); adherence to Beer's law for absorption maximum at 300 nm (right).

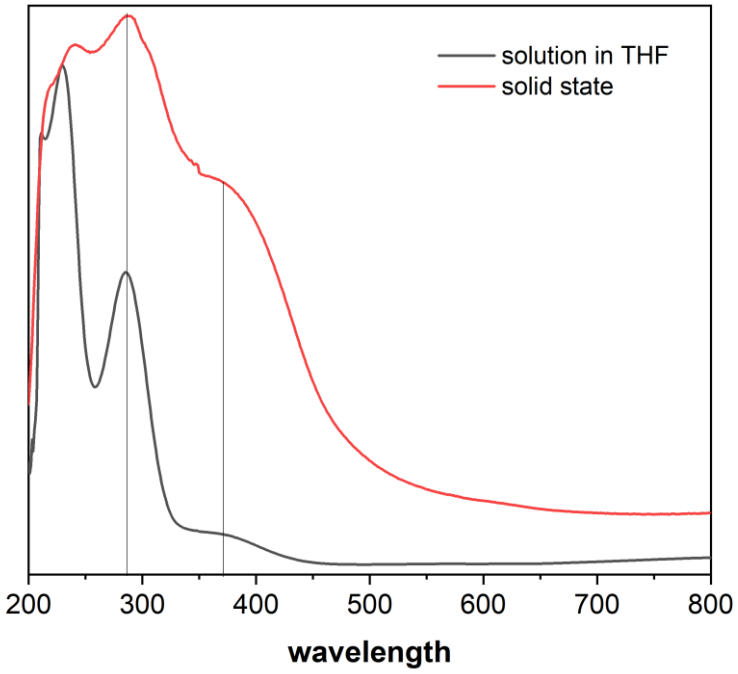

Figure 4.10. Solid state vs solution UV-Vis spectrum of cluster **1**.

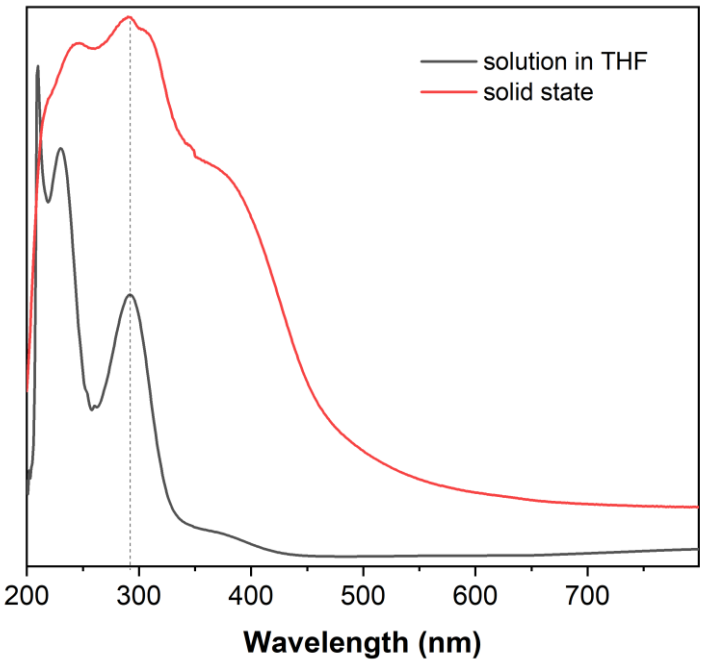

Figure 4.11. Solid state vs solution UV-Vis spectrum of cluster **2**.

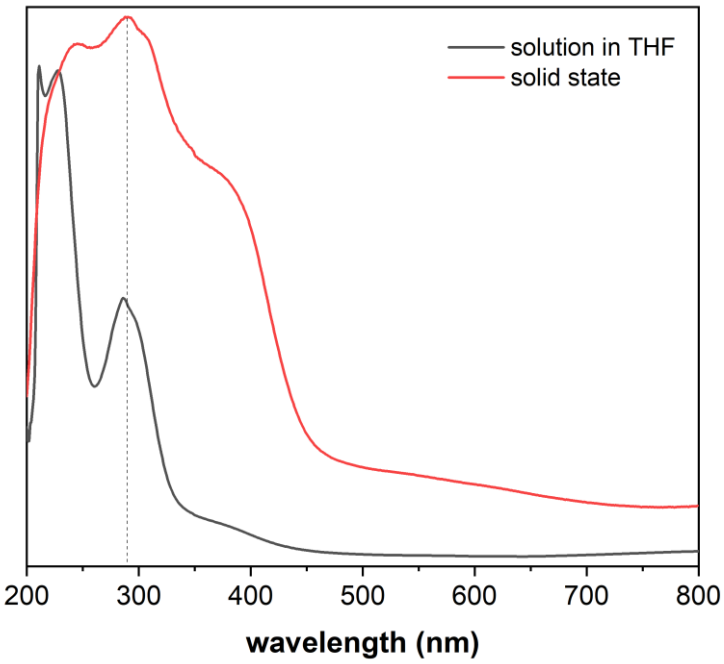

Figure 4.12. Solid state vs solution UV-Vis spectrum of cluster **5**.

4.5.6. NMR Spectra

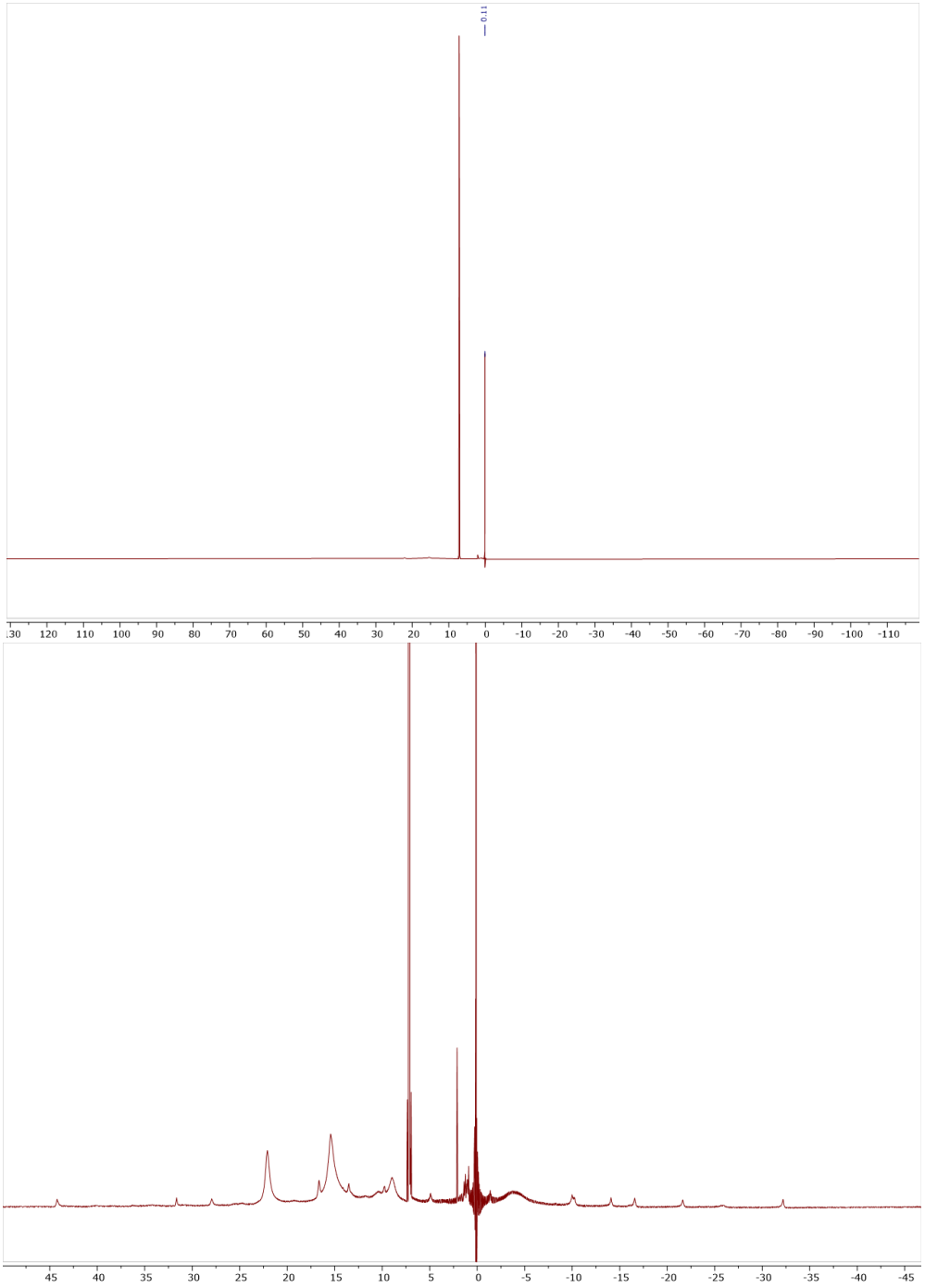

Figure 4.13. ^{1}H NMR of cluster **1** in $\mathbf{C_6D_6}$ (top); magnified part of the spectrum showing multiple paramagnetically shifted signals of low intensity which were not assigned due to complexity (bottom).

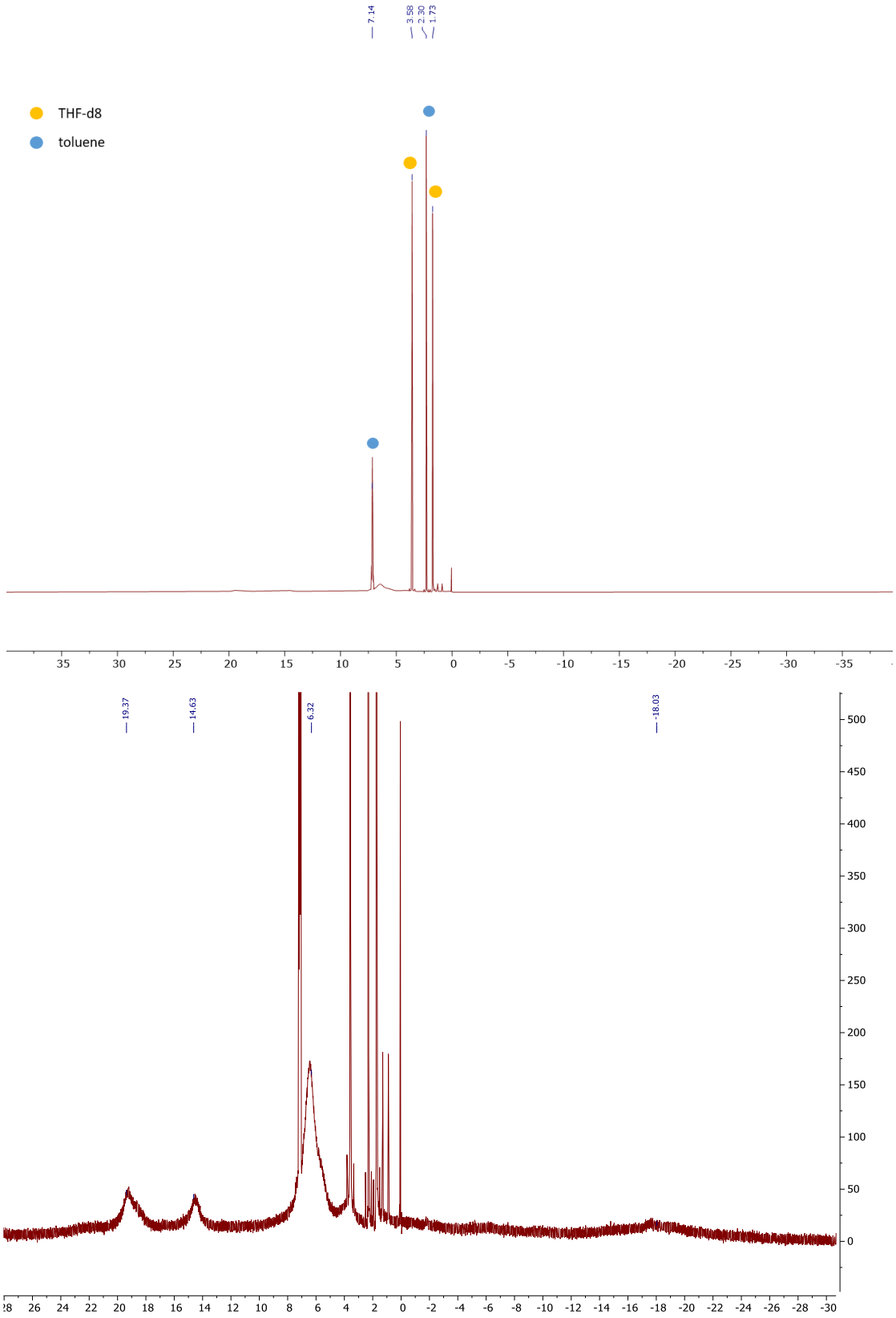

Figure 4.14. ^{1}H NMR of cluster **2** in THF-d_8 (top); magnified part of the spectrum showing several paramagnetically shifted signals of low intensity which were not assigned due to complexity (bottom).

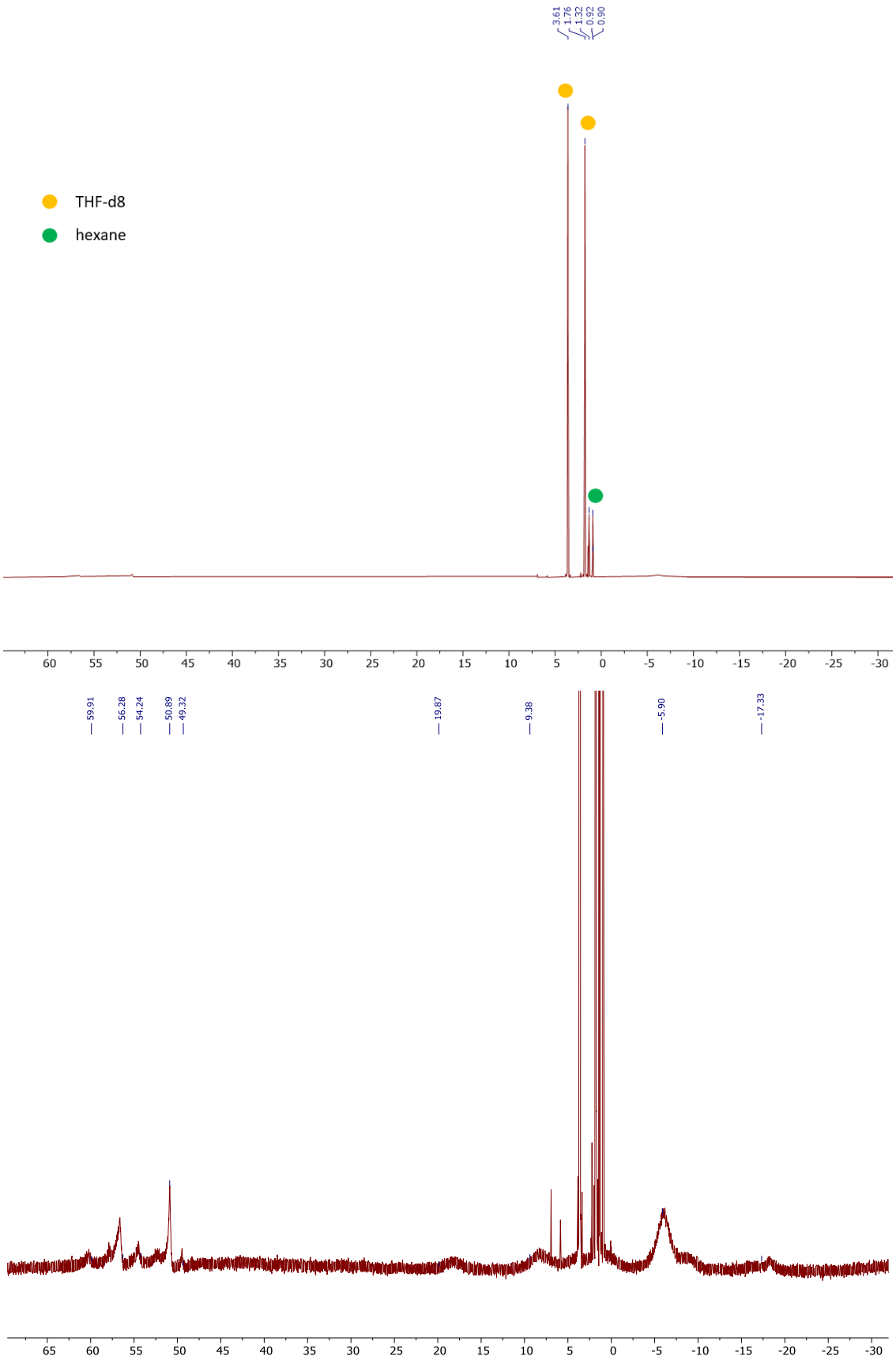

Figure 4.15. ^1H NMR of cluster **5** in THF-d_8 (top); magnified part of the spectrum showing several paramagnetically shifted signals of low intensity which were not assigned due to complexity (bottom).

4.5.7. Crystallographic Details

Single-crystal X-ray experiments were performed at 100 K using a SuperNova four-circle diffractometer in Kappa geometry with a 50 W Cu or Mo (Kα radiation) microfocus tube, an Atlas CCD detector (Rigaku Oxford Diffraction), and a Cryostream 700 Plus cooler (Oxford Cryosystems Ltd). Data collection, cell refinement, data reduction, and absorption correction were done using CrysAlisPro[6]. Intensities were measured using omega scans.

Single-crystal X-ray data was solved and refined as follows: The space group was determined either by using XPREP (Bruker AXS Inc.[7]) or CrysAlisPro and the phase problem was solved either (a) by structure-invariant direct methods with SHELXS[8], or (b) by using the dual-space algorithm implemented in SHELXT[9]. In every case, full-matrix least-squares refinement was done on F^2 using SHELXL[9].

Missing secondary atom sites were located from the difference Fourier map. If possible, non-hydrogen atoms were refined using individual, anisotropic displacement parameters. The fully refined data was reviewed using PLATON[10]. Carbon atom-bound hydrogen atoms were positioned geometrically and refined riding on their respective parent atoms. U_{iso}(H) was fixed at 1.5 (CH_3) or 1.2 (all other H atoms) of the parent atom's isotropic displacement parameter.

Table 4.2. Crystallographic data for compounds **1**- **6**.

Identification code	**1**	**2•C_7H_8**	**2•2C_4H_8O**	**3•0.5$C_4H_{10}O$**
Empirical formula	$C_{54}H_{96}Fe_5N_{10}O_6Si_8$	$C_{55}H_{80}Fe_4N_8O_6Si_4$	$C_{56}H_{88}Fe_4N_8O_8Si_4$	$C_{92}H_{110}Fe_7N_9O_{13.5}$
Formula weight	1485.37	1285.03	1337.10	1948.83
Temperature/K	100	99.97(16)	100.0(2)	100
Crystal system	tetragonal	triclinic	orthorhombic	triclinic
Space group	*I-4*	*P-1*	*$Pca2_1$*	*P-1*
a/Å	12.91770(10)	11.6469(5)	11.5698(3)	15.799(2)
b/Å	12.91770(10)	11.8768(5)	20.0415(3)	17.241(2)
c/Å	22.1984(3)	13.0322(5)	28.1222(6)	17.497(2)
α/°	90	76.464(3)	90	105.769(2)
β/°	90	80.667(3)	90	94.551(2)
γ/°	90	64.058(4)	90	93.052(2)
Volume/$Å^3$	3704.18(8)	1572.35(12)	6520.9(2)	4558.5(11)
Z	2	1	4	2
$\rho_{calc}g/cm^3$	1.332	1.357	1.362	1.420
μ/mm^{-1}	9.299	8.400	1.001	1.148
Crystal size/mm^3	0.29 × 0.179 × 0.154	0.267 × 0.193 × 0.113	0.26 × 0.18 × 0.04	0.2 × 0.04 × 0.01
Radiation	CuKα (λ = 1.54184)	CuKα (λ = 1.54184)	Mo Kα (λ = 0.71073)	MoKα (λ = 0.71073)
2Θ range /°	7.966 to 152.306	6.994 to 152.642	5.952 to 59.08	2.43 to 52.808
Reflections collected	10447	32530	166920	48172
Independent reflections	3723	6530	17245	18531
Data/restraints /parameters	3723/0/223	6530/45/371	17245/715/740	18531/358/1241
GoF	1.048	1.029	1.058	1.013
R ind. [I>=2σ (I)] R_1 (wR_2)	0.0197 (0.0490)	0.0402 (0.1086)	0.0438 (0.0854)	0.0409 (0.0976)
Final R ind. [all data] R_1 (wR_2)	0.0199 (0.0491)	0.0429 (0.1117)	0.0561 (0.0904)	0.0638 (0.1085)
Largest diff. peak/hole / e $Å^{-3}$	0.17/-0.20	0.96/-0.47	0.88/-0.56	0.79/-0.63

Table 4.2. *Continued….*

Identification code	**4•5C_4H_8O**	**5**	**6**
Empirical formula	$C_{138}H_{136}B_2F_{48}Fe_4N_6O_{17}$	$C_{66}H_{82}Fe_4N_6O_8$	$C_{74}H_{98}Fe_4N_6O_{10}$
Formula weight	3307.54	1310.77	1454.98
Temperature/K	100	99.96(16)	99.94(18)
Crystal system	monoclinic	triclinic	triclinic
Space group	*$P2_1/c$*	*P-1*	*P-1*
a/Å	12.166(2)	10.7172(7)	12.9102(2)
b/Å	29.592(5)	12.8771(4)	12.95350(10)
c/Å	20.670(4)	23.8664(8)	13.8956(2)
α/°	90	84.867(3)	108.7890(10)
β/°	101.948(2)	80.215(4)	111.3770(10)
γ/°	90	81.190(4)	92.9980(10)
Volume/$Å^3$	7280(2)	3200.7(3)	2010.29(5)
Z	2	2	1
$\rho_{calc}g/cm^3$	1.509	1.360	1.202
μ/mm^{-1}	0.516	7.589	0.762
Crystal size/mm^3	0.318 × 0.068 × 0.036	0.2 × 0.05 × 0.03	0.3 × 0.3 × 0.2
Radiation	MoKα (λ = 0.71073)	Cu Kα (λ = 1.54184)	Mo Kα (λ = 0.71073)
2Θ range /°	2.44 to 49	6.962 to 123.346	5.728 to 62.19
Reflections collected	62965	27873	106712
Independent reflections	12055	9822	12209
Data/restraints /parameters	12055/565/1016	9822/0/777	12209/0/438
GoF	1.024	1.023	1.041
R ind. [I>=2σ (I)] R_1 (wR_2)	0.0644 (0.1568)	0.0586 (0.1455)	0.0272 (0.0691)
Final R ind. [all data] R_1 (wR_2)	0.0881 (0.1704)	0.0827 (0.1619)	0.0306 (0.0712)
Largest diff. peak/hole / e $Å^{-3}$	0.96/-0.60	0.50/-0.75	0.43/-0.26

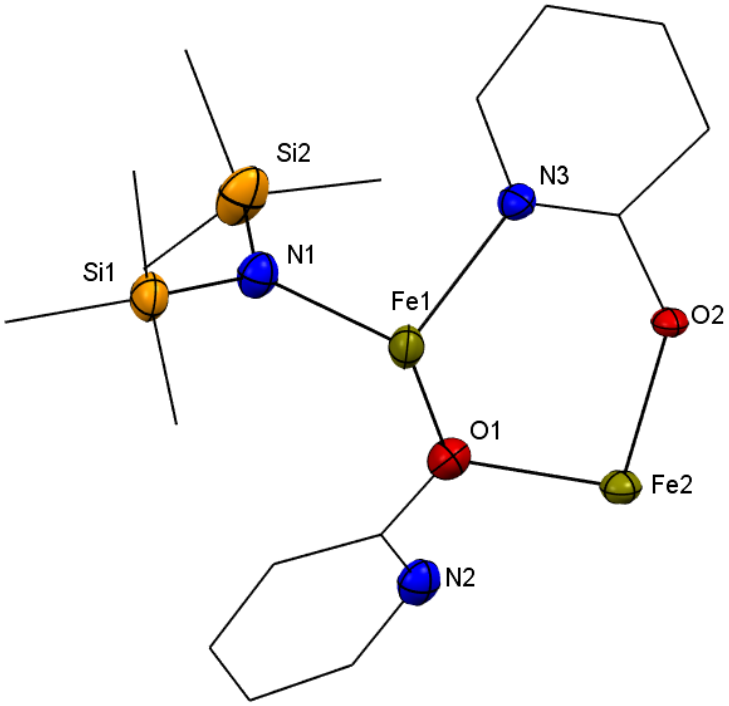

Figure 4.16. The asymmetric unit of the pentanuclear cluster **1**.

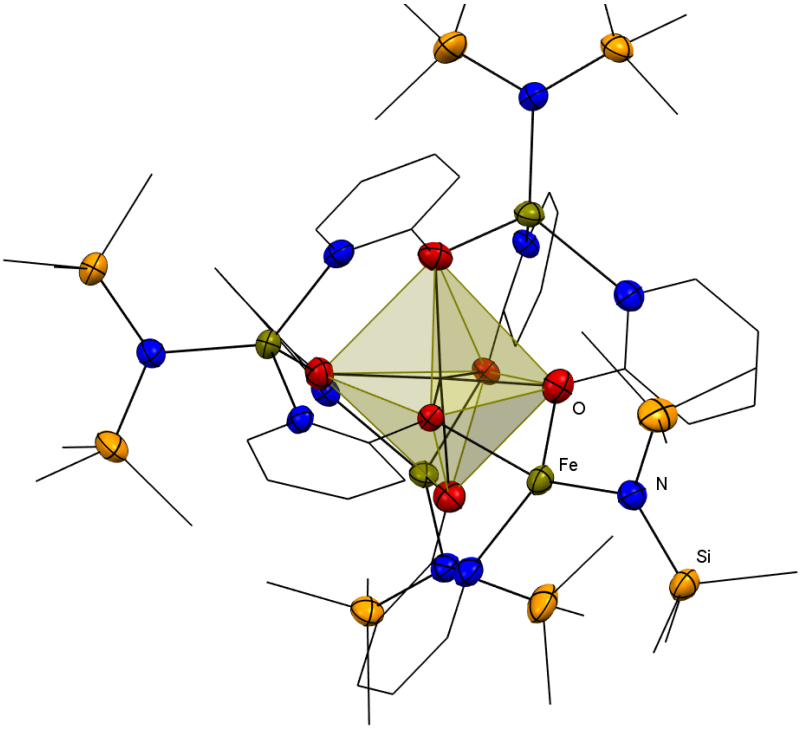

Figure 4.17. Polyhedral representation of the central Fe atom surrounded with 6 oxygen atoms in pentanuclear cluster **1** illustrating distorted octahedral environment.

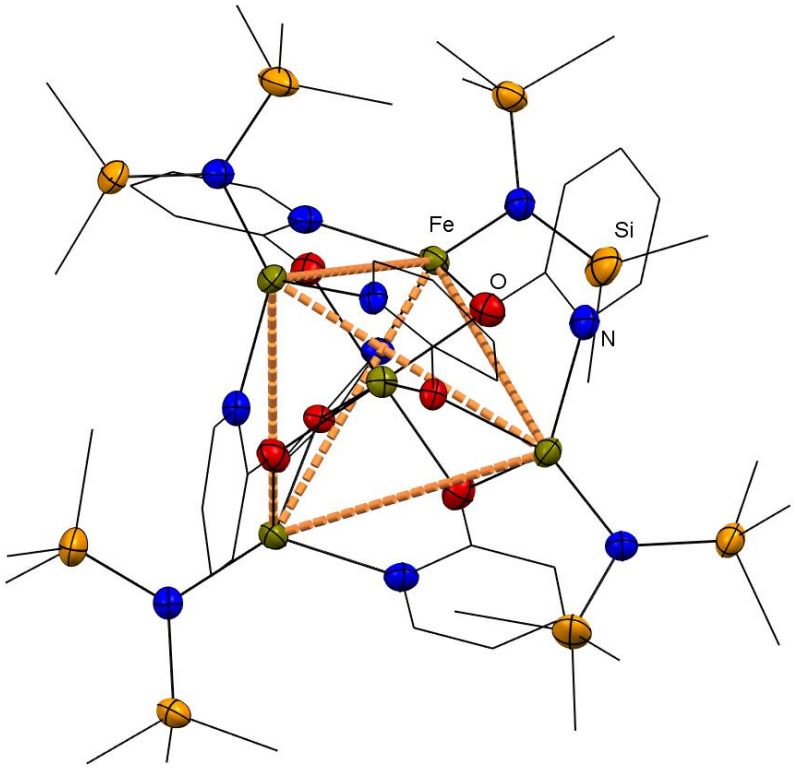

Figure 4.18. Structural drawing of cluster **1** illustrating Fe@Fe4 iron core.

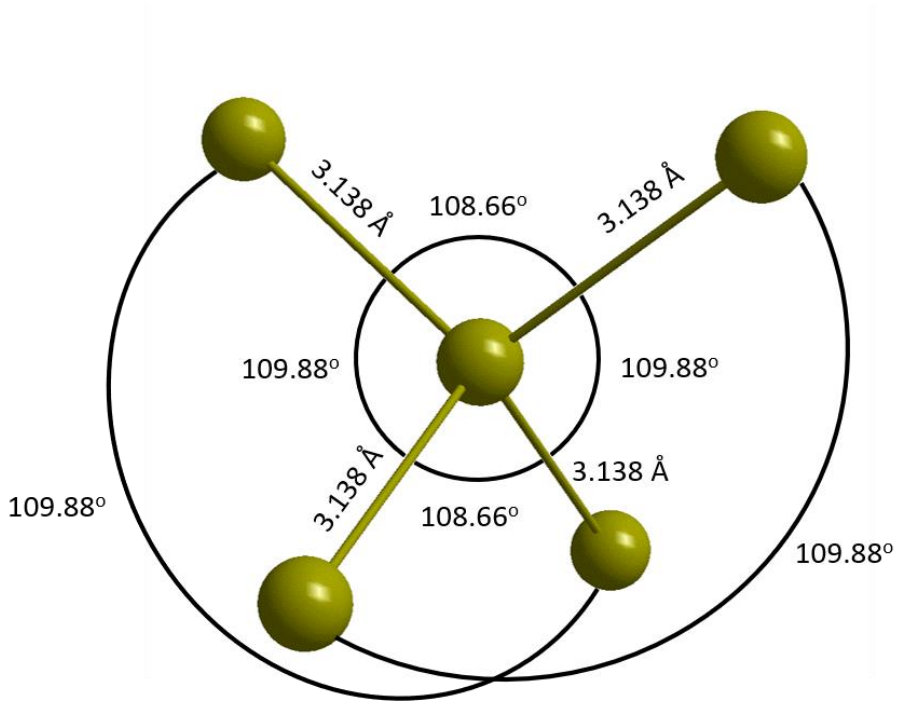

Figure 4.19. Structural properties of the cluster core in **1**, with distortions from T_d symmetry.

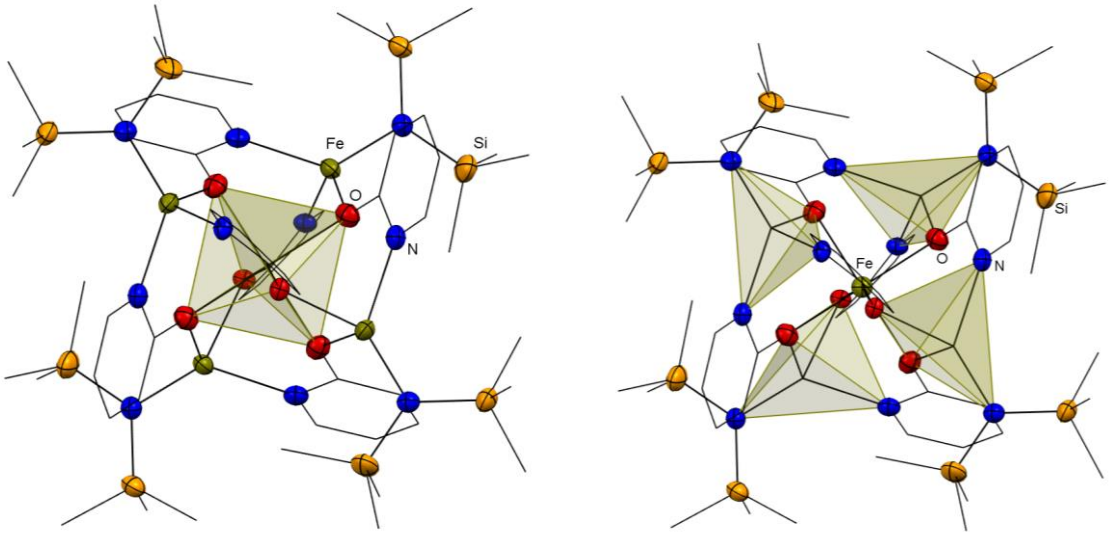

Figure 4.20. Polyhedral representation of the Fe_5 cluster **1** illustrating the coordination environments of central and peripheral Fe ions (polyhedra are centered with Fe). FeO_6 distorted octahedron (left); FeN_3O and FeN_2O_2 distorted tetrahedra (right).

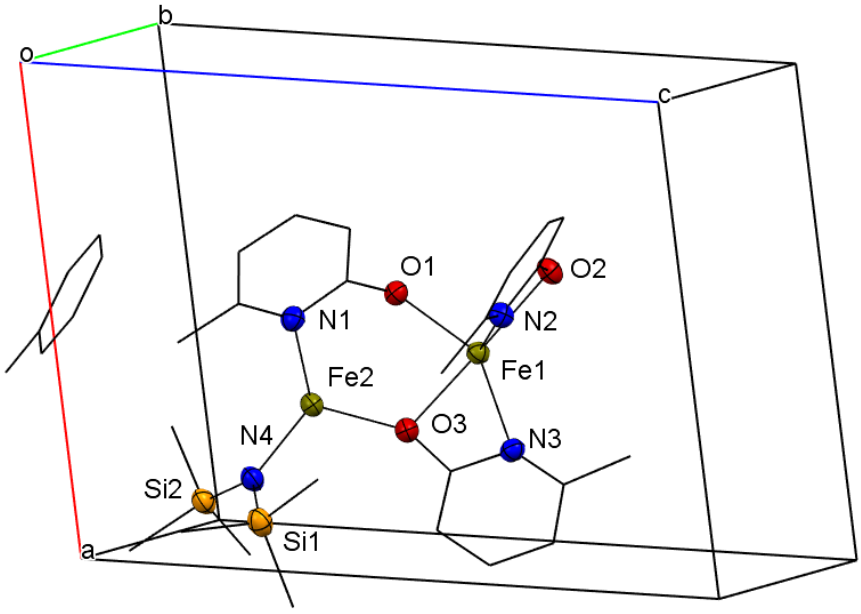

Figure 4.21. The asymmetric unit of the Fe_4 cluster **2** comprising two Fe ions.

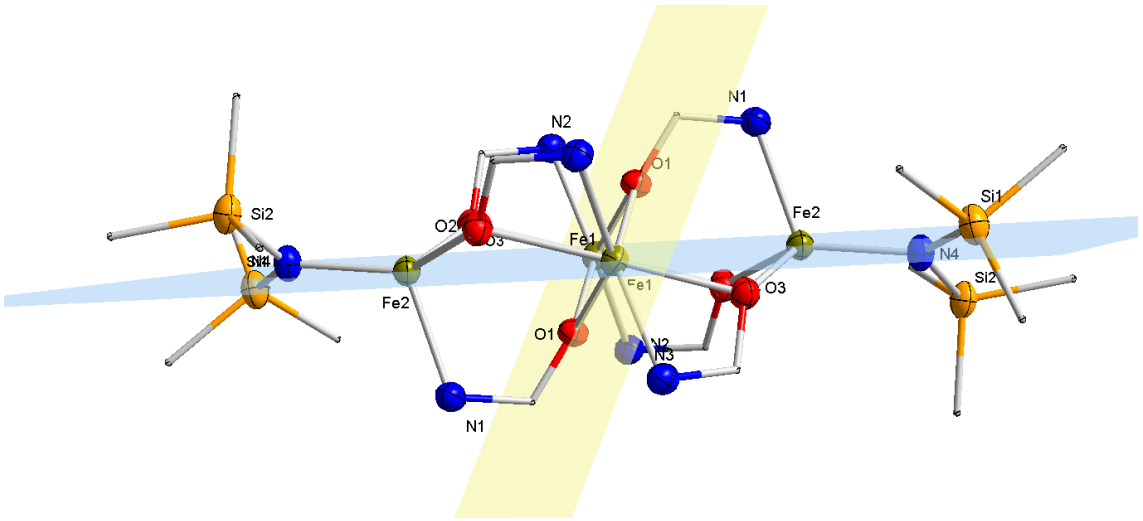

Figure 4.22. Molecular structure of Fe_4 cluster **2** (C atoms of pyridonates are omitted) showing coplanarity of four Fe atoms (blue plane) and planarity of the Fe_2O_2 unit (yellow plane).

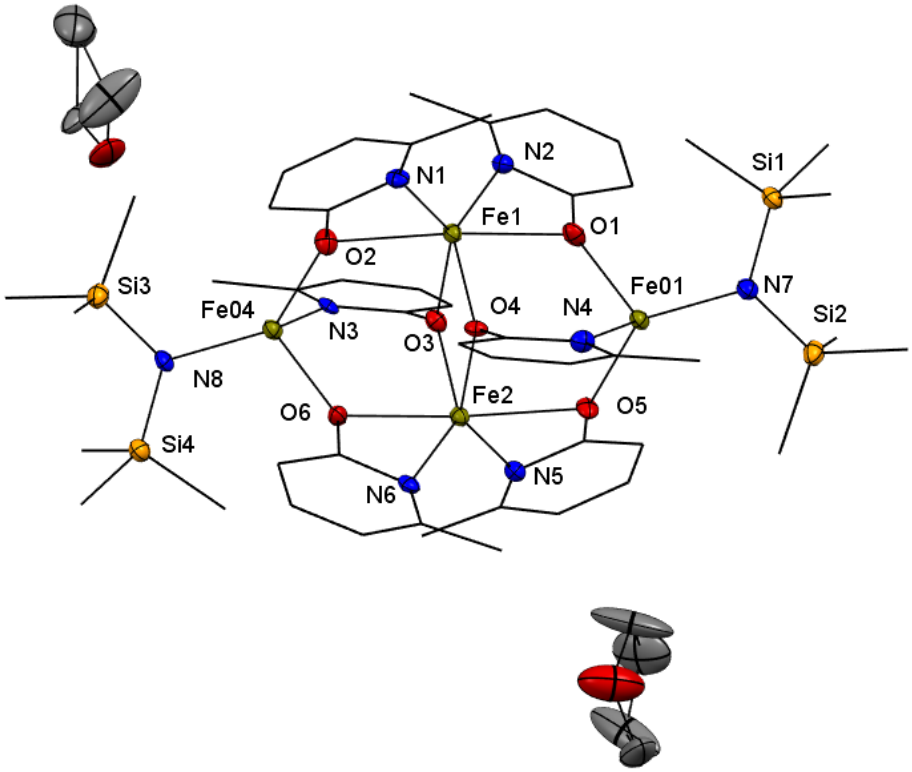

Figure 4.23. The asymmetric unit of the THF-solvate **2•2C$_4$H$_8$O**. Ellipsoids are shown at the 50% probability level. Hydrogen atoms are omitted for clarity.

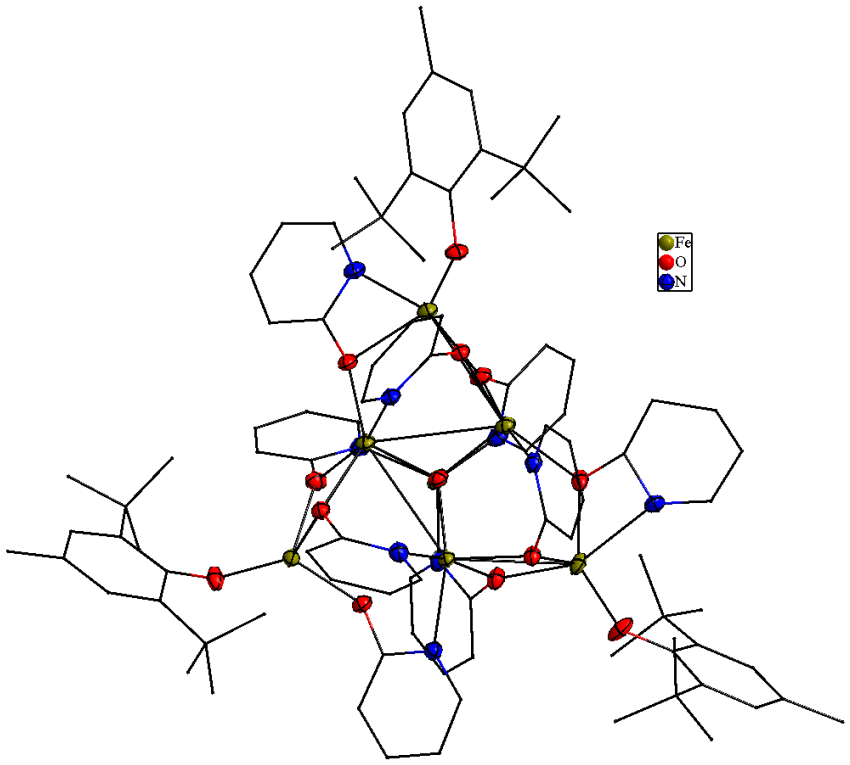

Figure 4.24. The molecular structure of heptanuclear cluster **3.** Ellipsoids are shown at 50% probability. Hydrogen atoms are omitted for clarity.

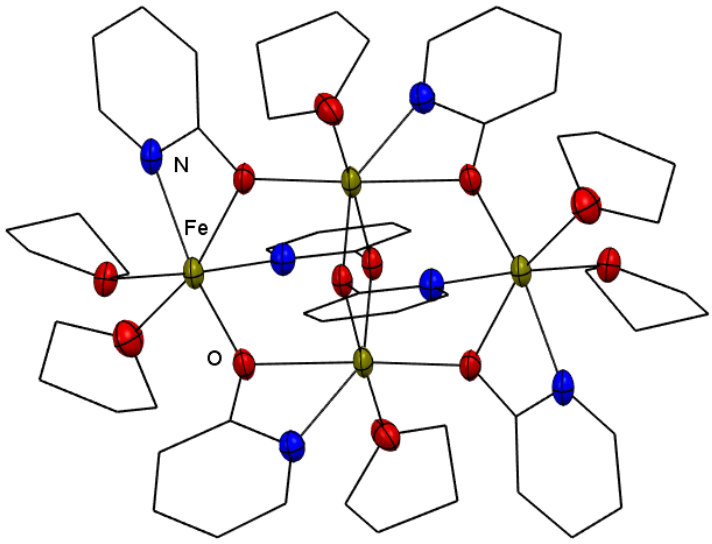

Figure 4.25. The molecular structure of the cationic molecular cluster **4;** hydrogen atoms and the counter anions $\mathbf{BAr^F_4}^-$ are not shown for clarity.

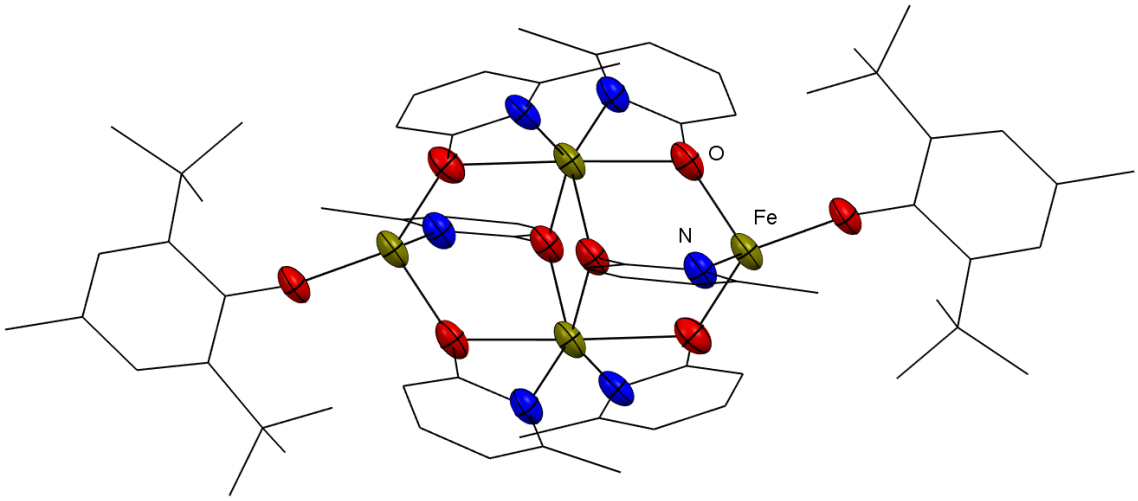

Figure 4.26. The molecular structure of the compound **5.** Ellipsoids are shown at 50% probability. Hydrogen atoms are omitted for clarity.

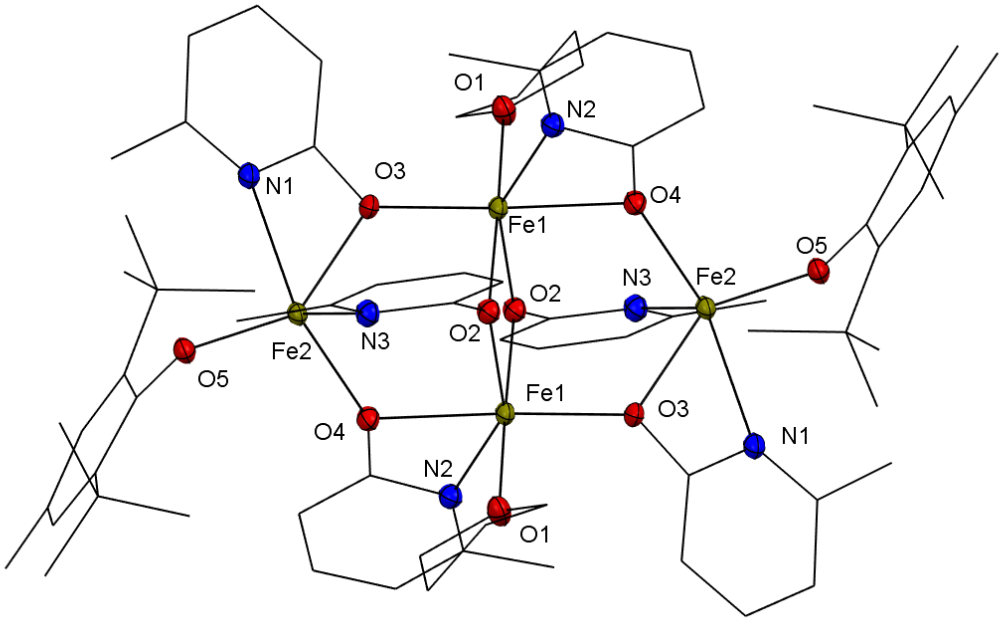

Figure 4.27. The molecular structure of the compound **6**. Ellipsoids are shown at 50% probability. Hydrogen atoms are omitted for clarity.

Table 4.3. Selected bond lengths and angles for Fe_5 cluster **1**.

Coordination environment	Bond distances (Å)		Bond angles (º)	
Fe1 (N_3O)	Fe1-N1	1.945(3)	O1-Fe1-N2[1]	110.21(11)
	Fe1-N2	2.133(3)	O1-Fe1-N3	116.29(16)
	Fe1-N3	2.136(6)	N1-Fe1-O1	112.18(11)
	Fe1-O1	2.049(3)	N1-Fe1-N2[1]	127.32(12)
			N1-Fe1-N3	102.23(17)
			N2[1]-Fe1-N3	85.32(19)
$Fe1^2$ (N_2O_2)	$Fe1^2$-N1[3]	1.945(3)	O2-$Fe1^2$-N2[3]	82.7(2)
	$Fe1^2$-N2[3]	2.133(3)	N2[3]-$Fe1^2$-N1[3]	127.3(1)
	$Fe1^2$-O1[2]	2.049(3)	N1[3]-$Fe1^2$-O1[2]	112.2(1)
	$Fe1^2$-O2	2.085(5)	O2-$Fe1^2$-O1[2]	76.0(1)
			O1[2]-$Fe1^2$-N2[3]	110.2(1)
			O2-$Fe1^2$-N1[3]	137.0(2)
Fe2 (O_6)	Fe2-O1	2.091(2)	O1[2]-Fe2-O1[3]	90.109(6)
	Fe2-O2	2.204(4)	O1[1]-Fe2-O1	90.110(6)
			O1[3]-Fe2-O1	90.109(6)
			O1[3]-Fe2-O1[1]	174.99(14)
			O1[2]-Fe2-O1	175.00(14)
			O1[2]-Fe2-O1[1]	90.109(6)
			O1[2]-Fe2-O2	72.63(14)
			O1-Fe2-O2	102.36(13)
			O1[1]-Fe2-O2	91.65(15)
			O1[3]-Fe2-O2	93.19(15)

Symmetry: [1](+Y,1-X,1-Z); [2](1-X,1-Y,+Z); [3](1-Y,+X,1-Z)

Table 4.4. Selected bond lengths and angles for Fe_4 cluster **2•C_7H_8**.

Bond distances (Å)		**Bond Angles (º)**			
O1-Fe1[1]	2.0983(14)	O1-Fe1-O1[1]	78.56(6)	N2-Fe1-N3	119.55(6)
O1-Fe1	2.0768(14)	O1[1]-Fe1-O2	83.37(5)	N3-Fe1-O2	119.37(6)
O2-Fe1	2.2256(14)	O1-Fe1-O2	95.62(6)	O2[1]-Fe2-O3	99.68(6)
O2-Fe2[1]	2.0297(15)	O1-Fe1-O3	82.75(5)	O2[1]-Fe2-N1	93.50(6)
O3-Fe1	2.1593(14)	O1[1]-Fe1-O3	93.67(6)	O3-Fe2-N1	104.62(6)
O3-Fe2	2.0535(14)	O1[1]-Fe1-N2	142.31(6)	N4-Fe2-O2[1]	131.66(7)
N1-Fe2	2.1671(17)	O1-Fe1-N2	92.70(6)	N4-Fe2-O3	110.20(7)
N2-Fe1	2.1395(17)	O1-Fe1-N3	140.32(6)	N4-Fe2-N1	113.54(7)
N3-Fe1	2.1770(16)	O1[1]-Fe1-N3	86.99(6)	Fe1-O1-Fe1[1]	101.44(6)
N4-Fe2	1.9762(17)	O3-Fe1-O2	176.87(5)	Fe2[1]-O2-Fe1	115.99(7)
		O3-Fe1-N3	61.33(6)	Fe2-O3-Fe1	118.54(7)
		N2-Fe1-O2	60.84(6)	N2-Fe1-O3	121.81(6)

Symmetry [1]1-X,1-Y,1-Z

Table 4.5. Selected bond lengths and angles for Fe_4 cluster **2•2C_4H_8O**.

Bond distances (Å)			**Bond Angles (º)**		
Fe2-O1	2.043(4)	O1-Fe2-N4	102.32(18)	O4-Fe1-N2	140.85(17)
Fe2-O5	2.034(4)	O5-Fe2-O1	96.78(17)	O1-Fe1-O2	175.41(17)
Fe2-N4	2.171(4)	O5-Fe2-N4	94.18(16)	O1-Fe1-N2	61.44(17)
Fe2-N7	1.966(5)	N7-Fe2-O1	111.25(19)	O3-Fe1-O1	93.11(16)
Fe1-O4	2.079(4)	N7-Fe2-O5	131.72(19)	O3-Fe1-O2	82.82(16)
Fe1-O1	2.141(4)	N7-Fe2-N4	115.8(2)	O3-Fe1-N1	141.52(17)
Fe1-O2	2.224(4)	O4-Fe1-O1	81.82(15)	O3-Fe1-N2	89.02(16)
Fe1-O3	2.088(4)	O4-Fe1-O2	95.29(16)	N1-Fe1-O1	122.35(18)
Fe1-N1	2.137(4)	O4-Fe1-O3	79.38(14)	N1-Fe1-O2	61.04(17)
Fe1-N2	2.180(5)	O4-Fe1-N1	90.56(17)	N1-Fe1-N2	119.48(18)
Fe3-O4	2.084(4)			N2-Fe1-O2	120.40(18)
Fe3-O6	2.143(4)				
Fe3-O5	2.247(4)				
Fe3-O3	2.087(4)				
Fe3-N6	2.172(4)				
Fe3-N5	2.126(5)				
Fe4-O2	2.042(4)				
Fe4-O6	2.042(4)				
Fe4-N8	1.977(5)				
Fe4-N3	2.170(4)				

Table 4.6. Selected bond lengths and angles for cluster **3**.

Bond distances (Å)		**Bond Angles (º)**	
Fe1-O1	1.9979(19)	Fe1-O1-Fe3	115.37(9)
Fe2-O1	1.9735(19)	Fe2-O1-Fe1	111.09(10)
Fe3-O1	2.009(2)	Fe2-O1-Fe3	109.75(9)
Fe4-O3_1	1.886(3)	Fe7-O1-Fe1	110.61(9)
Fe5-O3_4	1.8530(19)	Fe7-O1-Fe2	107.86(9)
Fe6-O3_3	1.858(2)	Fe7-O1-Fe3	101.57(9)
Fe7-O1	1.947(2)		

Table 4.7. Selected bond lengths and angles for cluster **4**.

Bond distances (Å)		**Bond Angles (º)**			
Fe1-N1_1	2.165(4)	N1_1-Fe1-N1_3[1]	92.45(14)	O1_1-Fe2-O1_1[1]	80.61(12)
	2.024(3)		87.58(13)		91.22(12)
Fe1-O1_2	2.221(4)	N1_1-Fe1-O1_3[1]	175.56(13)	O1_1[1]-Fe2-N1_2	149.27(12)
	2.205(3)		92.23(13)		88.89(11)
Fe1-N1_3[1]	2.151(3)	N1_1-Fe1-O2_6	162.21(13)	O1_1-Fe2-N1_2	95.14(12)
	2.208(3)		102.78(11)		90.01(11)
Fe1-O1_3[1]	2.184(3)	O1_2-Fe1-N1_1	93.90(13)	O1_1-Fe2-O1_2	61.36(12)
	2.064(3)		89.22(12)		86.46(11)
Fe1-O2_5	2.191(4)	O1_2-Fe1-N1_3[1]	60.31(12)	O1_1-Fe2-O3_4	97.24(11)
	2.160(3)		88.00(11)		111.86(13)
Fe1-O2_6	2.014(3)	O1_2-Fe1-O1_3[1]	91.13(14)	O1_2-Fe2-O1_1[1]	172.33(12)
	2.142(3)		103.15(13)		93.61(12)
Fe2-O1_1[1]		O1_2-Fe1-O2_5	163.31(12)	O1_2-Fe2-N1_2	175.72(12)
Fe2-O1_1		O1_2-Fe1-O2_6	92.96(12)	O1_3-Fe2-O1_1[1]	92.73(13)
Fe2-N1_2		O1_3[1]-Fe1-N1_3[1]	84.94(12)	O1_3-Fe2-N1_2	90.42(12)
Fe2-O1_2		O1_3[1]-Fe1-O2_6		O1_3-Fe2-O1_2	
Fe2-O1_3		O2_5-Fe1-N1_1		O1_3-Fe2-O3_4	
Fe2-O3_4		O2_5-Fe1-N1_3[1]		O3_4-Fe2-O1_1[1]	
		O2_5-Fe1-O1_3[1]		O3_4-Fe2-N1_2	
		O2_5-Fe1-O2_6		O3_4-Fe2-O1_2	
		O2_6-Fe1-N1_3			

Symmetry [1]2-X,1-Y,1-Z

***Table 4.8*.** Selected bond lengths and angles for cluster **5**.

Bond distances (Å)		**Bond Angles (º)**			
Fe1-O2	2.053(3)	O1-Fe2-O1[1]	76.71(12)	N3[2]-Fe2-O2	120.56(13)
Fe1-N1	2.133(4)	O1-Fe2-O2	84.12(11)	N3[2]-Fe2-N2	118.04(15)
Fe1-O3	2.004(3)	O1[1]-Fe2-O2	92.38(12)	N3[2]-Fe2-O3[1]	61.01(13)
Fe1-O4	1.872(3)	O1-Fe2-N2	141.80(13)	Fe2-O1-Fe2[1]	103.29(12)
Fe2-O1[1]	2.117(3)	O1[1]-Fe2-N2	87.18(13)	Fe1-O2-Fe2	118.23(15)
Fe2-O1	2.077(3)	O1-Fe2--O3[1]	94.15(12)	O2-Fe1-N1	103.27(13)
Fe2-O2	2.146(3)	O1[1]-Fe2-O3[1]	85.73(11)	O3-Fe1-O2	104.31(12)
Fe2-N2	2.169(4)	O1-Fe2--N3[1]	93.34(13)	O3-Fe1-N1	92.56(14)
Fe2-O3[1]	2.220(3)	O1[1]-Fe2-N3[1]	144.74(13)	O4-Fe1-O2	100.95(14)
Fe2-N3[1]	2.139(4)	O2-Fe2-N2	61.90(12)	O4-Fe1-N1	116.52(14)
		O2-Fe2-O3[1]	177.69(13)	O4-Fe1-O3	135.44(13)
		N2-Fe2-O3[1]	119.25(12)	Fe1-O3-Fe2[1]	114.79(14)

Symmetry [1] 1-X,2-Y,1-Z

Table 4.9. Selected bond lengths and angles for compound **6**.

Bond distances (Å)		**Bond Angles (º)**			
Fe1-O2	2.0425(7)	O2-Fe1-O2[1]	80.02(3)	N2[1]-Fe1-O1	93.47(3)
Fe1-O2[1]	2.1655(8)	O2-Fe1-O4[1]	86.84(3)	O4-Fe2-O3	101.92(3)
Fe1-O4[1]	2.1546(7)	O2-Fe1-O1	95.71(3)	O4-Fe2-N3[1]	93.06(3)
Fe1-O3	2.0260(7)	O2[1]-Fe1-O1	175.22(3)	O4-Fe2--N1	161.10(3)
Fe1-O1	2.2018(8)	O2-Fe1-N21		O3-Fe2-N3[1]	91.59(3)
Fe1-N2[1]	2.1540(9)	O4[1]-Fe1-O2[1]	147.52(3)	O3-Fe2-N1	59.68(3)
Fe2-O4	2.1299(7)	O4[1]-Fe1-O1	93.01(3)	O5-Fe2-O4	99.27(3)
Fe2-O3	2.1441(7)	O3-Fe1-O2	88.86(3)	O5-Fe2-O3	129.57(3)
Fe2-O5	1.9187(7)	O3-Fe1-O2[1]	99.13(3)	O5-Fe2-N3[1]	132.31(3)
Fe2-N3[1]	2.1911(9)	O3-Fe1-O4[1]	84.96(3)	O5-Fe2-N1	90.82(3)
Fe2-N1	2.3197(9)	O3-Fe1-O1	173.23(3)	N3[1]-Fe2-N1	91.85(3)
		O3-Fe1-N2[1]	93.67(3)	Fe1-O2-Fe1[1]	99.98(3)
		N2[1]-Fe1-O2[1]	111.30(3)	Fe2-O4-Fe1[1]	117.76(3)
		N2[1]-Fe1-O4[1]	91.30(3)	Fe1-O3-Fe2	122.01(4)
			62.23(3)		

Symmetry [1]1-X,1-Y,1-Z

4.5.8. Magnetic Measurements

Magnetic measurements for complexes **1** and **2** were carried out with a Quantum-Design MPMS3 SQUID magnetometer equipped with a 7.0 T magnet. Direct current (dc) magnetic susceptibility measurements were performed under an applied dc field of 0.5 T with powdered polycrystalline samples packed in polycarbonate in a non-magnetic sample holder and covered with low viscosity perfluoropolyether-based inert oil Fomblin Y45 in the range from 200.0 K to 2.0 K (the upper temperature limit was chosen because of the pour point of the oil). The oil was dried under vacuum and degassed prior to use. Sample preparation was performed inside a glove box under N_2 atmosphere. Each raw data of the measured magnetic moment was corrected for the diamagnetic contribution of the capsules according to $M_{dia}(\text{capsule}) = \chi_g \cdot m \cdot H$, with an experimentally obtained gram susceptibility of the capsules including the inert oil. The diamagnetic contribution of the compounds was corrected using Pascal's constants. Alternating current (ac) susceptibility measurements were carried out in an oscillating ac field of 3.0 Oe and frequencies ranging from 0.1 to 1000 Hz.

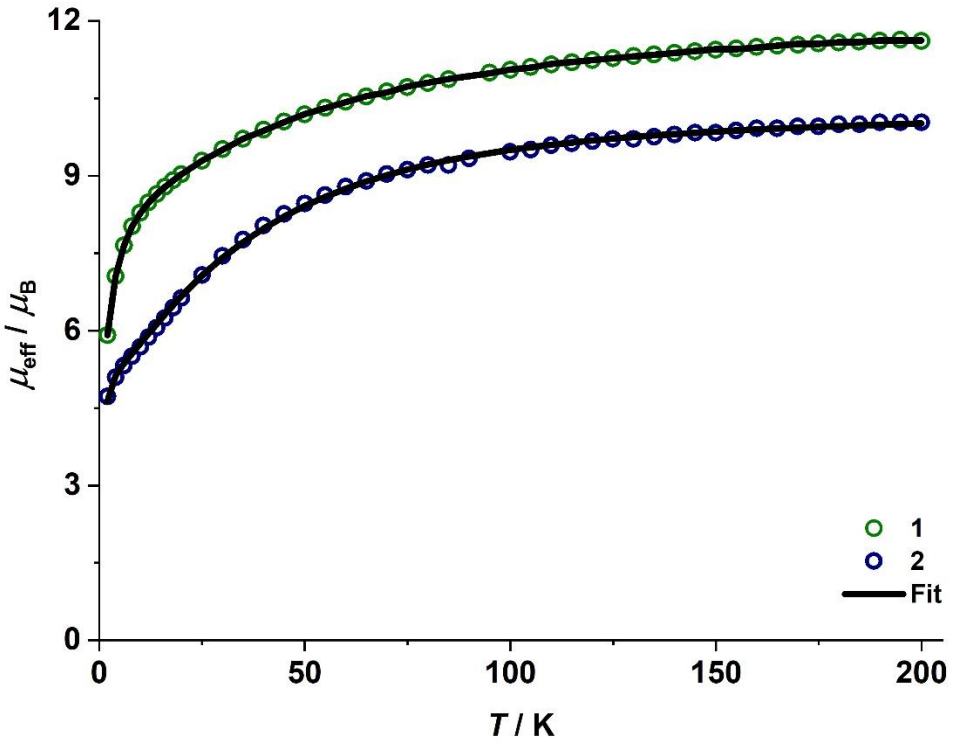

Figure 4.28. Plot of the variable temperature effective magnetic moment for Fe(II) clusters (green (**1**), blue (**2**)). Solid black lines are the best fits.

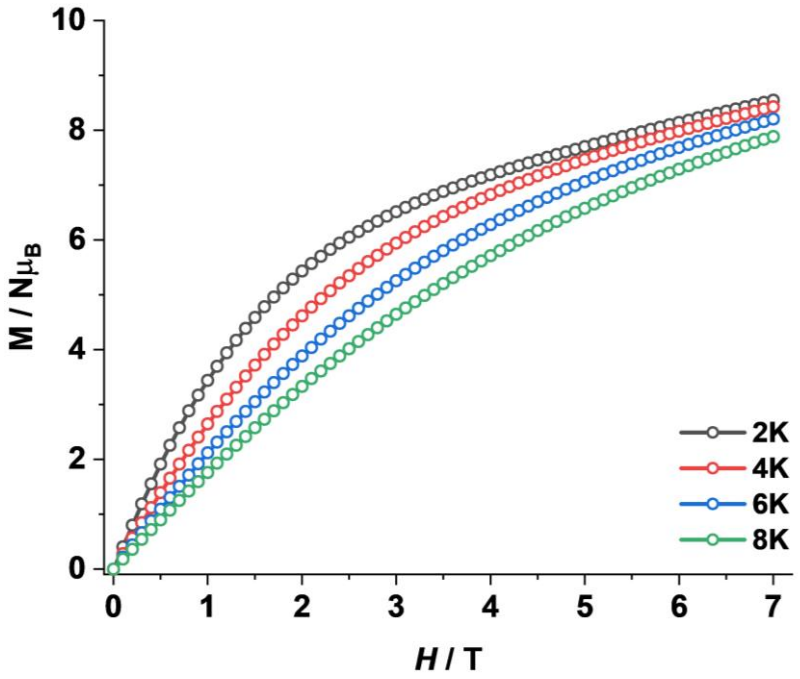

Figure 4.29. Isothermal magnetization data at indicated temperatures for complex **1**.

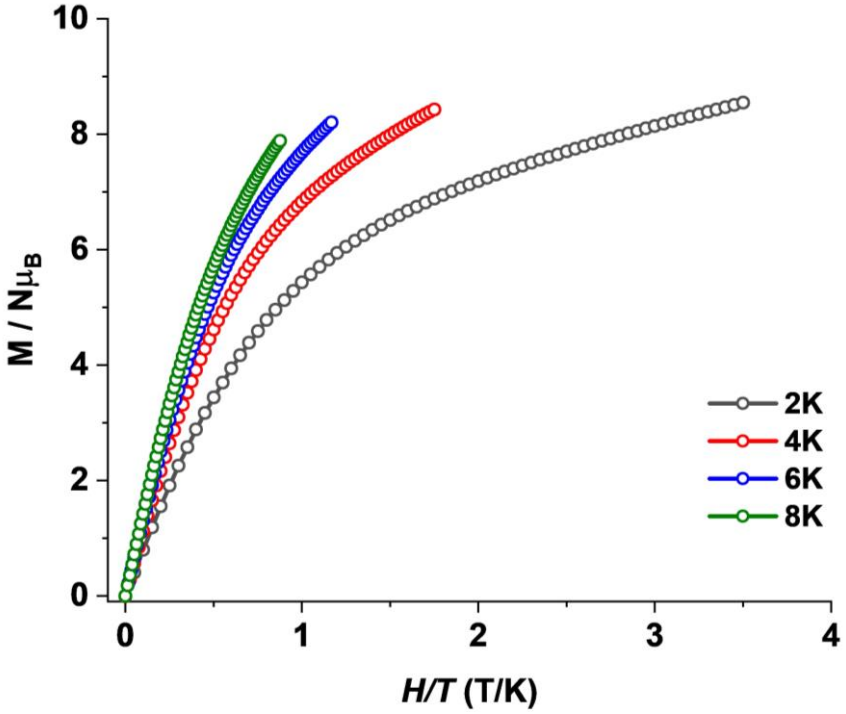

Figure 4.30. Isothermal reduced magnetization data at indicated temperatures for complex **1**.

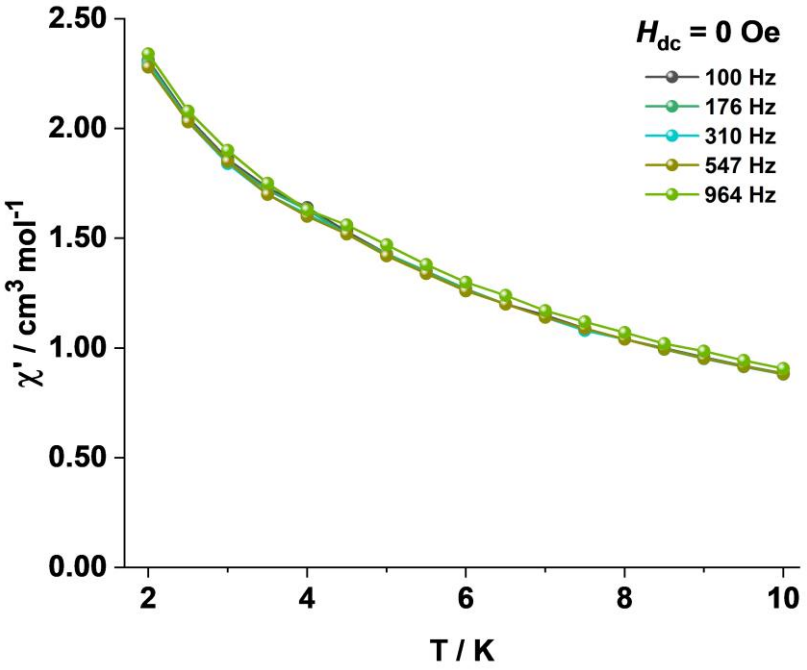

Figure 4.31. Temperature dependence of the in-phase (χ_M') component of the ac susceptibility for complex **1** under zero dc field.

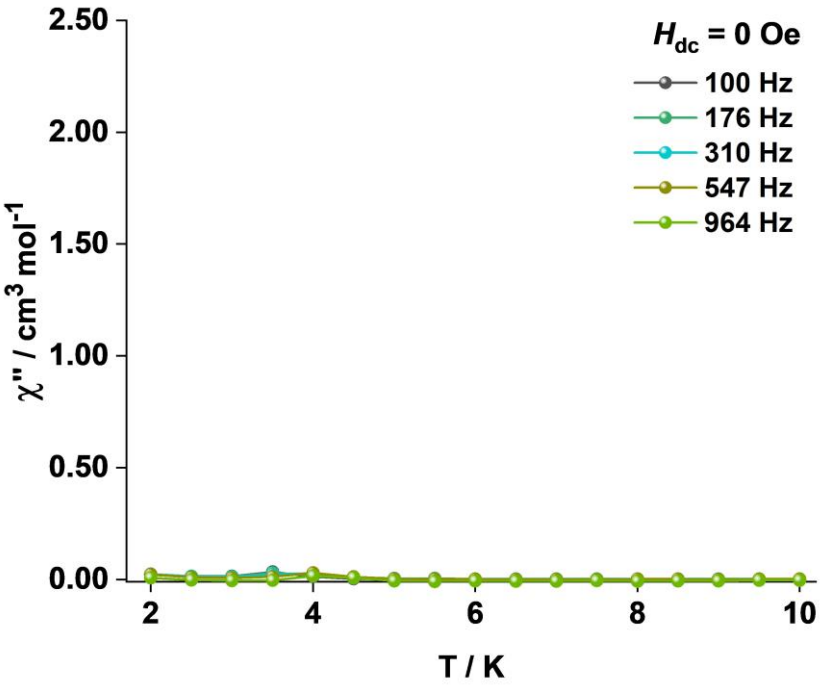

Figure 4.32. Temperature dependence of the out-of-phase (χ_M") component of the ac susceptibility for complex **1** under zero dc field.

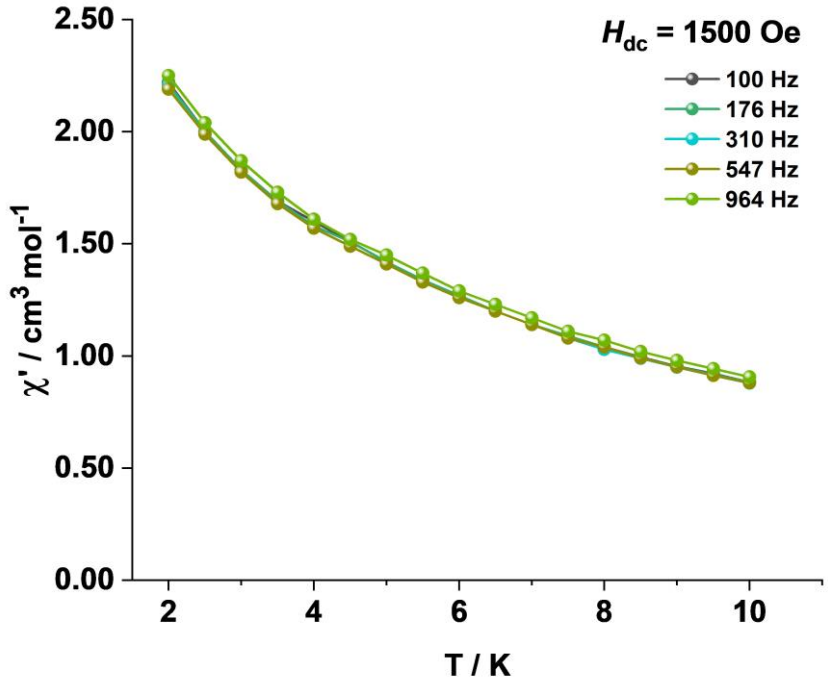

Figure 4.33. Temperature dependence of the in-phase (χ_M') component of the ac susceptibility for complex **1** under an applied dc field of 1500 Oe.

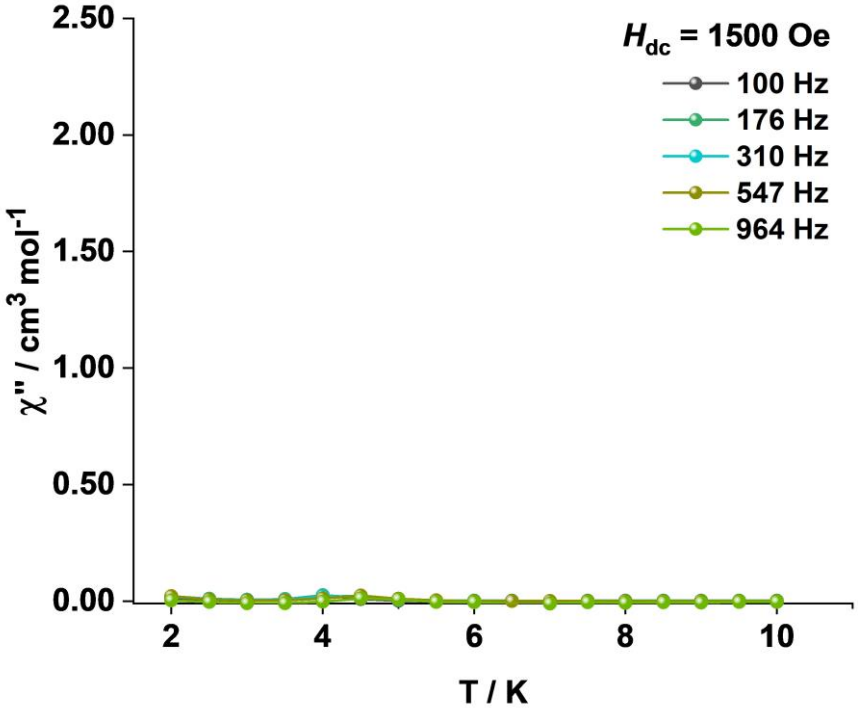

Figure 4.34. Temperature dependence of the out-of-phase (χ_M") component of the ac susceptibility for complex **1** under an applied dc field of 1500 Oe.

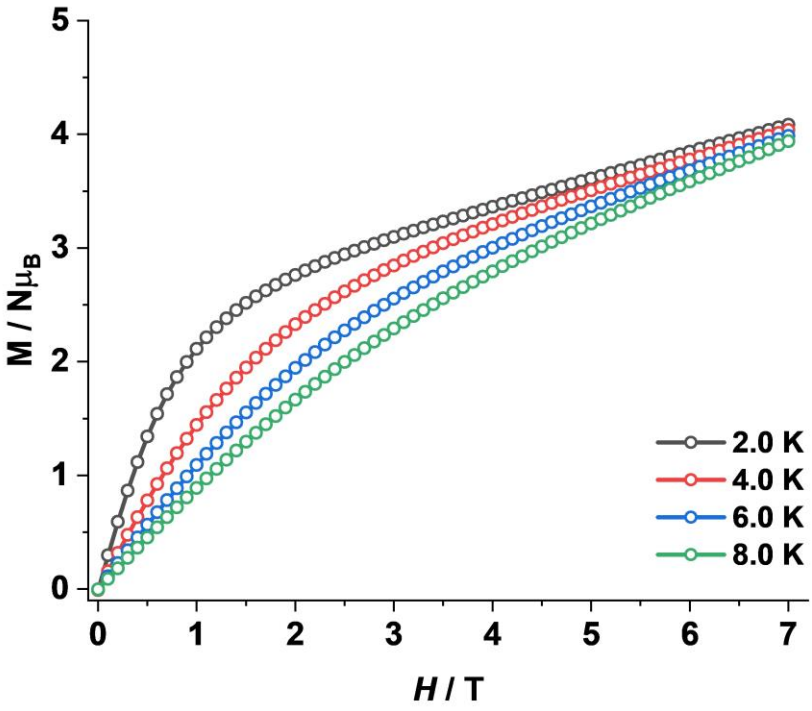

Figure 4.35. Isothermal magnetization data at indicated temperatures for complex **2**.

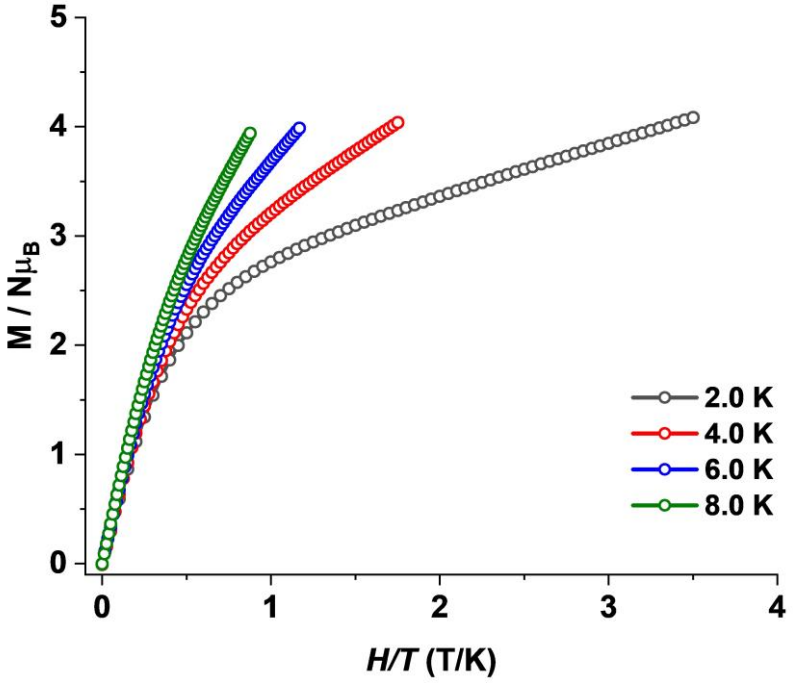

Figure 4.36. Isothermal reduced magnetization data at indicated temperatures for complex **2**.

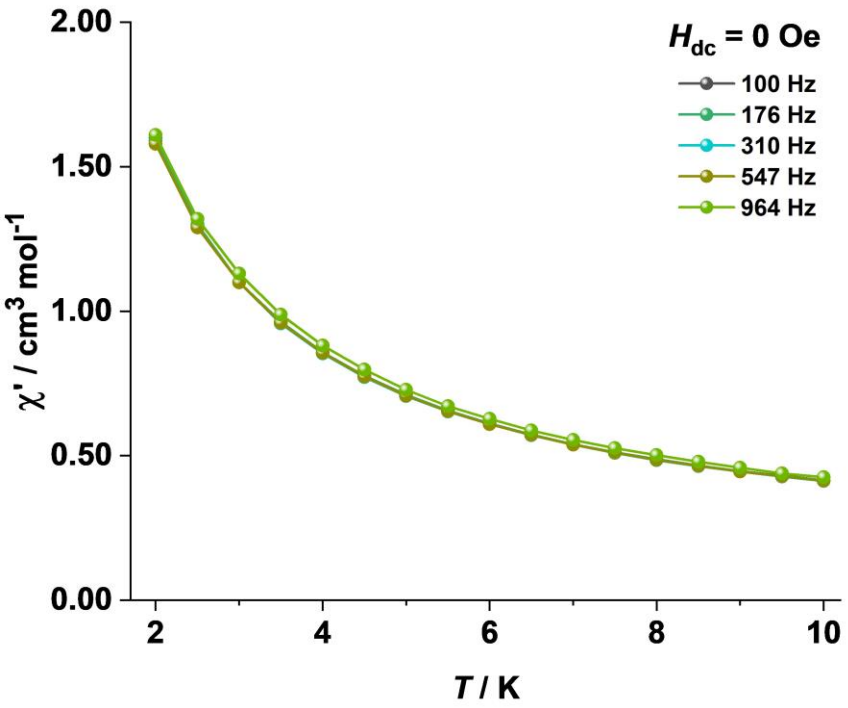

Figure 4.37. Temperature dependence of the in-phase (χ_M') component of the ac susceptibility for complex **2** under zero dc field.

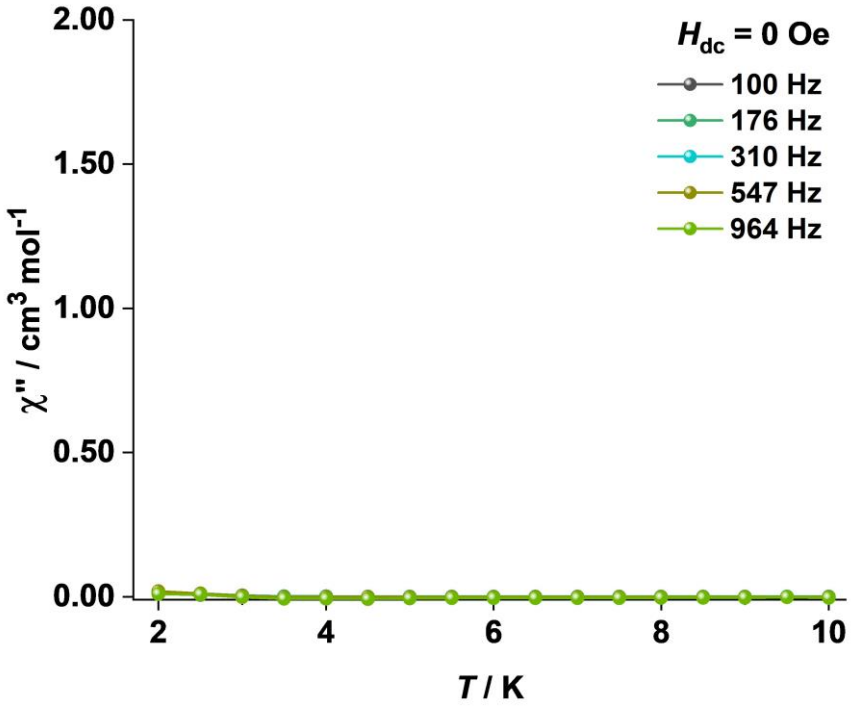

Figure 4.38. Temperature dependence of the out-of-phase (χ_M") component of the ac susceptibility for complex **2** under zero dc field.

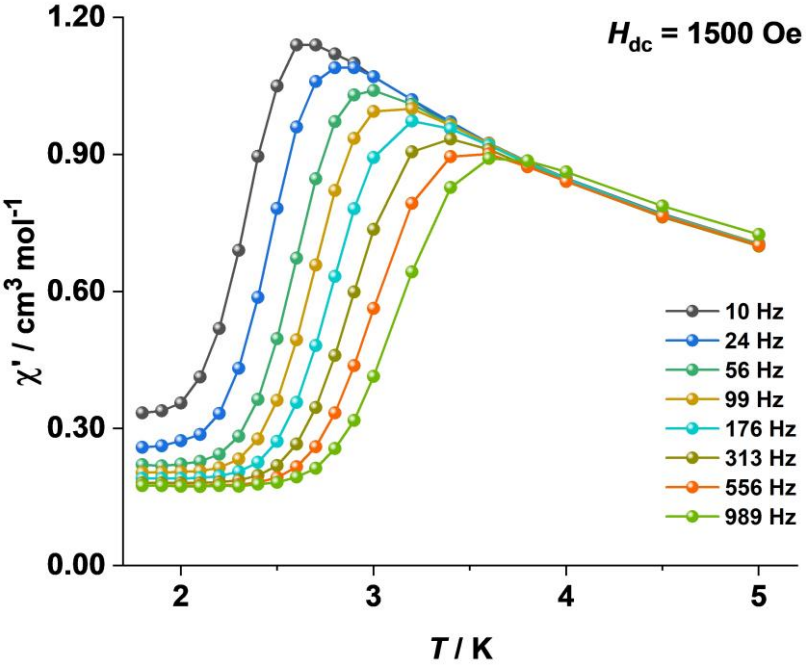

Figure 4.39. Temperature dependence of the in-phase (χ_M') component of the ac susceptibility for complex **2** under an applied dc field of 1500 Oe.

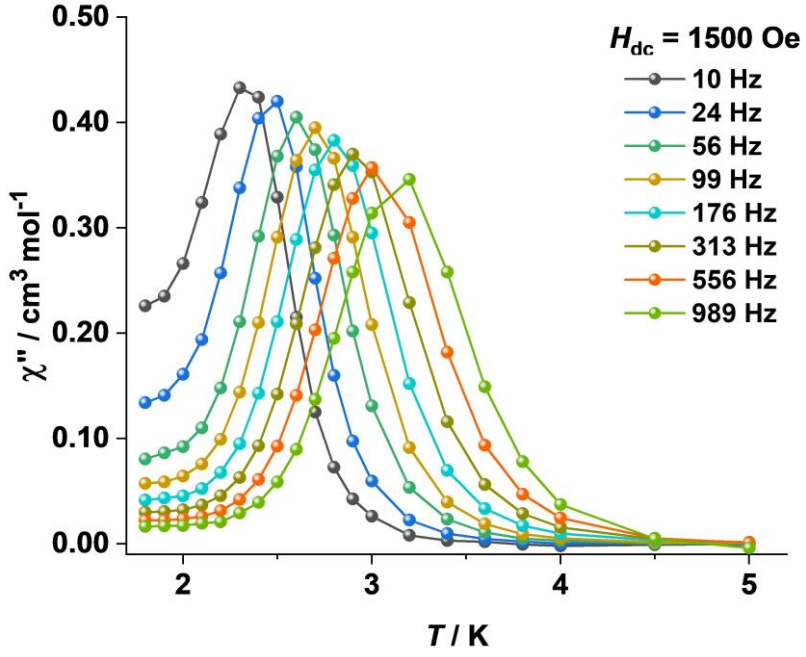

Figure 4.40. Temperature dependence of the out-of-phase (χ_M") component of the ac susceptibility for complex **2** under an applied dc field of 1500 Oe.

Table 4.10. Best-fit parameters obtained from treatment of χ_M'' and χ_M' data with Debye model.

T (K)	χ_S ($cm^3\ mol^{-1}$)	χ_T ($cm^3\ mol^{-1}$)	τ (s)	α
1.8	0.17522	1.85486	0.17028	0.27598
1.9	0.17383	1.86465	0.15702	0.27485
2.0	0.17516	1.69605	0.10381	0.24526
2.1	0.17153	1.57673	0.06549	0.23098
2.2	0.17056	1.46582	0.03685	0.20985
2.3	0.16632	1.39715	0.01993	0.1991
2.4	0.1653	1.33207	0.01047	0.18313
2.5	0.16407	1.2779	0.00553	0.17324
2.6	0.16527	1.23127	0.00298	0.16125
2.7	0.1675	1.18765	0.00166	0.15152
2.8	0.17466	1.14875	9.64E-04	0.13942
2.9	0.18435	1.11327	5.82E-04	0.12835
3.0	0.19485	1.08343	3.65E-04	0.12149

4.5.9. LIFDI-MS

Mass spectra were performed on a Jeol AccuTOF GCX mass spectrometer with a LIFDI inlet by the analytical department of the University of Regensburg, Germany.

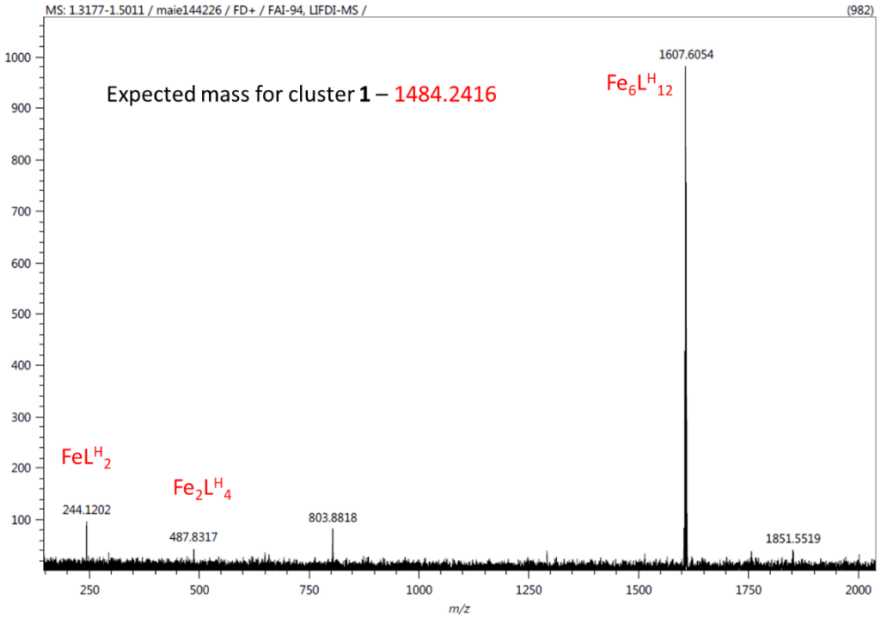

Figure 4.41. LIFDI-MS spectrum of the cluster **1** solution in DME.

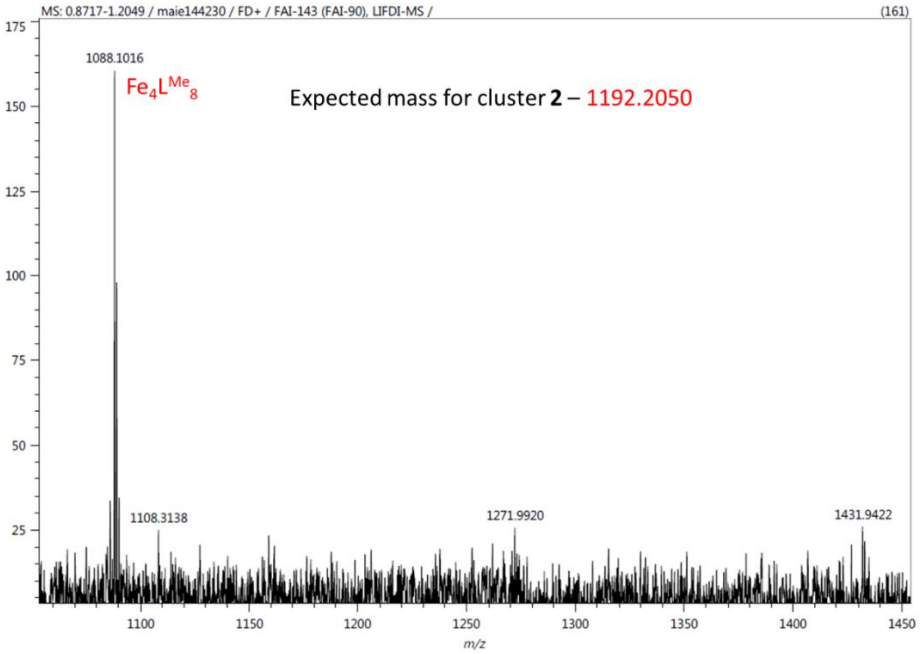

Figure 4.42. LIFDI-MS spectrum of the cluster **2** solution in DME.

4.5.10. References

[1] D. L. Broere, I. Coric, A. Brosnahan, P. L. Holland, *Inorg. Chem.* **2017**, *56*, 3140.

[2] M. Brookhart, B. Grant, and A. F. Volpe *Organometallics* **1992** *11* (11), 3920-3922.

[3] S. K. Sur, *J. Magn. Reson.* **1989**, 82, 169-173.

[4] J. Yang, T. D. Tilley, *Angew. Chem. Int. Ed.* **2010**, 49 (52), 10186-10188.

[5] E. Peterson, A. Y. Khalimon, R. Simionescu, L. G. Kuzmina, J. A. K. Howard, G. I. Nikonov, *J. Am. Chem. Soc,* **2009,** *131* (3), 908-909.

[6] Agilent Technologies Ltd, Yarnton, Oxfordshire, England, **2014**.

[7] Bruker AXS Inc., Madison, Wisconsin, USA, **2014**.

[8] G. M. Sheldrick, *Acta Crystallogr. A* **2008**, *64*, 112–122.

[9] G. M. Sheldrick, *Acta Crystallogr. A* **2015**, *71*, 3–8.

[10] A. L. Spek, *Acta Crystallogr. D* **2009**, *65*, 148–55.

5. Cobalt Pyridonate Complex Catalyzing Chemospecific Hydroboration of CO_2

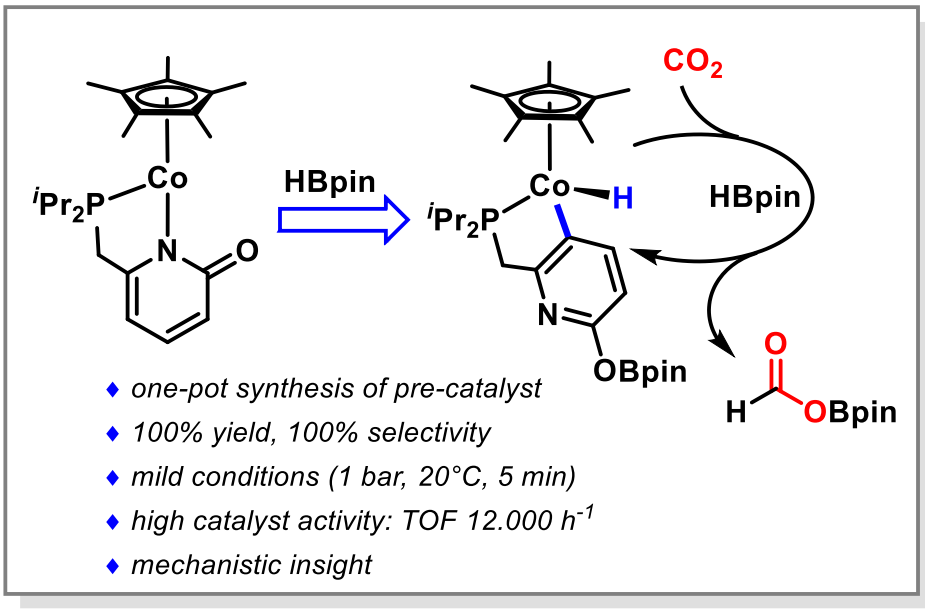

This chapter contains the unpublished manuscript.

5.1. Introduction

Reductive transformations of carbon dioxide are an integral part of all future scenarios of sustainable energy and chemical production technologies.[1,2] The use of CO_2 as chemical building block is strongly limited by its thermodynamic and kinetic stability, so that efficient catalytic mechanisms at mild conditions constitute a prime area of research. Various synthetic strategies of CO_2 reduction have been developed to formate, formaldehyde, and methanol derivatives and methane. Technical processes mostly utilize hydrogenation reactions under high pressures of H_2 and elevated temperatures, whereas lab-scale reactions often operate with more convenient liquid hydrogen surrogates such as boranes and silanes. Metal-catalyzed hydroborations of CO_2 have been demonstrated to enable facile reductions to borylformates, diborylacetals, and methoxyboranes (Scheme 5.1., top).[3] Major challenges reside in the highly selective formation of a single reduced C1 building block, the use of inexpensive yet highly reactive catalysts and reducing reagents, and the operation under mild conditions with no excess reagents and without waste formation. For example, the two-electron reduction of CO_2 with boranes in the presence of metal catalysts provides *O*-boryl formates that constitute valuable formyl and formate building blocks. So far, pincer-ligand supported noble metal catalysts, Pd[4,5], Ir[6], Ru[7], were the most active (Scheme 5.1., middle). An NHC-copper alkoxide catalyst gave 85% formic acid after hydrolysis;[8] ligand-coordinated zinc hydride catalysts afforded moderate activity.[9,10] Several examples of Mn,[11,12] Fe,[13] and Ni[14,15] catalysts are known for CO_2 hydroborations to diborylacetal and borylmethanol. A single example of a cobalt-catalyzed reduction of CO_2 selectively to boryl formate was reported, with low to moderate yields and little mechanistic insight.[16]

Pyridonate ligands entertain a rich coordination chemistry with most transition metals due to their flexible binding modes, hemilability, and potential metal-ligand cooperativity. We reasoned that such multi-functional behavior of metal pyridonates may be effectively exploited for CO_2 hydroborations by sequential BH bond splitting, CO_2 coordination, and hydride transfer onto CO_2. Herein, we report a highly efficient cobalt pyridonate catalyst (TOF >12.000 h^{-1}) that operates under very mild conditions with perfect chemospecificity toward the formate reduction level (Scheme 5.1., bottom). Adjustment of reaction conditions enables further reduction to methoxyborane (methanol level).

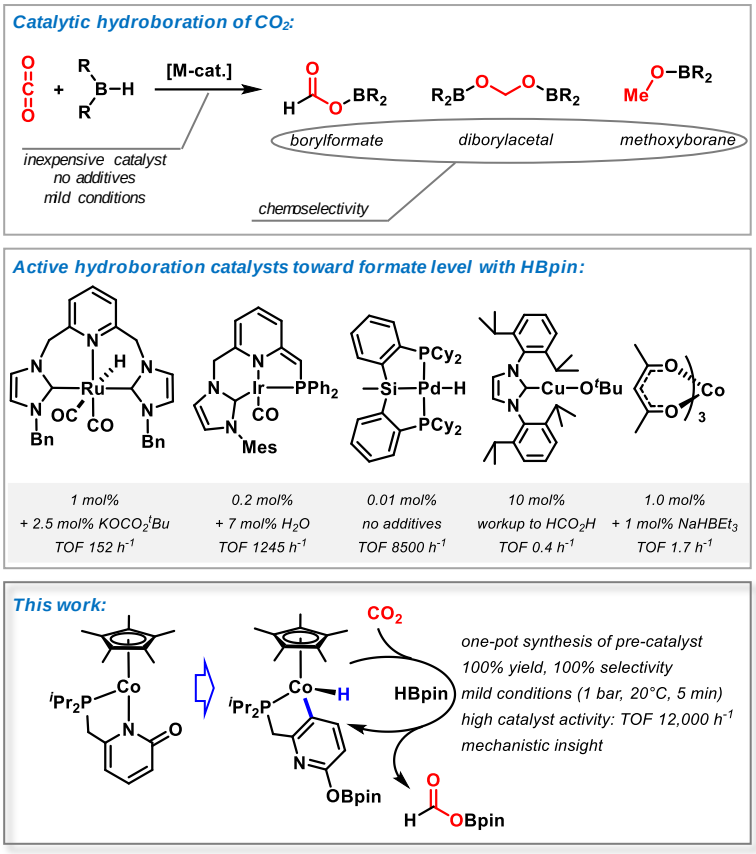

Scheme 5.1. Metal catalyzed hydroboration of carbon dioxide (top); cobalt pyridonate for chemospecific CO_2 hydroboration (bottom).

5.2. Method Development

The introduction of a pyridonate unit confers high degrees of versatility to a metal complex by virtue of multiple binding modes, wide stereoelectronic control by diverse substitution patterns, and hemilability. In combination with polar substrates, ligand-metal cooperativity may be effectively exploited. We believed that a combination of a pyridonate motif with a strongly binding phosphine chelate and a bulky spectator ligand would prohibit unwanted catalyst aggregation and coordinative saturation with substrate molecules and enable dual activation of the borane and CO_2. Consequently, we prepared the easily accessible complex Cp*Co^{II}(P∩N) (**Co1**) of the 6-phosphinomethyl-2-pyridonate ligand (**L1**) following a closely related literature precedent (Scheme 5.2).[17] 6-Methylpyridone was converted to the phosphinopyridone **L1H** by double lithiation and addition of ClP^{i}Pr$_2$. Base-mediated reaction of **L1H** with [Cp*CoCl]$_2$ afforded the desired half-sandwich complex **Co1** in 60% yield after recrystallization from MeCN. The air-sensitive complex was characterized by crystal structure analysis which confirmed the κ^2-P,N-chelating coordination to cobalt and a pendent C=O moiety. The bond distance C1-O1 of the pyridone (1.243(2) Å) indicates double bond character (C=O).[18,19] The magnetic moments (Evans method: 1.89 μB; SQUID: T-dependent $\chi_M T$ at dc field of 0.5 T, 1.90 μ_B) are in full agreement with a low-spin Co(II) center (d^7, S = ½) and an overall 17-electron complex. **Co1** is highly soluble

in THF and toluene, moderately soluble in acetonitrile, sparingly soluble in ether and insoluble in hexane.

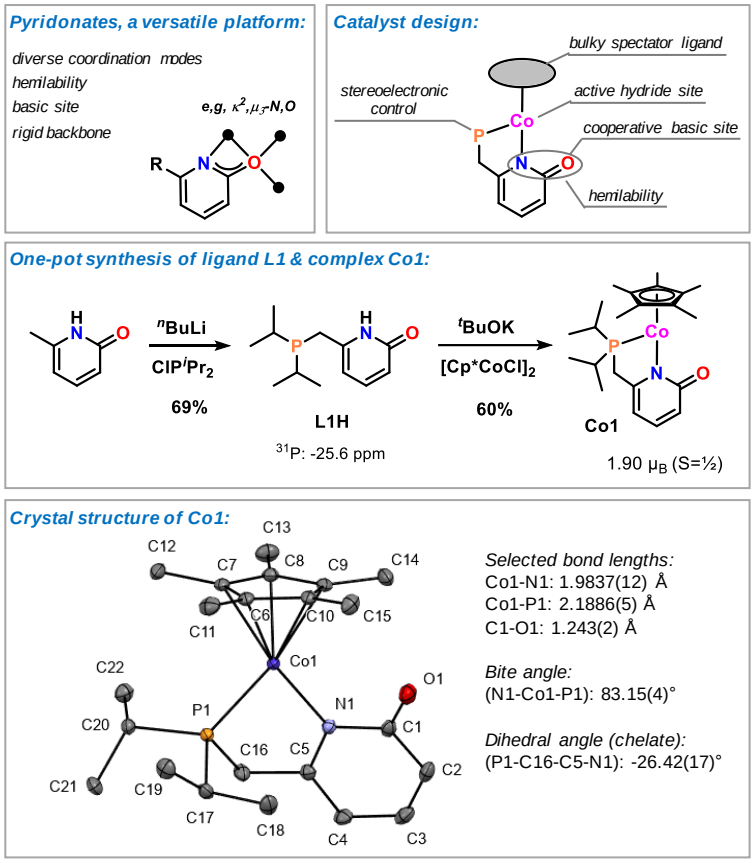

Scheme 5.2. Design concept, synthesis, and crystal structure of cobalt pyridonate **Co1**.

We initiated our investigations into the catalytic reduction of CO_2 with the hydroboration reaction in the presence of the inexpensive reductant pinacolborane (HBpin) and the pyridonate complex **Co1**. In contrast to the use of strongly hydridic boranes (e.g. L→BH_3, MBH_4, 9-BBN) that can operate in the presence of simple Lewis basic catalysts[20] or under catalyst-free conditions,[21,22] the use of the less reactive HBpin may enable higher selectivities and controlled access to the individual reduction intermediates (formate, acetal, methoxy levels). Consequently, the solution of catalyst and HBpin in THF-d_8 was degassed and an ambient pressure of CO_2 (1 bar) was applied. The reaction progress was monitored by ^{1}H NMR spectroscopy (*vs.* internal mesitylene). Full conversion was observed with 1 mol% **Co1** after 5 min(!) of exposure to 1 bar CO_2 at room temperature (i.e. in the first recorded ^{1}H NMR spectrum). Furthermore, the NMR spectrum exhibited perfect chemoselectivity toward the borylformate HCO_2Bpin which had formed as the only product in 100% yield (entry 1). The same productivity was afforded with 0.1 mol% catalyst loading after 5 min at 1 bar CO_2 (entry 2). Change of solvents to benzene and acetonitrile and a neat reaction gave lower yields (83%, 21%, 32%, entry 4), respectively. A wide set of control reactions were performed that documented the crucial role of each component of the modular catalyst **Co1**: The diphenylphosphino derivative of the catalyst (**Co2**) afforded similarly

perfect chemoselectivity toward the borylformate, but with only 34% yield (entry 5). The hydroboration did not proceed in the absence of catalyst (entry 6). The pyridone-free complexes $[Cp^*CoCl]_2$ and Cp^*_2Co (**Co3** and **Co4**) were no competent catalysts, respectively (entry 7). The use of pyphos (which can be viewed as a truncated deoxo-derivative of **L1**) with **Co3** gave very low conversion and low yield of the borylformate; whereas the in situ formed catalyst (from **L1H**, ^{t}BuOK, and **Co3**) afforded good conversion (entries 8 and 9). The ligand alone showed no activity in its neutral form (**L1H**) or after deprotonation with potassium hexamethyldisilazide (**L1K**), respectively (entry 10). Likewise, conversion of **L1H** to the borylated derivative **L1Bpin** - which may be operative under hydroboration conditions – did not afford an active catalyst (entry 11), despite the related pyridonate borane was previously reported to be active in hydrogenation.[23,24] It is important to note that the catalytic hydroboration of CO_2 operated with low amounts of the pre-catalyst **Co1** (0.1 mol%) under very mild conditions (room temp., 1 bar CO_2) within (less than) 5 min reaction time to completion and perfect chemoselectivity toward the borylformate (100% yield). The highly active catalyst (**Co1**) operated with a turnover number (TON) of greater than 1000 and a turnover frequency (TOF) of greater than 12.000 h^{-1} (after 5 min; limited by time of sampling and NMR measurement, entry 2). To the best of our knowledge, these values document a higher catalytic activity in CO2 reduction to formate than all literature methods based on main group element and 3d transition metal catalysts. There is a single metal-catalyzed hydroboration of CO_2 with HBpin that exhibited higher activity utilizing a palladium complex with a silyl-pincer ligand (TON 37.200 after 1 day; up to 63.500 after 5 days; TOF up to 8500 h^{-1}).

Table 5.1. Selected optimization experiments of the cobalt-catalyzed hydroboration of CO_2. [a]

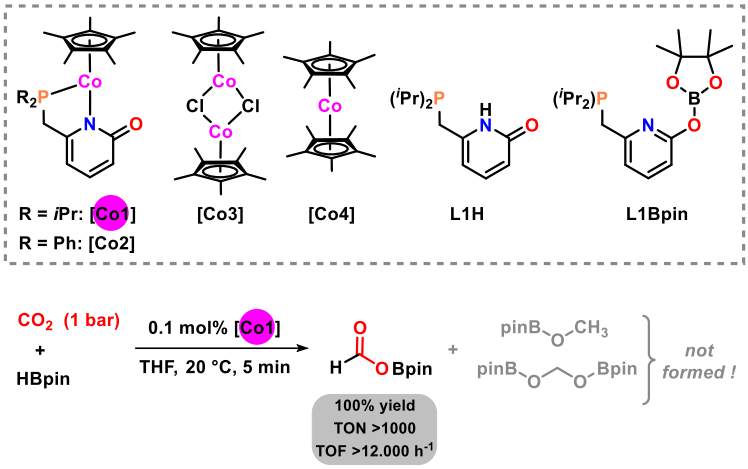

Entry	Change from conditions above [a]	Yield [%]
1	1 mol% [**Co1**]	100
2	**none**	**100**
3	0.05 mol% [**Co1**]	33
4	C_6D_6, CD_3CN, neat; each with 1 mol% [**Co1**]	83/21/32
5	1 mol% [**Co2**]	34
6	*without* catalyst	0
7	1 mol% [**Co3**] or [**Co4**]	0/0
8	2 mol% [pyphos + **Co3**]	8
9 [b]	2 mol% [**L1H** + ^{t}BuOK + **Co3**]	56
10	2 mol% [**L1H**] or [**L1H** + Khmds]	0/0
11 [c]	2 mol% **L1-Bpin**	0

[a] Reaction conditions: An NMR tube was charged in argon-filled glovebox with HBpin (0.27 or 0.14 mmol), mesitylene (as internal NMR standard), the catalyst (solid or stock solution), and 0.6 mL solvent. The mixture was degassed by two cycles of freeze-pump-thaw and backfilled with CO_2 for 5 min. The NMR tube was sealed, shaken vigorously, and subjected to ^{1}H and ^{11}B NMR analysis. ^{1}H NMR yields were determined by integration *vs.* internal mesitylene as an average of two runs. [b] Equimolar amounts of **L1H**, ^{t}BuOK and **Co3** were pre-mixed in a vial. [c] A stock solution of **L1Bpin** in THF-d_8 was prepared by heating equimolar amounts of **L1H** and HBpin at 60 °C for 16 h.

The choice of using pinacolborane (HBpin) as reductant for highly selective hydroboration of CO_2 was evident from a brief screening of alternative boranes (Table 5.2). The observed trend of borane reactivities can be partially interpreted with their thermodynamic hydridicities ($\Delta G°(H^-)$).[25] The least hydridic borane HBcat ($\Delta G°(H^-)$ = 159 kcal/mol) afforded very low conversions and only minor amount of reduction product (8% methoxycatecholborane). The absence of the borylformate may be a consequence of lower steric bulkiness of the catechol vs. the pinacol substituent. 9-BBN (more hydridic with a $\Delta G°(H^-)$ = 99 kcal/mol) gave full conversion in <1 h to a

mixture of the diborylacetal (46%) and the methoxy borane (26%). Again, no formate intermediate was observed. The most hydridic borane in this series, $BH_3{\cdot}SMe_2$ ($\Delta G°(H^-)$ = 77 kcal/mol), led to rapid catalyst decomposition to a dark precipitate without any detectable formation of CO_2 reduction products.

Table 5.2. Selection of boranes and chemoselectivities of CO_2 reduction. [a]

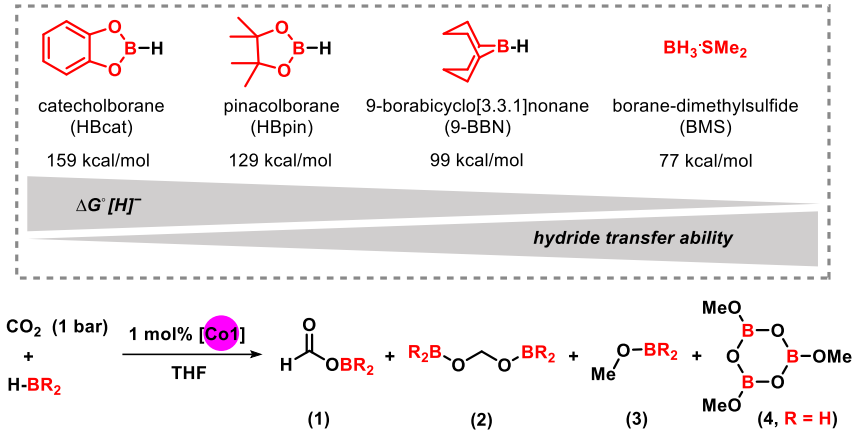

Entry	Borane HBR_2	T [°C]	time	1 / 2 / 3 / 4 [%] [b]
1	HBcat	60	18 h	0 / 0 / 9 / -
2	HBpin	20	5 min	**100** / 0 / 0 / -
3	9-BBN	20	24 h	0 / 46 / 26 / -
4	$BH_3{\cdot}SMe_2$	60	18 h	- / - / - / 0

[a] Reaction conditions: An NMR tube was charged with HBpin(0.27 mmol), mesitylene (0.1078 mmol), **Co1** (2.7µmol, 1 mol%), and 0.6 mL THF-d_8. The mixture was degassed by two cycles of freeze-pump-thaw and backfilled with CO_2 for 5 min. The NMR tube was sealed, shaken vigorously and heated in an oil bath, if required. Reaction progress was monitored by ^1H and ^{11}B NMR. ^1H NMR yields were determined by integration *vs.* internal mesitylene as an average of two runs. [b] 1, 2 and 3 equiv. of HBR_2 relative to CO_2 are required for the formations of products **1**, **2** and **3**, respectively. 1 equiv. $BH_3{\cdot}SMe_2$ and 3 equiv. CO_2 are required to produce **4**. Equimolar amounts of diboryloxide and methoxyborane **3** are formed.

While the hydroboration of CO_2 with HBpin and catalytic **Co1** under standard conditions (1 bar CO_2, THF, 20 °C, 5 min) cleanly afforded the borylformate in perfect yield and selectivity, change of the reaction conditions enabled onward reduction to the methanol level. Addition of the Lewis acid $B(OPh)_3$ as co-catalyst (10 mol%) fully inhibited the hydroboration at 20 °C (no conversion of HBpin after 1 h), but afforded the corresponding methoxyborane as single reduction product in 74% yield after 16 h at 60 °C (Scheme 5.3, top).[5] More conveniently, full conversion to the methoxyborane could be easily achieved when adding excess amounts of HBpin to the crude borylformate and further reaction at 60 °C (Scheme 5.3, middle). The synthetic utility of the borylformate product was explored by addition of aniline to the hydroboration reaction. Reaction of aniline and 3 equiv. HBpin in the presence of **Co1** (1 mol%) in THF under 1 bar CO_2 at room temperature resulted in the formation of a mixture of HCO_2Bpin and the undesired dehydrocoupling product PhNHBpin (2/1; see 5.6. for details). The same reaction with 0.5 mol% **Co1** at 60 °C gave clean formylation of the

aniline to afford *N*-formanilide and *N*,*N*-diformyl aniline in overall 87% isolated yield (5/1; see Experimental section for details).

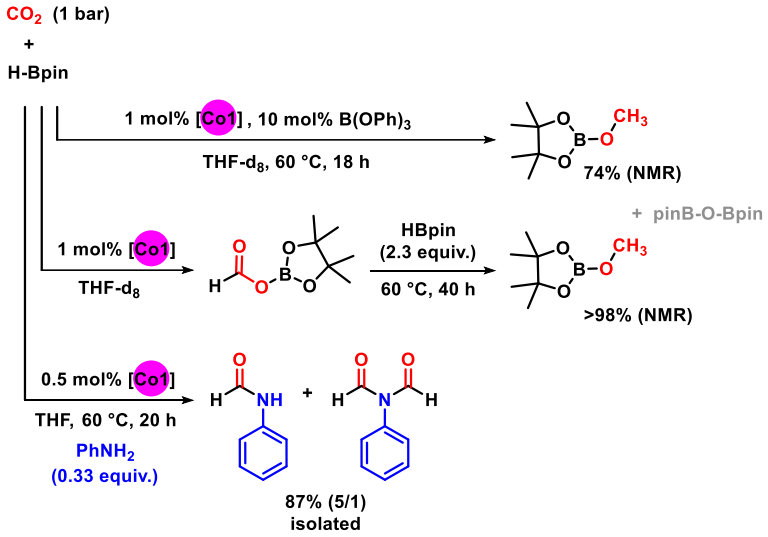

Scheme 5.3. Variations of the general protocol toward selective formations of borylformate, methoxyborane, and formylanilines, respectively.

5.3. Mechanistic Studies

A set of preparative and spectroscopic experiments were performed in order to gain insight into the nature of the catalytically active species (Scheme 5.4). Stoichiometric reaction of the cobalt-pyridonate complex **Co1** with pinacolborane (1.2 equiv.) in THF-d_8 resulted in immediate color change from orange to black. We postulate the formation of a transient labile cobalt(II) hydride complexes which underwent rapid disproportionation[26], possibly via dinuclear hydride or pyridonate-bridged species. ^{1}H NMR monitoring indicated the formation of diamagnetic and paramagnetic species: *i)* Very minor amounts of the borylated ligand **L1Bpin** were observed by ^{1}H NMR. *ii)* We postulate the formation of dinuclear (or higher) complexes of the formula $[(Cp^*Co)_2H_n(\mathbf{L1})_m]$ as major paramagnetic species with Co(I), Co(II), or mixed valence states. ESI-MS spectra showed m/z = 612.2216 (n=0, m=1) and 837.3498 (n=1, m=2). Similar hydride- and pyridonate-bridged dinuclear complexes were prepared from $[Cp^*CoCl]_2/LiAlH_4$[27] and from [Cp*IrCl(2-pyridonate)][28] by hydrogen transfer, respectively. *iii)* Two distinct doublets of hydride complexes were observed at -16.7 ppm ($^2J_{HP}$ = 87.5 Hz) and -18.37 ppm ($^2J_{HP}$ = 84.3 Hz) and assigned to Co(III)-hydride species, which is in agreement with closely related $CpCo^{III}H(PR_3)$ complexes.[29–31] The former resonance originates from the monohydride complex **Co5**, which was isolated as a pure compound and characterized in solid state (XRD) and solution (NMR, ESI-MS). The complex involves a cyclometalated 2-oxypyridone ligand motif that led to a cobalt(III)-hydride by C-H activation of the ligand. The more upfield hydride resonance appeared to be a dihydride species with a phosphine ligand bearing a borate substituent and was tentatively assigned to complex **Co6** (Scheme 5.4, center right). Complex **Co5** was crystallized from diethylether and *n*-hexane (20% crystal yield). The

single crystal structure analysis showed a three-legged piano stool complex with terminal hydride and a 5-membered metallocycle with P∩C-coordination of the pyridonate ligand. The 2-oxo position of the ligand bears a Bpin substituent.

^{1}H NMR monitoring of the formation of the cobalt(III) hydride complexes **Co5** and **Co6** supported the notion of two distinct pathways, possibly originating from the same precursor. Borane activation by metal-ligand cooperativity is believed to result in a labile cobalt(II) hydride complex which most likely engage in redox disproportionation and ligand exchange. The hemilability of the phosphinopyridonate ligand becomes evident from the observed aryl-H activation and formation of the cobalt hydride **Co5**. The same labile intermediate may also produce the cobalt hydride complex **Co6**. An identical reaction with the deutero-isotopologue DBpin cleanly documented that formation of the ligand-derived cobalt hydride complex **Co5** is rather unaffected, while the borane-derived complex **Co6** shows very low intensity in the ^{1}H NMR spectrum.

Interestingly, complex **Co5** was equally active as **Co1** in the hydroboration of CO_2 under standard conditions. Full conversion of HBpin to the borylformate was observed after reaction at room temperature for 5 min with 1 mol% **Co5**. Further evidence that **Co5** is a competent catalyst was derived from its instantaneous reaction with CO_2 which was followed by ^{1}H NMR spectroscopy (rapid disappearance of the 16.5 ppm doublet). **Co5** is stable toward higher excess amounts of the borane. The addition of up to 4 equiv. HBpin did not result in any detectable shift or disappearance of the ^{1}H NMR resonance at 16.5 ppm. (However, trace amounts of other hydride species were detected by ^{1}H NMR.) Indeed, **Co5** rapidly reacted with HBpin in the presence of CO_2. Interestingly, the ^{1}H signal at 16.7 ppm disappeared instantaneously while the 18.4 ppm hydride resonance remained unchanged for several hours before it also slowly disappeared over night. However, we cannot exclude the formation of undetected alternative catalyst species. Likewise, the presumably formed cobalt species in lower oxidation states may also be catalytically active but could not be isolated or monitored by NMR spectroscopy.

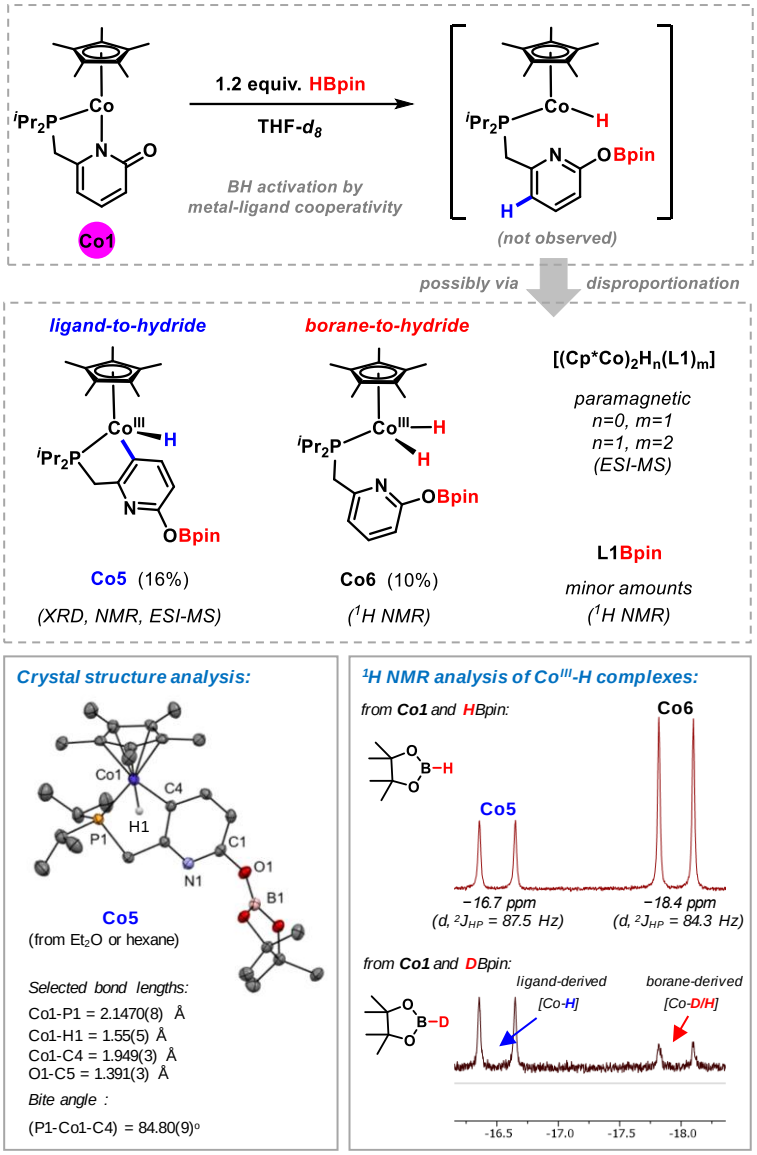

Scheme 5.4. Selected mechanistic studies: Synthesis and characterization of potential catalyst intermediates.

5.4. Summary and Conclusions

The hydroboration of CO_2 was realized under very mild conditions (1 bar CO_2, room temperature, 5 min) with very low catalyst loading (0.1 mol%) of a simple cobalt catalyst. Perfect chemoselectivity toward the borylformate was achieved (100% yield). The modular pre-catalyst **Co1** was prepared in a one-pot synthesis from commercial 6-methyl-2-pyridone by deprotonation, phosphinylation, and substitution at $[Cp^*CoCl]_2$. This pre-catalyst enabled very high productivity (TON 1000, TOF 12.000 h^{-1}). Mechanistic studies on potential catalytic intermediates revealed two distinct modes of hydride complex formation under the reaction conditions: ligand-centered CH activation to the monohydride cobalt(III) complex **Co5** and, presumably, a borane-induced formation of the dihydridocobalt(III) complex **Co6**. Complex **Co5** contained a cyclometalated oxypyridone motif that documented the hemilabile nature of the

employed PNO-ligand. High catalytic activity of **Co5** was observed in the hydroboration of CO_2. The modular composition of **Co1** and the identification of **Co5** as active catalyst intermediate may prompt further studies into the exploitation of the hemilability concept of rigid polydentate ligands for the generation of active metal hydride complexes. Applications to the wide space of hydrofunctionalization and hydrogenation reactions are easily foreseeable.

5.5. References

[1] Q. Liu, L. Wu, R. Jackstell, M. Beller, *Nat. Commun.* **2015**, *6*, 5933.

[2] J. Artz, T. E. Müller, K. Thenert, J. Kleinekorte, R. Meys, A. Sternberg, A. Bardow, W. Leitner, *Chem. Rev.* **2018**, *118*, 434–504.

[3] S. Kostera, M. Peruzzini, L. Gonsalvi, *Catalysts* **2021**, *11*, 1–26.

[4] Y. C. A. Sokolovicz, O. Nieto Faza, D. Specklin, B. Jacques, C. S. López, J. H. Z. Dos Santos, H. S. Schrekker, S. Dagorne, *Catal. Sci. Technol.* **2020**, *10*, 2407–2414.

[5] M. R. Espinosa, D. J. Charboneau, A. Garcia De Oliveira, N. Hazari, *ACS Catal.* **2019**, *9*, 301–314.

[6] P. Sánchez, M. Hernández-Juárez, N. Rendón, J. López-Serrano, E. Álvarez, M. Paneque, A. Suárez, *Dalton Trans.* **2018**, *47*, 16766–16776.

[7] C. K. Ng, J. Wu, T. S. A. Hor, H. K. Luo, *Chem. Commun.* **2016**, *52*, 11842–11845.

[8] R. Shintani, K. Nozaki, *Organometallics* **2013**, *32*, 2459–2462.

[9] X. Wang, K. Chang, X. Xu, *Dalton Trans.* **2020**, *49*, 7324–7327.

[10] R. Chambenahalli, R. M. Bhargav, K. N. McCabe, A. P. Andrews, F. Ritter, J. Okuda, L. Maron, A. Venugopal, *Chem. Eur. J.* **2021**, *27*, 7391–7401.

[11] C. Erken, A. Kaithal, S. Sen, T. Weyhermüller, M. Hölscher, C. Werlé, W. Leitner, *Nat. Commun.* **2018**, *9*, 1–9.

[12] S. Kostera, M. Peruzzini, K. Kirchner, L. Gonsalvi, *ChemCatChem* **2020**, *12*, 4625–4631.

[13] G. Jin, C. G. Werncke, Y. Escudié, S. Sabo-Etienne, S. Bontemps, *J. Am. Chem. Soc.* **2015**, *137*, 9563–9566.

[14] S. Chakraborty, J. Zhang, J. A. Krause, H. Guan, *J. Am. Chem. Soc.* **2010**, *132*, 8872–8873.

[15] L. J. Murphy, H. Hollenhorst, R. McDonald, M. Ferguson, M. D. Lumsden, L. Turculet, *Organometallics* **2017**, *36*, 3709–3720.

[16] S. R. Tamang, M. Findlater, *Dalton Trans.* **2018**, *47*, 8199–8203.

[17] X. Zhuang, J. Y. Chen, Z. Yang, M. Jia, C. Wu, R. Z. Liao, C. H. Tung, W. Wang, *Organometallics* **2019**, *38*, 3752–3759.

[18] G. S. Nichol, W. Clegg, *Acta Crystallogr. Sect. C Cryst. Struct. Commun.* **2005**, *61*, 383–385.

[19] F. Jiang, M. Achard, T. Roisnel, V. Dorcet, C. Bruneau, *Eur. J. Inorg. Chem.* **2015**, *2015*, 4312–4317.

[20] C. Das Neves Gomes, E. Blondiaux, P. Thuéry, T. Cantat, *Chem. Eur. J.* **2014**, *20*, 7098–7106.

[21] I. Knopf, C. C. Cummins, *Organometallics* **2015**, *34*, 1601–1603.

[22] K. Fujiwara, S. Yasuda, T. Mizuta, *Organometallics* **2014**, *33*, 6692–6695.

[23] F. G. Wech Urs, *Synthesis.* **2021**, *54*, 3421–3431.

[24] U. Gellrich, *Angew. Chemie Int. Ed.* **2018**, *57*, 4779–4782.

[25] S. Ilic, A. Alherz, C. B. Musgrave, K. D. Glusac, *Chem. Soc. Rev.* **2018**, *47*, 2809–2836.

[26] U. Koelle, B. Fuss, M. Belting, E. Raabe, *Organometallics* **1986**, *5*, 980–987.

[27] J. L. Kersten, A. L. Rheingold, K. H. Theopold, C. P. Casey, R. A. Widenhoefer, C. E. C. A. Hop, *Angew. Chemie Int. Ed.* **1992**, *31*, 1341–1343.

[28] A. M. Royer, T. B. Rauchfuss, D. L. Gray, *Organometallics* **2010**, *29*, 6763–6768.

[29] J. A. Zurakowski, B. J. H. Austen, M. C. Dufour, M. Bhattacharyya, D. M. Spasyuk, M. W. Drover, *Dalton Trans.* **2021**, *50*, 12440–12447.

[30] D. M. Heinekey, A. Liegeois, M. van Roon, *J. Am. Chem. Soc.* **1994**, *116*, 8388–8389.

[31] U. Koelle, S. Paul, *Inorg. Chem.* **1986**, *25*, 2689–2694.

5.6. Experimental Section

5.6.1. General Information

All experiments for air-sensitive compounds were performed under an atmosphere of dry argon, by using the standard Schlenk and glove box techniques.
Chemicals and solvents: Solvents (Et_2O, *n*-hexane, toluene, acetonitrile) were purified by an SPS solvent purification system under N_2; THF was distilled over sodium and benzophenone. Dry solvents were stored over molecular sieves (4 Å). Deuterated solvents (THF-d_8, C_6D_6, toluene-d_8, acetonitrile-d_3) were distilled over sodium or potassium metal and stored over molecular sieves (4 Å). Pentamethylcyclopentadiene, triphenylborate, aniline, chlorodiphenylphosphine, chlorodiisopropylphosphine, decamethylcobaltocene, pinacolborane (HBpin), catecholborane (HBcat), 9-borabicyclo[3.3.1]nonane (9-BBN, 0.5 M solution in THF), borane dimethylsulfide (BMS) were purchased from commercial vendors and used as received. Aniline was distilled in vacuum dried over molecular sieves (4 Å) prior to use. 6-Methyl-2-pyridone was purchased from *Sigma Aldrich* and sublimed in vacuum prior to use. Carbon dioxide gas (99.999 Vol%) was purchased from Westfalen AG. Ligands 2-(2-(diphenylphosphanyl)ethyl)pyridine(PyPhos)[1], 6-((diphenylphosphanyl)methyl)pyridin-2(1H)-one[2] and cobalt complexes $(Cp^*CoCl)_2$[3] and **Co2**[4] were prepared according to previously reported literature procedures.
NMR spectroscopy (^1H, ^{13}C, ^{11}B, ^{31}P). Nuclear magnetic resonance spectra were recorded on a Bruker Avance 400 (400 MHz), Bruker Avance 500 (400 MHz) and Bruker Avance 600 (600 MHz). ^1H-NMR: The following abbreviations are used to indicate multiplicities: s = singlet; d = doublet; t = triplet, q = quartet; m = multiplet, dd =doublet of doublet, dt = doublet of triplet, dq = doublet of quartet, ddt = doublet of doublet of quartet. Chemical shifts δ are given in ppm referenced to the residual solvent peak.
Solution magnetic moment was determined by performing an NMR experiment following the procedure of Evans[5].
Melting points of the compounds were measured on a *DigiMelt SRS* instrument using a glass capillary sealed under vacuum.
Elemental analyses were determined in an inert atmosphere by the analytical service department at the Dept of Chemistry of the University of Hamburg.
UV/visible absorption spectra were acquired at room temperature on an Agilent Cary 5000 UV-Vis-NIR double beam spectrometer with a 10 mm quartz cuvette with a Teflon valve.
FT-IR spectra were recorded on an Agilent Cary 630 FTIR with ATR-device at room temperature inside the nitrogen filled glovebox.
ESI-MS was measured on a Q-TOF mass spectrometer micrO-TOF-Q II (Bruker Daltonik) with ESI, APCI, and cryospray-ionization sources (Dept. of Chemistry, University of Göttingen).

5.6.2. Synthetic Procedures

Synthesis of 6-((diisopropylphosphanyl)methyl)pyridin-2(1H)-one (L1H)

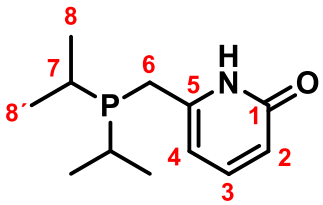

Suspension of 6-methyl-2-pyridone (1.50 g, 13.8 mmol, 1.00 equiv.) in THF (15 mL) was cooled to 0 °C and *n*-butyllithium (1.6 M in hexane, 18 mL, 29 mmol, 2.1 eq.) was added dropwise over a period of 10 min while stirring. During the addition, the reaction mixture turned orange and the colourless solid dissolved continuously. The orange solution was then stirred at 0 °C for 2 h. Subsequently, the reaction mixture was cooled to -78 °C and added dropwise to a solution of chlorodiisopropylphosphine (2.20 mL, 13.8 mmol, 1.00 eq.,) in THF (10 mL) at -78 °C over 20 min with vigorous stirring. After stirring the orange reaction mixture at -78 °C for 1 h, it was allowed to warm up to room temperature and stirred for an additional 19 h. The solvent was removed under reduced pressure and the degassed aqueous NH_4Cl solution (3.3 M, 30 mL) was added to the red residue. The suspension was stirred for 10 min and then extracted with DCM (4x15 mL). The combined organic layers were dried over anhydrous $MgSO_4$, filtered and the solvent was evaporated *in vacuo*. The resulting yellow solid was crystallized from hexane at -30 °C. Slightly yellow crystalline solid was collected by filtration, washed with cold hexane and dried in vacuum. Yield: 2.13 g (69%).

m.p. = 84–85 °C.

^{1}H-NMR (500.1 MHz, C_6D_6, 24.9 °C): δ [ppm] = 14.34 (s, 1 H, -NH), 6.85 (dd, $^3J_{(H,H)}$ = 9.1 Hz, $^3J_{(H,H)}$ = 7.0 Hz, 1 H, 3-H), 6.42 (d, $^3J_{(H,H)}$ = 9.1 Hz, 1 H, 2-H), 6.09–6.06 (m, 1 H, 4-H), 2.69 (s, 2 H, 6-H), 1.61 (heptd,f $^3J_{(H,H)}$ = 7.1 Hz, $^2J_{(P,H)}$ = 1.1 Hz, 2 H, 7-H), 1.01–0.93 (m, 12 H, 8-H and 8'-H).**^{13}C NMR** (125.8 MHz, C_6D_6, 24.7 °C): δ[ppm] = 166.4 (C-1), 149.9 (d, $^2J_{(P,C)}$ = 11.3 Hz, C-5), 141.5 (C-3), 116.4 (d, $^5J_{(P,C)}$ = 1.7 Hz, C-2), 106.1 (d, $^3J_{(P,C)}$ = 11.1 Hz, C-4), 26.9 (d, $^1J_{(P,C)}$ = 24.7 Hz, C-6), 23.9 (d, $^1J_{(P,C)}$ = 15.8 Hz, 2 C, C-7), 19.7 (d, $^2J_{(P,C)}$ = 15.0 Hz, 2 C, C-8/8'), 19.1 (d, $^2J_{(P,C)}$ = 11.3 Hz, 2 C, C-8/8'). **^{31}P{^{1}H}-NMR** (202.5 MHz, C_6D_6, 25.1 °C): δ[ppm] = 25.6 (s).

Elemental analysis: calc. for $C_{12}H_{20}NOP$: C 63.98, H 8.95, N 6.22; found: C 63.72, H 8.90, N 6.23.

*Synthesis of complex **Co1***

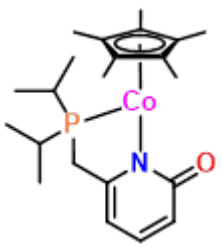

A solution of potassium *tert*-butoxide (458 mg, 3.96 mmol) in 10 mL THF was added dropwise to the solution of the L1H (850 mg, 3.77 mmol) in 120 mL THF. The reaction mixture was stirred at ambient temperature for 2 hours followed by dropwise addition of the solution of $[Cp^*CoCl]_2$ (866 mg, 3.77 mmol) in 10 mL THF. The mixture turned from slightly yellow to dark orange (almost black). After stirring at ambient temperature overnight, all volatiles were removed under vacuum, orange solid residue was extracted with toluene (30 mL) and the toluene

extract was filtered through a short pad of Celite®. The filtrate was concentrated in vacuum and the brown-orange solid residue was crystallized from 70 mL acetonitrile at -30 °C. A large crop of dark-red crystals was collected by filtration, washed with hexane and dried in vacuum. Yield: 954 mg (60%). Single crystal suitable for X-ray analysis was collected during the described crystallization procedure.

m.p. = 184–186 °C.

Evans-NMR (300.2 MHz, C_6D_6, 24.9 °C): μ = 1.89 μ_B, unpaired electrons (spin-only) n = 1.

UV-Vis (THF, 0.05 mg/mL): λ_{max} (ε) = 396 nm (3358 $L \cdot mol^{-1} \cdot cm^{-1}$), 332 nm (8633 $L \cdot mol^{-1} \cdot cm^{-1}$), 240 nm (15906 $L \cdot mol^{-1} \cdot cm^{-1}$), 209 nm (18409 $L \cdot mol^{-1} \cdot cm^{-1}$).

Elemental analysis: calc. (%) for $C_{22}H_{34}CoNOP$: C 63.15, H 8.19, N 3.35; found: C 62.87, H 8.28, N 3.28.

ESI-MS: ($C_{22}H_{34}CoNOP$) Calculated: 418.1704; Found: 418.1649

*Synthesis of complex **Co5***

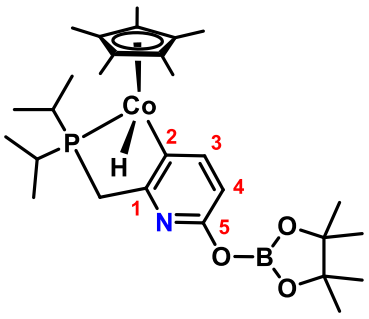

Complex **Co1** (157 mg, 0.375 mmol) was dissolved in 3.0 mL THF and HBpin (67 µL, 0.462 mmol, 1.2 equiv.) was added. Colour change from orange-red to black was observed. Reaction mixture was stirred at room temperature for 22 h. All volatiles were removed in vacuum and the oily residue was treated with approx. 1 mL hexane followed by solvent removal in vacuum (manipulation was repeated two times). Addition of the new portion of hexane (approx. 2 mL) was accompanied by formation of the orange solid. Solid was collected by filtration, extracted with approx. 5 mL hexane and residual solid was dissolved in 2.0 mL Et_2O. Both hexane and Et_2O fractions were stored overnight at -35°C. From hexane fraction dark-orange crystals (27 mg) were isolated. Diethyl ether fraction yielded orange microcrystalline solid (27 mg). Single crystals suitable for X-ray analysis were obtained by slow evaporation of the hexane fraction. Both solids, collected from hexane and Et_2O were proved to be identical Co-H species on the basis of ^{1}H NMR analysis. Combined yield 26%.

^{1}H NMR (600 MHz, THF-d_8) δ [ppm] = 7.53 (d, $^3J_{H,H}$ = 8.1 Hz, 1 H, H-3), 6.34 (d, J = 8.3 Hz, 1H, H-4), 2.64 – 2.52 (m, 2H, C$\underline{H}_2$-P), 2.16 (hept, J = 7.3 Hz, 2H, *i*-Pr-C$\underline{H}$), 1.82 (s, 15H, Cp*-C$\underline{H}_3$), 1.26 (dd, 3H, dd, overlapped, 3H, *i*-Pr-C$\underline{H}_3$), 1.23 (s, 12H, Bpin-C$\underline{H}_3$), 1.17 (dd, $^3J_{P,H}$ = 12.4 Hz, $^3J_{H,H}$ = 6.8 Hz, 3H, *i*-Pr-C$\underline{H}_3$), 1.05 (dd, $^3J_{P,H}$ = 13.9 Hz, $^3J_{H,H}$ = 7.1 Hz, 3H, *i*-Pr-C$\underline{H}_3$), 0.93 (dd, $^3J_{P,H}$ = 12.9, $^3J_{H,H}$ = 6.9 Hz, 3H, *i*-Pr-C$\underline{H}_3$), -16.70 (d, $^2J_{P,H}$ = 87.5 Hz, 1H, Co-$\underline{H}$). **^{13}C NMR** (151 MHz, THF-d_8) δ [ppm] = 165.32 (d, $^2J_{P,C}$ = 19.7 Hz, C1), 157.18 (C5), 150.03 (C4), 148.50 (C2), 110.14 (C3), 93.05 (Cp*-C), 82.92 (C-Bpin), 37.15 (d, $^1J_{C,P}$ = 39.0 Hz, C$\underline{H}_2$Py), 24.93 (Bpin-C$\underline{H}_3$ overlaped with THF-d_8), 27.34 (d, 13.4 Hz *i*-Pr-C$\underline{H}$), 23.90 (d, J = 26.1 Hz, *i*-Pr-CH), 20.07 (*i*-Pr-C$\underline{H}_3$), 19.12 (*i*-Pr-C$\underline{H}_3$), 18.78 (*i*-Pr-C$\underline{H}_3$), 18.57 (*i*-Pr-*C*H$_3$), 11.41 (Cp*-C$\underline{H}_3$).

^{31}P NMR (243 MHz, THF-d_8) δ 91.63 (br). **^{11}B NMR** (193 MHz, THF-d_8) δ 21.98.
IR-FTIR (ATR, cm^{-1}): ν_{Co-H} =1924.

Elemental analysis calculated for $C_{28}H_{46}BCoNO_3P$ C 61.66, H 8.50, N 2.57; found 61.71, 8.67, 2.57
ESI-MS: ($C_{28}H_{46}BCoNO_3P$) Calculated: 545.2640; Found: 545.2546.

5.6.3. Catalytic CO_2 hydroboration

General procedure for CO_2 hydroboration to formylborane

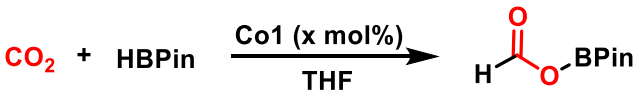

Method A: Catalyst **Co1** (selected amound of solid or aliquot of the stock solution in THF-d_8), internal standard mesitylene (15 µL, 0.1078 mmol) and 0.6 mL THF-d_8 were mixed in a scindilation vial. Pinacolborane HBpin (41 µL, 0.27 mmol) was added and reaction mixure was transfered to J. Young NMR tube. Solution in was degassed with two freeze-pump-thaw cycles. Then solution was immersed to the liquid nitrogen for the third time and vacuum was applied to a frozen solution. NMR tube was lifted form the liquid nitrogen and reaction mixture was exposed to 1 atm of CO_2 for 5 min. The J. Young tube was then sealed, shaken vigorously and subjected to ^{1}H and ^{11}B NMR analysis. ^{1}H NMR yield was determined by integration of signals of formylborane with reference to the internal standard mesitylene as an average of two runs.

Method B: Catalyst **Co1** (selected amount of solid or aliquote of the stock solution in THF), internal standard mesitylene (15 µL, 0.108 mmol) and 0.6 mL of THF/THF-d_8 (5/1 mixture) were mixed in a scintillation vial. Pinacolborane HBpin (20 µL, 0.14 mmol) was added and reaction mixure was transfered to J. Young NMR tube. This solution was degassed with two freeze-pump-thaw cycles. Then, the solution was immersed in a liquid nitrogen bath for the third time and vacuum was applied to a frozen solution. NMR tube was lifted form the liquid nitrogen and reaction mixture was exposed to 1 atm of CO_2 for 5 min. The J. Young tube was then sealed, shaken vigorously and subjected to ^{1}H and ^{11}B NMR analysis. ^{1}H NMR yield was determined by integration of signals of formylborane with reference to the internal standard mesitylene as an average of two runs.

NMR data of HCO_2Bpin[6]:

^{1}H NMR (400 MHz, THF-d_8) δ [ppm] = 8.40 (s, 1H, HCO_2Bpin), 1.31 (s, 12H, HCO_2Bpin). **^{13}C NMR** (101 MHz, THF-d_8) δ [ppm] = 158.54, 85.33, 24.99. **^{11}B NMR** (128 MHz, THF-d_8) δ [ppm] = 22.68.

Hydroboration of HCO_2Bpin

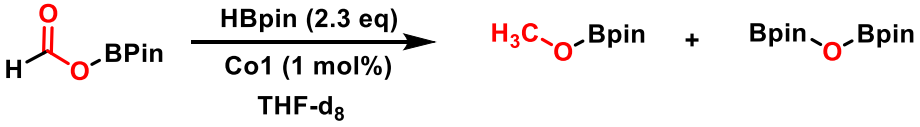

Co1 (1.1 mg), internal standard mesitylene (15 µL, 0.1078 mmol) and 0.6 mL THF-d_8 were mixed in a scindilation vial. Pinacolborane HBpin (41 µL, 0.27 mmol) was added and reaction mixure was transfered to J. Young NMR tube. This solution was degassed with two freeze-pump-thaw cycles. Then, the solution was immersed into a liquid nitrogen bath for the third time and vacuum was applied to the frozen solution. The NMR tube was lifted form the liquid nitrogen and reaction mixture was exposed to 1 atm of CO_2 for 5 min. The J. Young tube was then sealed, shaken vigorously and subjected to ^{1}H NMR to confirm full conversion to HCO_2Bpin. Then the reaction mixture was carefully degassed under static vacuum to remove CO_2. The J. Young tube was transfered to argon-filled glovebox and HBpin (90 µL, 0.62 mmol) was added. The J. Young NMR tube was placed to 60 °C oil bath and reaciton progreass was monitored by ^{1}H NMR. Colour of the reaciton mixture changed gradually from yellow to bright green. After heating for 40 hours almost full conversion of HCO_2Bpin to CH_3OBpin and $(pinB)_2O$ was achived.

NMR data for CH_3OBpin[6,7]:

^{1}H NMR (400 MHz, THF-d_8) δ [ppm] = 3.50 (s, 3H), 1.20 (s, 12H). **^{13}C NMR** (101 MHz, THF-d_8) δ [ppm] = 83.21, 52.66, 25.17. **^{11}B NMR** (128 MHz, THF-d_8) δ [ppm] = 22.35.

NMR data for $(pinB)_2O$[6]:

^{1}H NMR (400 MHz, THF-d_8) δ [ppm] = 1.21 (s, 24H) **^{13}C NMR** (101 MHz, THF-d_8) δ [ppm] = 83.52, 25.10. **^{11}B NMR** (128 MHz, THF-d_8) δ [ppm] = 21.24.

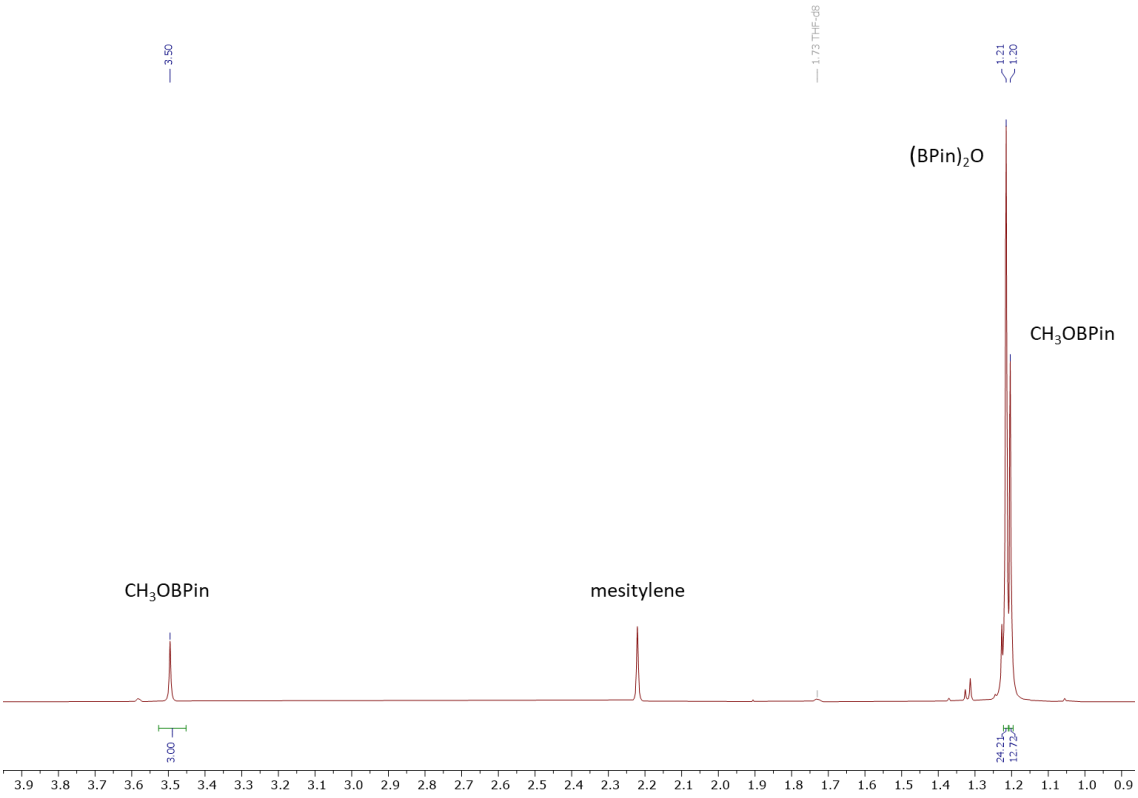

Figure 5.5. Crude ^{1}H NMR spectrum (400 MHz, THF-d_8) of HCO_2Bpin hydroboration to CH_3OBpin.

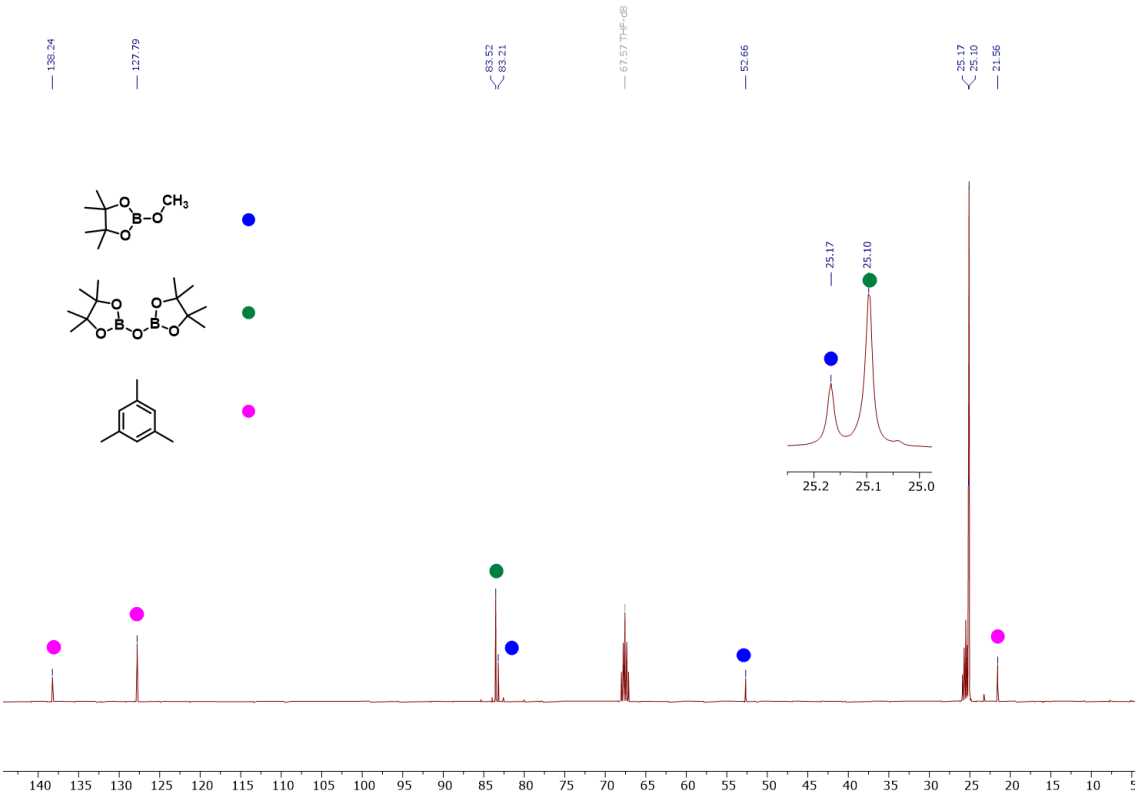

Figure 5.6. Crude ^{13}C NMR spectrum of HCO_2Bpin hydroboration to CH_3OBpin.

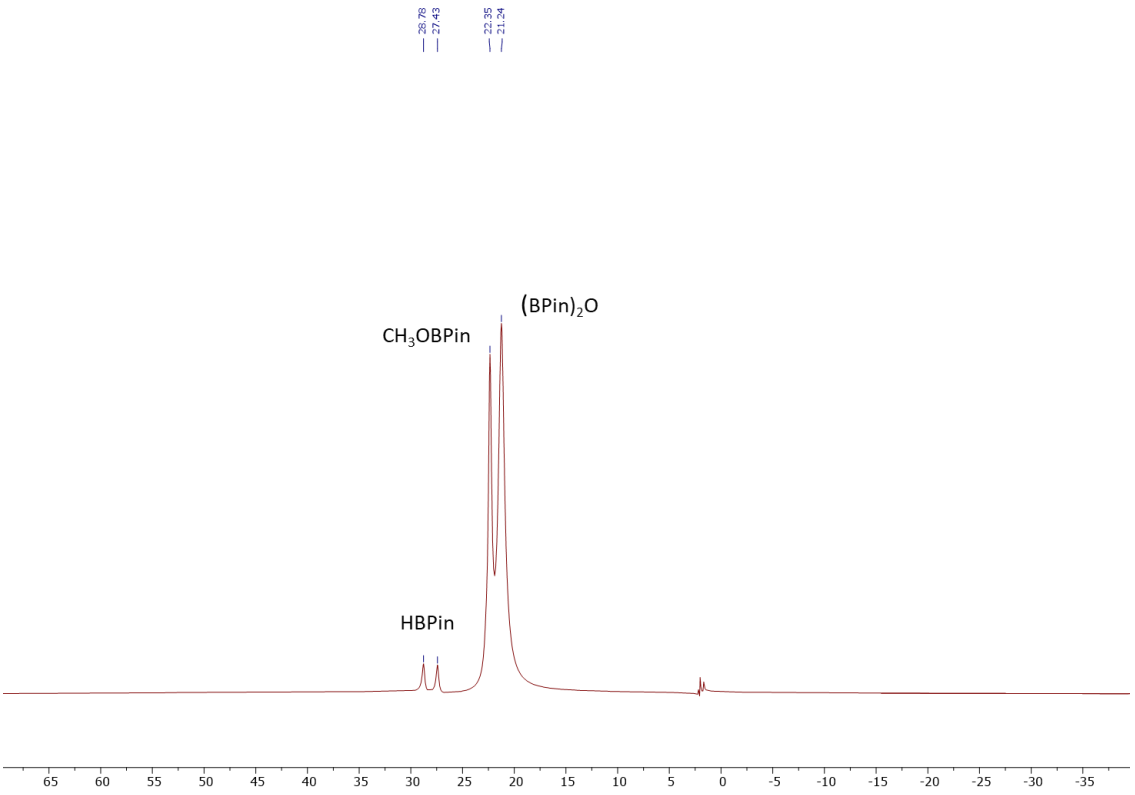

Figure 5.7. Crude ^{11}B NMR spectrum of HCO_2Bpin hydroboration to CH_3OBpin.

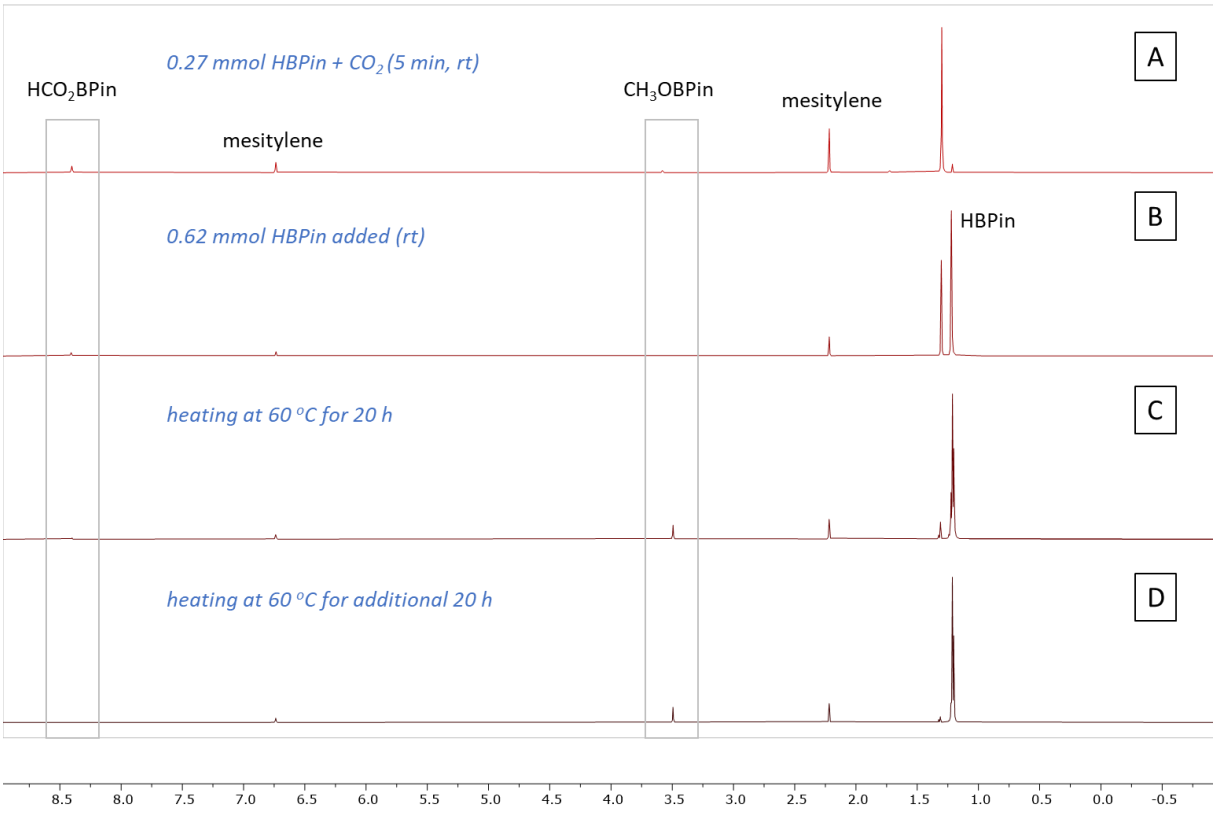

Figure 5.8. Stepwise ^1H NMR monitoring of crude reaction to HCO_2Bpin and CH_3OBpin **A**: HBpin (0.27 mmol) + CO_2, 5 min at rt; **B**: addition of 2.3 equiv. HBpin to

reaction mixture A at rt; **C**: heating for 20 h at 60 °C, 84% CH_3OBpin; **D**: heating for additional 20 h at 60 °C, >99% CH_3OBpin.

Lewis acid assisted hydroboration of CO_2

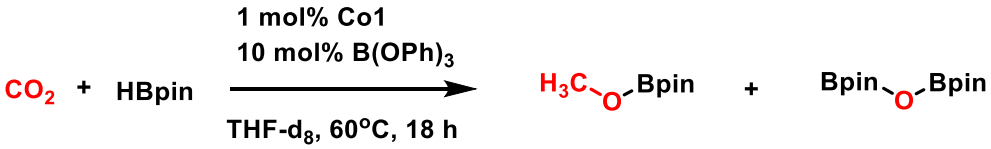

Co1 (1.1 mg, 2.7 µmol), internal standard mesitylene (15 µl, 0.1078 mmol), triphenylborate $B(OPh)_3$ (7.8 mg, 0.027 mmol) and 0.6 mL THF-d_8 were mixed in a scintillation vial. Pinacolborane HBpin (41 µL, 0.27 mmol) was added and reaction mixure was transferred to a J. Young NMR tube. The solution was degassed with two freeze-pump-thaw cycles, then immersed into a liquid nitrogen bath for the third time and vacuum was applied to the frozen solution. The J. Young NMR tube was lifted form the liquid nitrogen and reaction mixture was exposed to 1 atm of CO_2 for 5 min. The J. Young tube was then sealed, shaken vigorously and placed to the 60 °C oil bath. Reacton progress was monitored by ^1H NMR. Colour of the reaction mixture changed gradually from yellow to bright green. After heating for 18 h, 74% (NMR) of CH_3OBpin was formed.

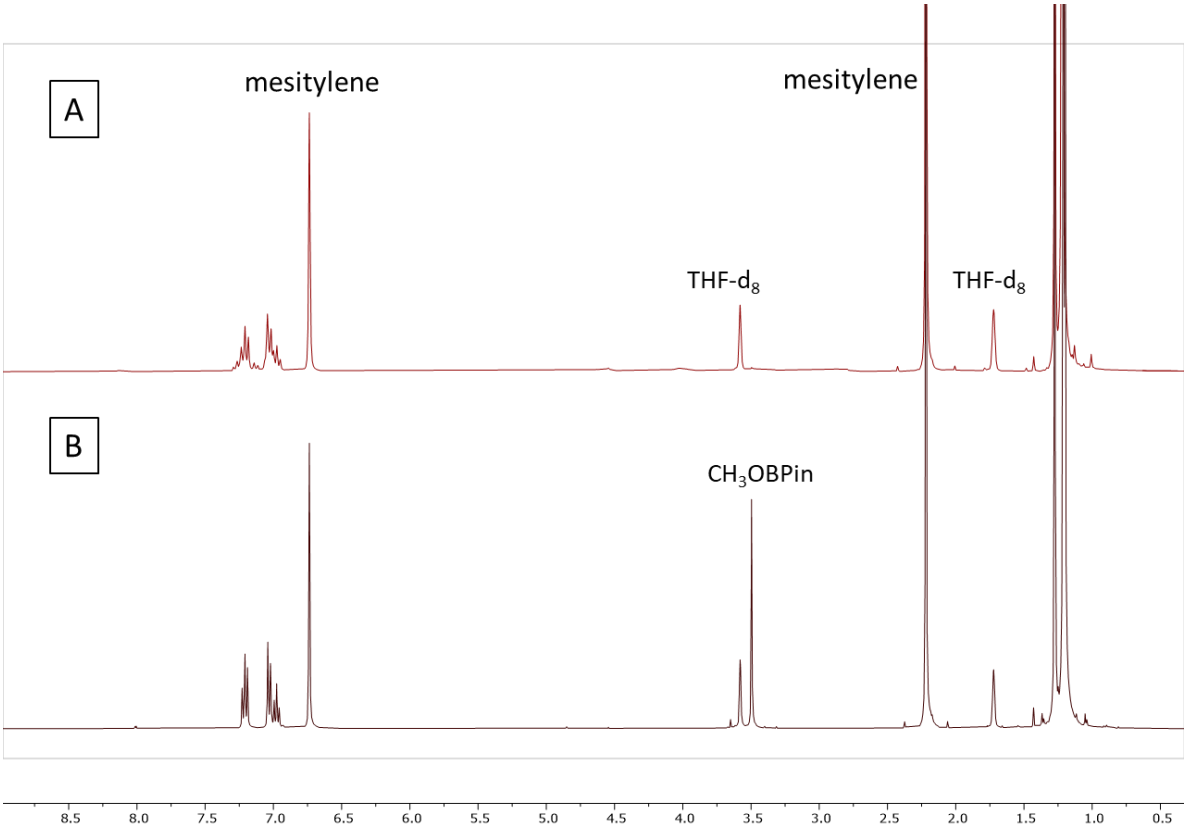

Figure 5.9. ^{1}NMR spectra (400 MHz, THF-d_8) for CO_2 hydroboration (1 mol% **Co1** and 10 mol% $B(OPh)_3$ **A**: rt, 5 min (no conversion of HBpin). **B**: 60 °C, 18 h (full conversion of HBpin, 74% yield of CH_3OBpin).

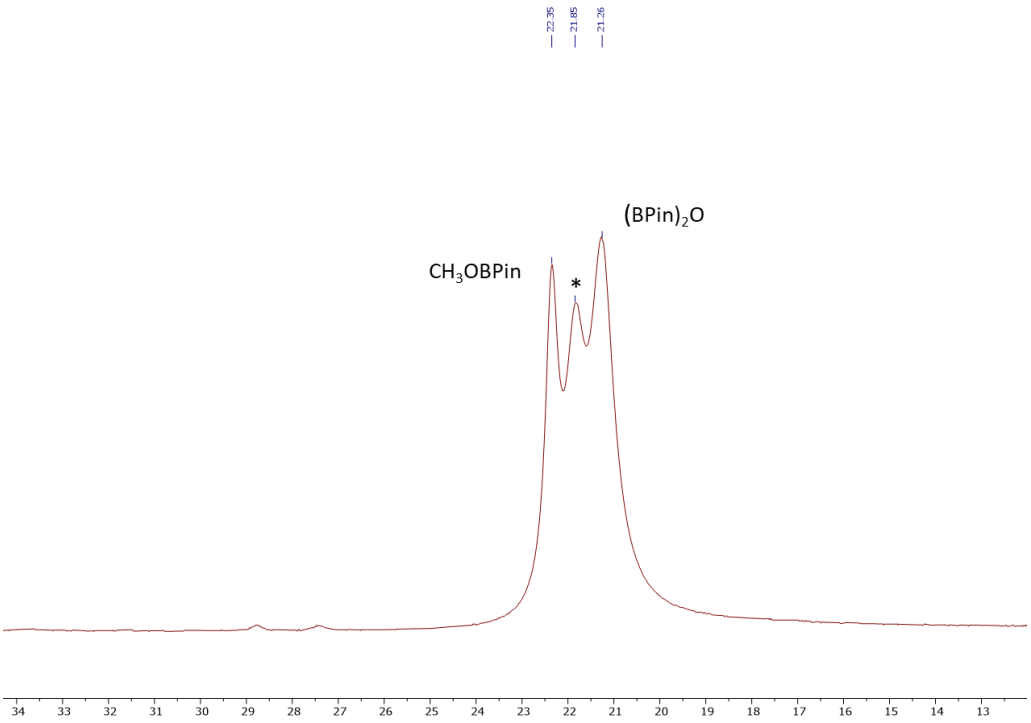

Figure 5.10. ^{11}B NMR spectrum (400 MHz, THF-d_8) for CO_2 hydroboration (1 mol% **Co1** and 10 mol% $B(OPh)_3$) at 60 °C for 18 h; asterisks denote signals that belong to $B(OPh)_3$ or related species.

*Preparative-scale N-formylation of aniline in presence of **Co1***

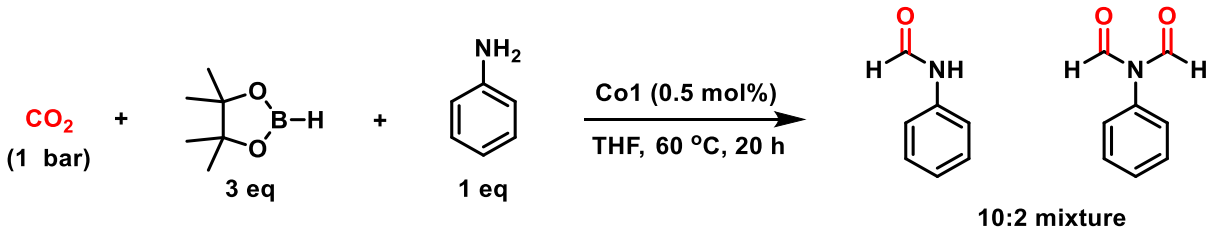

The 10 mL Teflon-cock Schlenk tube was charged with **Co1** (5.2 mg, 0.0125 mmol), aniline (76 µL, 0.833 mmol) and 3 mL THF. Pinacolborane (373 µL, 2.5 mmol, 3 equiv.) was added to reaction mixture at room temperature. Intensive gas evolution and colour change from orange to brown was observed. Then, the Schlenk tube was sealed, and solution was degassed with two freeze-pump-thaw cycles. Then, the solution was immersed into a liquid nitrogen bath for the third time and vacuum was applied to the frozen solution. The Schlenk tube was removed form the liquid nitrogen, reaction mixture was exposed to 1 atm of CO_2 for 5 min. Then, the Schlenk-tube was sealed and reaction mixture was stirred for 16 h at 60 °C to give a colorless solution. All volatiles were removed under vacuum and the residue was purified by column chromatography on silica gel using CH_2Cl_2 as eluent. Yield: 87 mg (86%). The isolated

product constitues the unseparated mixture of N-formamide / N-formyl-N-phenylformamide = 10/2. NMR data is in agreement with previous literature reports.[8,9]

N-formanilide is a mixture of rotamers (major and minor);

^{1}H NMR (600 MHz, $CDCl_3$): δ [ppm] = 8.70 (d, *J* = 11.3 Hz, 1H, major rotamer), 8.57 (br.s, 0.9H, major rotamer), 8.36 (d, *J* = 1.9 Hz, 0.8H, minor rotamer), 7.65 (br. s, 0.8H, minor rotamer), 7.57 – 7.53 (m, 1.7H, minor + major rotamer), 7.39 – 7.30 (m, 3.7H, minor + major rotamer), 7.20 – 7.17 (m, 1H, major rotamer), 7.15 – 7.12 (m, 0.8H, minor rotamer), 7.11 – 7.08 (m, 1.8H, minor + major rotamer). **^{13}C NMR** (75 MHz, $CDCl_3$, 25 °C) δ [ppm] = Major rotamer: 162.72, 136.81, 129.90, 125.44, 118.97 Minor rotamer: 159.11, 136.97, 129.25, 124.97, 120.10.

N-formyl-N-phenylformamide

^{1}H NMR (600 MHz, $CDCl_3$, 25 °C) δ [ppm] = 9.10 (br. s), 7.50 (d, *J* = 16.2 Hz, 3H), 7.23 (br. d, *J* = 7.7 Hz, 2H).

*NMR-scale N-formylation of aniline in presence of **Co1***

The J. Young NMR tube was charged with **Co1** (1.1 mg, 2.7 µmol), aniline (8 µL, 0.09 mmol) and 0.6 mL THF-d_8. Pinacolborane HBpin (41 µL, 0.27 mmol) was added to the reaction mixture and vigorous gas evolution was observed for few seconds after addition. The J. Young NMR tube was sealed and attached to a CO_2 gas supply line. The reaction mixure was degassed with two freeze-pump-thaw cycles. Then, the solution was immersed into a liquid nitrogen bath for the third time and vacuum was applied to the frozen solution. The J. Young NMR tube was lifted form the liquid nitrogen and reaction mixture was exposed to 1 atm of CO_2 for 5 min. The J. Young tube was then sealed, shaken vigorously and placed to the 60 °C oil bath. Reaction progress was monitored by ^{1}H NMR (see Figure 5.11).

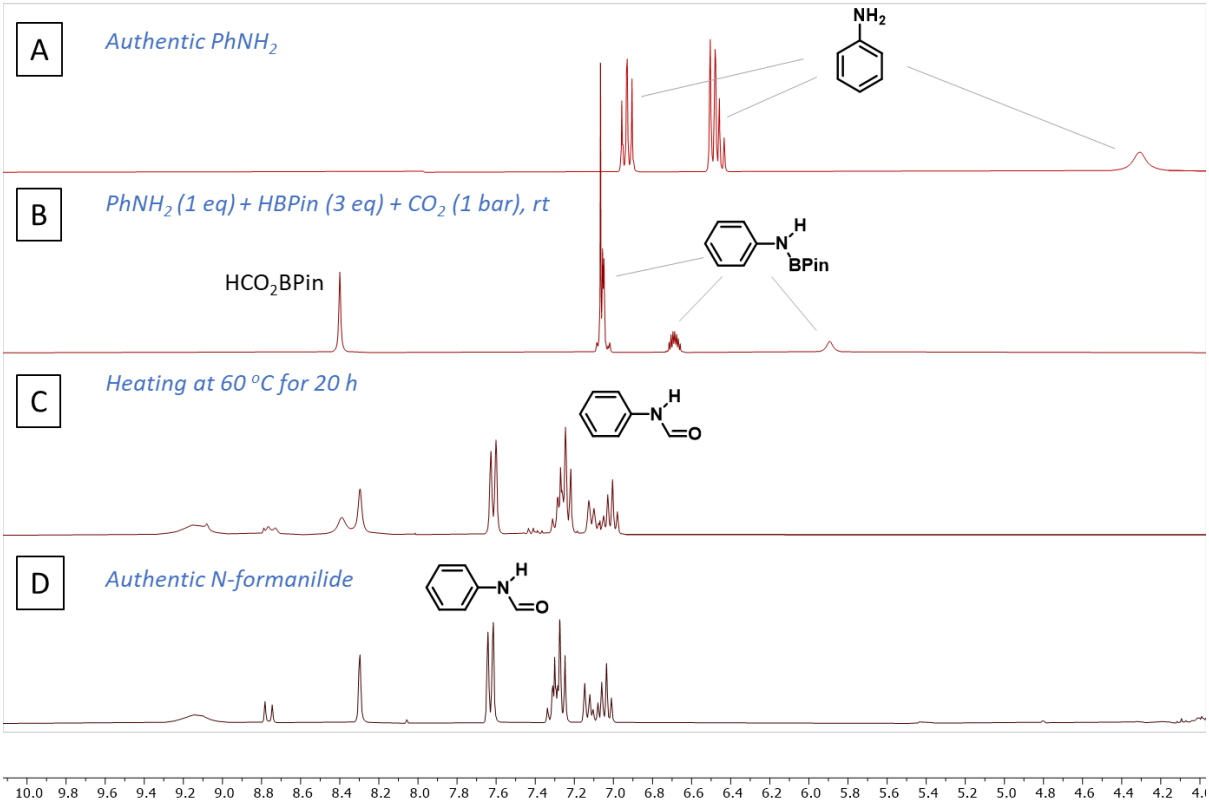

Figure 5.11. ^{1}H NMR spectra (300 MHz, THF-d_8): **A**) Pure aniline in THF-d_8; **B**) Mixture of aniline (1 equiv.) and HBpin (3 equiv.) in presence of 1 mol% **Co1** after CO_2 addition for 5 min showing formation of 2:1 mixture of HCO_2Bpin and dehydrocoupling product PhNHBpin[10] ; **C**) heating at 60 °C for 20 h showing formation of N-formanilide as predominant product; **D**) pure N-formanilide in THF-d_8 for reference.

CO_2 hydroboration with different boranes

General procedure: Catalyst **Co1** (1.1 mg, 2.7 µmol), internal standard mesitylene (15 µL, 0.1078 mmol) and 0.6 mL THF-d_8 were mixed in a scintillation vial. The borane of choice (0.27 mmol) was added and reaction mixure was transferred to a J. Young NMR tube. The reaction mixture was degassed with two freeze-pump-thaw cycles. Then, the solution was immersed into a liquid nitrogen bath for the third time and vacuum was applied to the frozen solution. The J. Young NMR tube was lifted form the liquid nitrogen and reaction mixture was exposed to 1 atm of CO_2 for 5 min. The J. Young NMR tube was then sealed, shaken vigorously and subjected to ^{1}H and ^{11}B NMR analysis. ^{1}H NMR yield was determined by integration of signals of CO_2 hydroboration products with reference to the internal standard mesitylene.

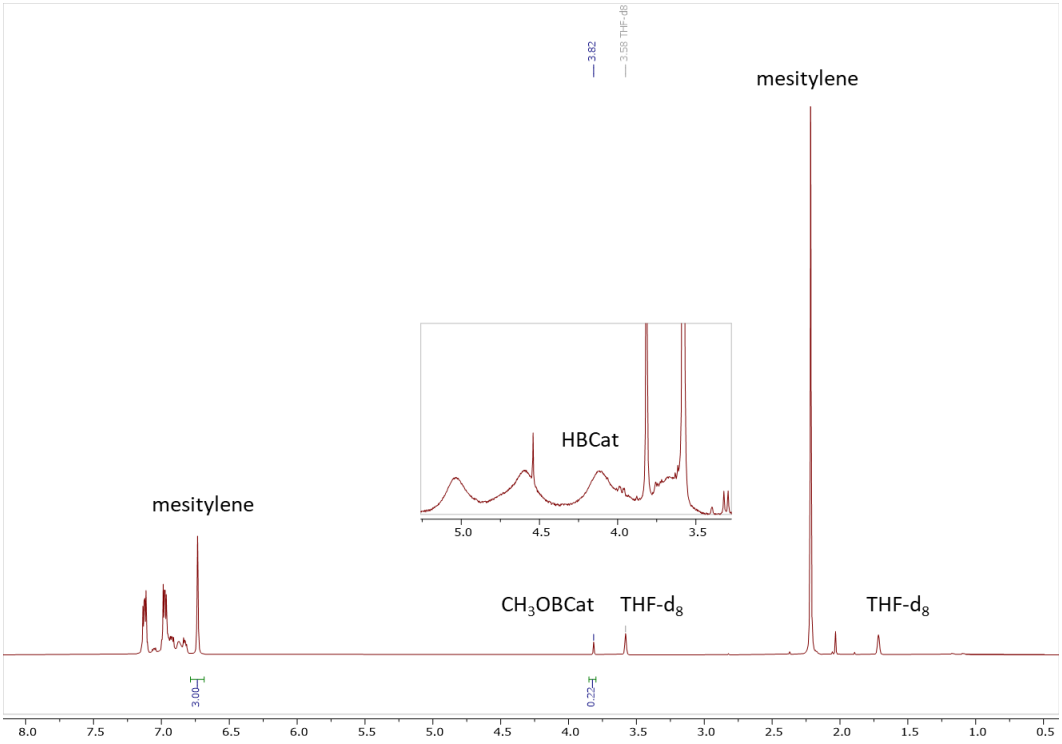

Figure 5.12. ^{1}H NMR spectrum (400 MHz, THF-d_8) of CO_2 hydroboration with HBcat (see manuscript Table 5.2, entry 1). BH resonance of unreacted HBcat is shown in the inset. Spectral data is in accordance with the literature.[6]

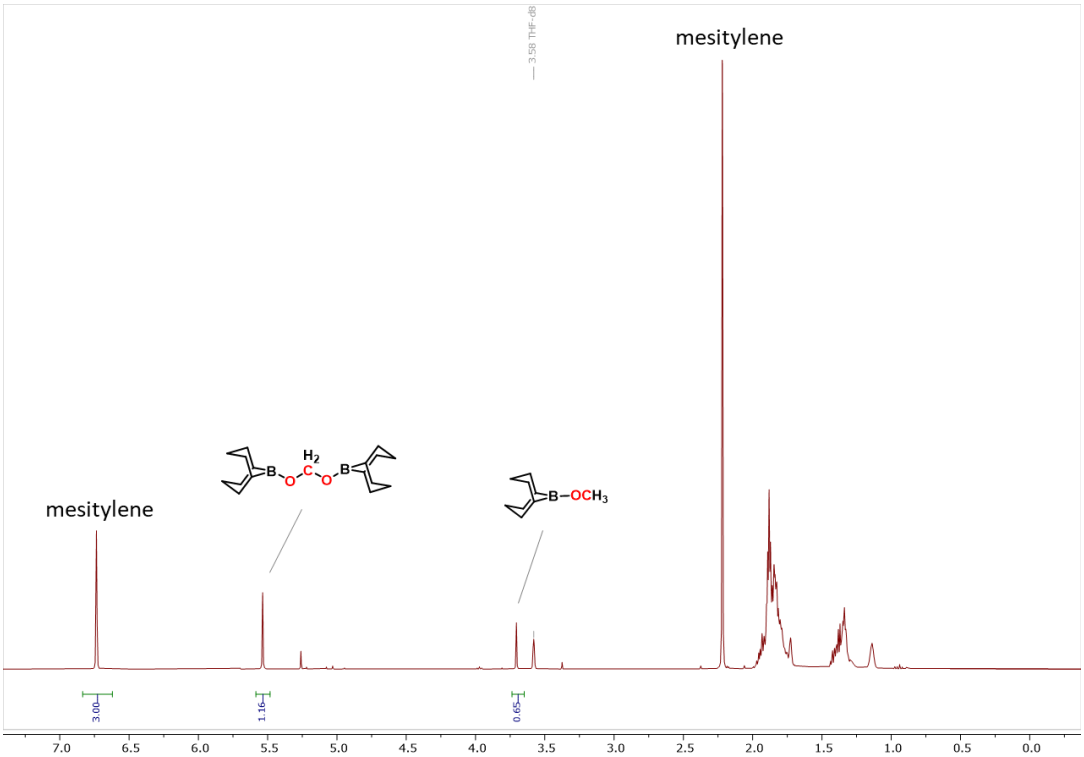

Figure 5.13. ^{1}H NMR spectrum of CO_2 hydroboration with HBcat (Table 5.2 manuscript, entry 3). Spectral data is in accordance with the literature.[6]

5.6.4. Mechanistic Experiments

*In situ generation of **L1Bpin***

The J. Young NMR tube was charged with **L1H** (15 mg, 67 µmol)**,** HBpin (10 µL, 67 µmol) and 0.6 mL THF-d_8 and the reaction mixture was heated at 60 °C for 16 h. Clean conversion of starting materials to form the coupling product **L1Bpin** was proved by ^{1}H, ^{11}B and ^{31}P spectra. Aliquots of the obtained solution were used to test background catalytic activity of **L1Bpin** (manuscript, entry 11, Table 5.1).

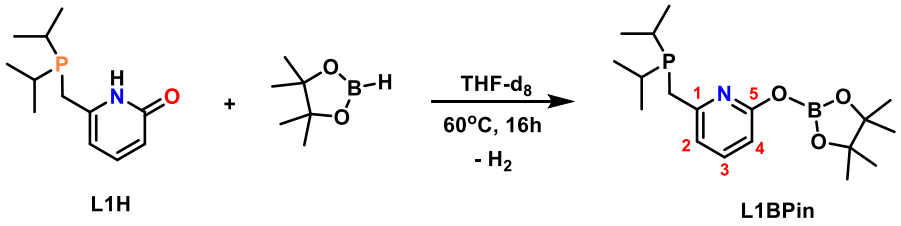

^{1}H NMR (400 MHz, THF-d_8) δ [ppm] = 7.52 (t, *J* = 7.7 Hz, 1H, H-3), 6.97 (d, *J* = 7.5 Hz, 1H, H-2), 6.62 (d, *J* = 8.1 Hz, 1H, H-4), 2.86 (br.s, 2H, CH_2-P), 1.80 (m, 1H, *i*-Pr-CH), 1.28 (s, 12H, Bpin-CH_3), 1.12 – 0.99 (m, 12H, *i*-Pr-CH_3) **^{13}C NMR** (75 MHz, THF-d_8) δ [ppm] = 159.63 (C5), 159.39 (C1), 138.82 (C3) 118.20 (C2), 109.35 (C4), 82.96 (C-BPin), 31.55 (d, $^{1}J_{C,P}$ = 23.9 Hz, CH_2Py), 23.91 (Bpin-CH_3 overlaped with THF-d_8), 23.36 (d, $^{3}J_{C,P}$ = 16.1 Hz), 19.17 (d, *J* = 15.5 Hz, *i*-Pr-CH_3), 18.53 (d, $^{3}J_{C,P}$ J = 11.4 Hz, *i*-Pr-CH_3) **^{31}P NMR** (162 MHz, THF-d_8) δ [ppm] = 12.07 **^{11}B NMR** (128 MHz, THF-d_8) δ [ppm] = 22.10.

*Stoichiometric reaction between **Co1** and HBpin*

HBpin (6 µL, 0.40 mmol) was added to the solution of **Co1** (16 mg, 0.38 mmol) in 0.6 mL THF-d_8 resulting in instant color change from orange-red to black. The reaction mixture was stirred overnight at ambient temperature and transferred to J. Young NMR tube. ^{1}H and ^{11}B NMR spectra were recorded. ^{11}B NMR spectrum showed complete consumption of HBpin (see Figure 5.14). ^{1}H NMR spectrum showed a mixture of paramagnetic and diamagnetic compounds (Figures 5.15 - 5.17).

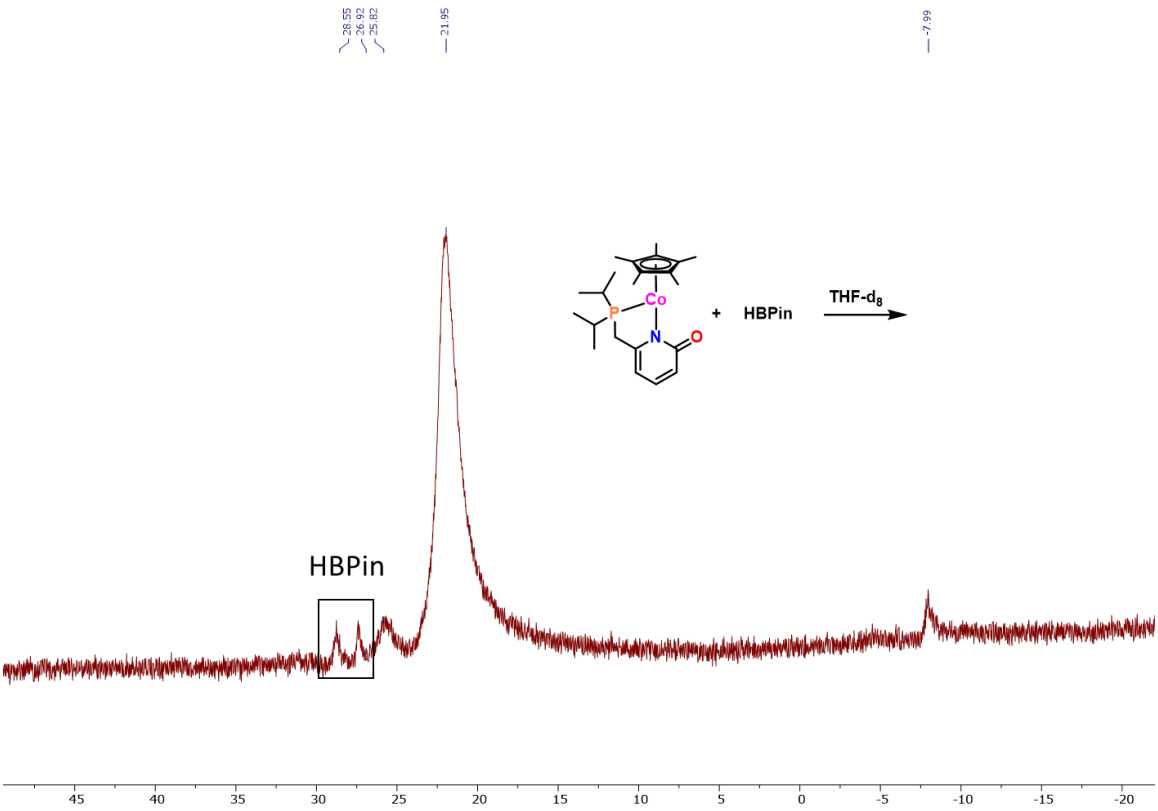

Figure 5.14. ^{11}B NMR spectrum (400 MHz, THF-d_8) of **Co1** + HBpin reaction mixture showing almost full consumption of HBpin and formation of new species.

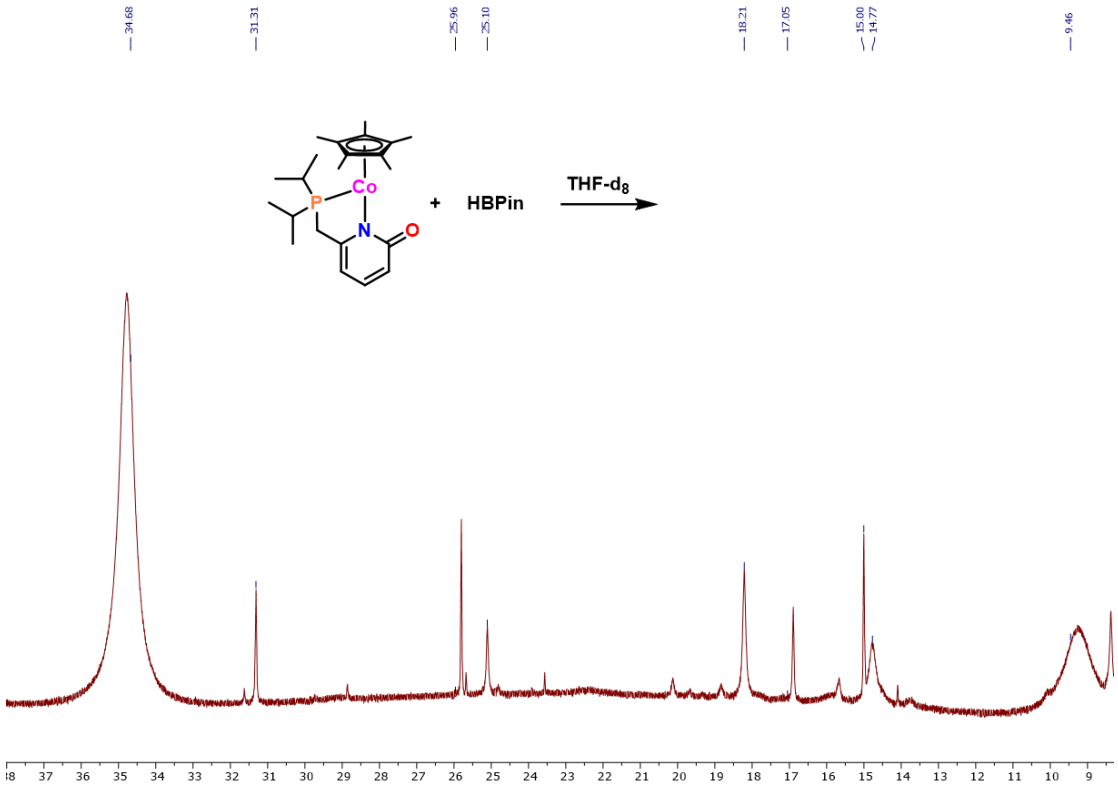

Figure 5.15. Fragment of ^{1}H NMR spectrum (600 MHz, THF-d_8) of **Co1** + HBpin reaction mixture showing paramagnetically shifted resonances (not assigned).

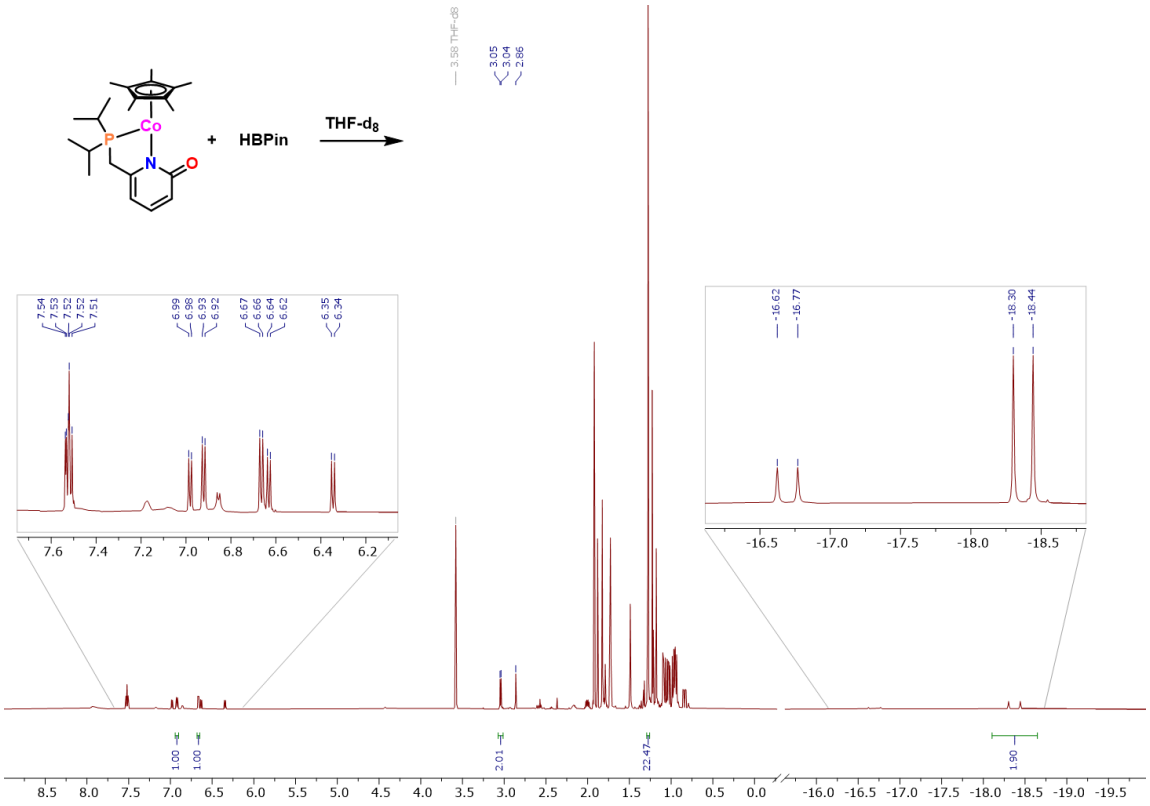

Figure 5.16. Diamagnetic region of the ^{1}H spectrum (600 MHz, THF-d_8) of the **Co1** + HBpin mixture.

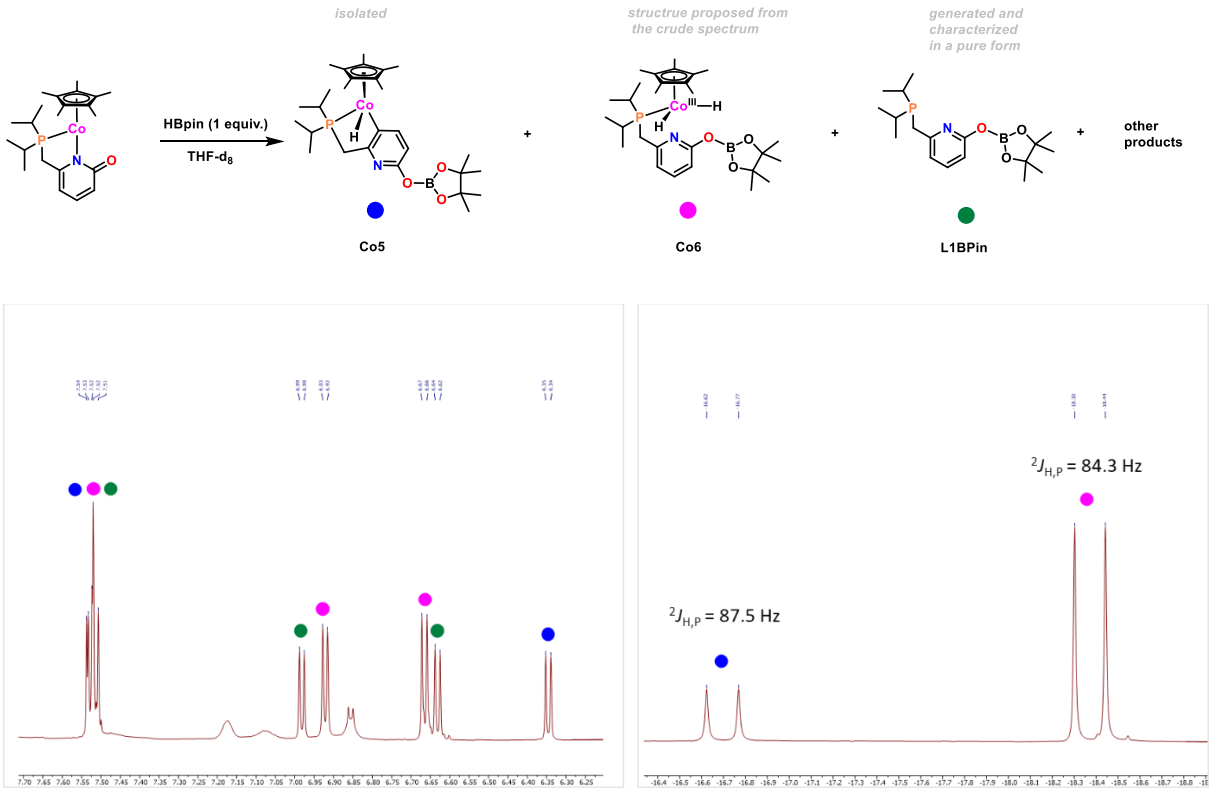

Figure 5.17. ^{1}H NMR spectrum (600 MHz, THF-d_8) of the **Co1** + HBpin mixture with assignments.

*Stoichiometric reaction between **Co1** and DBpin*

The aliquote of the 1.22 M stock solution of DBpin (47 µL, 57 µmol) was added to the solution of **Co1** (20 mg, 48 µmol). The reaction mixture was transferred to J. Young NMR tube and analyzed by ^{1}H NMR spectra.

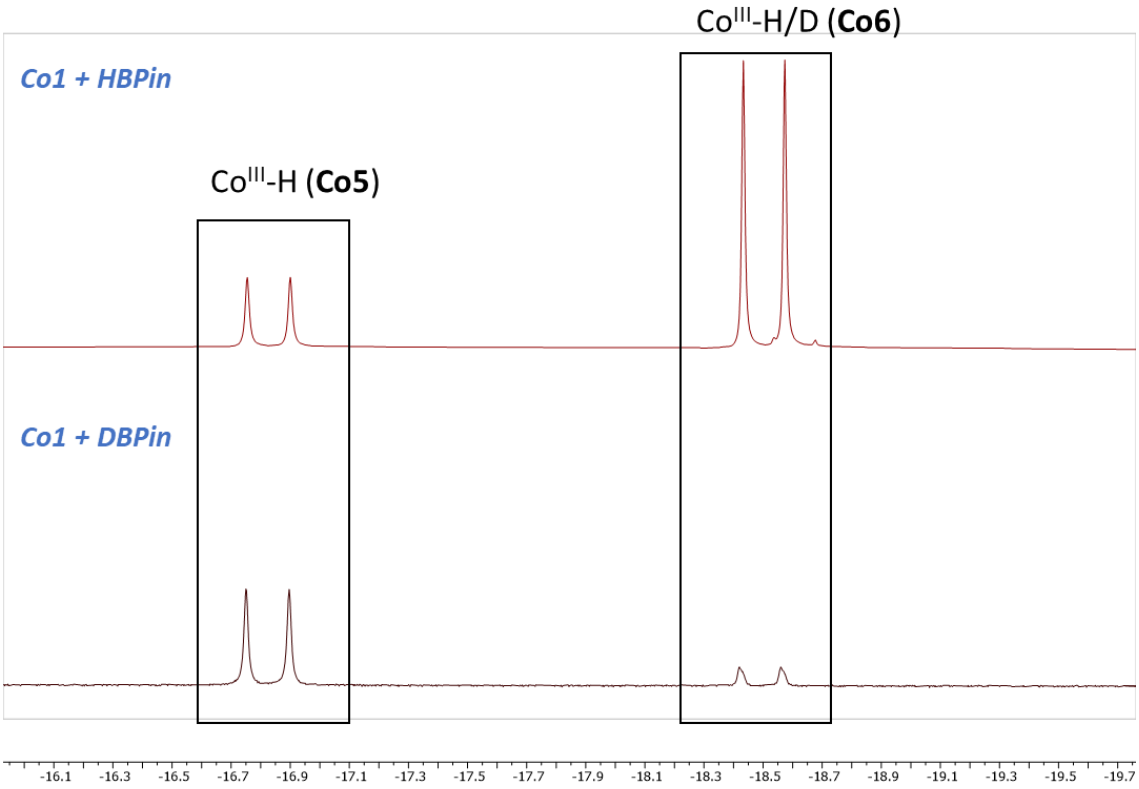

Figure 5.18. The upfield region of ^{1}H NMR spectrum of the reaction mixture of **Co1** and HBpin (top); **Co1** and DBpin (bottom).

5.6.5. NMR Spectra

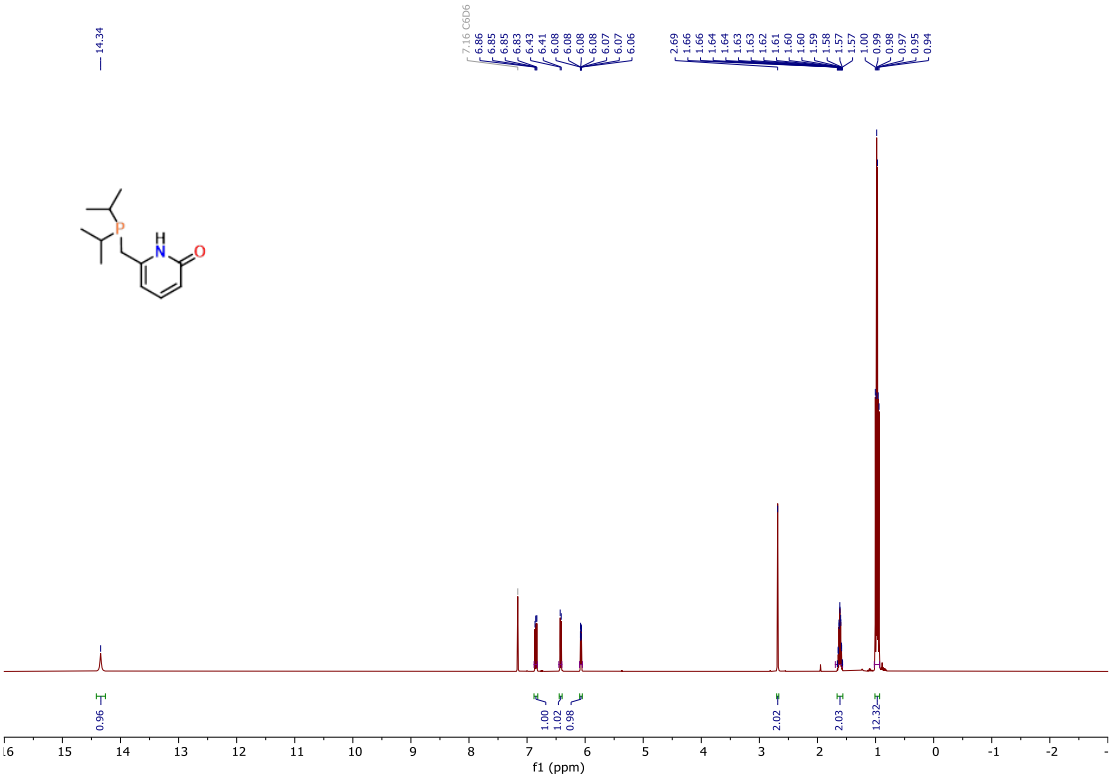

Figure 5.19. ^{1}H NMR spectrum (500.1 MHz, C_6D_6) of **L1H**.

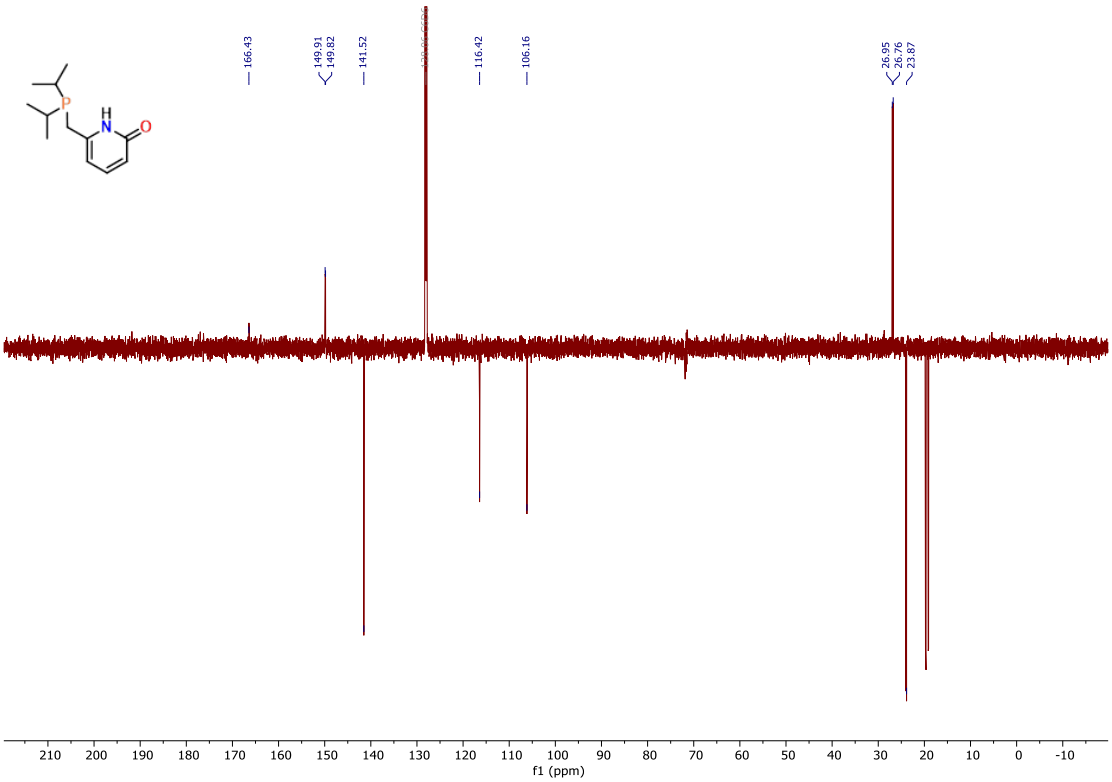

Figure 5.20. ^{13}C-DEPTQ NMR spectrum of (125.8 MHz, C_6D_6) of **L1H**.

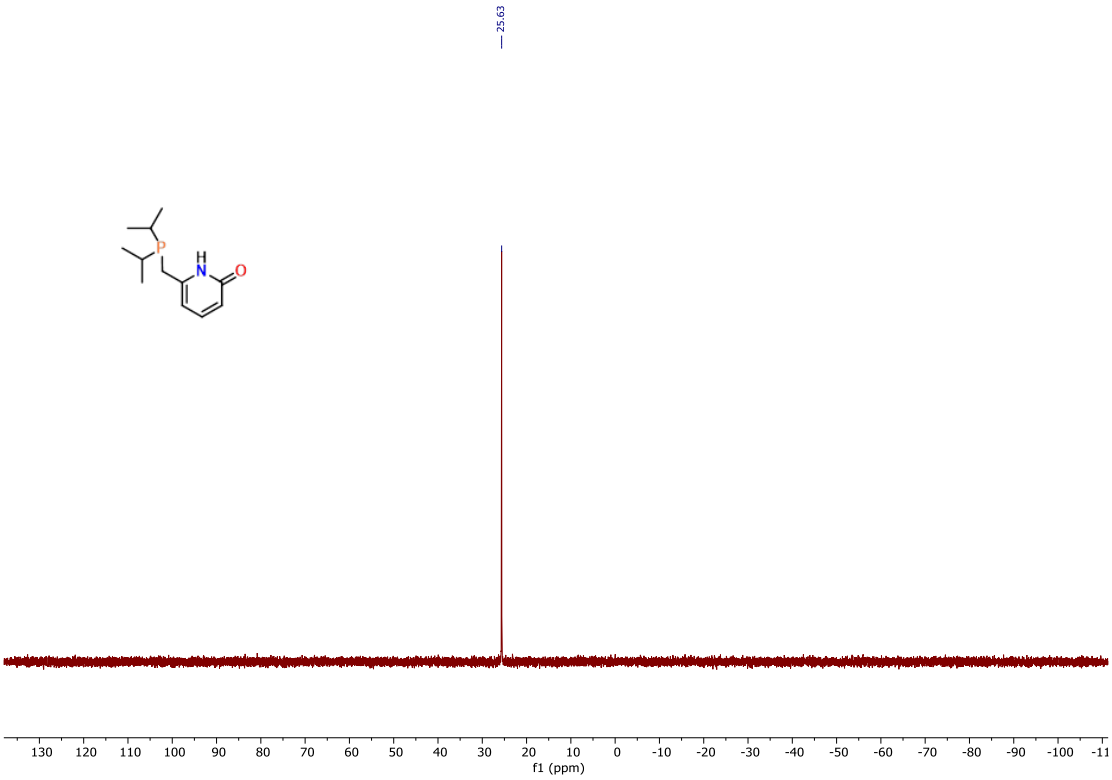

Figure 5.21. $^{31}P\{^{1}H\}$-NMR (202.5 MHz, C_6D_6) of **L1H**.

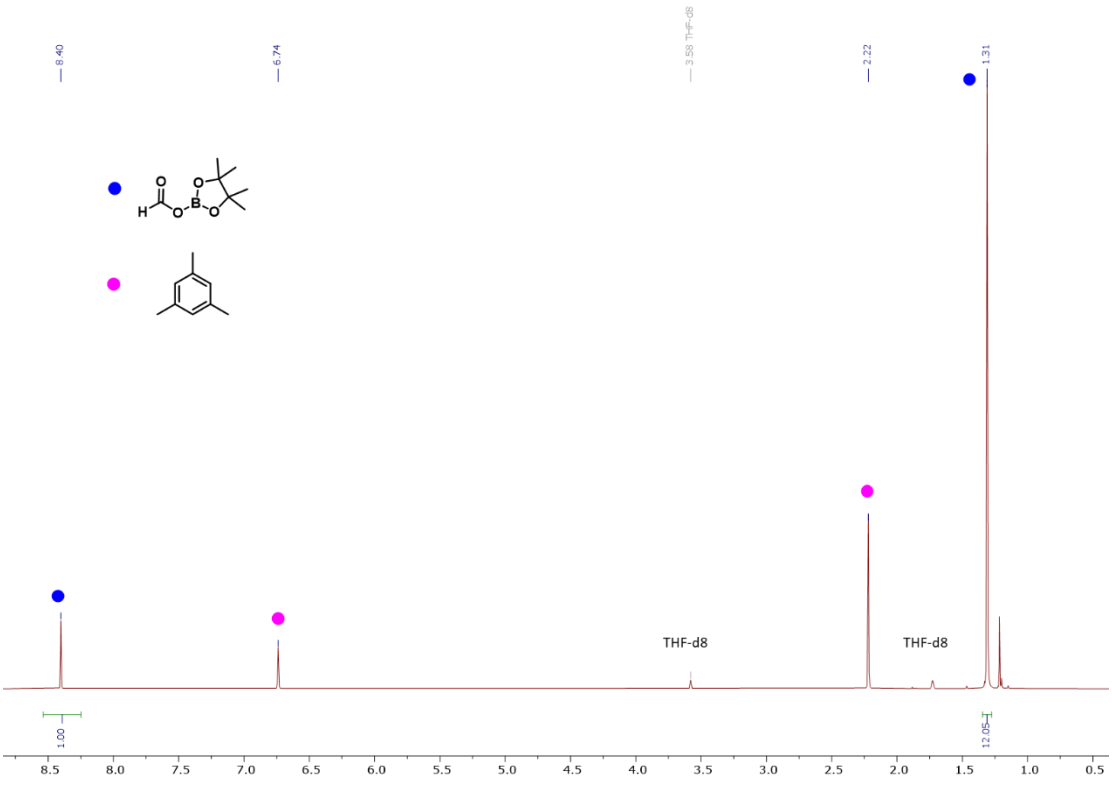

Figure 5.22. ^{1}H NMR spectrum (400 MHz, THF-d_8) of the crude product mixture of CO_2 hydroboration (see Table 5.1, entry 1).

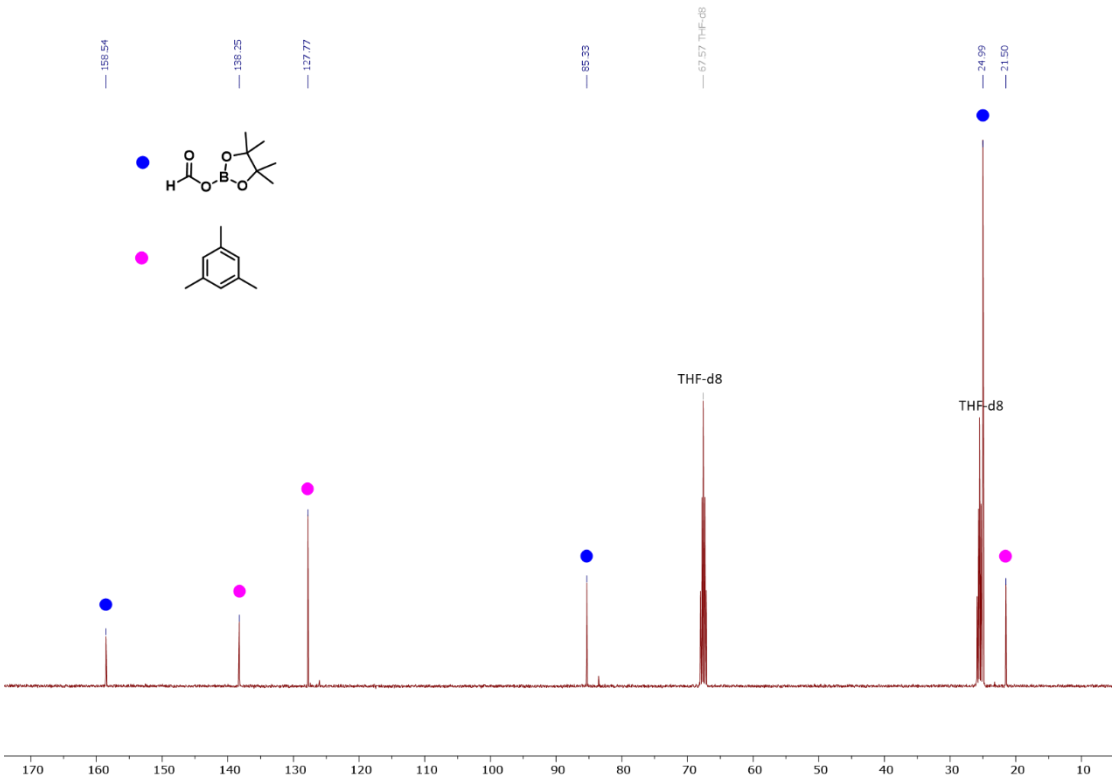

Figure 5.23. ^{13}C NMR spectrum (400 MHz, THF-d_8) of the crude product mixture of CO_2 hydroboration (see Table 5.1, entry 1).

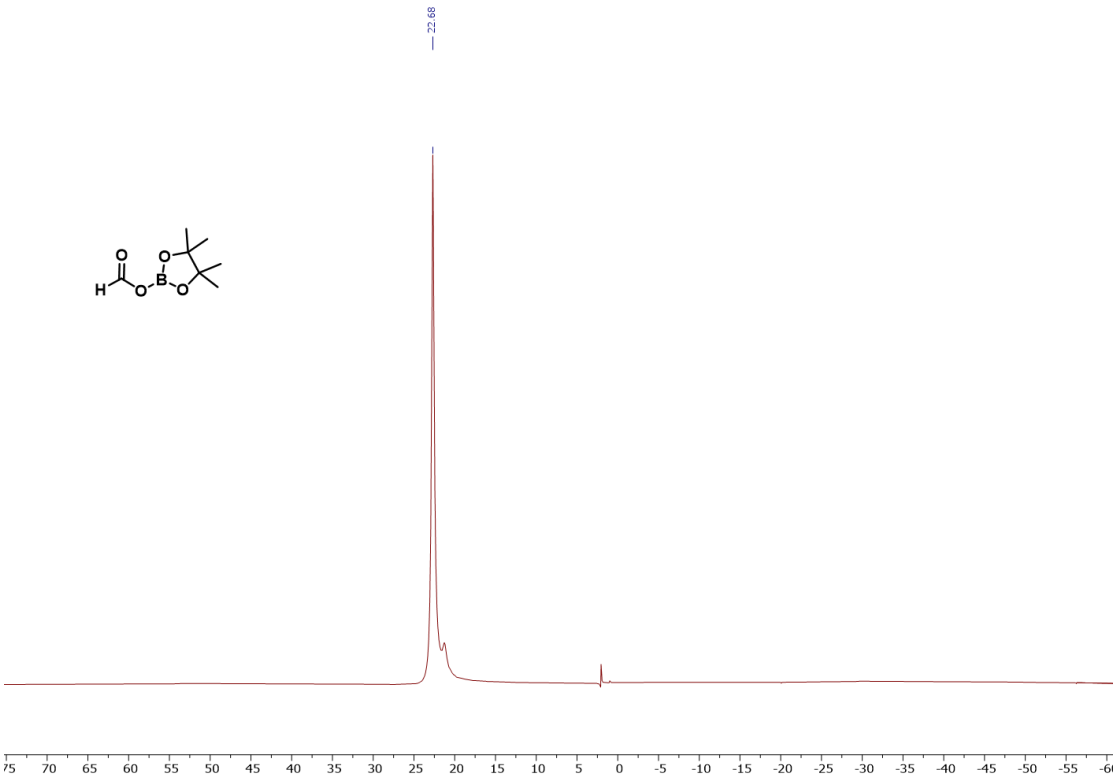

Figure 5.24. ^{11}B NMR spectrum (400 MHz, THF-d_8) of the crude product mixture of CO_2 hydroboration (see Table 5.1, entry 1).

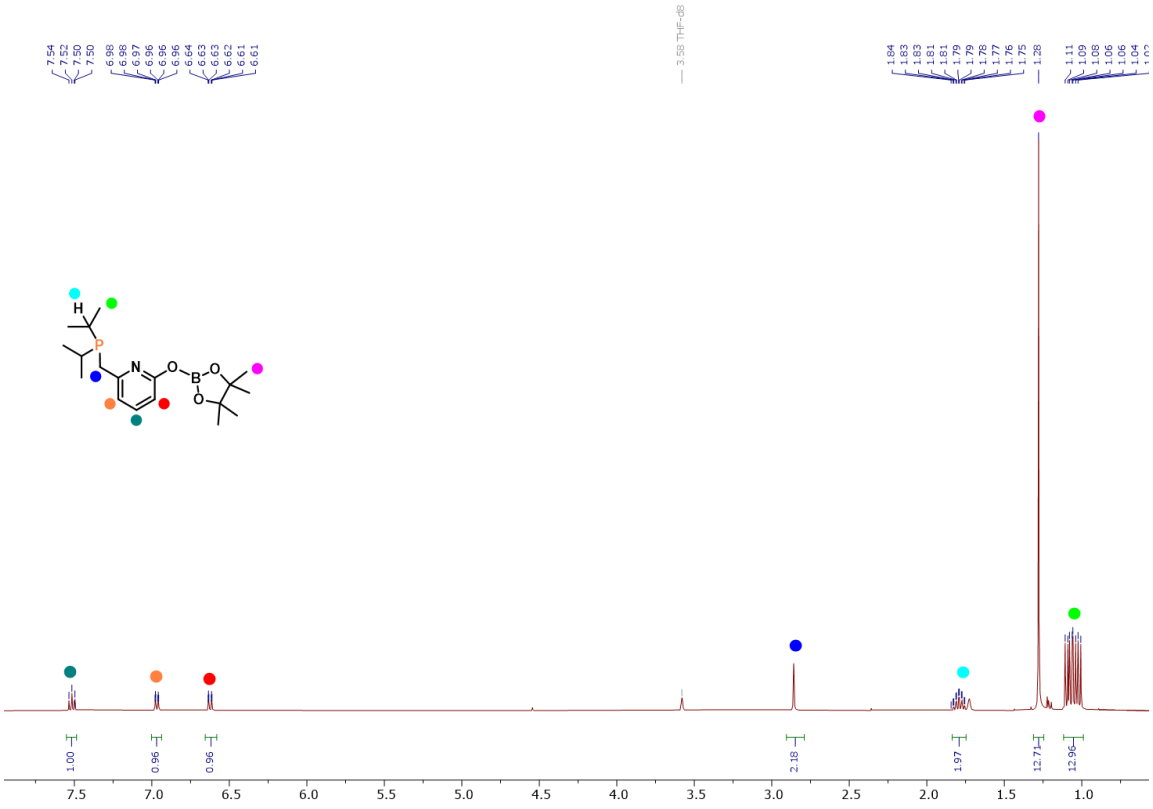

Figure 5.25. ^{1}H NMR spectrum (400 MHz, THF-d_8) of *in situ* generated **L1Bpin**.

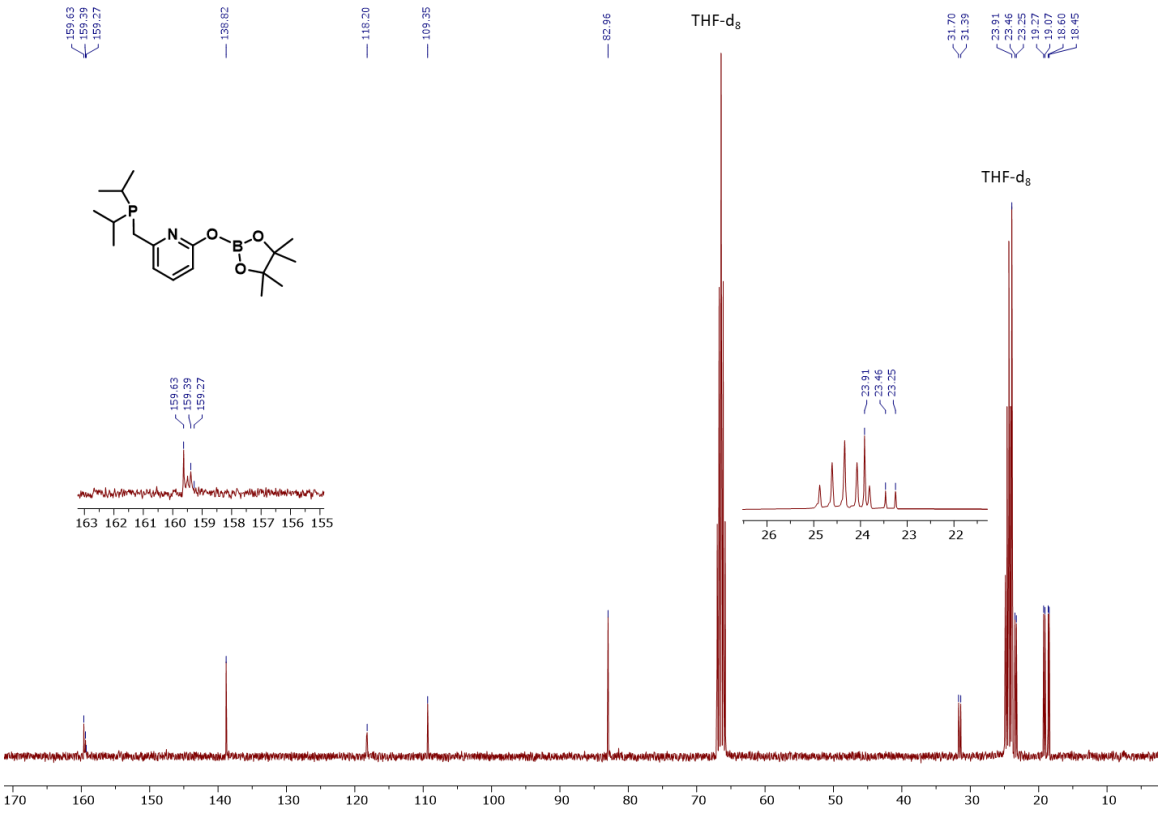

Figure 5.26. ^{13}C NMR spectrum (300 MHz, THF-d_8) of *in situ* generated **L1Bpin**.

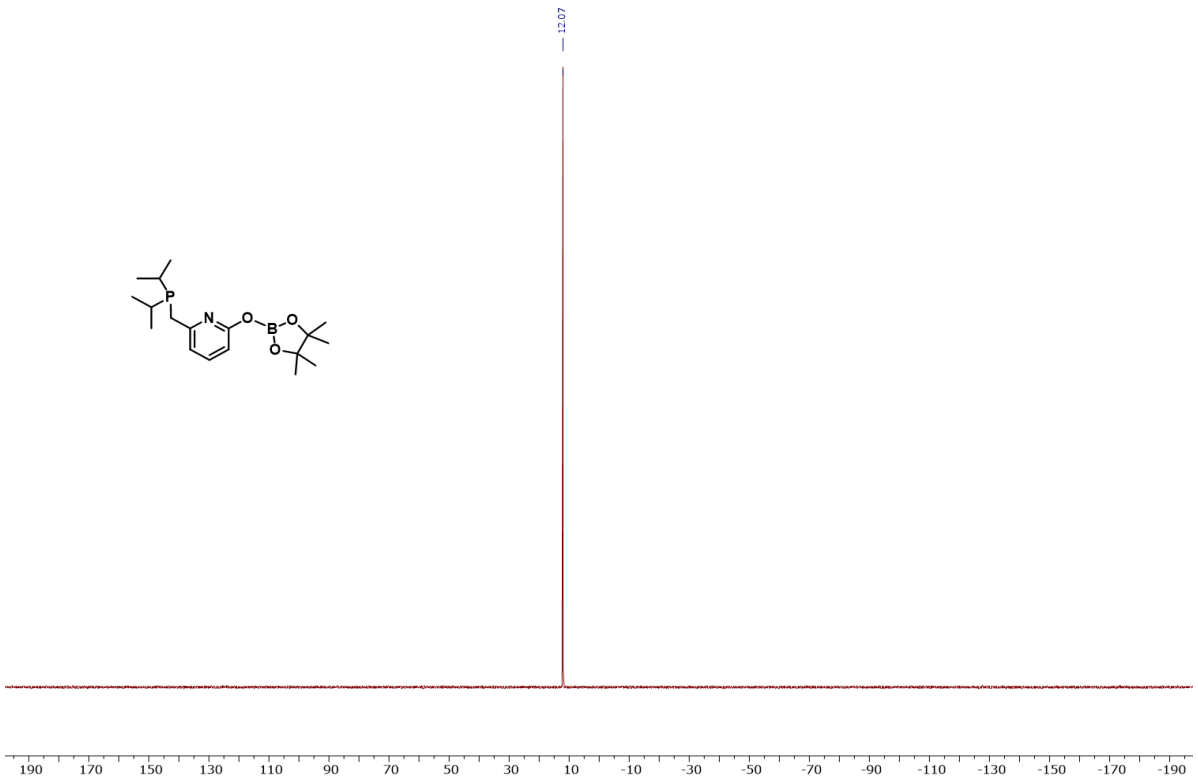

Figure 5.27. ^{31}P NMR spectrum (162 MHz, THF-d_8) of *in situ* generated **L1Bpin**.

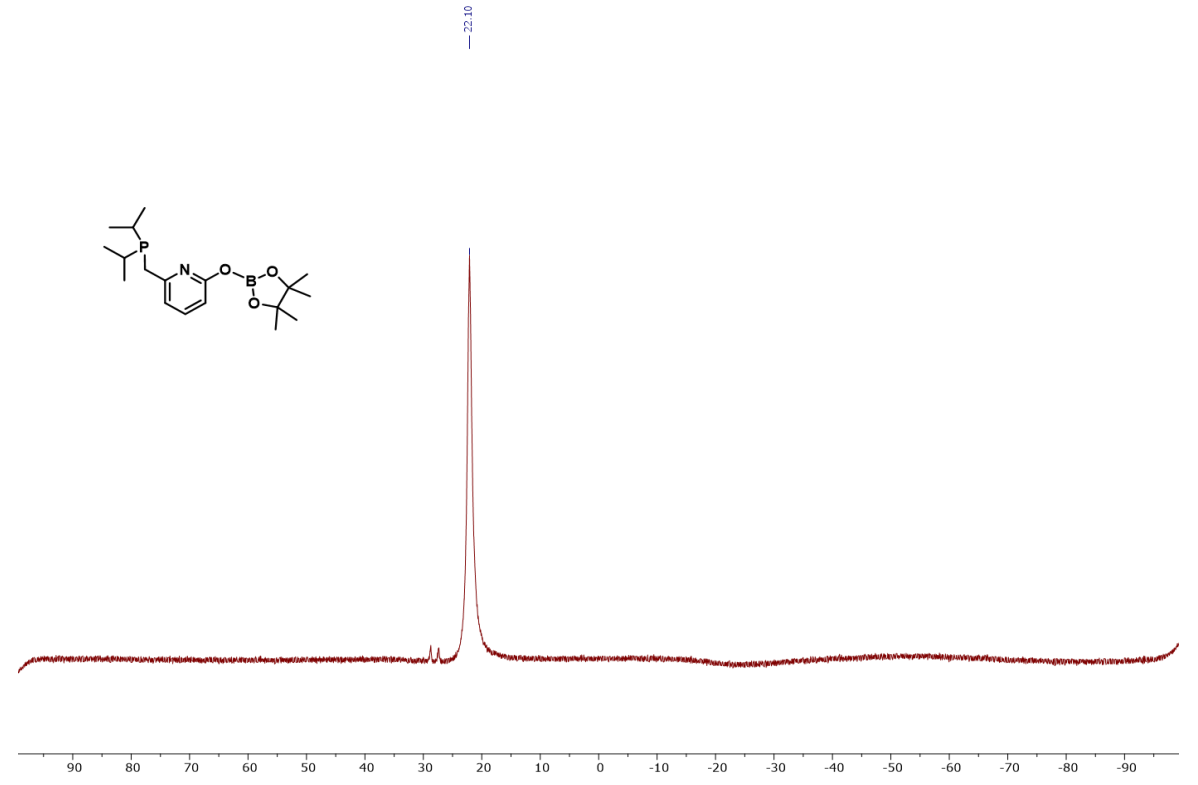

Figure 5.28. ^{1}H NMR spectrum (128 MHz, THF-d_8) of *in situ* generated **L1Bpin**.

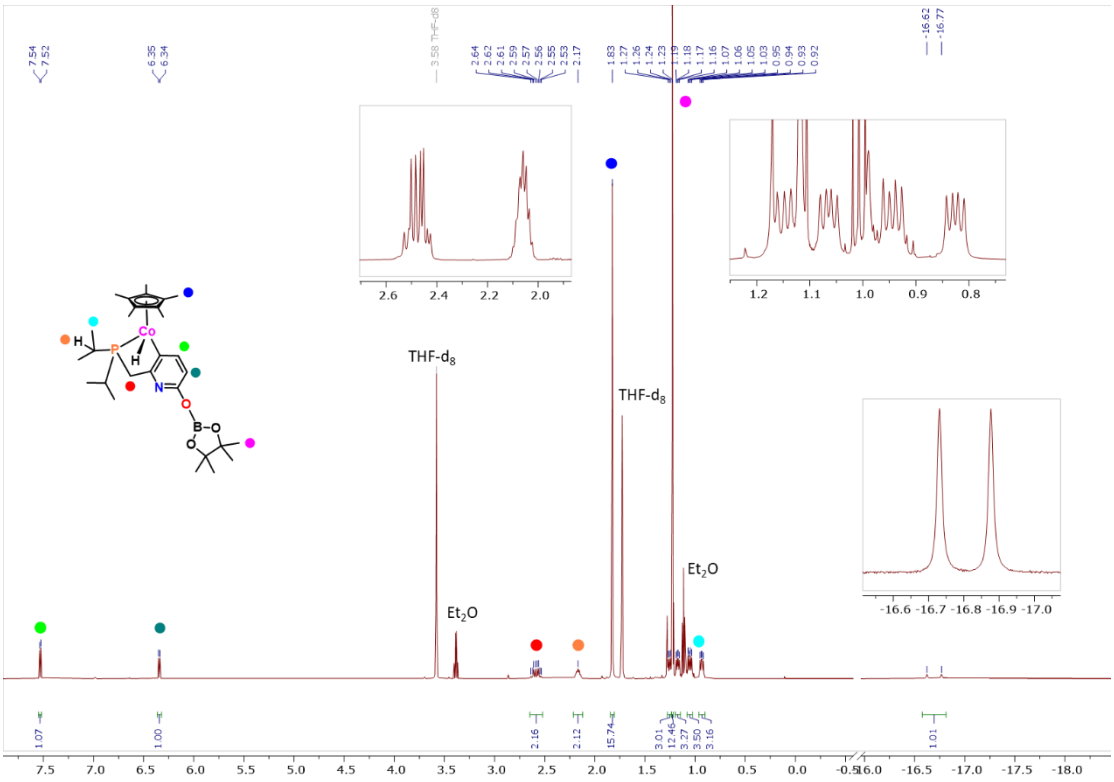

Figure 5.29. ^{1}H NMR spectrum (600 MHz, THF-d_8) of **Co5**.

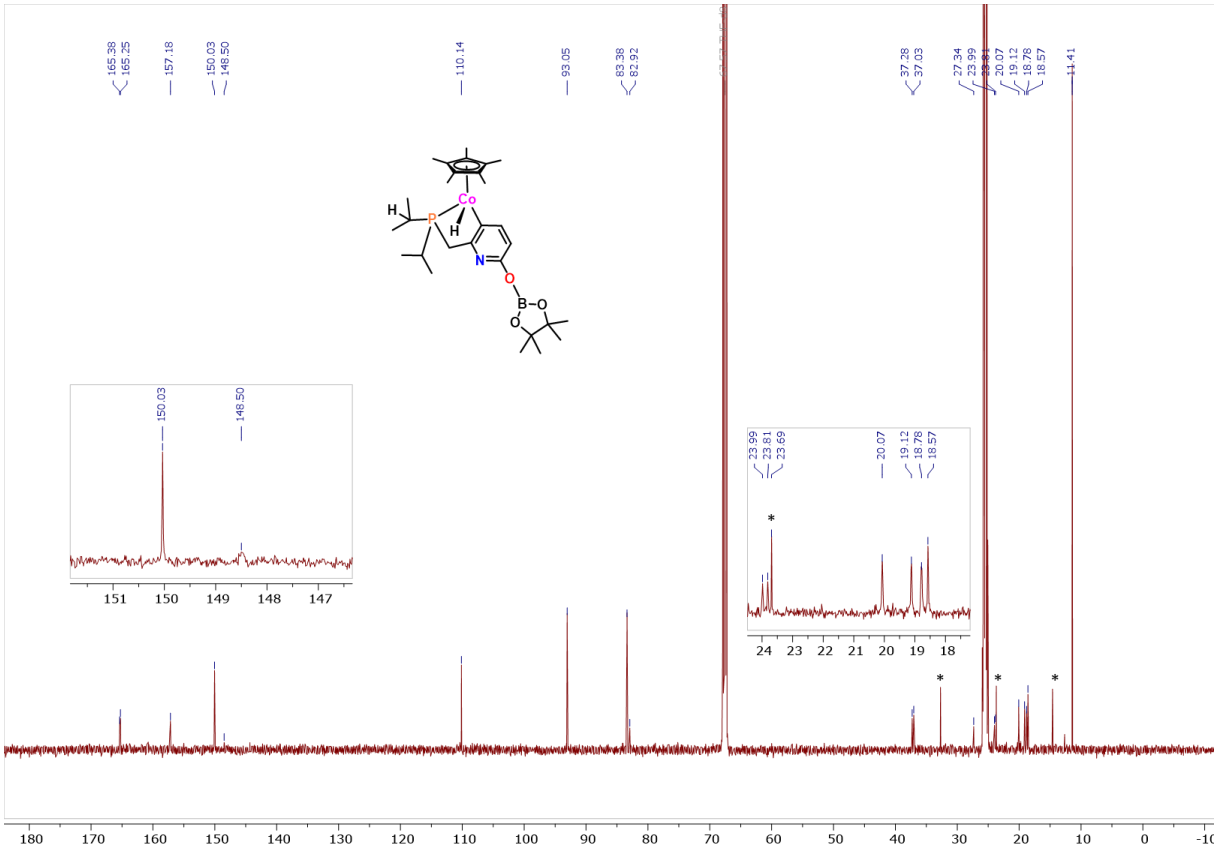

Figure 5.30. ^{13}C NMR spectrum (151 MHz, THF-d_8) of **Co5**. Asterisk denotes residual hexane.

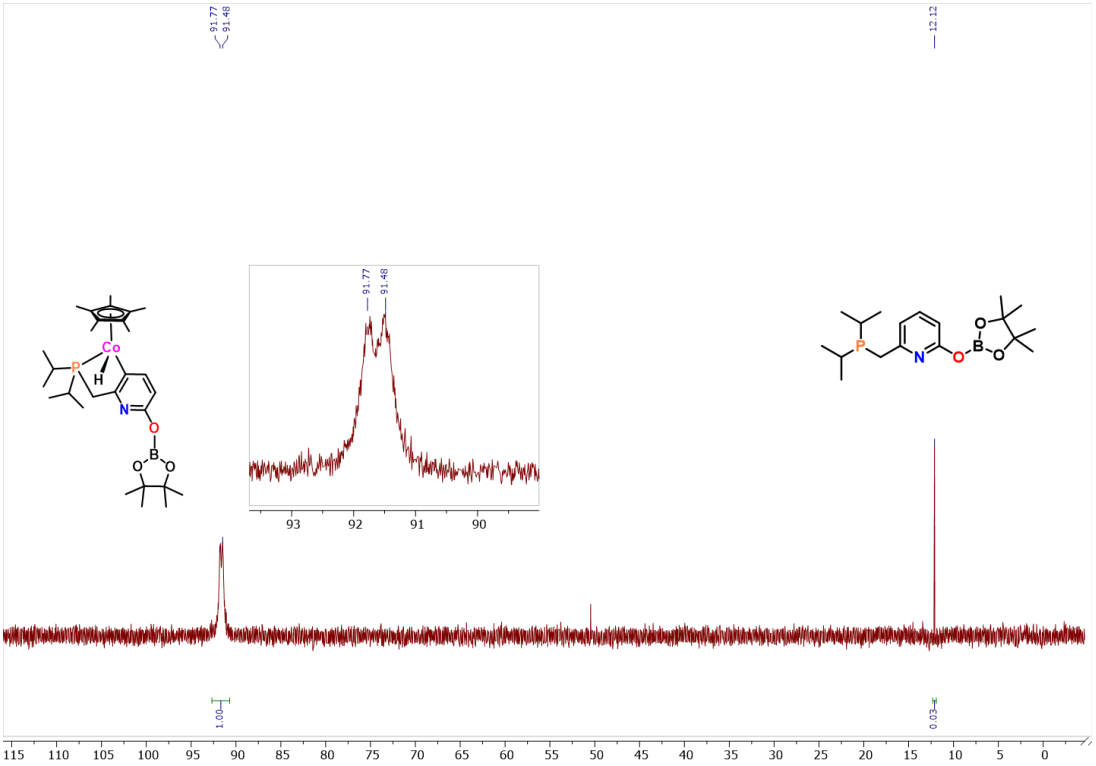

Figure 5.31. ^{31}P NMR spectrum (243 MHz, THF-d_8) of **Co5**.

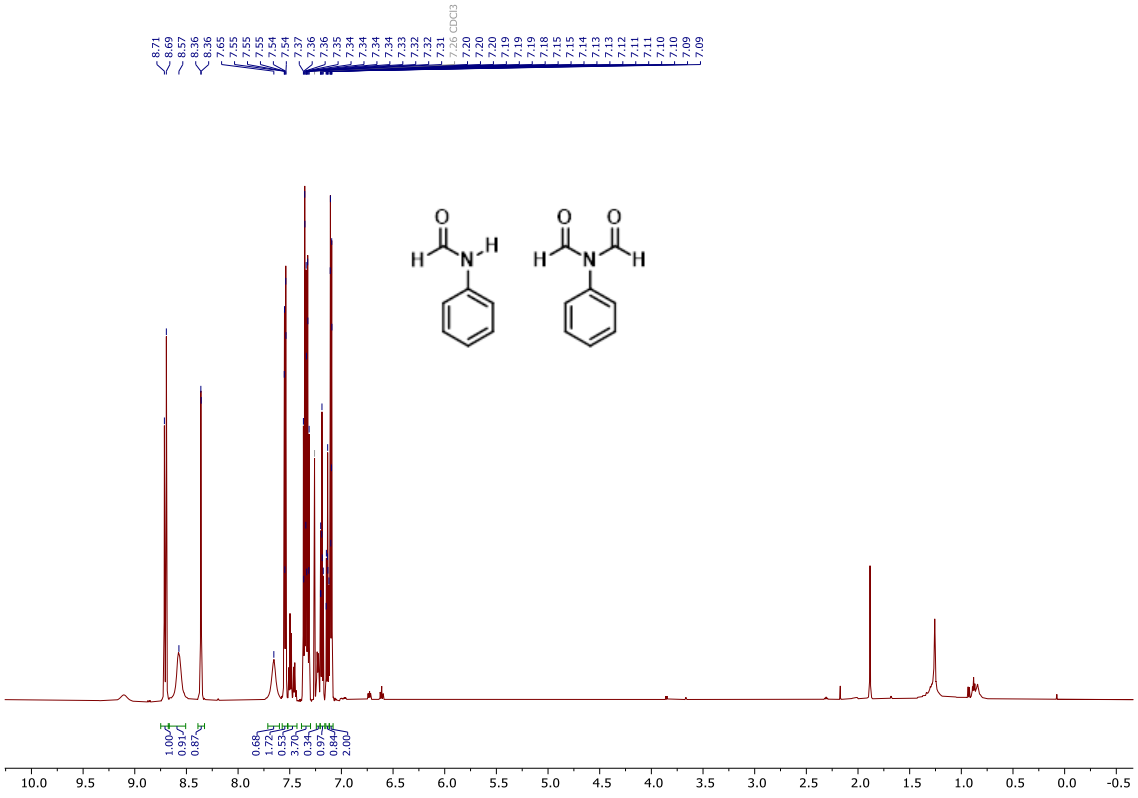

Figure 5.32. ^{1}H NMR spectrum (600 MHz, THF-d_8) of aniline N-formylation products (full window).

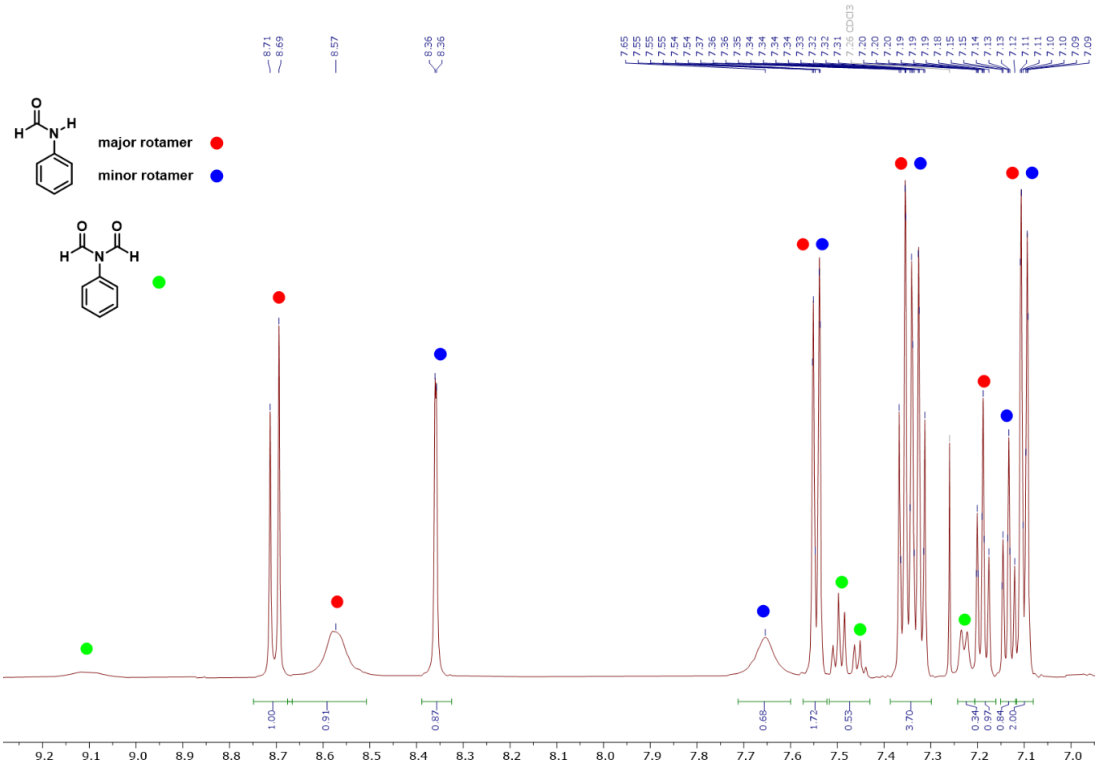

Figure 5.33. ^{1}H NMR (600 MHz, THF-d_8) spectrum of N-formylation products.

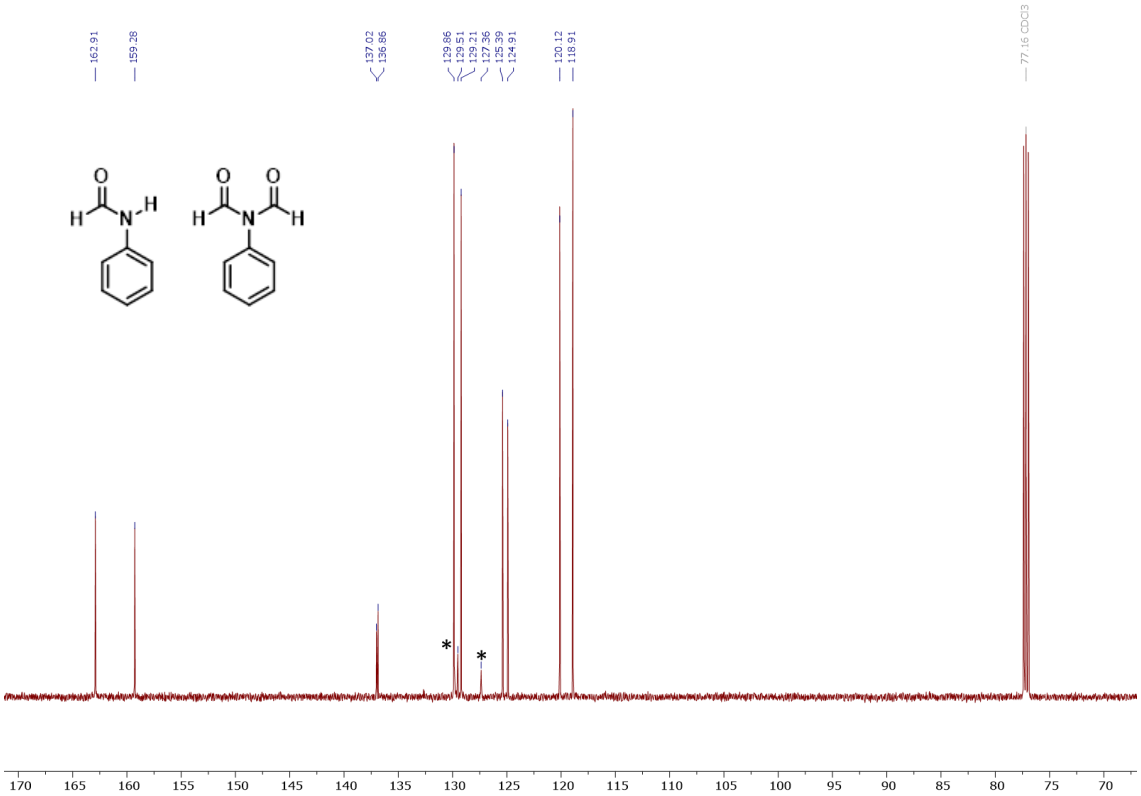

Figure 5.34. ^{1}H NMR (75 MHz, THF-d_8) spectrum of N-formylation products. Asterisks denotes signals that belong to N-formyl-N-phenylformamide.

5.6.6. IR-ATR Spectra

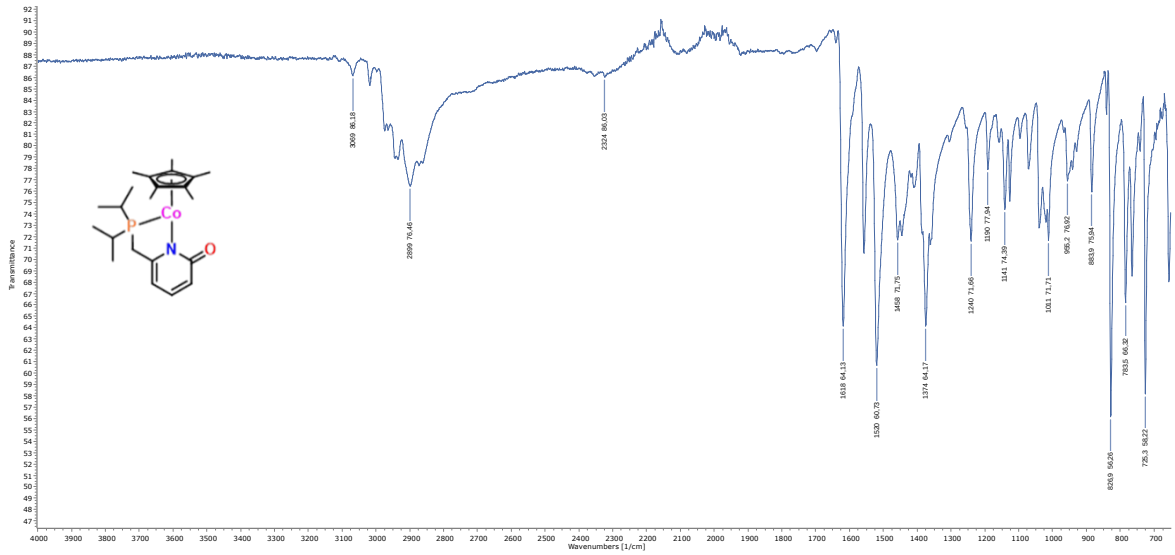

Figure 5.35. Transmission IR-ATR spectrum of **Co1**

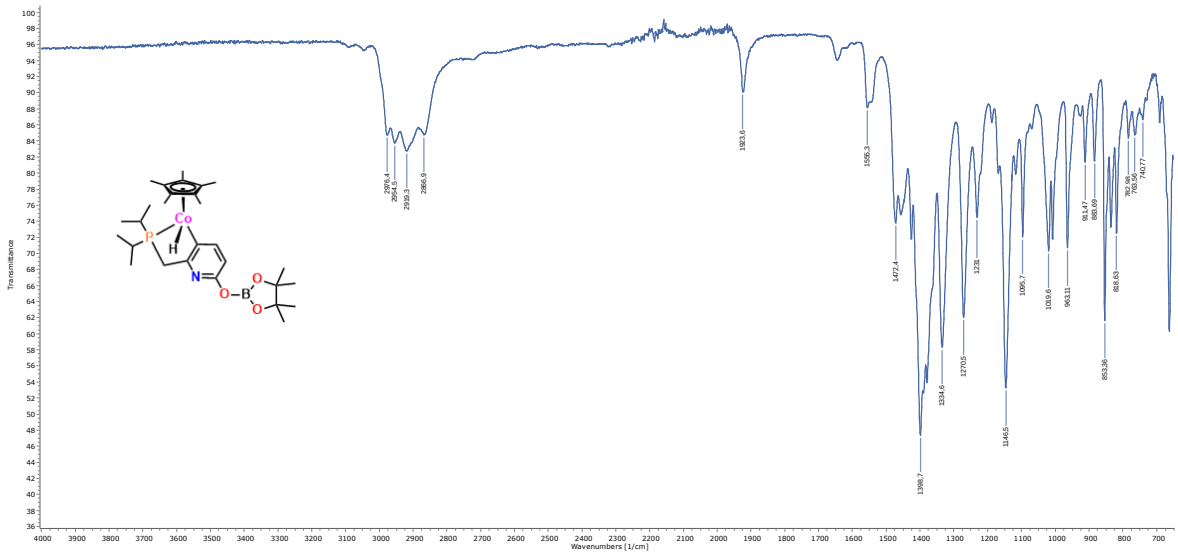

Figure 5.36. Transmission IR-ATR spectrum of **Co5**

5.6.7. ESI-MS Analysis

Sample preparation: crystalline sample of **Co1** was dissolved in THF and directly subjected to ESI-MS analysis; the mixture of **Co1** and HBpin (1.2 equiv.) was prepared *in situ* in THF at room temperature and directy subjected to ESI-MS analysis.
Sample solutions were transferred into a gas-tight syringe and fed into the ESI source of a micrOTOF-Q II mass spectrometer (Bruker Daltonik) at a flow rate of 0.5 mL h^{-1}. The ESI source was operated at a voltage of 4500 V with N_2 as nebulizer (8.0 psi backing pressure) and drying gas (heated to 333 K and held at 3.0 L min^{-1} flow rate). The thus produced ions with 50 ≤ m/z ≤ 3000 were then allowed to pass the instrument's quadrupole mass filter and collision cell before entering the time-of-flight (TOF) mass analyzer. Ions were identified on the basis of their *m/z* ratio, their isotope pattern, and fragmentation patterns.

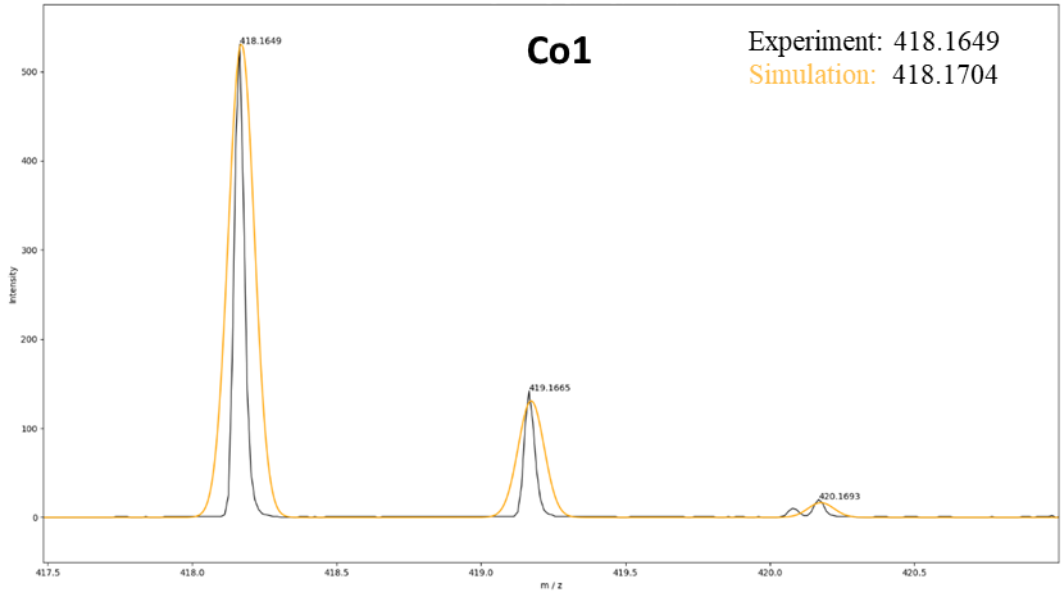

Figure 5.37. Fragment of positive-ion mode ESI mass spectrum of **Co1** in THF. Measured and simulated isotopic patterns depicted in black and orange respectively.

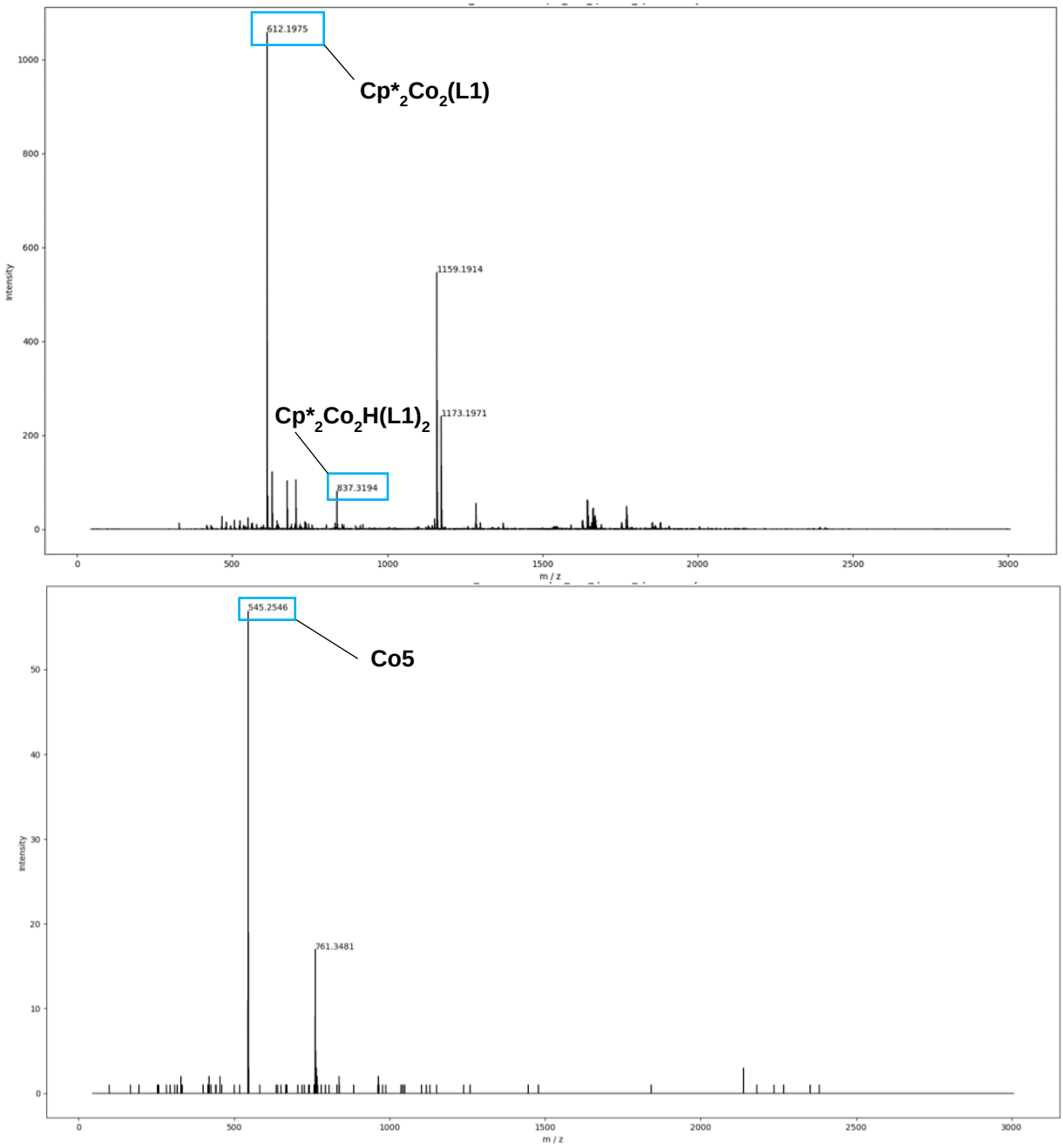

Figure 5.38. Positive-ion mode ESI mass spectra of a solution of the products formed in the reaction of **Co1** with HBpin (1.2 equiv.) in THF.

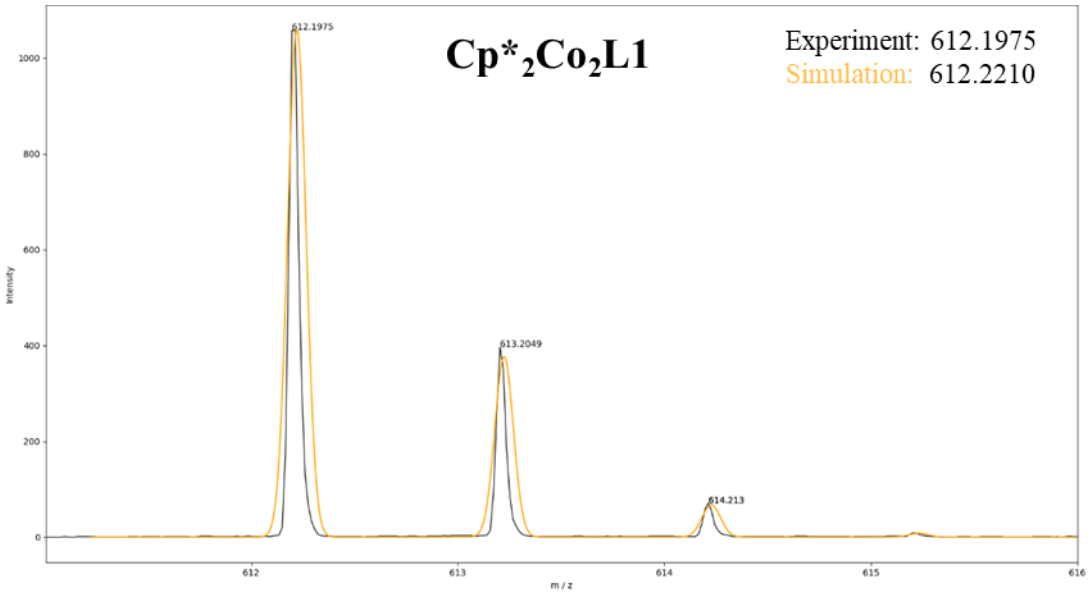

Figure 5.39. Measured (black) and simulated (orange) isotopic patterns of *in situ* generated Cp*$_2$Co$_2$(L1).

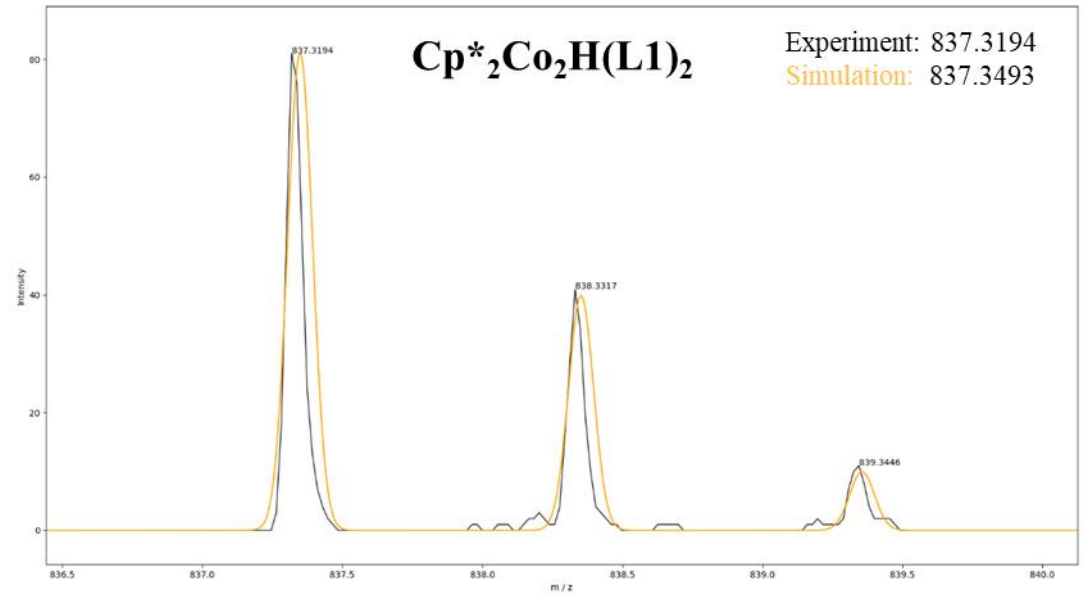

Figure 5.40. Measured (black) and simulated (orange) isotopic patterns of *in situ* generated Cp*$_2$Co$_2$H(L1)$_2$.

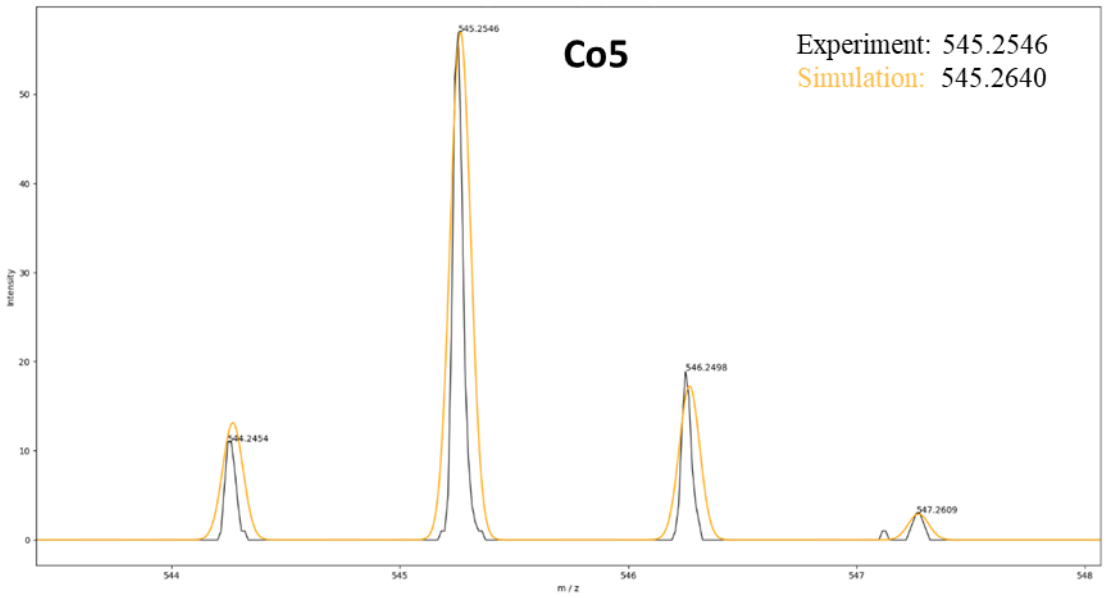

Figure 5.41. Measured (black) and simulated (orange) isotopic patterns of *in situ* generated **Co5**.

5.6.8. X-ray Crystallography

Single-crystal X-ray experiments were performed at 100 K using a SuperNova four-circle diffractometer in Kappa geometry with a 50 W Cu or Mo (Kα radiation) microfocus tube, an Atlas CCD detector (Rigaku Oxford Diffraction), and a Cryostream 700 Plus cooler (Oxford Cryosystems Ltd). Data collection, cell refinement, data reduction, and absorption correction were done using CrysAlisPro[20]. Intensities were measured using omega scans.

Single-crystal X-ray data was solved and refined as follows: The space group was determined either by using XPREP (Bruker AXS Inc.[21]) or CrysAlisPro and the phase problem was solved either (a) by structure-invariant direct methods with SHELXS[22], or (b) by using the dual-space algorithm implemented in SHELXT[23]. In every case, full-matrix least-squares refinement was done on F^2 using SHELXL[23].

Missing secondary atom sites were located from the difference Fourier map. If possible, non-hydrogen atoms were refined using individual, anisotropic displacement parameters. The fully refined data was reviewed using PLATON[24]. Carbon atom-bound hydrogen atoms were positioned geometrically and refined riding on their respective parent atoms. U_{iso}(H) was fixed at 1.5 (CH_3) or 1.2 (all other H atoms) of the parent atom's isotropic displacement parameter.

Table 5.1. Crystal data and structure refinement for **Co1**.

Identification code	Co1
Empirical formula	$C_{22}H_{34}CoNOP$
Formula weight	418.40
Temperature/K	99.99(10)
Crystal system	orthorhombic
Space group	$Pna2_1$
a/Å	14.8126(2)
b/Å	10.46320(10)
c/Å	13.4959(2)
α/°	90
β/°	90
γ/°	90
Volume/Å^3	2091.69(5)
Z	4
ρ_{calc}g/cm^3	1.329
μ/mm^{-1}	0.908
F(000)	892.0
Crystal size/mm^3	0.32 × 0.25 × 0.2
Radiation	Mo Kα (λ = 0.71073)
2Θ range for data collection/°	6.038 to 59.16
Reflections collected	88285
Independent reflections	5666 [R_{int} = 0.0366, R_{sigma} = 0.0142]
Data/restraints/parameters	5666/1/244
Goodness-of-fit on F^2	1.050
Final R indexes [I>=2σ (I)]	R_1 = 0.0179, wR_2 = 0.0473
Final R indexes [all data]	R_1 = 0.0183, wR_2 = 0.0475
Largest diff. peak/hole / e Å^{-3}	0.25/-0.20
Flack parameter	-0.003(2)

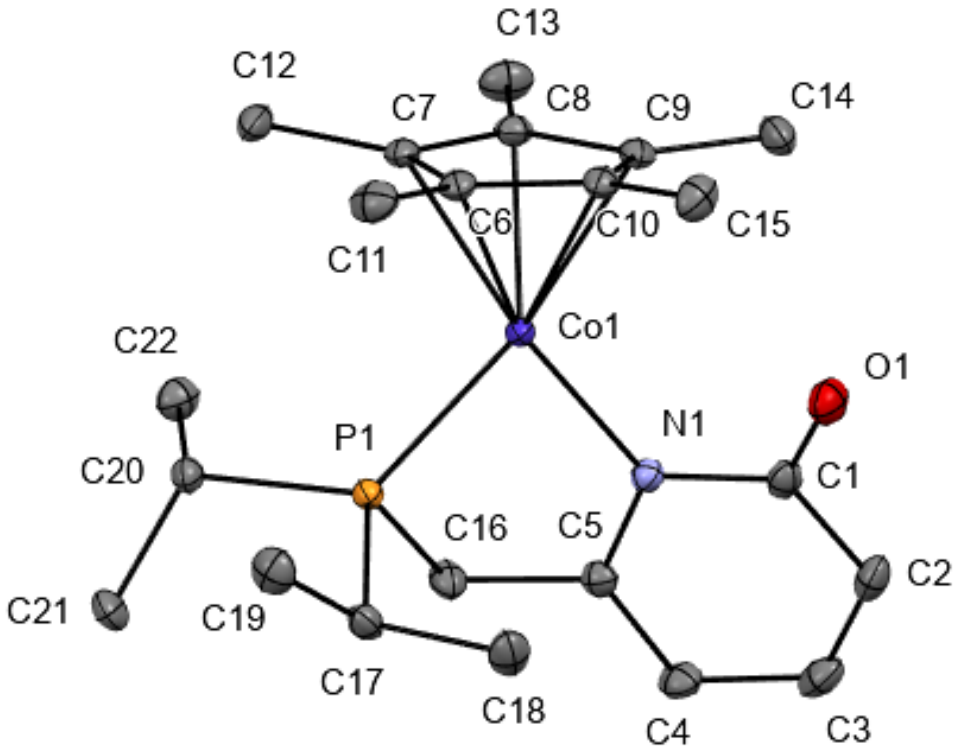

Figure 5.42. The molecular structure of **Co1.** Ellipsoids are shown at 50% probability. Hydrogen atoms are omitted for clarity.

Table 5.2. Crystal data and structure refinement for **Co5**.

Identification code	Co5
Empirical formula	$C_{28}H_{46}BCoNO_3P$
Formula weight	545.37
Temperature/K	99.97(13)
Crystal system	triclinic
Space group	P-1
a/Å	8.5688(5)
b/Å	12.8423(5)
c/Å	13.3857(5)
α/°	100.810(3)
β/°	95.593(4)
γ/°	92.022(4)
Volume/Å^3	1437.81(12)
Z	2
ρ_{calc}g/cm^3	1.260
μ/mm^{-1}	5.418
F(000)	584.0
Crystal size/mm^3	0.24 × 0.14 × 0.08
Radiation	CuKα (λ = 1.54184)
2Θ range for data collection/°	6.76 to 153.768
Reflections collected	28557
Independent reflections	5969 [R_{int} = 0.0465, R_{sigma} = 0.0310]
Data/restraints/parameters	5969/0/325
Goodness-of-fit on F^2	1.112
Final R indexes [I>=2σ (I)]	R_1 = 0.0561, wR_2 = 0.1494
Final R indexes [all data]	R_1 = 0.0611, wR_2 = 0.1588

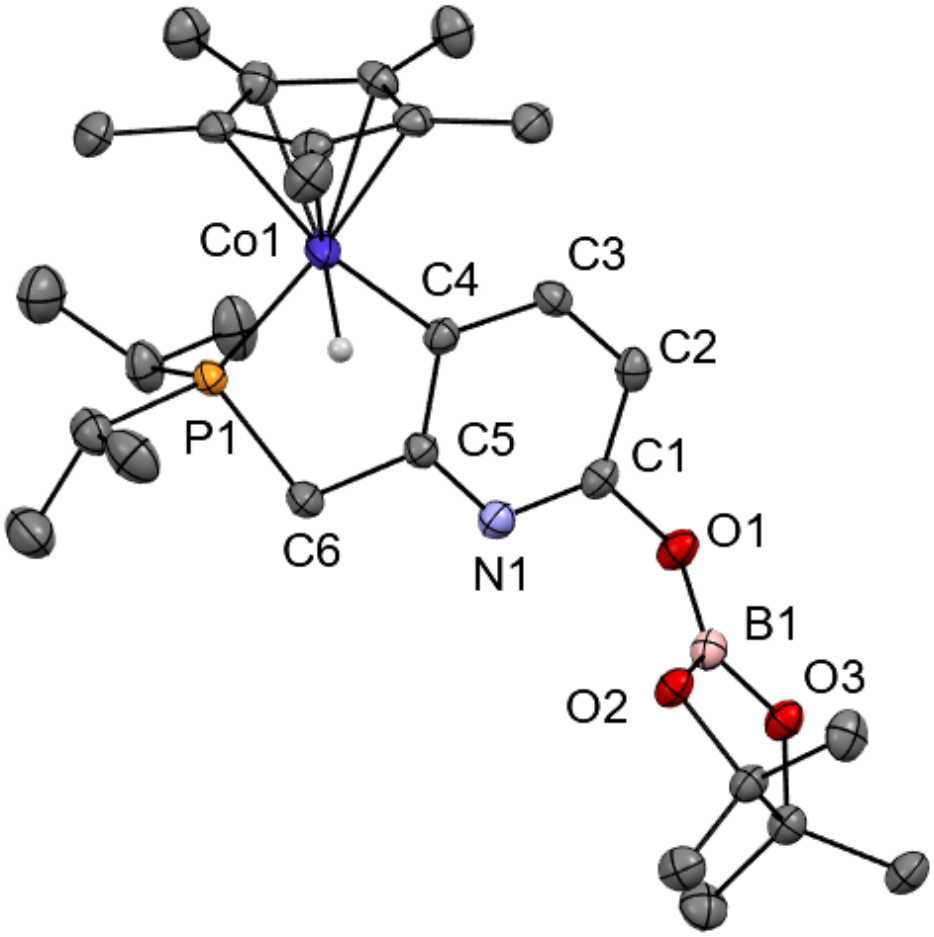

Figure 5.43. The molecular structure of **Co5.** Ellipsoids are shown at 50% probability. Hydrogen atoms are omitted for clarity (except of Co-H).

5.6.9. Magnetic Measurements

Magnetic measurements for complex **Co1** were carried out with a Quantum-Design MPMS3 SQUID magnetometer equipped with a 7.0 T magnet. Direct current (dc) magnetic susceptibility measurements were performed under an applied dc field of 0.5 T with powdered polycrystalline samples packed in polycarbonate in a non-magnetic sample holder and covered with low viscosity perfluoropolyether-based inert oil Fomblin Y45 in the range from 200.0 K to 2.0 K (the upper temperature limit was chosen because of the pour point of the oil). The oil was dried under vacuum and degassed prior to use. Sample preparation was performed inside a glove box under N_2 atmosphere. Each raw data of the measured magnetic moment was corrected for the diamagnetic contribution of the capsules according to M_{dia}(capsule) = $\chi_g \cdot m \cdot H$, with an experimentally obtained gram susceptibility of the capsules including the inert oil. The diamagnetic contribution of the compounds was corrected using Pascal's constants. Alternating current (ac) susceptibility measurements were carried out in an oscillating ac field of 3.0 Oe and frequencies ranging from 0.1 to 1000 Hz.

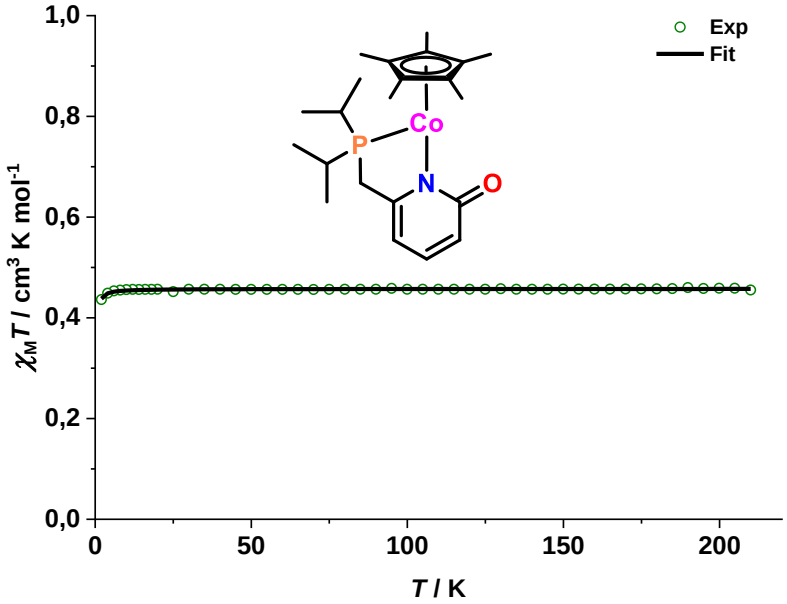

Figure 5.44. Temperature dependence of $\chi_M T$ product for the mononuclear Co(II) complex measured under an applied dc field of 0.5 T

Low-spin Co(II) complex, S = ½, g = 2.21, θ = - 0.07 K (intermolecular interaction), TIP = 157 x 10^{-6} cm^3 mol^{-1}

5.6.10. Literature Overview of Catalysts and Reaction Conditions in Hydroboration of CO_2

Table 5.3. Overview of literature-reported catalysts and reaction conditions in the hydroboration of CO_2 to the formate level.

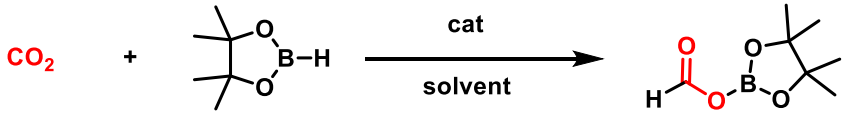

Entry	Catalyst	cat. loading (mol%)	Solvent	Temp °C	Time	Additives	Yield	Best TON/TOF(h^{-1})	Ref
1	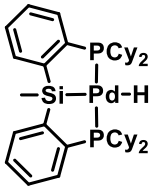	0.01	C_6D_6	rt	1 h	none	85	8500/8500	[11]
		0.001	C_6D_6	rt	120 h	none	64	63500/530	
2	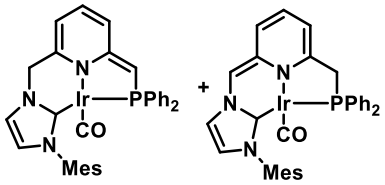	0.1	THF-d_8	30	1 h	H_2O (3 mol%)	74	740/740	[12]
		0.2	THF-d_8	30	20 min	H_2O (7 mol%)	83	415/1245	
3	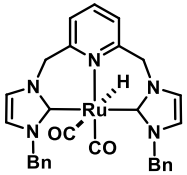	1.0	CH_2Cl_2	rt	30 min	KO^tBu (2.5mol%)	70	70/140	[13]
		1.0	CH_2Cl_2	rt	30 min	$KOCO_2{}^tBu$ (2.5 mol%)	76	76/152	

Entry	Catalyst	cat. loading (mol%)	Solvent	Temp °C	Time	Additives	Yield	Best TON/TOF(h^{-1})	Ref
4*	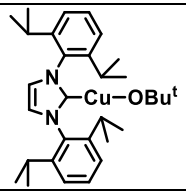	10	THF	35	24 h	none	85	8.5/0.4	[14]
5	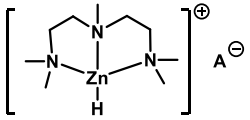 A = $[B(C_6F_5)_4]$ or $[B(3,5\text{-}Me_2\text{-}C_6H_3)_4]$	1.0	CH_3CN-d_3	60	2 h	none	94	94/42	[15]
6	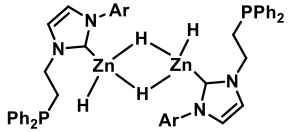 Ar = DIPP	5.0	C_6D_6	rt	12 h	none	85	17/1.4	[16]
7	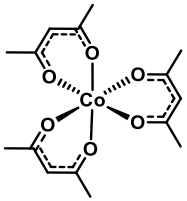	1.0	THF-d_8	50	16 h	$NaHBEt_3$ (1.0 mol%)	27	27/1.7	[6]
8	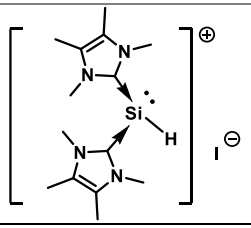	10.0	C_6D_6	90	10 min	none	98	9.8/58.8	[17]

Entry	Catalyst	cat. loading (mol%)	Solvent	Temp °C	Time	Additives	Yield	Best TON/TOF(h^{-1})	Ref
9	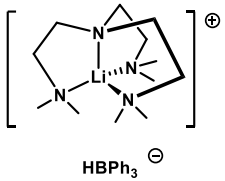	1.0	THF-d_8	25	10 h	none	100	100/10	[18]
10	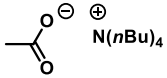	5.0	C_6D_6	90	2 h	none	62	12.4/6.2	[19]

* yield of formic acid after hydrolysis

5.6.11. References

[1] S. D. Toto, J. T. Doi, *J. Org. Chem.* **1987**, *52*, 4999–5003.

[2] F. Jiang, M. Achard, T. Roisnel, V. Dorcet, C. Bruneau, *Eur. J. Inorg. Chem.* **2015**, *2015*, 4312–4317.

[3] U. Kölle, F. Khouzami, B. Fuss, *Angew. Chemie Int. Ed.* **1982**, *21*, 230–240.

[4] X. Zhuang, J. Y. Chen, Z. Yang, M. Jia, C. Wu, R. Z. Liao, C. H. Tung, W. Wang, *Organometallics* **2019**, *38*, 3752–3759.

[5] S. K. Sur, *J. Magn. Reson.* **1989**, *82*, 169–173.

[6] S. R. Tamang, M. Findlater, *Dalton Trans.* **2018**, *47*, 8199–8203.

[7] C. Erken, A. Kaithal, S. Sen, T. Weyhermüller, M. Hölscher, C. Werlé, W. Leitner, *Nat. Commun.* **2018**, *9*, 1–9.

[8] X.-T. Lin, K. Matsumoto, Y. Maegawa, K. Takeuchi, N. Fukaya, K. Sato, S. Inagaki, J.-C. Choi, *New J. Chem.* **2021**, *45*, 9501–9505.

[9] P. Nad, K. Gupta, A. Sen, A. Mukherjee, *Chem. – An Asian J.* **2022**, *17*, e202200800.

[10] M. R. I. I. I. Smith, R. Bisht, C. Haldar, G. Pandey, J. E. Dannatt, B. Ghaffari, R. E. J. Maleczka, B. Chattopadhyay, *ACS Catal.* **2018**, *8*, 6216–6223.

[11] H. W. Suh, L. M. Guard, N. Hazari, *Chem. Sci.* **2014**, *5*, 3859–3872.

[12] P. Sánchez, M. Hernández-Juárez, N. Rendón, J. López-Serrano, E. Álvarez, M. Paneque, A. Suárez, *Dalton Trans.* **2018**, *47*, 16766–16776.

[13] C. K. Ng, J. Wu, T. S. A. Hor, H. K. Luo, *Chem. Commun.* **2016**, *52*, 11842–11845.

[14] R. Shintani, K. Nozaki, *Organometallics* **2013**, *32*, 2459–2462.

[15] R. Chambenahalli, R. M. Bhargav, K. N. McCabe, A. P. Andrews, F. Ritter, J. Okuda, L. Maron, A. Venugopal, *Chem. Eur. J.* **2021**, *27*, 7391–7401.

[16] X. Wang, K. Chang, X. Xu, *Dalton Trans.* **2020**, *49*, 7324–7327.

[17] B. X. Leong, J. Lee, Y. Li, M. C. Yang, C. K. Siu, M. Der Su, C. W. So, *J. Am. Chem. Soc.* **2019**, *141*, 17629–17636.

[18] D. Mukherjee, H. Osseili, T. P. Spaniol, J. Okuda, *J. Am. Chem. Soc.* **2016**, *138*, 10790–10793.

[19] Y. C. A. Sokolovicz, O. Nieto Faza, D. Specklin, B. Jacques, C. S. López, J. H. Z. Dos Santos, H. S. Schrekker, S. Dagorne, *Catal. Sci. Technol.* **2020**, *10*, 2407–2414.

[20] Agilent Technologies Ltd, Yarnton, Oxfordshire, England, **2014**.

[21] Bruker AXS Inc., Madison, Wisconsin, USA, **2014**.

[22] G. M. Sheldrick, *Acta Crystallogr. A* **2008**, *64*, 112–122.

[23] G. M. Sheldrick, *Acta Crystallogr. A* **2015**, *71*, 3–8.

[24] A. L. Spek, *Acta Crystallogr. D* **2009**, *65*, 148–55.

6. Synthesis and Catalysis of Anionic Amido Iron(II) Complexes

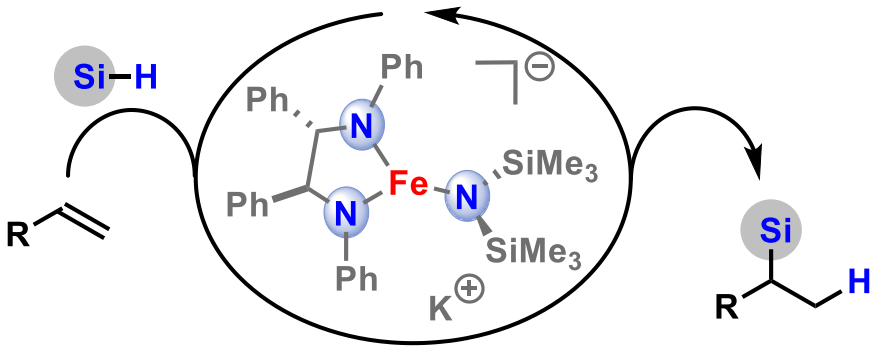

Abstract: Low-coordinate, open-shell 3d metal complexes have attracted great attention due to their critical role in several catalytic transformations but have been notoriously difficult to prepare and study due to their high lability. Here, we report the synthesis of a heteroleptic tri-coordinate amidoferrate that displays high catalytic activity in the regioselective hydrosilylation of alkenes.

[i] Reproduced from Chakraborty, U., Fedulin, A., Jacobi von Wangelin, A.Synthesis and Catalysis of Anionic Amido Iron(II) Complexes., *ChemCatChem*, **2022**, 14 (UC and AF contributed equally). with permission of Wiley-VCH. Schemes, tables and text may differ from published version.

[ii] Author contributions: UC initiated the project; UC and AF performed synthesis of complexes, their analytical characterization and catalytic reactions. AJvW guided the project. All authors contributed to the writing of the manuscript.

6.1. Introduction

Amides constitute a diverse family of monoanionic ligands that exhibit hard σ-donating and π-donating ability. An especially rich coordination chemistry is known with main group metal ions, f-block elements, and early transition metals.[1,2] Amide ligands fulfil various roles in stoichiometric coordination chemistry and catalysis: as labile placeholders for rapid (often protolytic) ligand exchange reactions; as strong bases for deprotonative substrate activations; as sterically demanding ligands that stabilize low-coordinate and low-valent metal complexes; and as halide-free precursors to nanomaterials preparations. Metal amide bonds have also attracted attention due to their stereoelectronic similarity with organometallic complexes bearing σ-organyl and cyclopentadienyl ligands.[3] Among the various structural motifs connected to the anionic N-atom, silyl groups have seen especially diverse applications due to their easy availability and modular assembly from amines and silyl halides, their bulky lipophilic backbone, reduced basicity of the amide function, and the enhanced conjugation length across the ligand by interaction with the C-Si σ*-orbitals. Consequently, homoleptic metal(II) hexamethyldisilazides $M^{II}(hmds)_2$ have evolved as highly convenient and versatile low-coordinate precursors to numerous molecular complexes, catalysts, clusters, and nanomaterials (Scheme 6.1, top).[4] Protolytic ligand substitution, addition of donor ligands to give tri-coordinate complexes,[5] and oligomerizations via μ_2-amido bridging[6–8] are the common reactions. Most transition metal amide complexes form anionic metalates $[MX_3]^-$ by coordination with an additional amide or related anionic ligand X. All first-row transition metals except for Ti and Cu give anionic triamido adducts $M'[M(NR_2)_3]$ with alkali metal hexamethylsilazides. Counterion complexation (crown ethers, aminoglycols) provides separated ionic pairs with trigonal tri(silylamide) metalate anions (Sc,[9] V,[10] Cr,[10] Mn, Fe, Co,[11] Ni[12], Scheme 6.1., middle). Werncke et al. studied the related metal(I) congeners K(crypt/18-crown-6)$[M(hmds)_2]$ for M = Cr–Ni.[13–15] In the absence of hard donor ligands, contact ion pairs are formed where the alkali metal ions occupy the bridging position between two hmds ligands (Scheme 6.1., middle).[16–18] Such heterobimetallic complexes enabled selective metallations as shown by Hevia and coworkers in the ferration of fluoroarenes by the alkali metal ferrates $AMFe(hmds)_3$, AM = Li, Na.[19–22] Catalytic applications of amido metalates(II) are extremely rare: Neidig et al. postulated the ferrate $Li[X_2Fe^{II}Cl]$ (X_2 = ethylene-1,2-diamido) to be the active species in Kumada-type cross-coupling reactions;[23] catalytic hydrosilylation of vinylcyclohexane was reported to proceed in the presence of a triamido nickelate(II).[12] The coordination chemistry and catalytic activity of anionic iron(II) amide complexes is especially poorly explored. In continuation of our previous studies of amidoiron complexes, clusters, and catalytic applications,[24,25] we envisioned that the chemical space of triamido metalates(II) could be expanded by the use of chelate ligands in a heteroleptic ligand sphere. We reasoned that catalytic applications of triamido metalates would greatly benefit from the combination of a basic and labile ligand site for polar substrate activation and a stable κ^2-diamido spectator ligand that is retained during catalytic turnover and confers stereoelectronic stabilization onto the metal center. Only one example of such 3d metal complexes was reported with M = Mn, AM

= K;[26] catalytic applications have not yet been reported. Consequently, we prepared the heteroleptic triamidoferrate K[Fe(κ^2-N∩N)N(SiMe$_3$)$_2$], with κ^2-N∩N = 1,2-diphenylethylene-1,2-diamido, and evaluated its catalytic application to regioselective alkene hydrosilylations (Scheme 6.1., bottom).

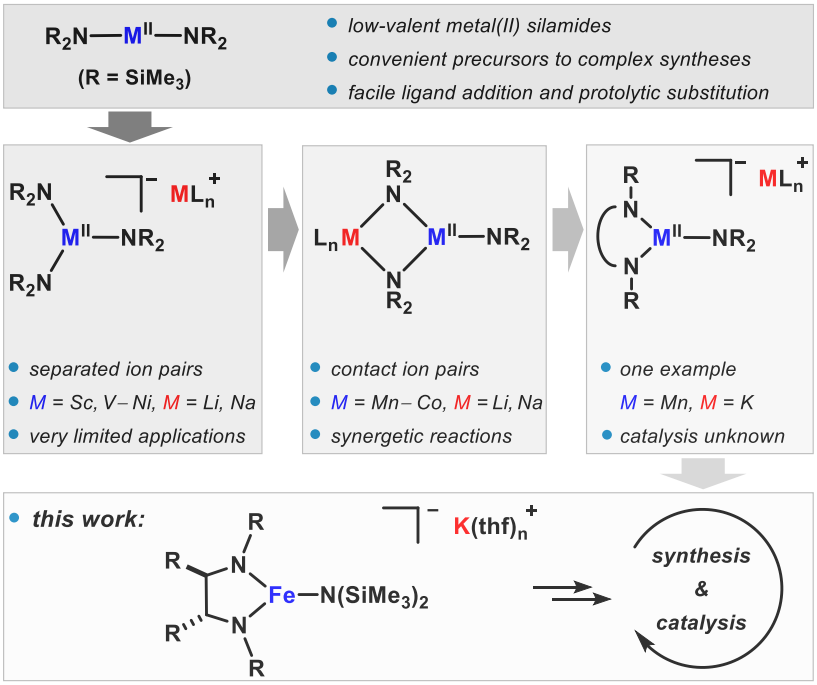

Scheme 6.1. Amido metal(II) and amido metalate(II) complexes with hexamethyldisilazide ligands (hmds, R = SiMe$_3$).

6.2. Results and Discussion

6.2.1. Synthesis and Characterization of Complexes

Consequently, *N*,*N'*-diphenyl-1,2-diphenylethane-1,2-diamide (^{Ph}LH$_2$) was prepared from the KC$_8$-mediated reductive dimerization of *N*-benzylideneaniline as mostly *rac*-diastereomer (>99/1, by ^{1}H NMR). Reaction of ^{Ph}LH$_2$ with the easily prepared iron(II) amide precursor Fe(hmds)$_2$ (hmds = hexamethyldisilazide, N(SiMe$_3$)$_2$) afforded the heteroleptic triamidoferrate(II) K(thf)$_6$[Fe(^{Ph}L)(hmds)], **1**. This highly air-sensitive, light-yellow solid was isolated by crystallization from THF/*n*-hexane at –35 °C as pure *rac*-diastereoisomer in 44% yield (Scheme 6.2., top).[27] Complex **1** was difficult to separate from the homoleptic triamido ferrate KFe(hmds)$_3$ which formed as by-product (XRD, see 6.5 for details). Therefore, an alternative synthesis route was adopted starting from *rac*-tetraphenyl ethylenediamine (^{Ph}LH$_2$) via sequential addition of 1 equiv. K(hmds) and 1 equiv. Fe(hmds)$_2$. This monobase approach eliminated the formation of KFe(hmds)$_3$ and afforded pure ***rac*-1** in 88% yield. The only by-product was HN(SiMe$_3$)$_2$ which could easily be removed in vacuum (Scheme 6.2., middle). A very similar deprotonative complexation was utilized by Hevia *et al.* in the syntheses of potassium amido metalates of Zn, Mg, and Mn.[26,28] A third synthesis attempt involving

trans-amination of the homoleptic triamido ferrate $K(Et_2O)_2[Fe(hmds)_3]$ (**3**) with the *rac* $^{Ph}LH_2$ showed no conversion by ^1H NMR despite a closely literature precedent.[29,30] Crystalline ***rac*-1** was isolated as THF-monosolvate (by elemental analysis; m.p. 176 °C, decomp. >235 °C) which is well soluble in THF but very poorly soluble in benzene. The ^1H NMR spectrum showed broad signals (δ = 41.6, 32.7, 2.3, −5.8, −47.5 ppm). The solution magnetic moment of 5.0(1) μ_B agrees well with a high-spin Fe(II), such as homoleptic complexes $[Fe(hmds)_3]^-$ (4.91–5.15 μ_B).[17]

The very similar reactions starting from the less bulky *N,N'*-diphenyl ethylenediamine ($^HLH_2$) via deprotonation with 2 equiv. K(hmds) and addition of $Fe(hmds)_2$ afforded a structurally distinct complex, the homoleptic tetraamido ferrate $K_2[Fe(^HL)_2]$ (**2**, Scheme 6.2). Compound **2** was obtained as a highly air-sensitive but thermally very stable (>260 °C) crystalline solid in 72% yield. This paramagnetic complex showed broad ^1H NMR resonances at δ = 82.87, 34.87, 21.54, −34.25 and −45.89 ppm in THF-d_8. The solution magnetic moment of 4.7(1) μ_B is in full accord with a high-spin tetrahedral Fe(II) configuration. The single crystal structure of ***rac*-1** contained both enantiomers as separated ion pairs with almost identical structural parameters and $[K(thf)_6]^+$ counterions (Figure 2). The planar three-coordinate Fe center displayed a very small N–Fe–N bite angle (87.9(1)°, 88.0(1)° in both enantiomers).[31–34] The Fe–NSi bond lengths in ***rac*-1** (1.931(2)–1.938(2) Å) are slightly longer than the terminal Fe–NSi bonds in $[Fe(hmds)_2]_2$ (1.923(3), 1.927(3) Å) and $[Fe(hmds)_2(thf)]$ (1.916(5) Å).[8] The 1,2-*trans*-diphenyl substituents of the backbone adopt a 153.98° angle. Single crystals of the homoleptic tetraamido ferrate **2** that were collected exhibited two different three-dimensional network structures through K^+-coordination to amido-*N*, phenyl, and solvent moieties. The asymmetric units were $K_4[Fe_2(^HL)_4(thf)_2]$, **2a**, and $K_6[Fe_3(^HL)_6(thf)_3]$, **2b** (see 6.5 for details). The Fe(II) ions adopt a distorted tetrahedral coordination (τ_4 = 0.75 and 0.77 in **2a**).[35] Dianionic ferrates with $[N]_4$-ligands have been reported with unsaturated π-backbone ligands, *e.g.* ketimides,[36] amidinates,[37] azaindoles,[38] porphyrinogens[39–41]. Complex **2** constitutes a rare example of an amidoferrate bearing saturated diamide ligands. The Fe–N bond lengths in **2** (1.970 – 2.016 Å) are slightly longer than those in the neutral $Fe(dcpe)(^HL)$ (1.923(4), 1.938(5) Å, dcpe = 1,2-bis(dicyclohexylphosphino)-ethane).[42] The N-Fe-N bite angle in the polymeric **2** (85.07(8)– 87.07(8)°) is smaller than in complex **1**.

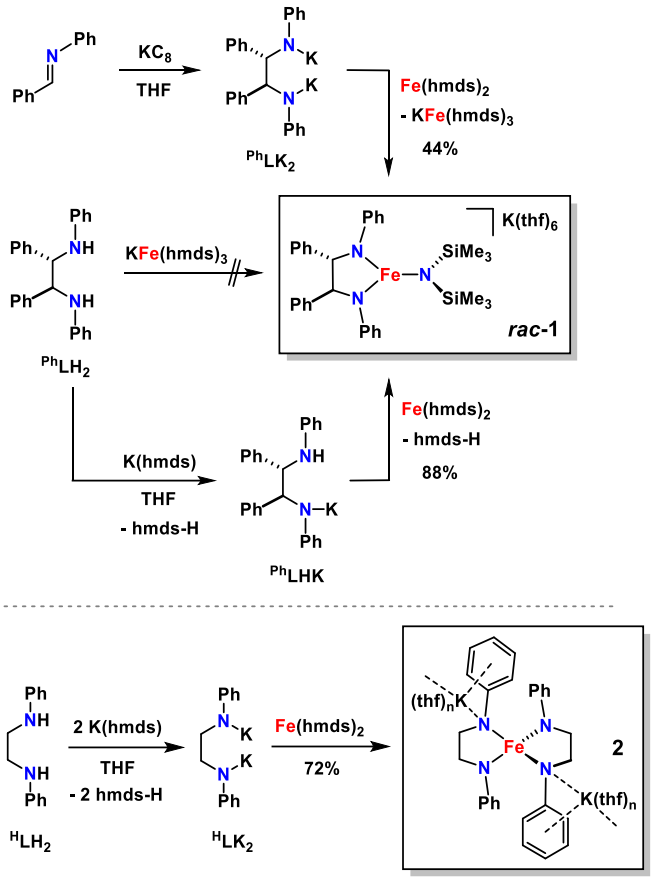

Scheme 6.2. Synthesis of the heteroleptic triamido ferrate **1** with the ligand ^{Ph}L and the homoleptic tetraamido ferrate **2** with ^{H}L.

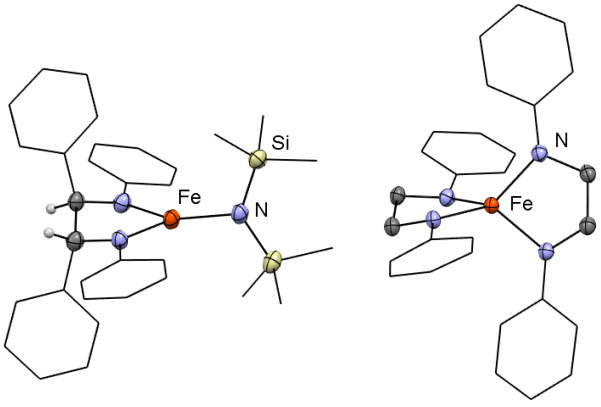

Figure 6.1. Molecular structures of the ferrates *rac*-**1** (only one enantiomer shown, left) and **2** (right). Thermal ellipsoids at the 50% probability level, H atoms and K+ counterions were omitted for clarity.

6.2.2. Catalytic Reactions

Iron(II) amine complexes have found diverse applications in catalytic transformations[43,44]. Based on the HSAB principle, the combination of Fe(II) with

strongly basic (amide) ligands appears especially suited to catalyze reactions between π-substrates and polar main group reagents.[45,46] Several protocols of catalytic hydrofunctionalizations of carbonyl derivatives were reported with iron amide complexes,[47–50] while there are no applications to hydrofunctionalization of alkenes known. Among the reported iron catalysts for hydrosilylations of alkenes, the vast majority provide linear silanes with high regiocontrol, often in the presence of pincer-type ligands,[45] while the selective formation of the branched silanes is a rarity.[51-53] We surmised that the diamido-*N*,*N*'-iron(II) complex **1** may enable effective catalytic hydrosilylation of alkenes by dual substrate activation: π-alkene coordination to the low-coordinate Fe(II) and Si←N Lewis acid-base interaction of the silane. The anionic nature of the catalyst species may further enhance silane activation and hydride transfer steps.[54] We initiated our study of catalytic hydrosilylations with the model reaction between styrene and phenylsilane, $PhSiH_3$. This reaction poses several challenges: the suppression of undesired polymerization in the presence of basic and electron-rich metal complexes; the suppression of the competing hydrogenation mechanism with silane acting as hydrogen source; the control of regioselectivity toward linear or branched alkylsilanes (Scheme 6.3).

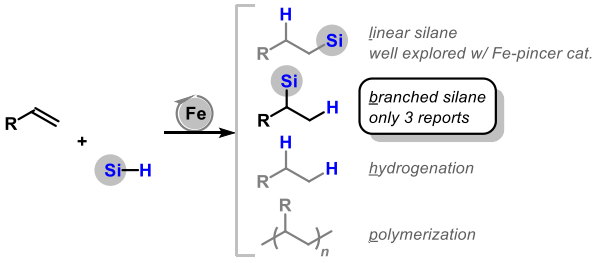

Scheme 6.3. Potential pathways under the conditions of alkene hydrosilylation reactions with Fe catalysts. l: linear silane regioisomer; b: branched silane regioisomer; h: hydrogenation product; p: polymer product.

Pre-catalyst **1** displayed no activity in benzene solution (partially due to low solubility), whereas reactions in THF gave very high conversions (entries 1-4). Gratifyingly, the use of 5 mol% pre-catalyst **1** enabled the formation of almost quantitative yields of the branched alkylsilane at room temperature (after 48 h) or at 60 °C (after 20 h). No linear silane product was observed; ethyl-benzene was the only by-product formed in a competing hydrogenation (3-5%). The complete regiocontrol toward the branched silanes is remarkable and complements the very few other literature methods.[55] To the best of our knowledge, three protocols of iron-catalyzed alkene hydrosilylation with high Markovnikov selectivity were reported,[51-53] that utilize complex ligands and/or the addition of activators. The distinct reactivity profile of catalyst **1** was further documented by the very poor catalytic activities of the related tetraamido ferrate **2**, $Fe(hmds)_2$, and the triamido complex $KFe(hmds)_3$ (entries 5-7). The latter anionic complex led to rapid polymerization. Interestingly, the special role of the diamido ligand ^{H}L could also be determined from reactions in the presence of the Fe-free bases:

K(hmds) and KH afforded almost quantitative polymerization (entries 9 and 10); potassium tetraphenylethanediamide ^{H}L gave no conversion (entry 11). The bulkier silane PhMe$_2$SiH was unreactive (entry 12).

Table 6.1. Optimization experiments of iron-catalyzed styrene hydrosilylation.

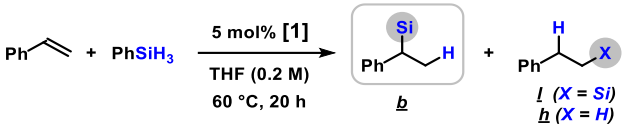

Entry	Change from conditions above	Yield of ***b*** [%] [a]	Ratio ***b***/***l***/***h*** [a]
1	reaction in C_6D_6, 23 °C	0	-
2	reaction in C_6D_6	0	-
3	23 °C, 48 h	84 (91)	>20/1/1
4	**-**	**95 (96)**	**>20/1/1**
5	**2** instead of **1**, 23 °C	7	3/0/1
6	10 mol% Fe(hmds)$_2$, 23 °C, 48 h	<5 (20)	>20/1/1
7	10 mol% KFe(hmds)$_3$,[b] 23 °C, 48 h	14 (100) [c]	>20/1/1
8	no catalyst, 66 h	0	-
9	10 mol% K(hmds), 23 °C, 48 h	2 (100) [c]	- [d]
10	5 mol% KH	0 (100)	-
11	5 mol% ^{H}LK$_2$,[e] 23 °C	0	-
12	with PhMe$_2$SiH, 23 °C, 66 h	0 (7)	-

[a] Yields (conversions of alkenes) and product ratios were determined by ^{1}H NMR *vs.* internal mesitylene. No linear silane was observed by ^{1}H NMR (except for allylbenzene). Conversion[%]–yield[%]= polymer[%]. [b] KFe(hmds)$_3$ was generated *in situ* from equimolar Fe(hmds)$_2$ and K(hmds) in THF-d$_8$. [c] Major amounts of polymers formed. [d] Minor traces (~2%) of linear product. [e] ^{H}LK$_2$ was prepared *in situ* from equimolar PhN=CHPh and KC$_8$ in THF-d$_8$.

The optimized conditions were applied to a set of 12 styrene derivatives (Scheme 6.4). Generally, very high regioselectivities toward the branched hydrosilanes were observed (>20/1). In some cases, minor amounts of hydrogenation products were obtained. However, polymerization operated rapidly for several substrates. Methylstyrenes and vinyl naphthalene gave the best yields of the branched silanes. Electron-deficient styrenes under-went competing polymer formation. Fluorostyrenes engaged in very minor hydrodefluorination. The pre-catalyst itself was not active toward defluorination, as the reaction of **1** with 4-fluoro-styrene gave no conversion. Formation of the hydrogenation product was rather significant with the 4-CF_3, 4-OMe, and naphthyl derivatives. Allylbenzene showed low conversion to the linear silane, possibly as a consequence of a different π-coordination to the catalyst (*e.g.* η^2 instead of η^4). *trans*-β-Methyl-styrene and α-methylstyrene were poorly reactive. Alkyl-substituted alkenes did not react (see Scheme 6.4, bottom).

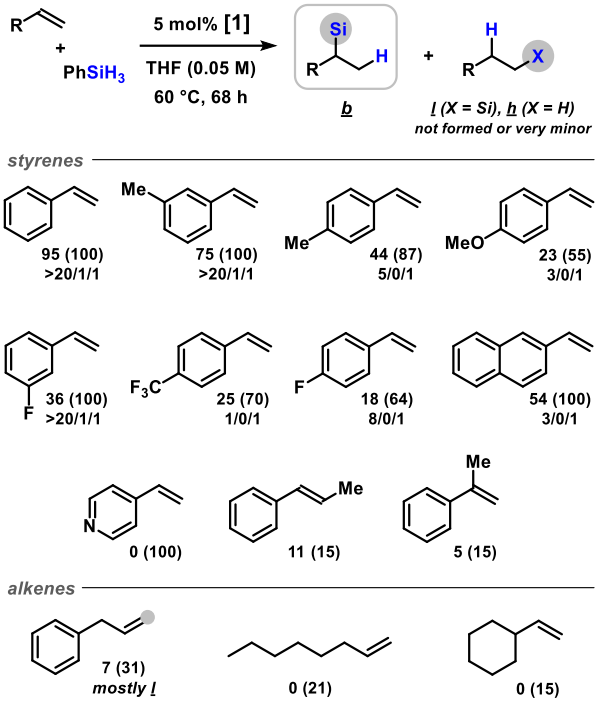

Scheme 6.4. Substrate scope of the Fe-catalyzed hydrosilylation of alkenes. Conditions: 0.2 M alkene in THF, 5 mol% **1**, 60 °C, 24-68 h. [a] Yield of *b*+*h*, (alkene conversion) and ratio of branch/linear/hydrogenated products (*b*/*l*/*h*) are given (determined by ^{1}H NMR *vs.* internal mesitylene or CH_2Br_2).

6.2.3. Mechanistic Studies

Key mechanistic data were collected from preparative and analytical experiments. Complex **1** showed no reaction with styrene. Instead, reaction with $PhSiH_3$ at 60 °C in THF-d_8 was observed to give $PhSiH_2N(SiMe_3)_2$ (GC-MS, ^{1}H NMR). This anionic ligand exchange is postulated to give an iron hydride species. The slow reaction is

significantly accelerated by the presence of styrene which argues in favor of alkene coordination to the catalyst (Scheme 6.5, top; ^{1}H NMR monitoring did not allow identification of an [Fe]-H complex, possibly due to paramagnetic line broadening). At higher temperature and longer reaction time between **1** and $PhSiH_3$, the diamidosilane $^{Ph}LSi(H)Ph$ formed (GC-MS, ^{1}H NMR). This unwanted Si-complex was independently prepared from the dilithium diamide and $PhSiCl_2H$ in THF-d_8 and shown to be no competent catalyst. Hydrosilylation of the β-D-labelled styrene $PhCH_2=CD_2$ gave complete conversion to the branched β-*d_2*-benzylsilane and no deuterium scrambling (Scheme 6.5, middle). The neutral metal amides K(hmds), $^{H}LK_2$ and $Fe(hmds)_2$ gave no hydrosilylation, while the related non-chelate triamidoferrate $KFe(hmds)_3$ showed some activity, however, with very poor yield (14%, see also Table 6.1). From these observations, we speculate that formation of a catalytically active iron hydride species is operating, which is in agreement with literature reports.[31] The low-coordinate catalyst may engage in η^4-coordination of the styrene, which is further supported by the observed inertness of alkyl-substituted alkenes, *i.e.* 1-octene and vinylcyclohexane. Regioselective and irreversible 2,1-insertion of the alkene results in the formation of a π-benzyliron intermediate that undergoes silylation with $PhSiH_3$ (Scheme 6.5, bottom).[55]

6.3. Conclusions

In conclusion, we have prepared the tri-coordinate, heteroleptic triamido ferrate(II) *rac*-**1** via transamination of $Fe(hmds)_2$ with tetraphenyl ethylenediamine. A rare tetraamido ferrate(II) (**2**) was isolated from the reaction of *N*,*N'*-diphenyl ethylenediamine with $Fe(hmds)_2$. **1** showed good activity in the regioselective hydro-silylation of simple styrenes to the branched benzylsilanes, while the related amido complexes K(hmds), $Fe(hmds)_2$, $KFe(hmds)_3$, and **2** gave poor results. This report is the first example of a catalytic application of triamido ferrates. Mechanistic studies indicated initial silylative amide dissociation and formation of a potential iron hydride species, a step that was significantly accelerated by the presence of the styrene.

Implications of this work are the following: The heteroleptic structure of **1** may provide ample opportunities of selective anionic ligand substitution of the hexamethyldisilazide group toward various other tri-coordinate ferrates(II). The wide availability of stereoelectronically diverse diamines may further allow careful fine-tuning of the catalytic activities of such amido ferrates for further applications to hydrofunctionalization, hydride transfer, and isomerization reactions. The consideration of counterion effects is expected to further modulate structural and chemical properties.

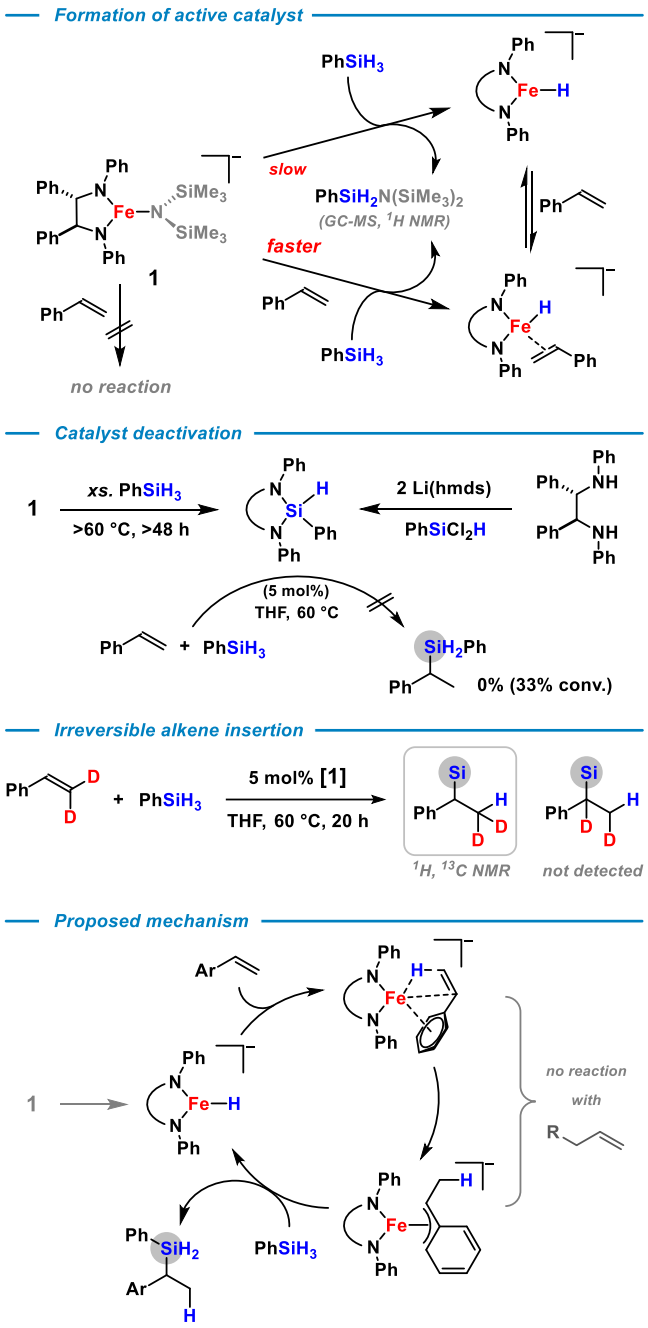

Scheme 6.5. Selected mechanistic studies (counterion K^+ omitted for clarity): Formation of the postulated active catalyst from pre-catalyst *rac*-**1** (top); H/D labelling studies of alkene insertion; catalyst deactivation by ligand transfer (middle); plausible catalytic mechanism (bottom).

6.4. References

[1] M. F. Lappert, P. P. Power, A. V. Protchenko, A. L. Seeber, *Metal Amide Chemistry*; Wiley, Chichester, **2009**.

[2] N. H. Co, A. R. Davis, C. Deng, V. Chantranuwathana, E. R. Himel Rubin, M. Subhan, W. Huang, P. L. Diaconescu, *Amide and Ketimide Metal Complexes*, Elsevier, **2021**.

[3] R. Kempe, *Angew. Chem. Int. Ed.* **2000**, *39*, 468–493.

[4] P. P. Power, *Chem. Rev.* **2012**, *112*, 3482–3507.

[5] C. Y. Lin, J. C. Fettinger, P. P. Power, *Inorg. Chem.* **2017**, *56*, 9892–9902.

[6] D. L. J. Broere, I. Čorić, A. Brosnahan, P. L. Holland, *Inorg. Chem.* **2017**, *56*, 3140–3143.

[7] A. M. Bryan, G. J. Long, F. Grandjean, P. P. Power, *Inorg. Chem.* **2013**, *52*, 12152–12160.

[8] M. M. Olmstead, P. P. Power, S. C. Shoner, *Inorg. Chem.* **1991**, *30*, 2547–2551.

[9] D. H. Woen, G. P. Chen, J. W. Ziller, T. J. Boyle, F. Furche, W. J. Evans, *Angew. Chem. Int. Ed.* **2017**, *56*, 2050–2053.

[10] C. L. Wagner, N. A. Phan, J. C. Fettinger, L. A. Berben, P. P. Power, *Inorg. Chem.* **2019**, *58*, 6095–6101.

[11] M. A. Putzer, B. Neumüller, K. Dehnicke, J. Magull, *Chem. Ber.* **1996**, *129*, 715–719.

[12] A. M. Borys, E. Hevia, *Organometallics* **2021**, *40*, 442–447.

[13] C. G. Werncke, E. Suturina, P. C. Bunting, L. Vendier, J. R. Long, M. Atanasov, F. Neese, S. Sabo-Etienne, S. Bontemps, *Chem. Eur. J.* **2016**, *22*, 1668–1674.

[14] C. G. Werncke, P. C. Bunting, C. Duhayon, J. R. Long, S. Bontemps, S. Sabo-Etienne, *Angew. Chem. Int. Ed.* **2015**, *54*, 245–248.

[15] A. Reckziegel, B. Battistella, A. Schmidt, C. G. Werncke, *Inorg. Chem.* **2022**, 61, 7794–7803.

[16] B. D. Murray, P. P. Power, *Inorg. Chem.* **1984**, *23*, 4584–4588.

[17] S. N. König, D. Schneider, C. Maichle-Mössmer, B. M. Day, R. A. Layfield, R. Anwander, *Eur. J. Inorg. Chem.* **2014**, *2014*, 4302–4309.

[18] S. Indris, T. Bredow, B. Schwarz, A. Eichhöfer, *Inorg. Chem.* **2022**, *61*, 554–567.

[19] L. C. H. Maddock, T. Nixon, A. R. Kennedy, M. R. Probert, W. Clegg, E. Hevia, *Angew. Chem. Int. Ed.* **2018**, *57*, 187–191.

[20] L. C. H. Maddock, A. Kennedy, E. Hevia, *Chimia* **2020**, *74*, 866–870.

[21] L. C. H. Maddock, M. Mu, A. R. Kennedy, M. García-Melchor, E. Hevia, *Angew. Chem. Int. Ed.* **2021**, *60*, 15296–15301.

[22] L. C. H. Maddock, A. R. Kennedy, E. Hevia, *Helv. Chim. Acta* **2021**, *104*, e2100206.

[23] P. G. N. Neate, B. Zhang, J. Conforti, W. W. Brennessel, M. L. Neidig, *Org. Lett.* **2021**, *23*, 5958–5963.

[24] T. N. Gieshoff, U. Chakraborty, M. Villa, A. Jacobi von Wangelin, *Angew. Chem. Int. Ed.* **2017**, *56*, 3585–3589.

[25] D. Brenna, M. Villa, T. N. Gieshoff, F. Fischer, M. Hapke, A. Jacobi von Wangelin, *Angew. Chem. Int. Ed.* **2017**, *56*, 8451–8454.

[26] P. Mastropierro, A. R. Kennedy, E. Hevia, *Eur. J. Inorg. Chem.* **2021**, *2021*, 1016–1022.
[27] The three-component reaction between $Fe(hmds)_2$, KC_8, and *N*-benzylidene aniline in Et_2O afforded very low yields of the ferrate **1**. NMR spectra showed a mixture of *rac* and *meso* isomers. Recrystallization from Et_2O at -35°C enabled isolation of crystalline *meso*-**1** (see 6.5 for details).
[28] P. Mastropierro, A. R. Kennedy, E. Hevia, *Chem. Commun.* **2022**, *58*, 5292–5295.
[29] L. C. H. Maddock, I. Borilovic, J. McIntyre, A. R. Kennedy, G. Aromí, E. Hevia, *Dalton Trans.* **2017**, *46*, 6683–6691.
[30] L. C. H. Maddock, R. Morton, A. R. Kennedy, E. Hevia, *Chem. Eur. J.* **2021**, *27*, 15180–15186.
[31] H. J. Lin, S. Lutz, C. O'Kane, M. Zeller, C. H. Chen, T. Al Assil, W. T. Lee, *Dalton Trans.* **2018**, *47*, 3243–3247.
[32] D. L. J. Broere, B. Q. Mercado, J. T. Lukens, A. C. Vilbert, G. Banerjee, H. M. C. Lant, S. H. Lee, E. Bill, S. Sproules, K. M. Lancaster, P. L. Holland, *Chem. Eur. J.* **2018**, *24*, 9417–9425.
[33] K. Y. Monakhov, J. van Leusen, P. Kögerler, E. L. Zins, M. E. Alikhani, M. Tromp, A. A. Danopoulos, P. Braunstein, *Chem. Eur. J.* **2017**, *23*, 6504–6508.
[34] A. Panda, M. Stender, R. J. Wright, M. M. Olmstead, P. Klavins, P. P. Power, *Inorg. Chem.* **2002**, *41*, 3909–3916.
[35] L. Yang, D. R. Powell, R. P. Houser, *Dalton Trans.* **2007**, 955–964.
[36] R. A. Lewis, G. Wu, T. W. Hayton, *J. Am. Chem. Soc.* **2010**, *132*, 12814–12816.
[37] W. Li, S. Di Bai, F. Su, X. E. Duan, D. S. Liu, *Z. Anorg. Allg. Chem.* **2017**, *643*, 737–741.
[38] J. A. Przyojski, M. L. Kiewit, K. L. Fillman, H. D. Arman, Z. J. Tonzetich, *Inorg. Chem.* **2015**, *54*, 9637–9645.
[39] S. De Angelis, E. Solari, C. Floriani, A. Chiesi-Villa, C. Rizzoli, *J. Am. Chem. Soc.* **1994**, *116*, 5702–5713.
[40] J. Bachmann, D. G. Nocera, *J. Am. Chem. Soc.* **2005**, *127*, 4730–4743.
[41] J. Jubb, D. Jacoby, C. Floriani, A. Chiesi-Villa, C. Rizzoli, *Inorg. Chem.* **1992**, *31*, 1306–1308.
[42] R. T. Baker, J. C. Gordon, C. W. Hamilton, N. J. Henson, P. H. Lin, S. Maguire, M. Murugesu, B. L. Scott, N. C. Smythe, *J. Am. Chem. Soc.* **2012**, *134*, 5598–5609.
[43] S. Rana, J. P. Biswas, S. Paul, A. Paik, D. Maiti, *Chem. Soc. Rev.* **2021**, *50*, 243–472.
[44] A. Fürstner, *ACS Cent. Sci.* **2016**, *2*, 778–789.
[45] D. Wei, C. Darcel, *Chem. Rev.* **2019**, *119*, 2550–2610.
[46] S. R. Tamang, M. Findlater, *Molecules* **2019**, *24*
[47] C. M. Macaulay, T. Ogawa, R. McDonald, O. L. Sydora, M. Stradiotto, L. Turculet, *Dalton Trans.* **2019**, *48*, 9581–9587.
[48] A. J. Ruddy, C. M. Kelly, S. M. Crawford, C. A. Wheaton, O. L. Sydora, B. L. Small, M. Stradiotto, L. Turculet, *Organometallics* **2013**, *32*, 5581–5588.
[49] A. Baishya, S. Baruah, K. Geetharani, *Dalton Trans.* **2018**, *47*, 9231–9236.
[50] J. Yang, T. D. Tilley, *Angew. Chem. Int. Ed.* **2010**, *49*, 10186–10188.

[51] M. Y. Hu, Q. He, S. J. Fan, Z. C. Wang, L. Y. Liu, Y. J. Mu, Q. Peng, S. F. Zhu, *Nat. Commun.* **2018**, *9*, 221.
[52] B. Cheng, W. Liu, Z. Lu, *J. Am. Chem. Soc.* **2018**, *140*, 5014–5017.
[53] S. Zhang, J. S. Liao, D. K. Unruh, G. Li, M. Findlater, *Org. Chem. Front.* **2021**, *8*, 2174–2181.
[54] W. Chen, H. Song, J. Li, C. Cui, *Angew. Chem. Int. Ed.* **2020**, *59*, 2365–2369.
[55] M. Zaranek, P. Pawluc, *ACS Catal.* **2018**, *8*, 9865–9876.

6.5. Experimental Section

6.5.1. General Information

All experiments with air-sensitive compounds were performed under an atmosphere of dry argon, by using standard Schlenk and glovebox techniques. Solvents (Et_2O, *n*-hexane, toluene) were purified by a solvent purification system under N_2; THF was distilled over sodium and benzophenone. Dry solvents were stored over molecular sieves (4 Å). $Fe(N(SiMe_3)_2)_2$ was prepared according to the literature procedure.[1] *rac*-tetraphenylethylenediamine ($^{Ph}LH_2$) was prepared according to a literature report and found to contain <1% *meso* isomer.[2] Alkenes were purchased from commercial sources; liquid samples were distilled before use. KC_8 was prepared by mixing the respective amounts of graphite (dried in vacuo at 120 °C for 24h) with freshly cut potassium metal. The mixture was heated at 100 °C until all potassium metal had reacted and a bronze homogeneous powder formed. Alkenes, deuterated styrene, *N,N'*-diphenylethylenediamine, $PhSiCl_2H$, and $PhSiH_3$. Elemental analyses were determined by the analytical department of the University of Hamburg. Melting points of the compounds were measured on a *DigiMelt SRS* instrument using a glass-capillary sealed under vacuum. FT-IR spectra were recorded on an Agilent Cary 630 FTIR with ATR-device at room temperature inside a nitrogen-filled glovebox. ^{1}H NMR spectral data were collected on 300 and 400 MHz Bruker Avance spectrometers at 20 °C. Solution magnetic moments were determined by a ^{1}H NMR experiment following the procedure of Evans.[3] UV/visible absorption spectra were recorded at room temperature on an Agilent Cary 5000 UV-vis-NIR double beam spectrometer with a 10 mm quartz cuvette and a Teflon valve.

6.5.2. Synthesis of Complexes

*Synthesis of rac-**1***
Under an atmosphere of argon, a mixture of *N*-benzylidene aniline (90 mg, 0.50 mmol) and KC_8 (67 mg, 0.50 mmol) was treated with 4 mL of freshly dried THF and stirred for 2 d at 20 °C. To the obtained grayish-black suspension, a solution of $Fe(hmds)_2$ (93 mg, 0.25 mmol) dissolved in THF (1 mL) was added dropwise under stirring. A greenish-yellow suspension formed and the mixture was stirred overnight under argon. The suspension was filtered through a syringe containing a Whatman glass filter paper. The yellow filtrate was layered with 5 mL hexane and stored at 20 °C for 2 days and then at –35 °C for 2 d. The resultant yellow crystals of pure *rac*-1 were collected and dried in vacuum. The mother liquor became slightly viscous upon standing so that 2 mL

hexane were added, the mixture was stirred for 1 h. Another batch of yellow solid *rac*-1 was obtained by filtration and dried in vacuum. *rac*-1 is a highly air and moisture sensitive compound that was kept under argon at room temperature**.** Combined yield: 76 mg (0.11 mmol, 44%) EA: calcd for K(THF)[Fe(hmds)^{Ph}L], $C_{36}H_{48}FeKN_3OSi_2$: C 62.67, H 7.01, N 6.09; found: C 62.62, H 6.67, N 6.17. ^{1}H NMR (THF-d_8, 300.2 MHz, 297K): δ in ppm: 41.55, 3.61 (m, THF), 1.77 (m, THF), 2.66, 2.29, −5.81, −47.45. m.p. 176 °C, dec. >235 °C. Solution magnetic moment determined by Evans method: 5.0(1) μ_B (THF-d_8, 300K).

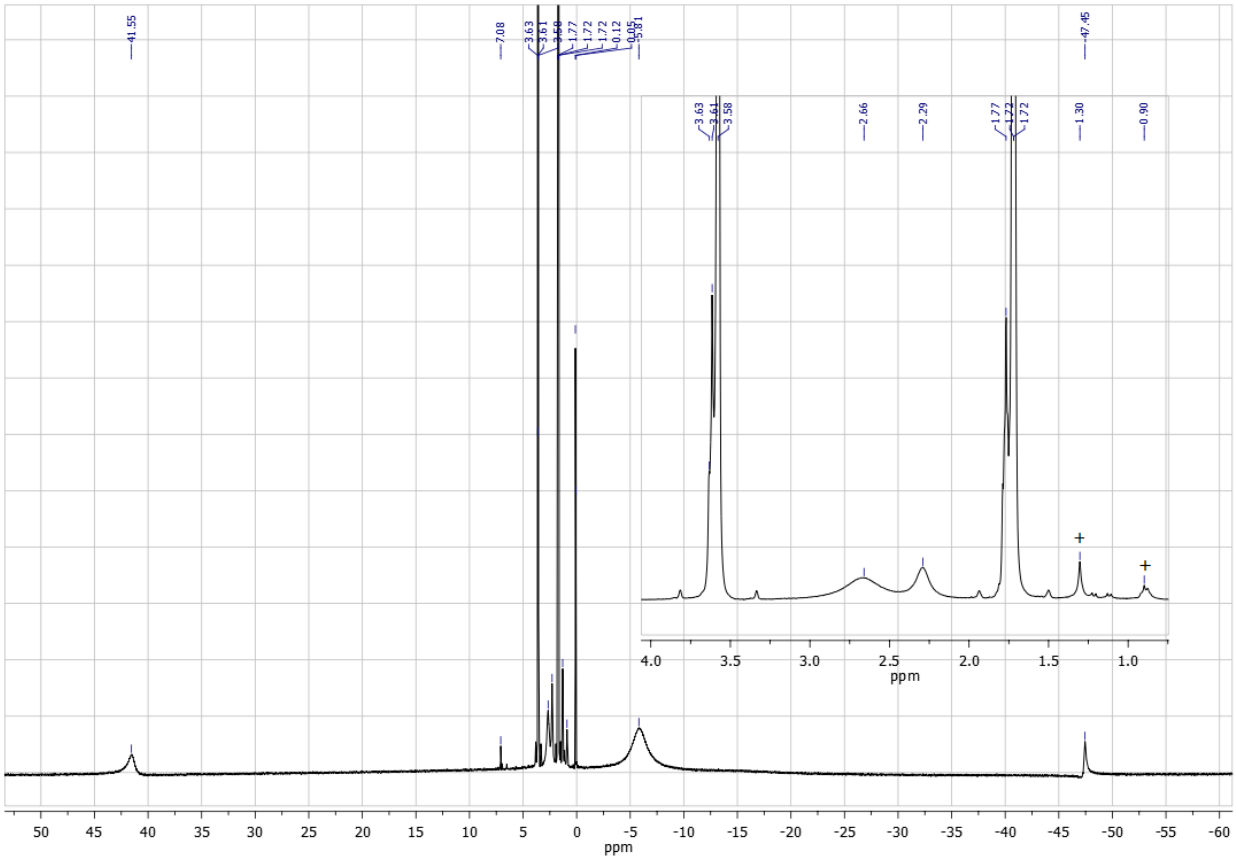

Figure 6.2. ^{1}H NMR (THF-d_8, 300.2 MHz, 297K) spectrum of *rac*-**1**. Peaks assigned with + are from *n*-hexane**.**

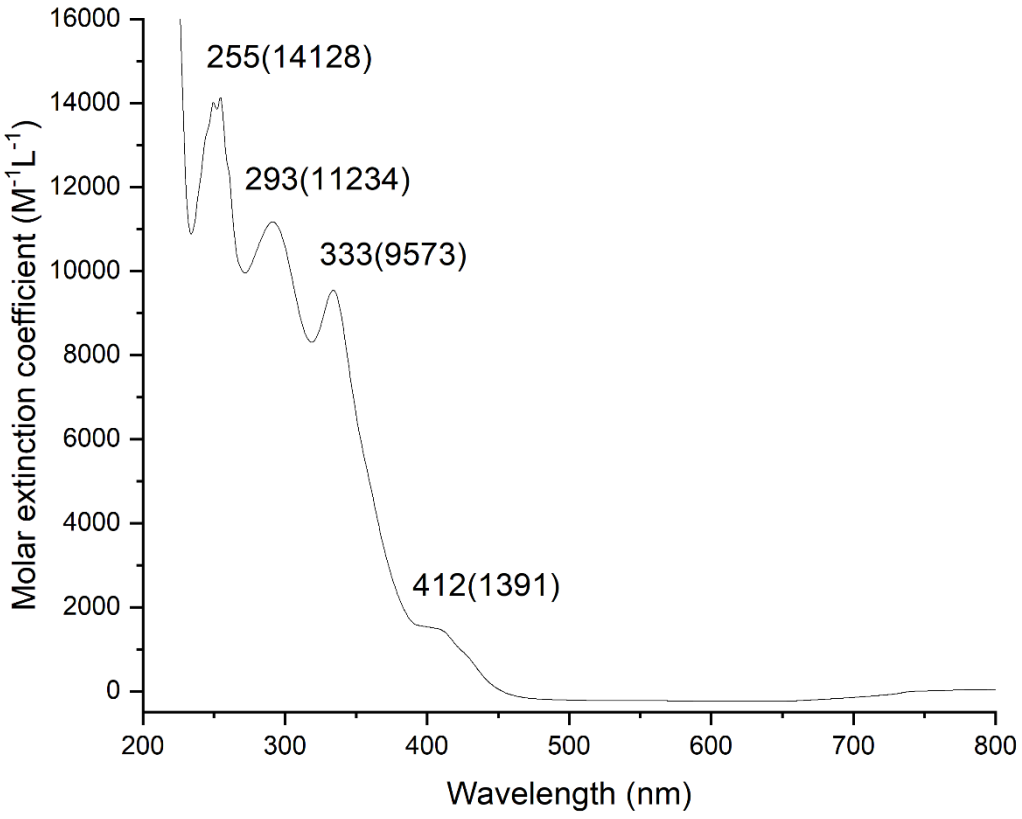

Figure 6.3. UV-Vis spectrum of *rac*-**1** in THF.

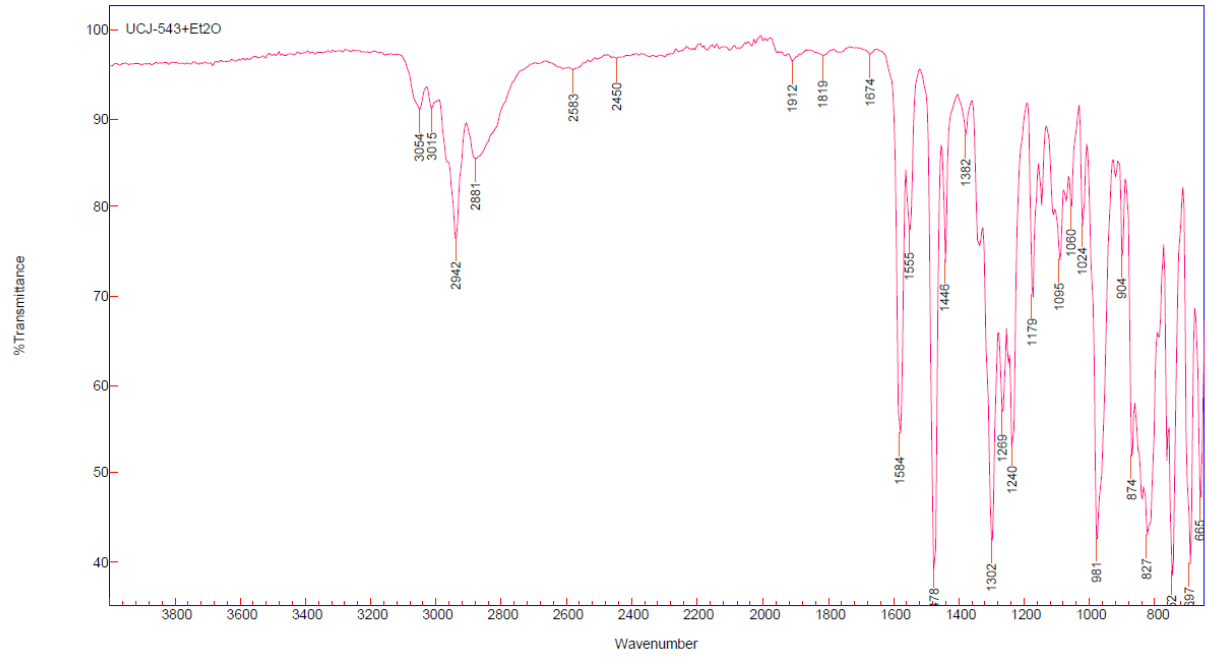

Figure 6.4. Solid-state (Et_2O film - solvent was added to the solid sample and evaporated before the measurement) IR (ATR) spectrum of *rac*-**1**.

*Synthesis of meso-**1***

A mixture of $Fe(hmds)_2$ (39 mg, 0.10 mmol), *N*-benzylideneaniline (22 mg, 0.12 mmol) and KC_8 (13.5 mg, 0.10 mmol) was treated with 2 mL diethyl ether at room temperature under an atmosphere of argon. The brownish suspension turned greenish in 30 min, was stirred overnight and filtered through a syringe containing a Whatman glass filter paper. The yellowish filtrate was stored at −35 °C overnight to obtain yellow crystals of *meso*-**1**. Yield: 5 mg (0.07mmol, 15%). ^{1}H NMR (THF-d_8, 300.2 MHz, 297K): δ in ppm: 39.28, 7.20, 5.91, 3.39 (q, Et_2O), 1.12 (t, Et_2O), − 2.50, − 8.08, − 53.73.

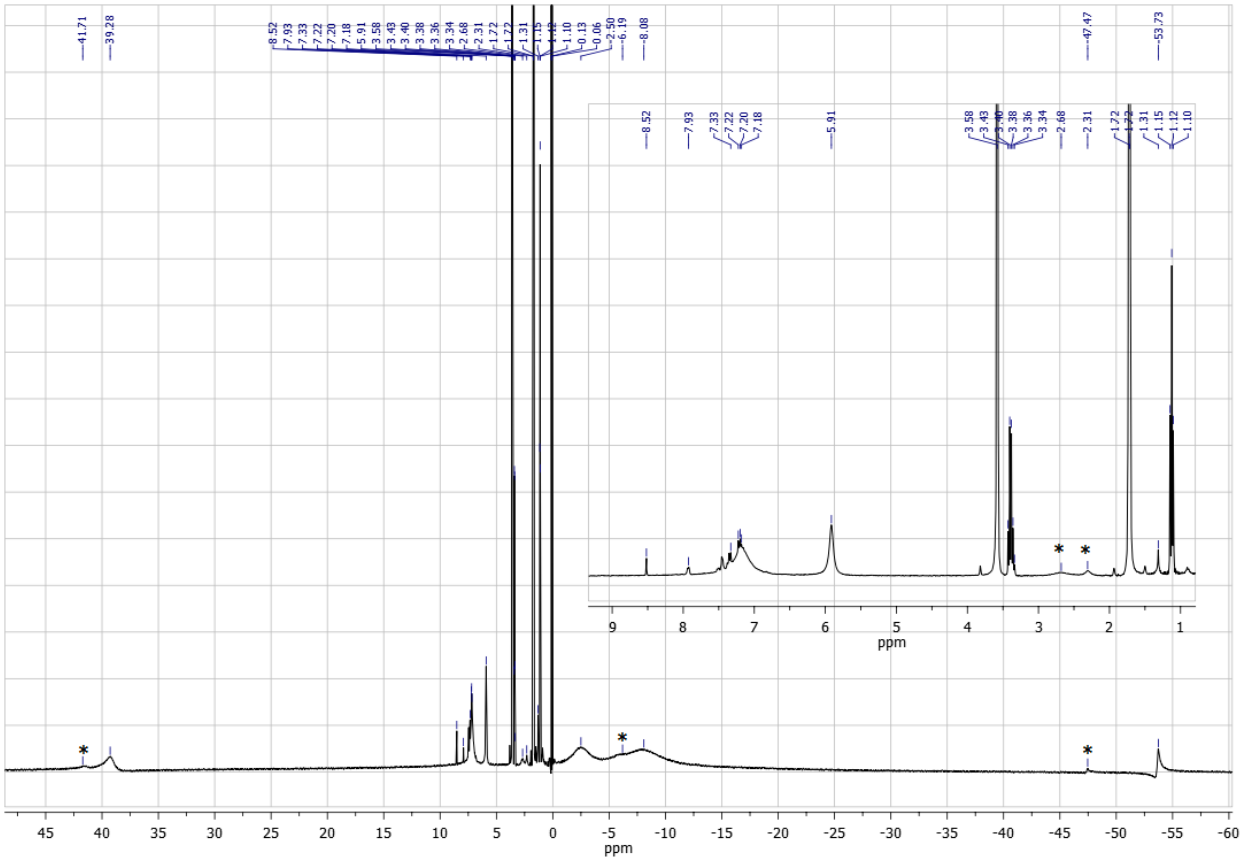

Figure 6.5. ^{1}H NMR (THF-d_8, 300.2 MHz, 297K) spectrum of *meso*-**1**. Peaks assigned with * are from *rac*-**1**.

*Synthesis of **rac-1** from $PhLH_2$ and K(hmds).*

A mixture of *rac*-tetraphenylethylenediamine $^{Ph}LH_2$ (150 mg, 0.41 mmol) and K(hmds) (86 mg, 0.41 mmol) in THF (3 mL) was stirred at room temperature for 1 h. To the resulting yellow-orange suspension, solid $Fe(hmds)_2$ (155 mg, 0.41 mmol) was added and the reaction mixture was stirred overnight. The obtained dark brown solution was filtered through a Whatman glass filter paper embedded in a syringe and the filtrate was layered with hexane (5 mL) and stored at −35 °C for several days. A yellow crystalline solid was isolated by decanting the mother liquor and dried in vacuum for

2 h. Yield: 251 mg (88%, as THF-monosolvate). ^{1}H NMR spectrum aligns well with that of *rac*-**1**.

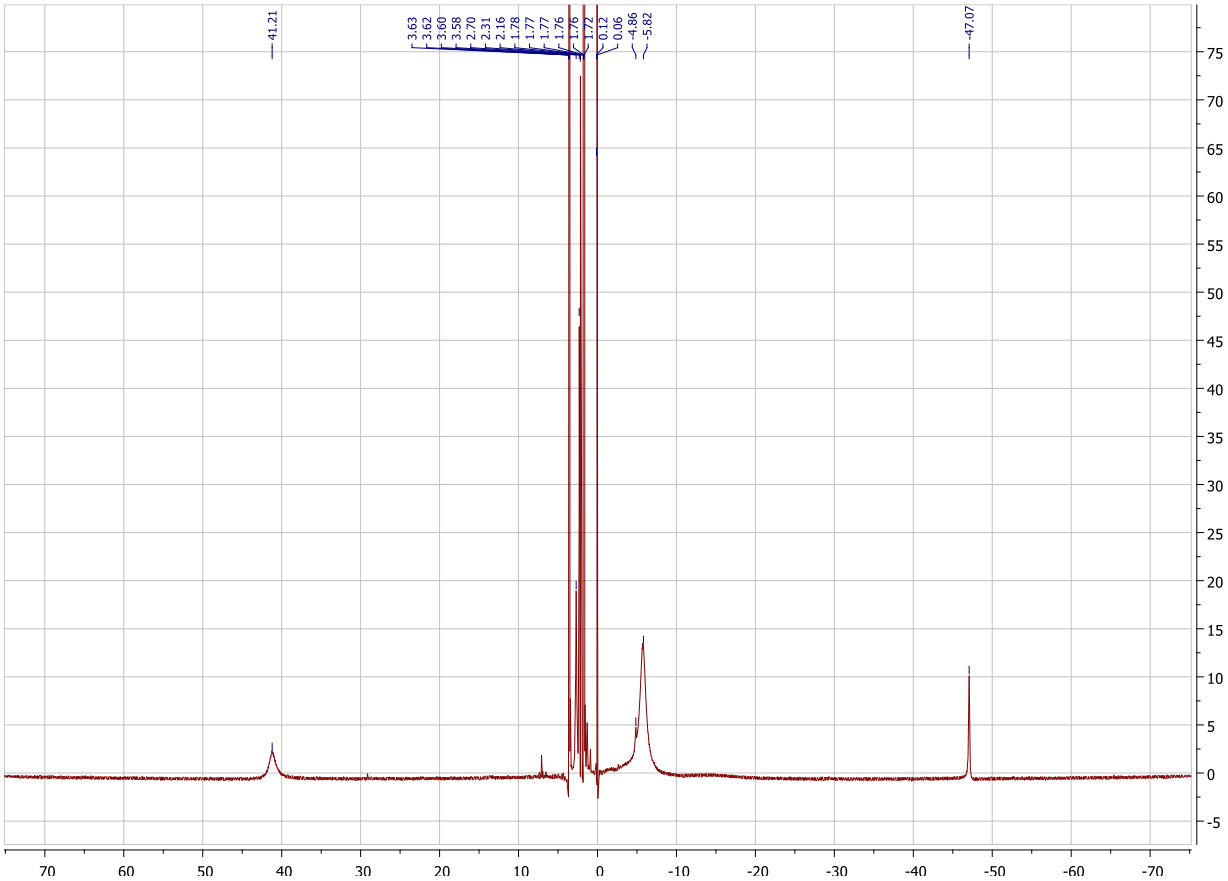

Figure .6.6. ^{1}H NMR (THF-d_8, 300.2 MHz, 297K) spectrum of *rac*-**1**.

*Synthesis of tetraamidoferrate **2**.*

A mixture of *N,N'*-diphenylethylenediamine (53 mg, 0.25 mmol) and K(hmds) (100 mg, 0.50 mmol) was dissolved in 3 mL THF and stirred for 2 h. To the yellow solution of the diamide, a solution of $Fe(hmds)_2$ (94 mg, 0.25 mmol) in 1 mL THF was added dropwise for 10 min. The deep yellow solution was filtered and the filtrate was layered with hexane (9 mL) for slow diffusion at room temp. for several days. The obtained yellow crystalline solid was isolated by decanting the mother liquor and dried in vacuum. Yield: 56 mg (0.089 mmol, 36% based on ligand).

Elemental analysis: calcd for **2**(thf), $C_{32}H_{36}FeK_2N_4O$: C 61.33, H 5.79, N 8.94; found: C 61.23, H 5.925, N 8.96. m.p.: no melting or decomposition up to 260 °C. **^{1}H NMR** (THF-d_8, 400.1 MHz, 300 K): δ in ppm: 82.87 (br), 34.87 (br), 21.54 (br), −34.25 (br), −45.89 (s). Solution magnetic moment determined by Evans method: 4.7(1) μ_B (THF-d_8, 300 K). Single crystals suitable for X-Ray diffraction analysis were obtained from the work-up procedure above. Two single crystals (**2a** and **2b**), suitable for X-Ray diffraction analysis, were obtained during the described crystallization procedure from the same crystallization batch. X-ray diffraction analysis showed that both crystals had

the same unit formula $C_{32}H_{36}FeK_2N_4O$ but were characterized by different asymmetric units: **2a** $(C_{32}H_{36}FeK_2N_4O)_2$ and **2b** $(C_{32}H_{36}FeK_2N_4O)_3$. For details, see Figures 6.43-6.46.

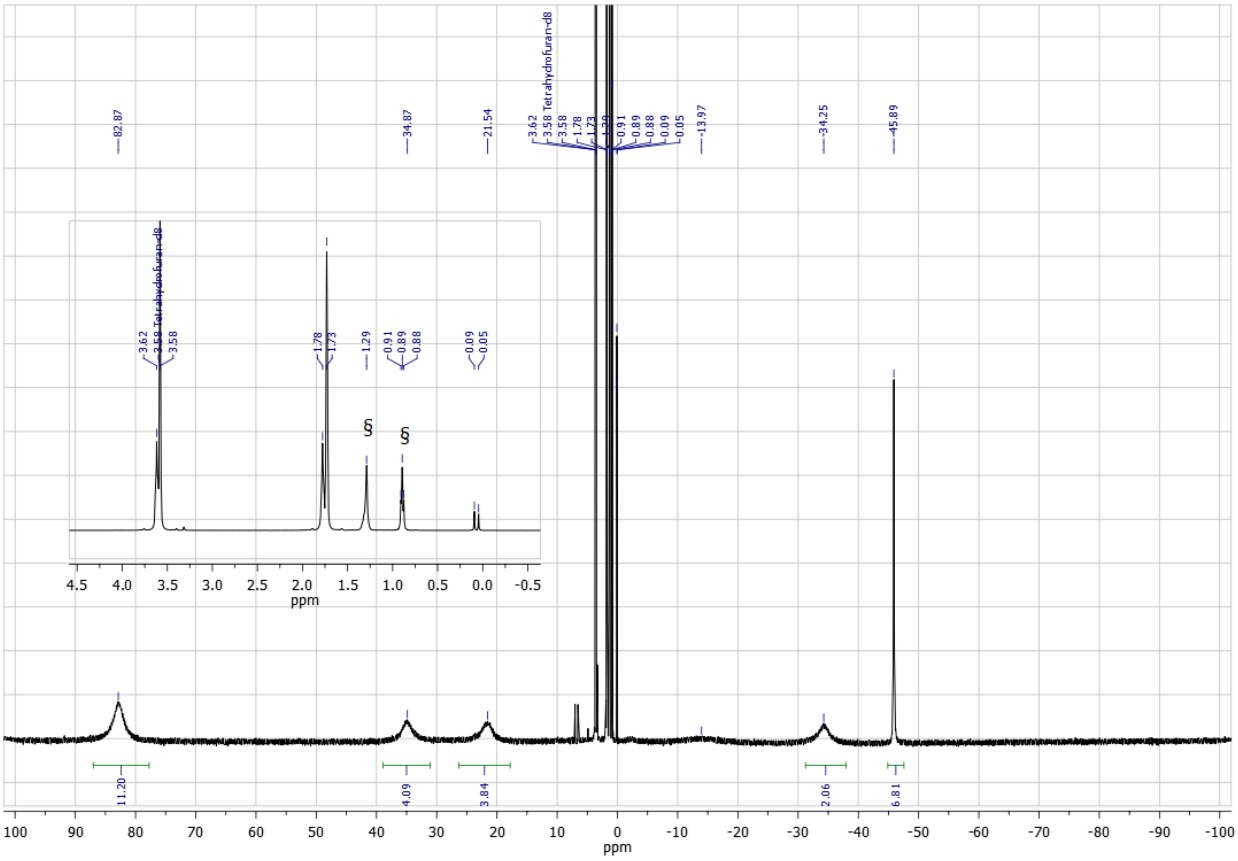

Figure .6.7. ^{1}H NMR (THF-d_8, 400.1 MHz, 300 K) spectrum of **2**.

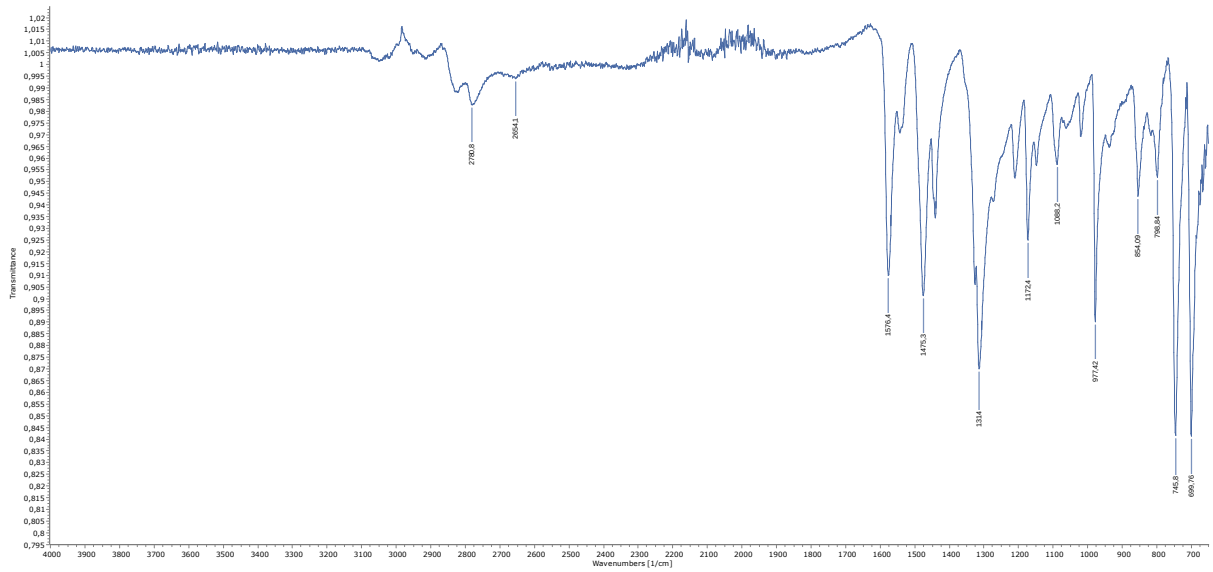

Figure .6.8. Transmission IR-ATR spectrum of **2**.

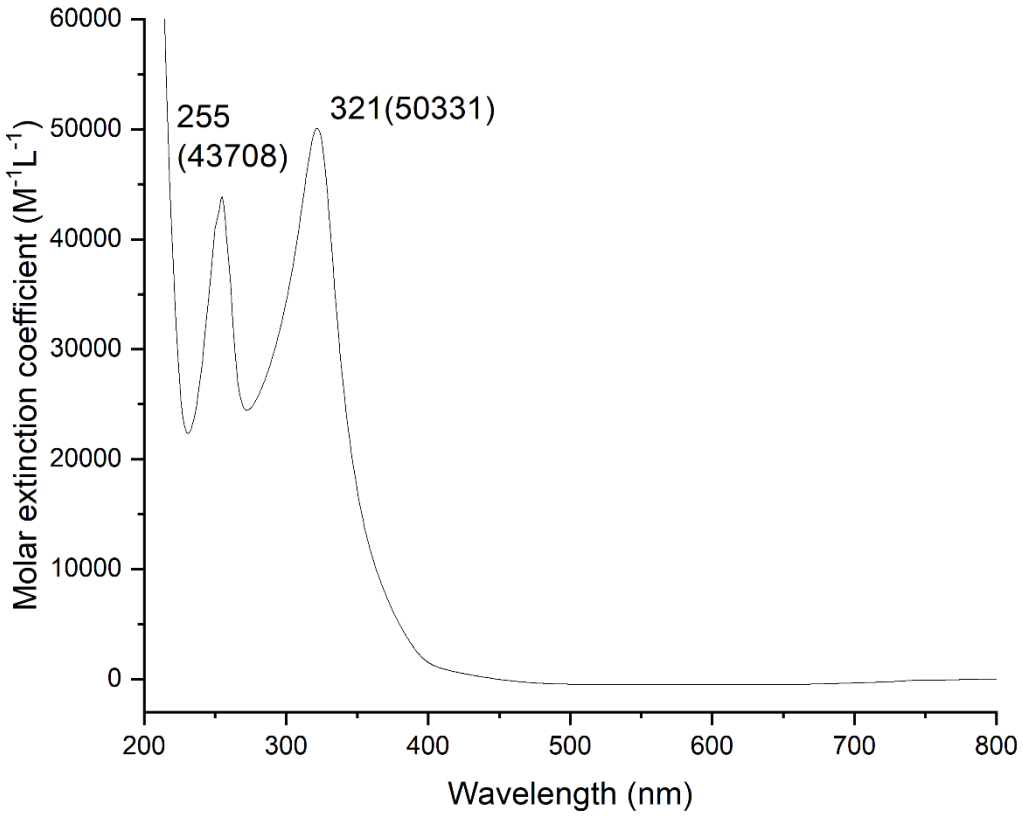

Figure 6.9. UV-Vis spectrum of **2** in THF.

Synthesis of KFe(hmds)$_3$

A mixture of Fe(hmds)$_2$ (188 mg, 0.5 mmol) and K(hmds) (100 mg, 0.5 mmol) was suspended in hexane (10 mL) and stirred for 15 min followed by addition of diethyl ether (4 mL). The obtained white suspension was stirred overnight at room temp., and then filtered through a Whatman glass filter paper embedded in a syringe. The white solid was washed with hexane (3 mL) and dried in vacuum to give a fine white powder. Yield: 263 mg, 83% of K[Fe(hmds)$_3$](Et$_2$O)$_{0.74}$ as determined by elemental analysis.

Elemental analysis calcd for K[Fe(hmds)$_3$](Et$_2$O)$_{0.74}$, $C_{20.96}H_{61.4}FeKN_3O_{0.74}Si_6$: C 39.90, H 9.81, N 6.66; found: C 39.89, H 10.16, N 6.49. ^{1}H NMR (C_6D_6 : THF-d_8 = 5:1, 300.2 MHz, 297 K): δ in ppm: −2.8 (br). Colorless single crystals suitable for X-ray diffraction were obtained by cooling the hexane washing fraction to −35 °C.

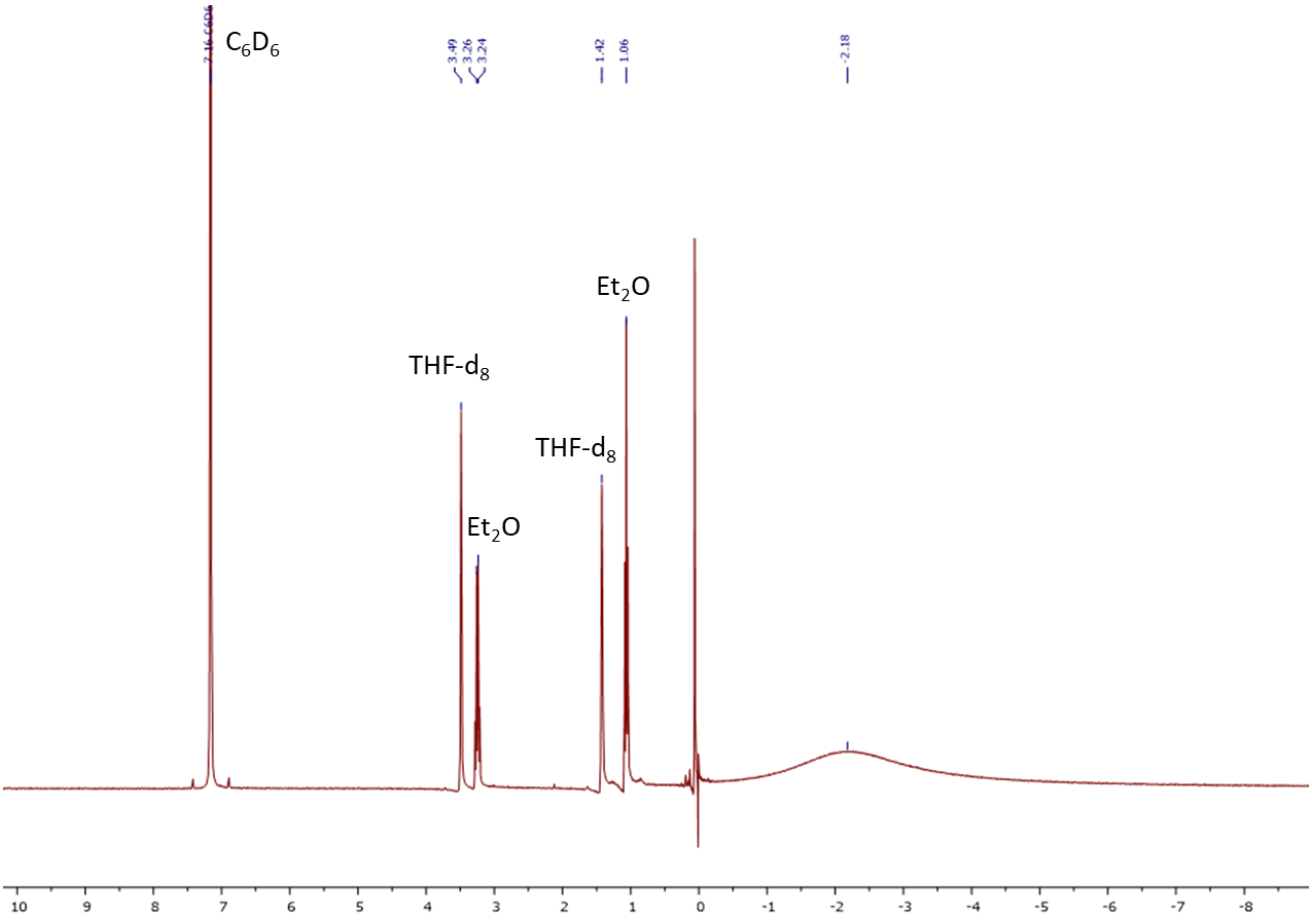

Figure 6.10. ^{1}H NMR (C_6D_6/THF-d_8 = 5:1, 300.2 MHz, 300 K) spectrum of $KFe(hmds)_3$.

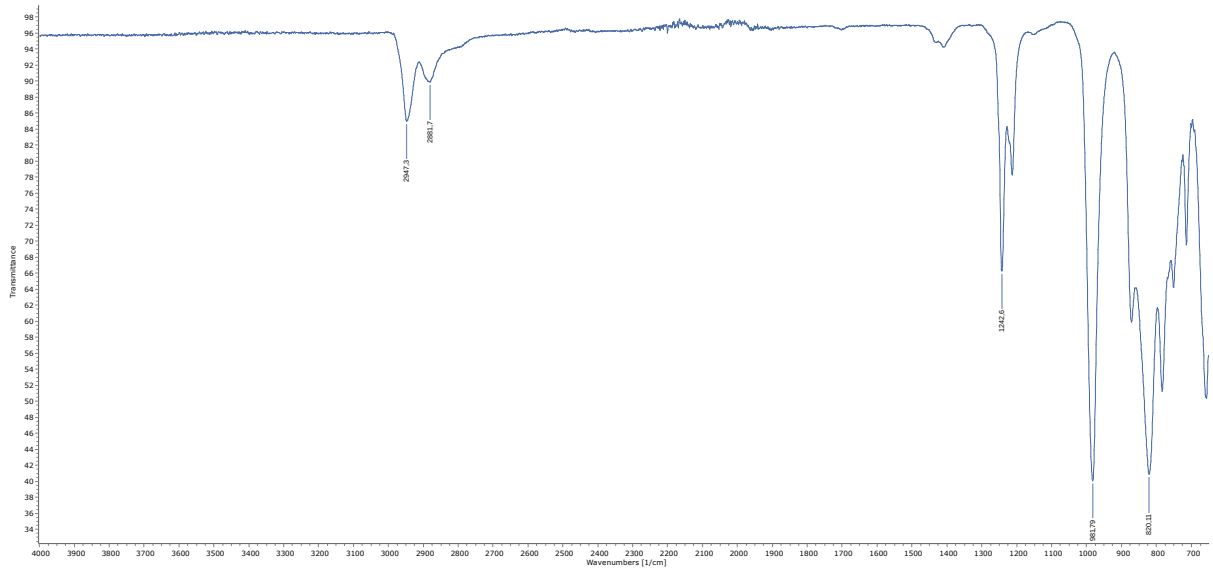

Figure .6.11. Transmission IR-ATR spectrum of $KFe(hmds)_3$.

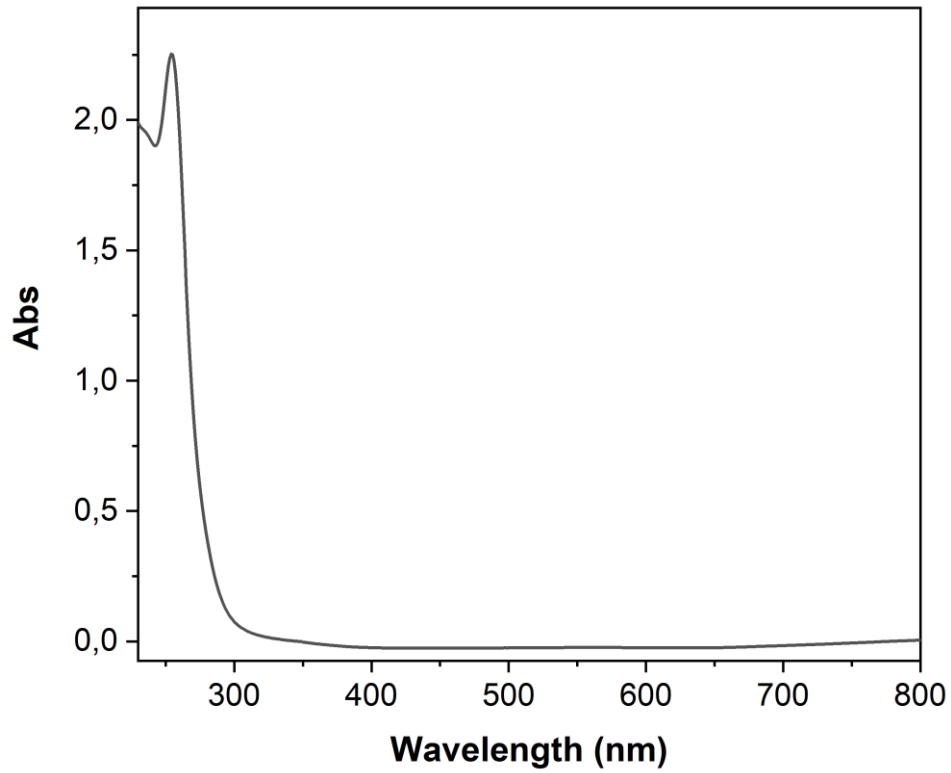

Figure .6.12. UV-Vis spectrum of $KFe(hmds)_3$ in THF.

Transamination of $KFe(hmds)_3$ with rac-tetraphenylethylenediamine.

A solution of *rac*-tetraphenylethylenediamine (9 mg, 24 µmol) in 0.8 mL THF-d_8 was added to solid $K(Et_2O)_{0.74}Fe(hmds)_3$ (15 mg, 24 µmol) and stirred for 10 h at room temp. The reaction was monitored by ^1H NMR spectroscopy whereby the formation of *rac*-**1** was not observed.

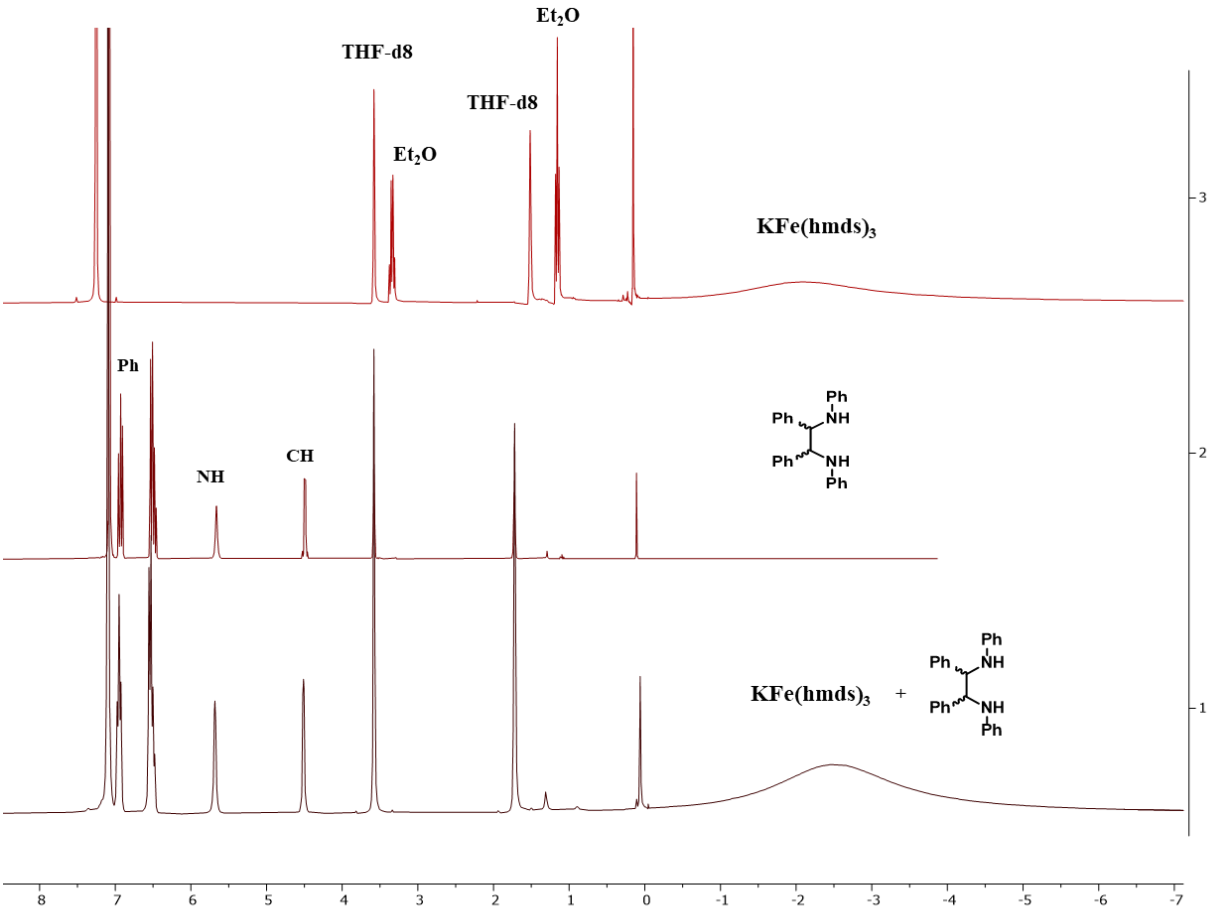

Figure 6.13. ^{1}H NMR monitoring of the attempted transamination of KFe(hmds)$_3$ with *rac*-tetraphenylethylenediamine.

6.5.3. General Procedure of the Catalytic Hydrosilylation of Styrenes

NMR scale reaction.

In an argon-filled glove box, a mixture of *rac*-**1** (3.5 mg, 0.005 mmol, 5 mol%), styrene (0.1 mmol) and $PhSiH_3$ (13 µL, 0.11 mmol) was dissolved in 0.5 mL THF-d_8 and transferred to a J. Young NMR tube with a small stirring bar. The NMR tube was taken outside the glove box and the reaction stirred at the given temperature and time. Then, an aliquot of the reaction mixture was directly subjected to ^{1}H NMR spectroscopy. Another aliquot was quenched with water or in air, extracted with ethyl acetate (2 mL) or passed through a small silica pad and then analyzed by GC-MS. The silane yield was determined by ^{1}H-NMR *vs.* the internal reference mesitylene.

Reaction in THF.

In an argon-filled glovebox, a mixture of *rac*-**1** (6.9 mg, 0.01 mmol, 5 mol%), 0.2 mmol of styrene and $PhSiH_3$ (25 µL, 0.2 mmol) was dissolved in 1 mL of THF in a Schlenk tube containing a stirring bar. The reaction was stirred at the given temperature and time. Then, the mixture was quenched in air and solvent was evaporated under vacuum (100 mbar) to obtain the crude product mixture which was analyzed by ^{1}H

NMR spectroscopy (using mesitylene or CH_2Br_2 as an internal reference) and by GC-MS after extraction with ethyl acetate.

Spectroscopic and analytical data of the products were compared with literature reports (characteristic ^{1}H NMR resonances of the silane products).

6.5.4. Mechanistic Experiments

Stoichiometric reactions of *rac*-1 with styrene: A J. Young NMR tube was charged with a stirring bar, *rac*-**1** (14 mg, 0.02 mmol), 1,3,5-trimethoxybenzene (as internal reference), 0.6 mL THF-d_8 and styrene (4.6 µL, 0.04 mmol). The mixture was heated to 70 °C and reaction progress was monitored by ^{1}H NMR.

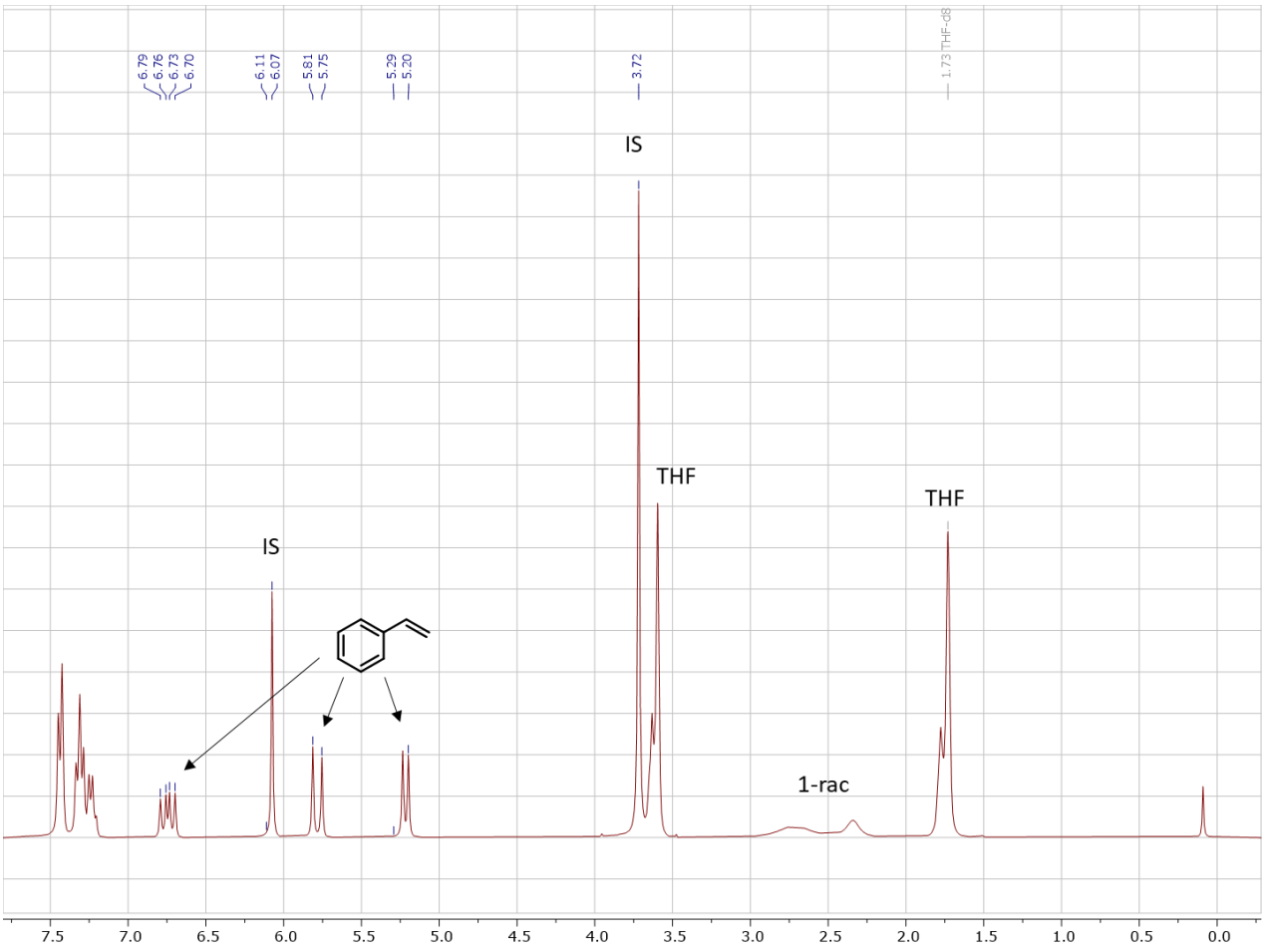

Figure 6.14. ^{1}H NMR monitoring of attempted reaction of *rac*-**1** with styrene, showing no styrene conversion or products formation.

Stoichiometric reactions of *rac*-1 with $PhSiH_3$: A J. Young NMR tube was charged with a stirring bar, *rac*-**1** (14 mg, 0.02 mmol), 1,3,5-trimethoxybenzene (as internal reference), 0.6 mL deuterated solvent and the given number of equivalents $PhSiH_3$. After stirring at indicated temperature, the reaction progress was monitored by ^{1}H NMR; the NMR yields of all diamagnetic products were determined.

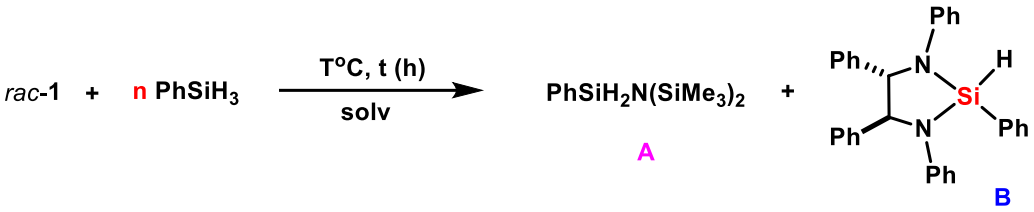

Table 6.2. NMR-scale stoichiometric reactions of *rac*-**1** with $PhSiH_3$.

entry	n (eq)	solvent	T (°C)	time (h)	yield **A**[a]	yield **B**[b]
1	2	THF-d_8	60	18	3	<1
2	2	THF-d_8/toluene-d_8 = 1:5	100	21	60	28
3[c]	20	THF-d_8	60	15	22	16

[a] the identity of compound **A** was also confirmed by ^{1}H-^{29}Si HSQC (Figure 6.18) [b] the identity of compound **B** was proved by independent synthesis (Figure 6.19-6.21); [c] 5.5 mg, 0.008 mmol of *rac*-**1** was used.

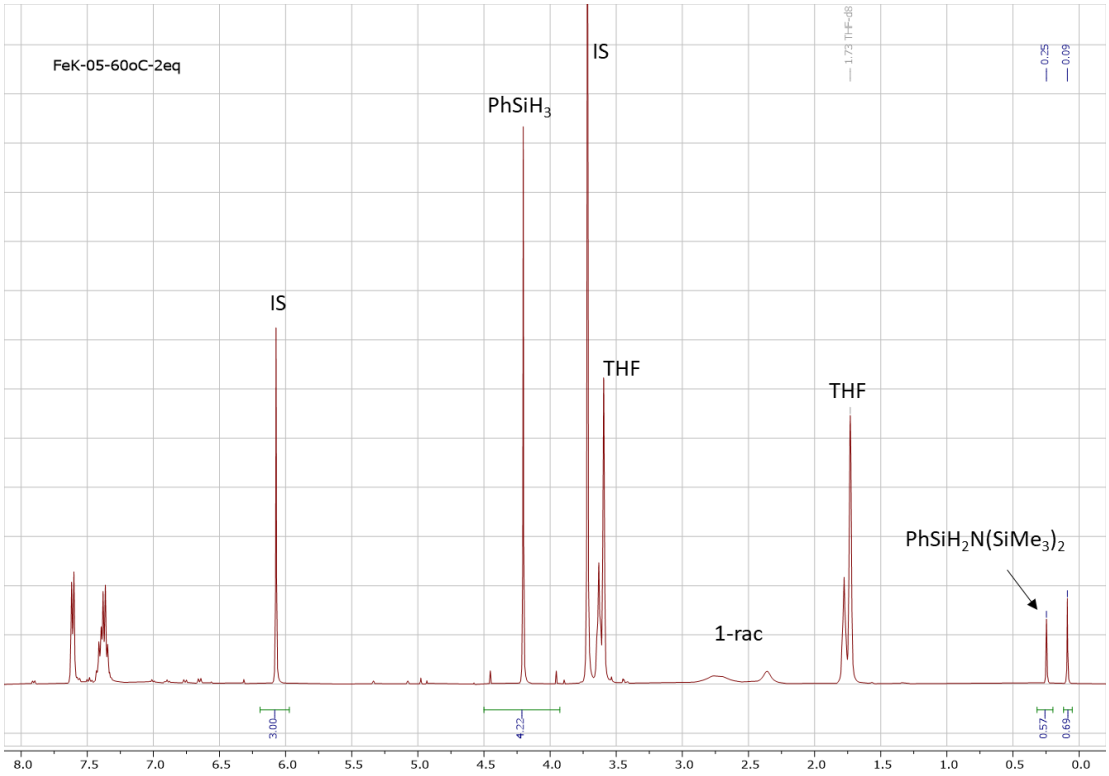

Figure 6.15. ^{1}H NMR (THF-d_8, 300.2 MHz, 298 K) spectrum of reaction of *rac*-**1** with 2 equiv. $PhSiH_3$ (60 °C, 18 h). NMR yields determined *vs.* 1,3,5-trimethoxybenzene (IS). For details, see Table 6.2, entry 1.

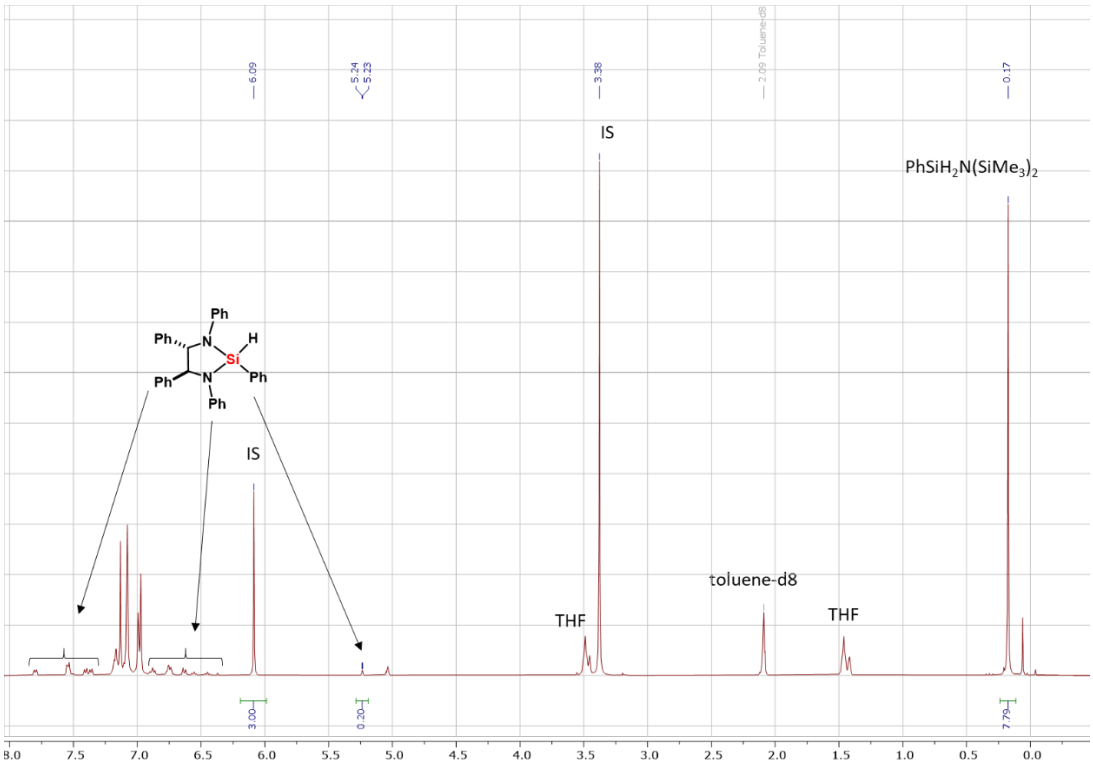

Figure 6.16. ^{1}H NMR (THF-d_8/toluene-d_8, = 5:1, 300.2 MHz, 298 K) spectrum of the reaction of *rac*-**1** with 2 equiv. $PhSiH_3$ (60 °C, 21 h). NMR yields were determined *vs.* 1,3,5-trimethoxybenzene (IS). For details, see Table 6.2., Entry 2.

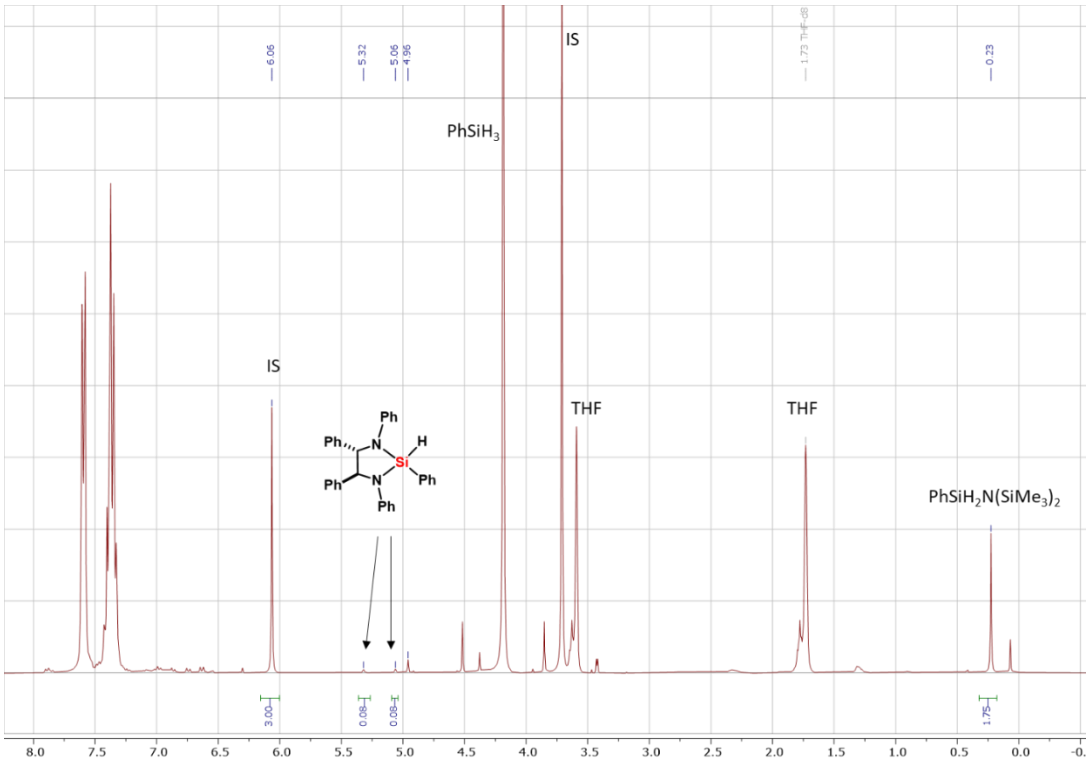

Figure 6.17. ^{1}H NMR (THF-d_8/toluene-d_8 = 5:1, 300.2 MHz, 298 K) spectrum of the reaction of *rac*-**1** with 20 equiv. $PhSiH_3$ (60 °C, 15 h). NMR yields were determined *vs.* 1,3,5-trimethoxybenzene (IS). For details, see Table 6.3., Entry 3.

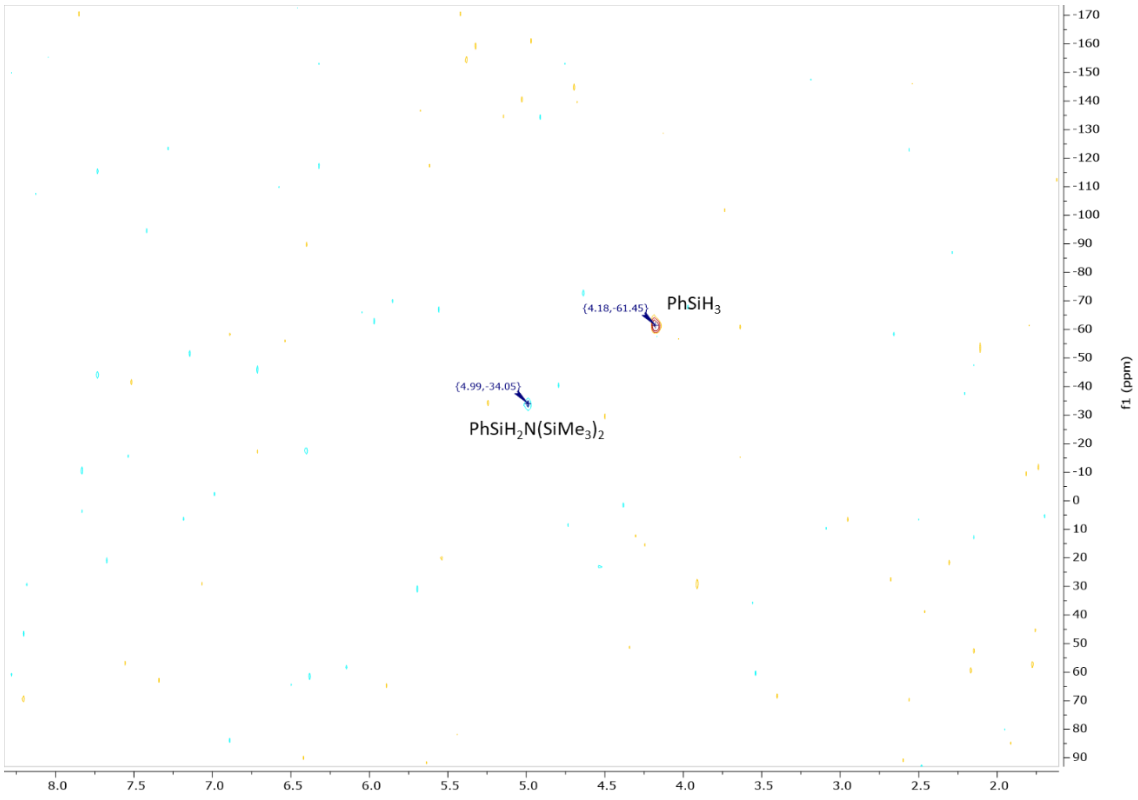

Figure 6.18. ^{1}H-^{29}Si HSQC (THF-d_8/toluene-d_8 = 5:1, 400.1 MHz, 298 °C) spectrum of the reaction of *rac*-**1** with 20 equiv. $PhSiH_3$ at 100 °C. The crosspeak assigned to $PhSiH_2N(SiMe_3)_2$ in agreement with literature.[4]

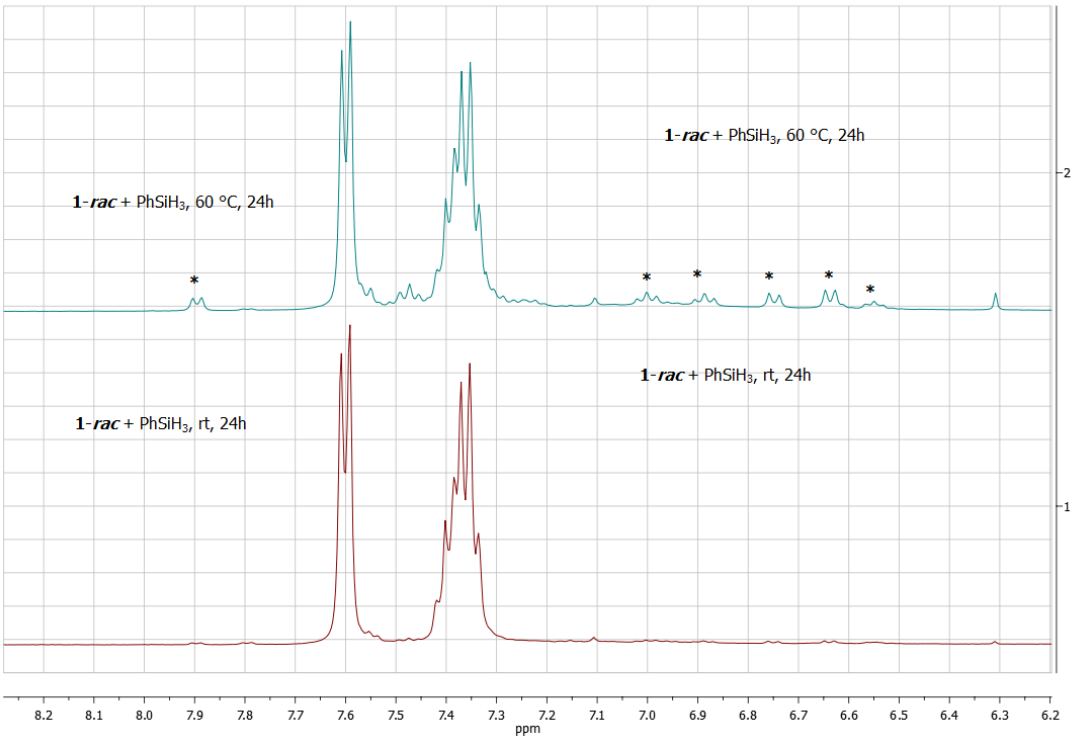

Figure 6.19. ^{1}H NMR monitoring (in the region δ = 6 – 8 ppm) of *rac*-**1** with $PhSiH_3$ in THF-d_8.

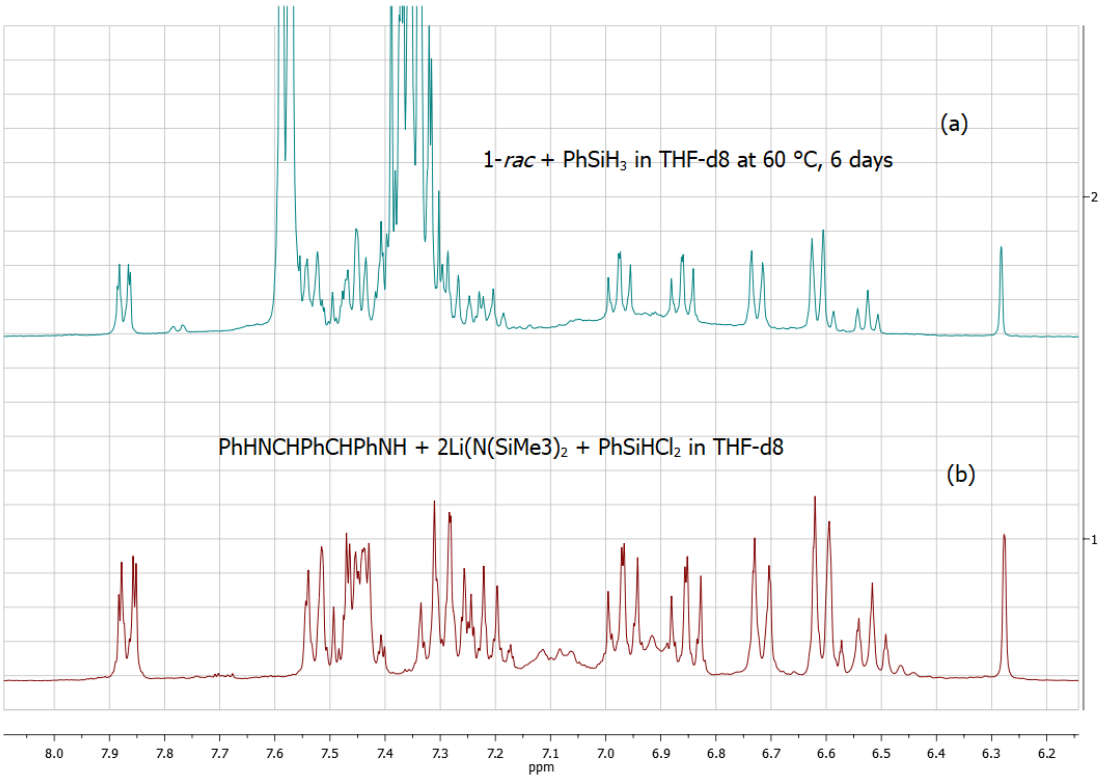

Figure 6.20. ^{1}H NMR (THF-d$_8$) spectra (in the region δ = 6 – 8 ppm) of: a) *rac*-**1** with PhSiH$_3$ in THF-d$_8$ (60 °C, 6 d); b) the reaction mixture of ^{Ph}LH$_2$ with 2 equiv. LiN(SiMe$_3$)$_2$ and PhSiCl$_2$H in THF-d$_8$ at 20 °C showing the formation of the same product.

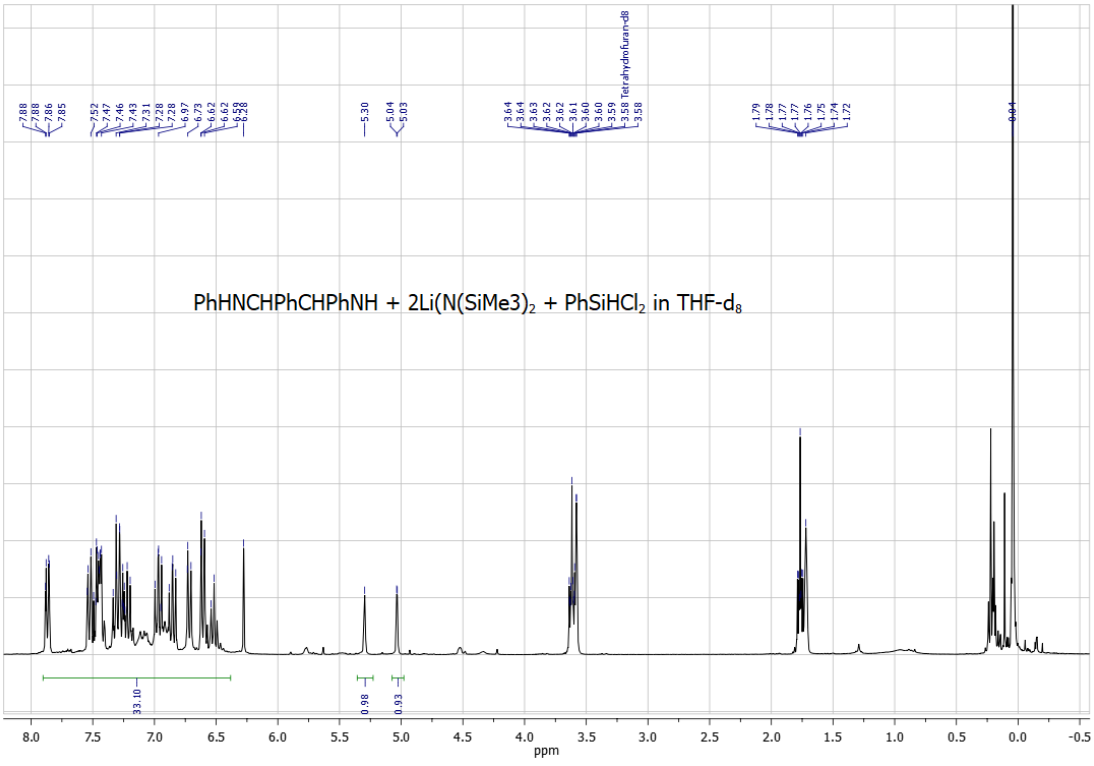

Figure 6.21. ^{1}H NMR (THF-d$_8$) spectrum of the reaction mixture of ^{Ph}LH$_2$ with 2 equiv. LiN(SiMe$_3$)$_2$ and PhSiCl$_2$H in THF-d$_8$ at 20 °C showing the formation of (^{Ph}L)SiHPh.

Acceleration of the reaction of *rac*-1 with $PhSiH_3$ in the presence of styrene:

A J. Young NMR tube was charged with a stirring bar, *rac*-**1** (5.5 mg, 0.008 mmol), 1,3,5-trimethoxybenzene (as internal reference), 0.6 mL THF-d_8, $PhSiH_3$ (20 µL, 0.16 mmol, 20 equiv.) and styrene (4.6 µL, 0.04 mmol, 5 equiv.). The mixture was heated to 60 °C and reaction progress was monitored by ^1H NMR. The NMR yield of $PhSiH_2N(SiMe_3)_2$ was determined *vs.* 1,3,5-trimethoxybenzene as internal reference.

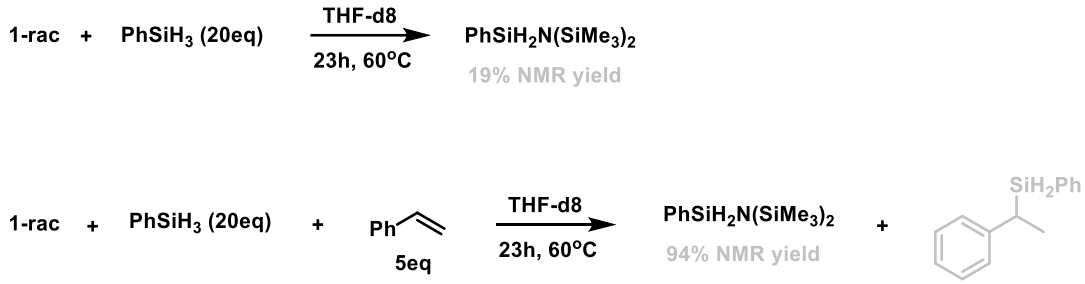

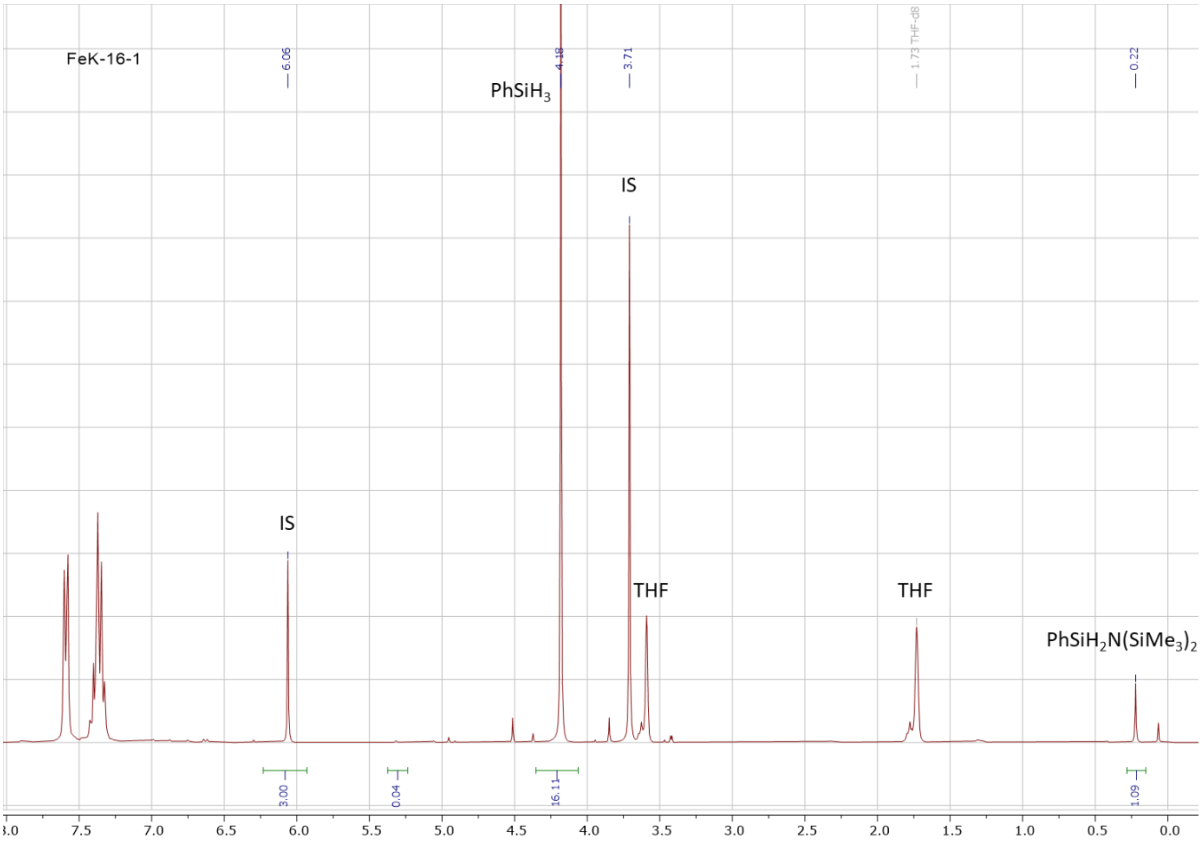

Figure 6.22. ^1H NMR (THF-d_8, 300.2 MHz, 298 K) spectrum of the reaction of *rac*-**1** with 20 equiv. $PhSiH_3$ at 60 °C after 23 h. NMR yields were determined *vs.* 1,3,5-trimethoxybenzene (IS).

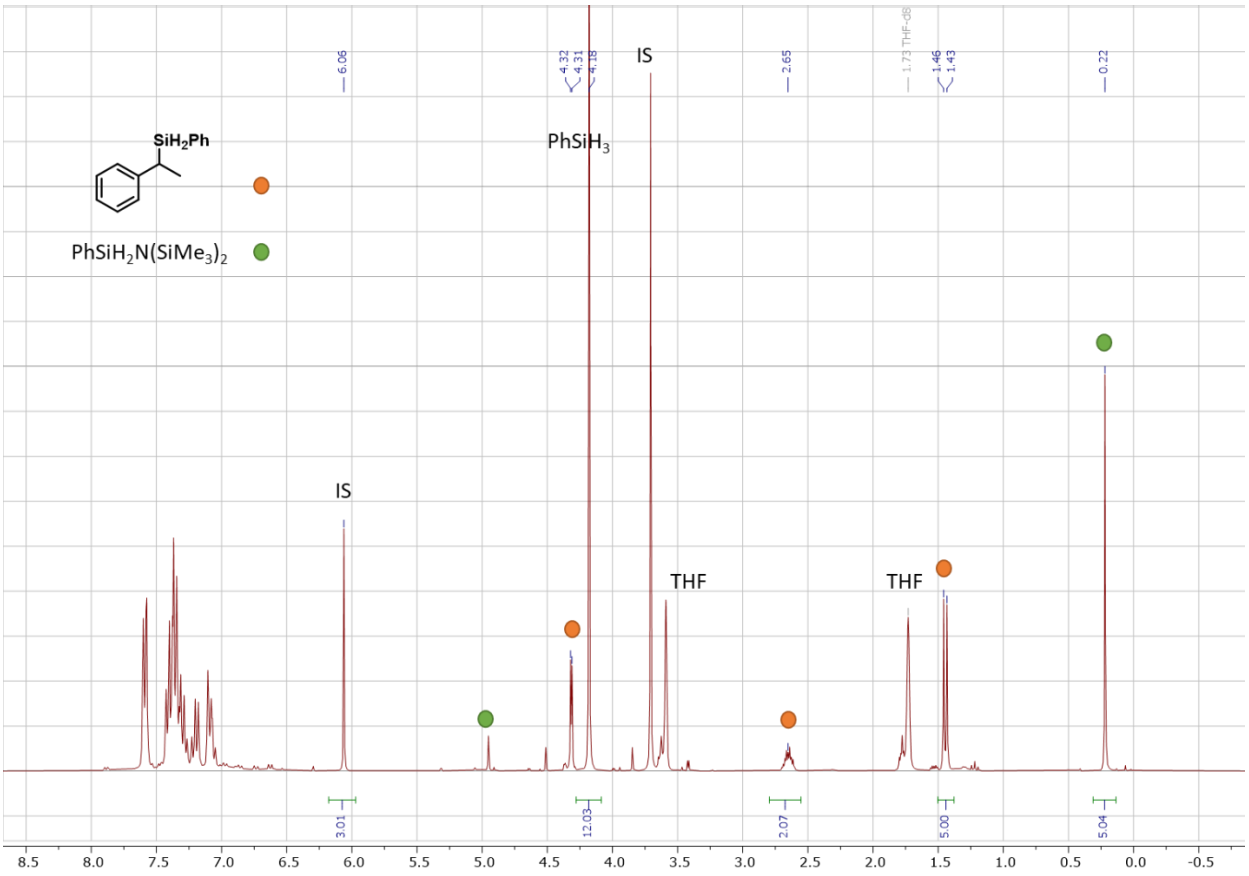

Figure 6.23. ^{1}H NMR (THF-d_8, 300 MHz, 298 K) spectrum of reaction of *rac*-**1** with 20 equiv. $PhSiH_3$ in the presence of styrene at 60 °C after 23 h. NMR yields determined vs. 1,3,5-trimethoxybenzene (IS).

Catalytic hydrosilylation of $PhCH=CD_2$ (0.1 mmol) with $PhSiH_3$ in THF-d_8 (0.5 mL) at 60 °C after 24 h:

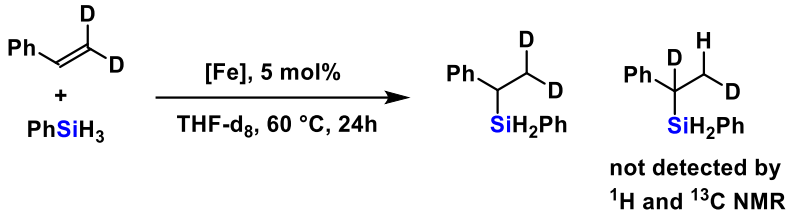

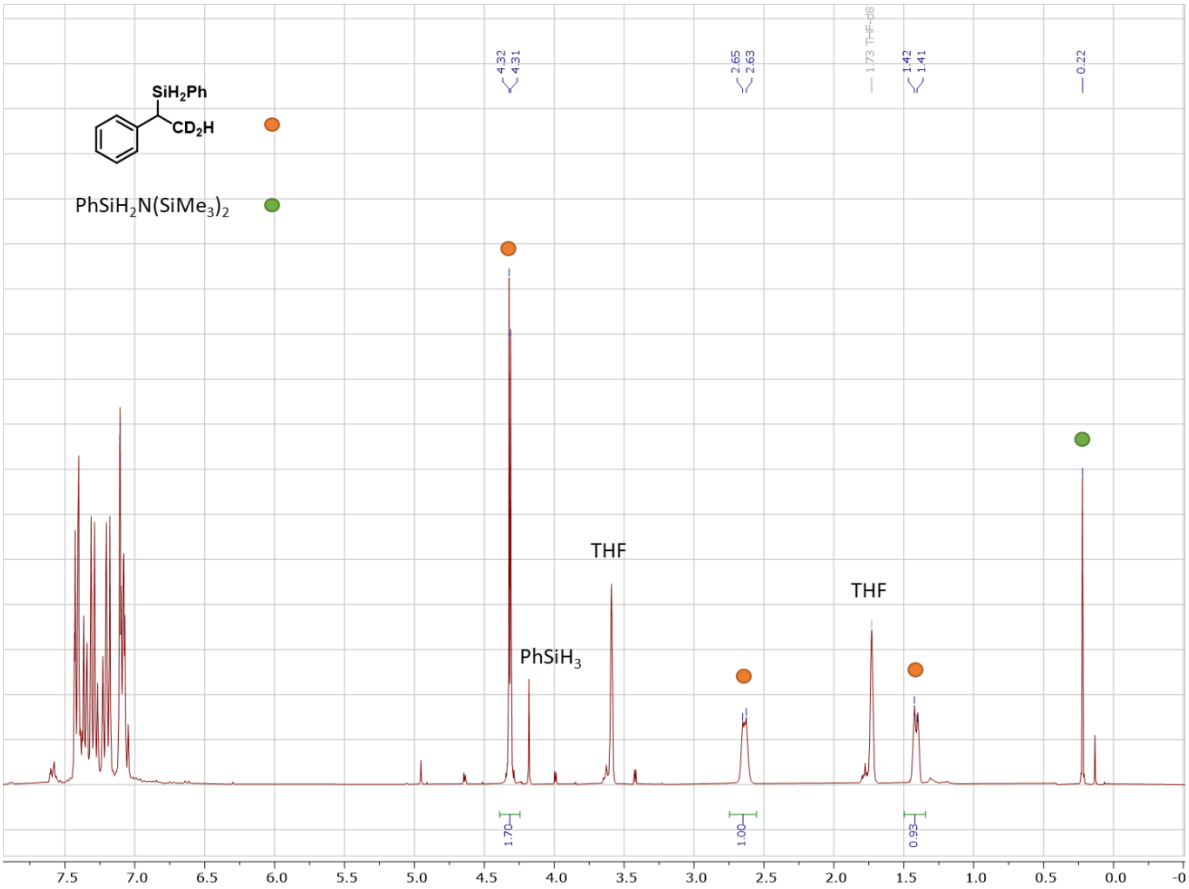

Figure 6.24. ^1H NMR (THF-d_8, 300.2 MHz, 298 K) of the reaction mixture showing only formation of $PhCH(SiH_2Ph)CD_2H$.

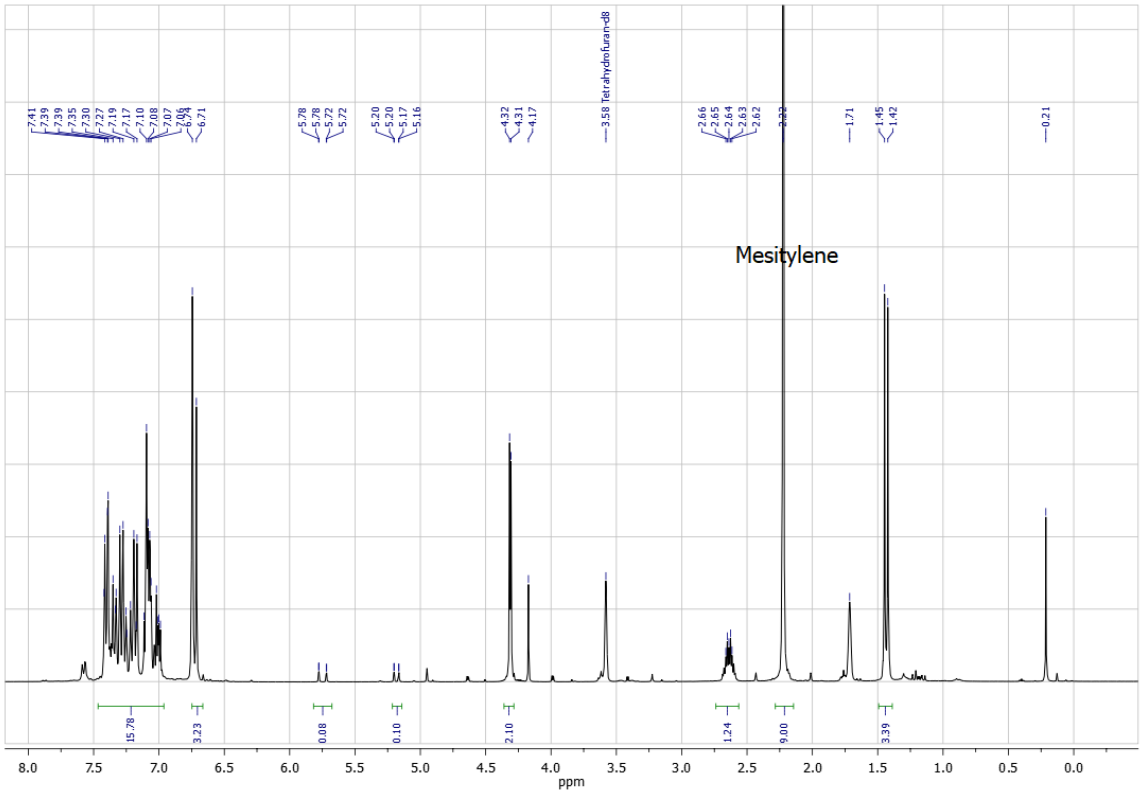

Figure 6.25. ^{1}H NMR (THF-d_8, 300.2 MHZ, 298 K) of the reaction mixture showing only formation of $PhCH(SiH_2Ph)CH_3$.[6]

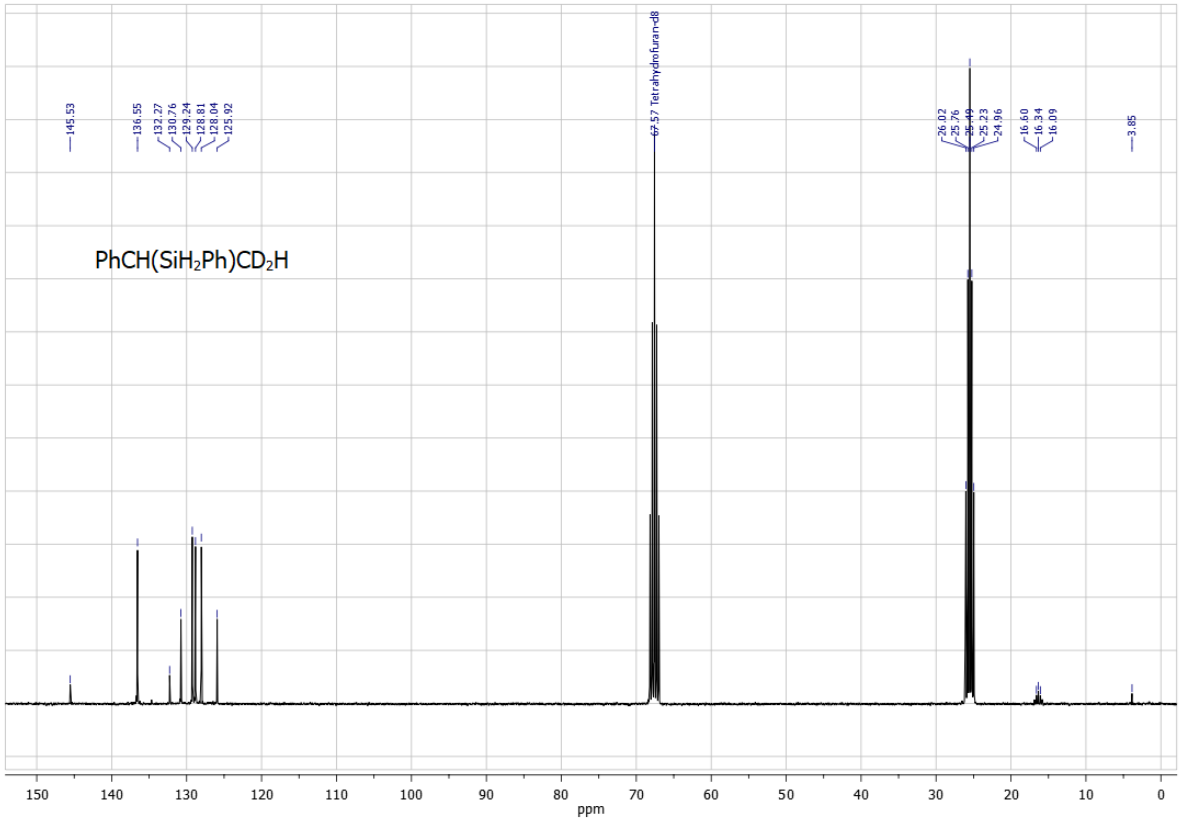

Figure 6.26. $^{13}C\{^{1}H\}$ NMR (THF-d_8, 75.5 MHz, 298 K) of the reaction mixture showing only formation of $PhCH(SiH_2Ph)CD_2H$.

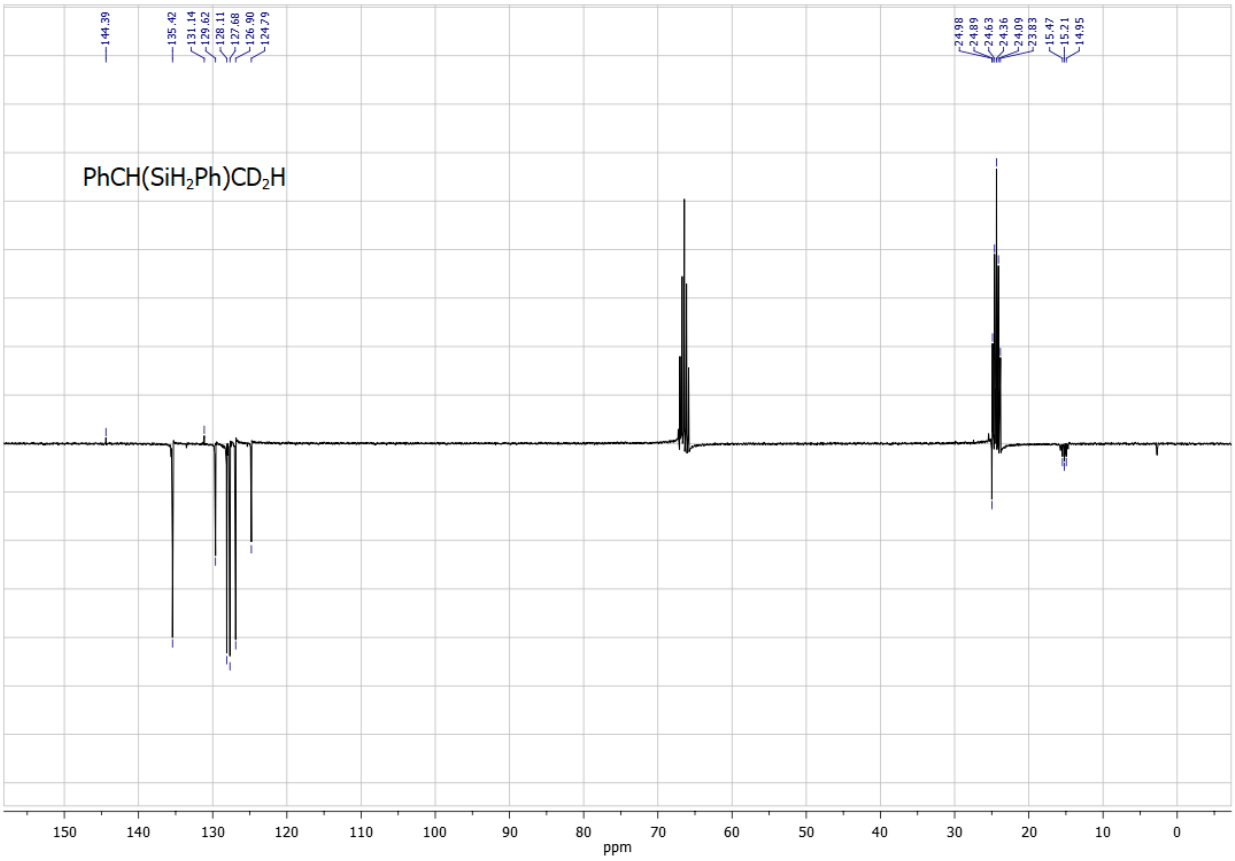

Figure 6.27. DEPTQ NMR (THF-d_8, 75.5 MHZ, 298 K) of the reaction mixture showing only formation of $PhCH(SiH_2Ph)CD_2H$.

Test of hydrosilylation of styrene by catalytic (^{Ph}L)SiHPh.

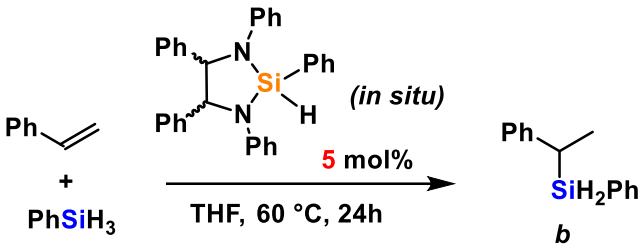

Yield: 0 (33% conversion)

(^{Ph}L)SiHPh was generated *in situ* by reaction of ^{Ph}LH$_2$ with 2 equiv. LiN(SiMe$_3$)$_2$ followed by addition of PhSiHCl$_2$ in THF.

Catalytic hydrosilylation of styrene (0.2 mmol) with PhSiH$_3$ (0.2 mmol) was carried out with 5 mol% of in situ generated (^{Ph}L)SiHPh at 60 °C for 24 h.

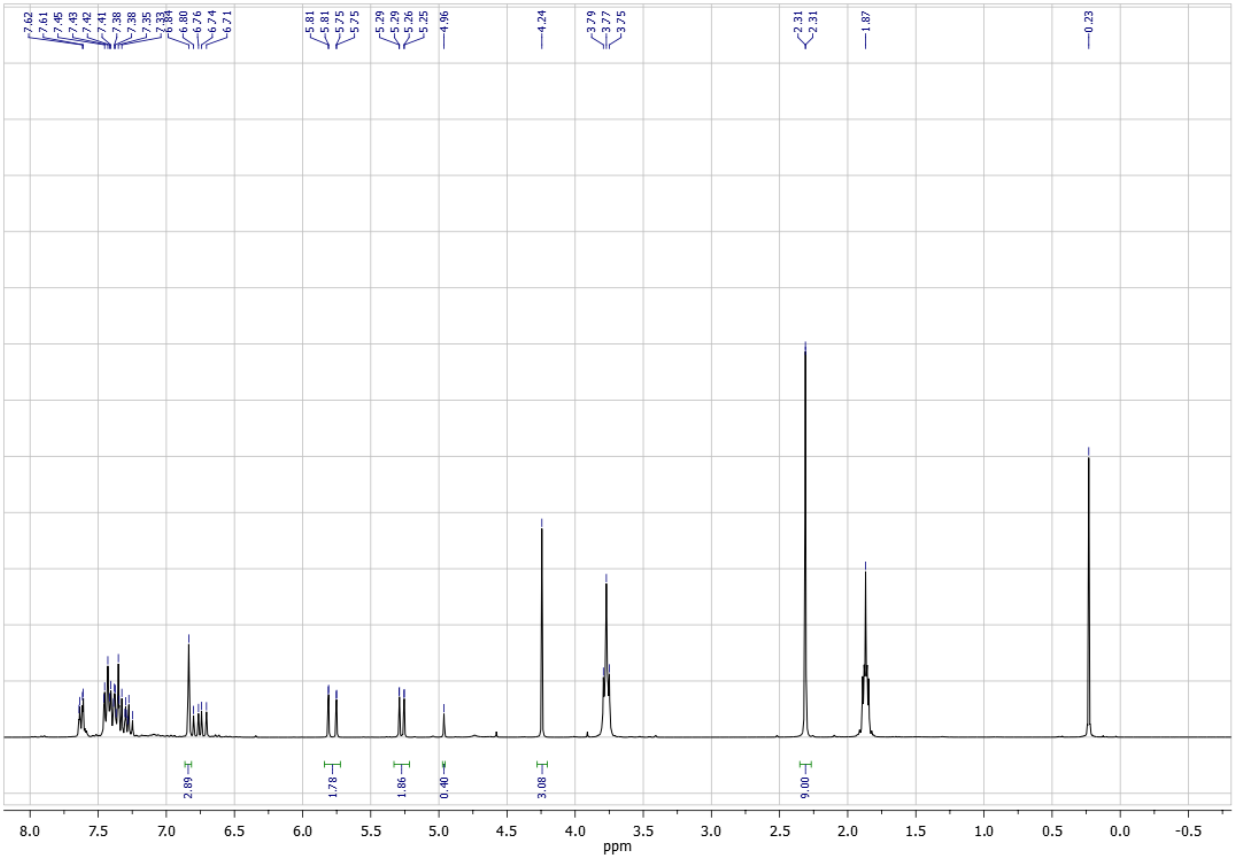

Figure 6.28. ^{1}H NMR (CDCl$_3$, 300.2 MHz, 298 K) of the reaction mixture showing only unreacted styrene and PhSiH$_3$ (mesitylene as internal standard).

6.5.5. ^{1}H NMR spectra of hydrosilylation products.

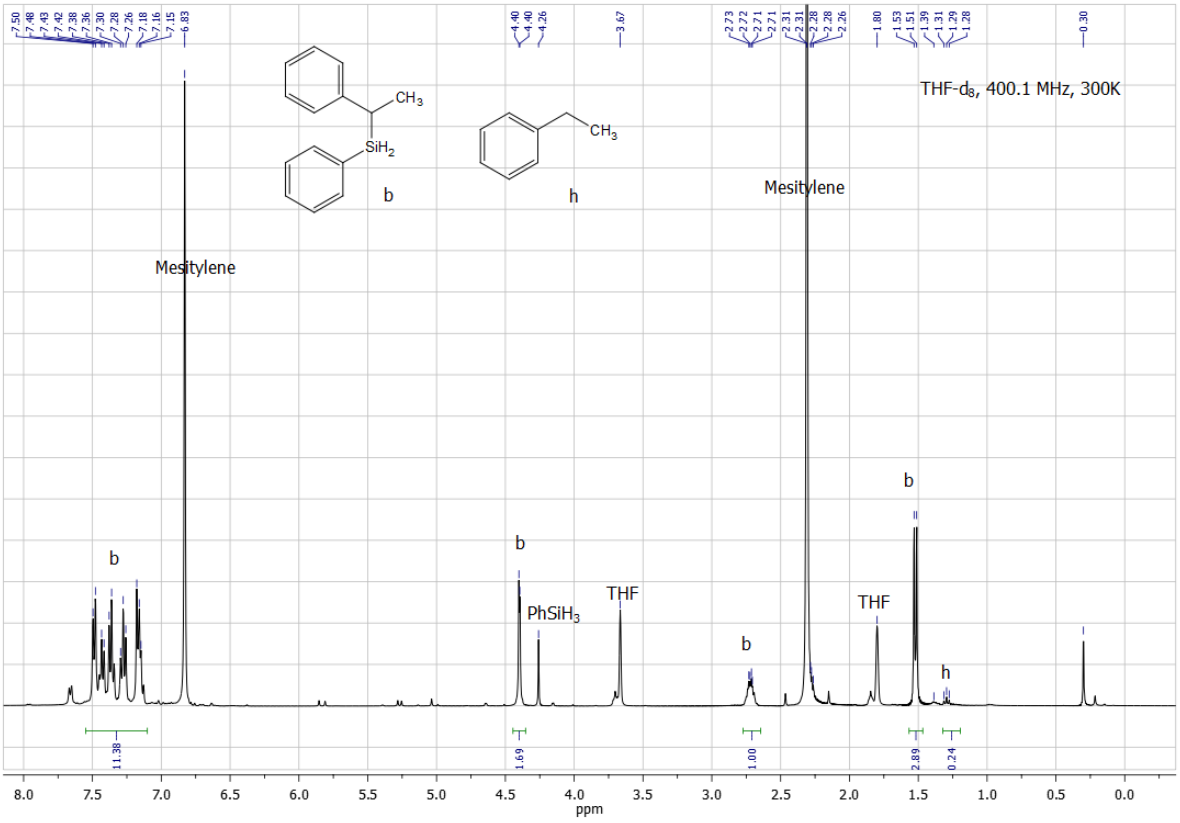

Figure 6.29. ^{1}H NMR spectrum of crude product mixture of hydrosilylation of styrene.[5]

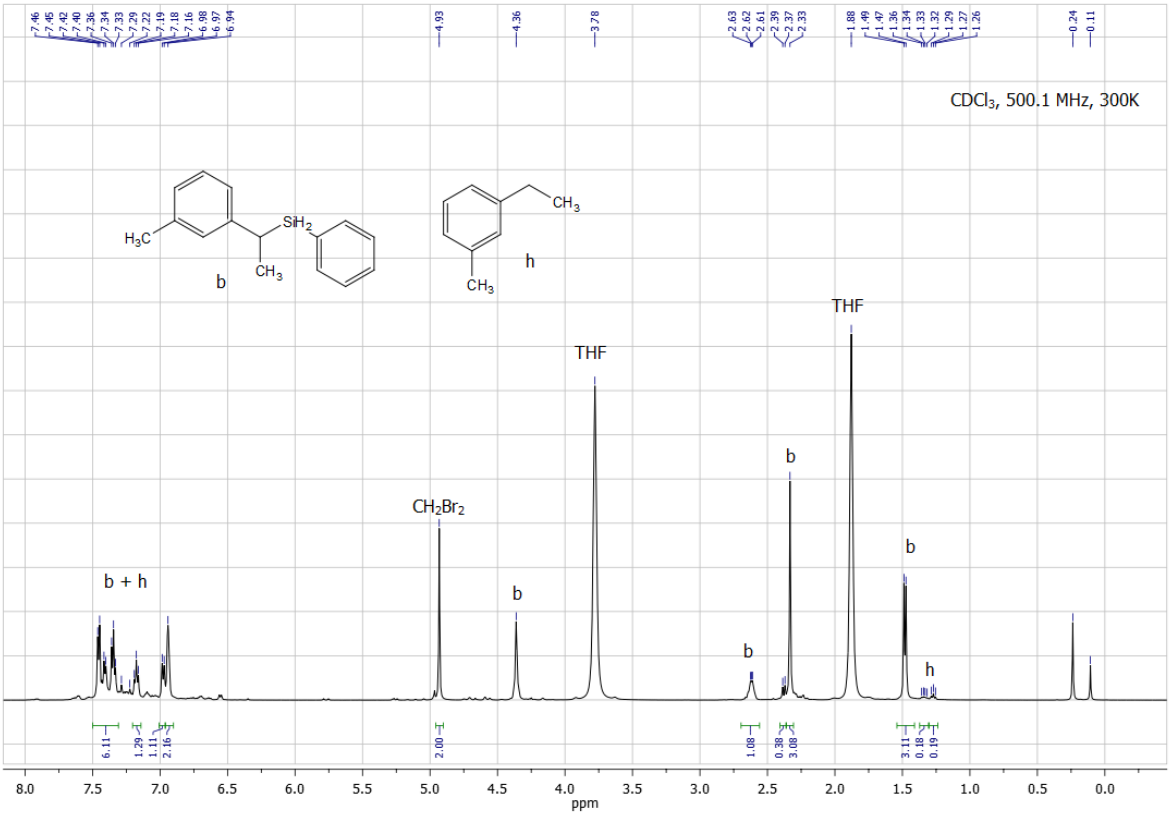

Figure 6.30. ^{1}H NMR spectrum of crude product mixture of hydrosilylation of styrene.[6]

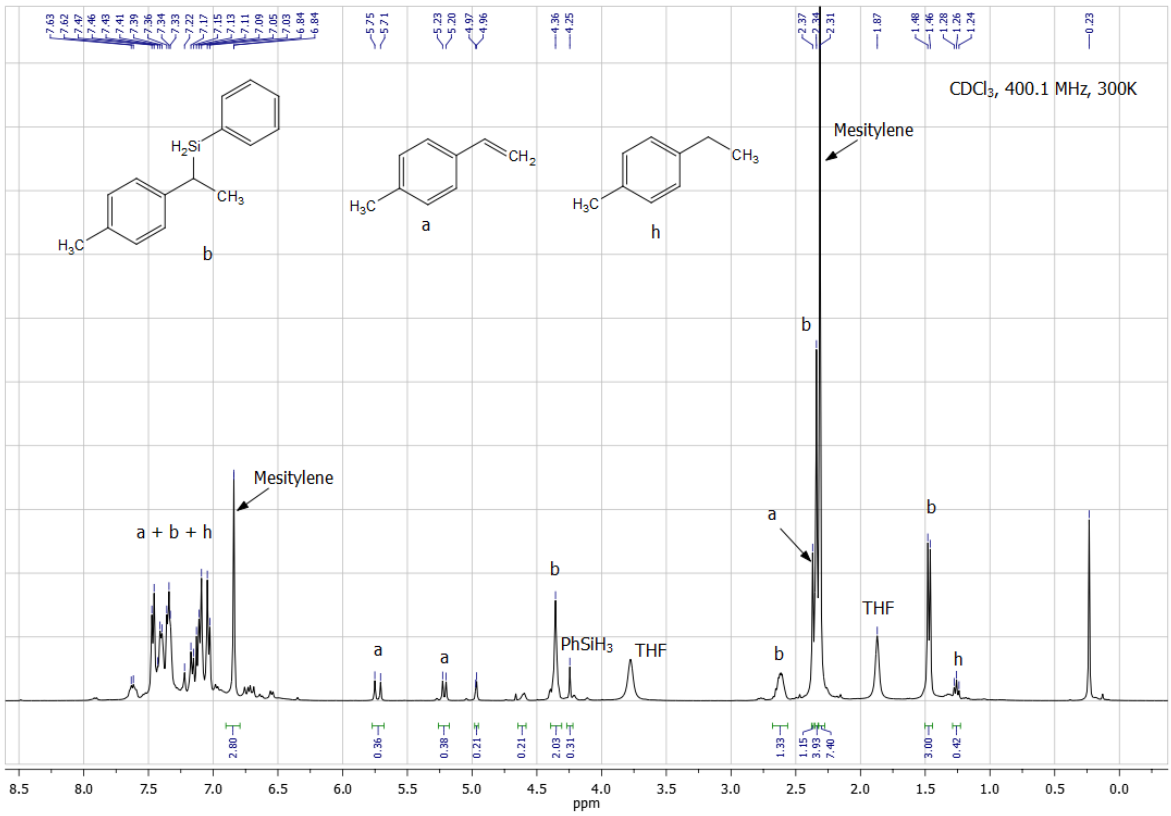

Figure 6.31. ^{1}H NMR spectrum of crude product mixture of hydrosilylation of 4-Methylstyrene. Conditions: THF, 60 °C, 68 h. Spectral data in accordance with report.[6]

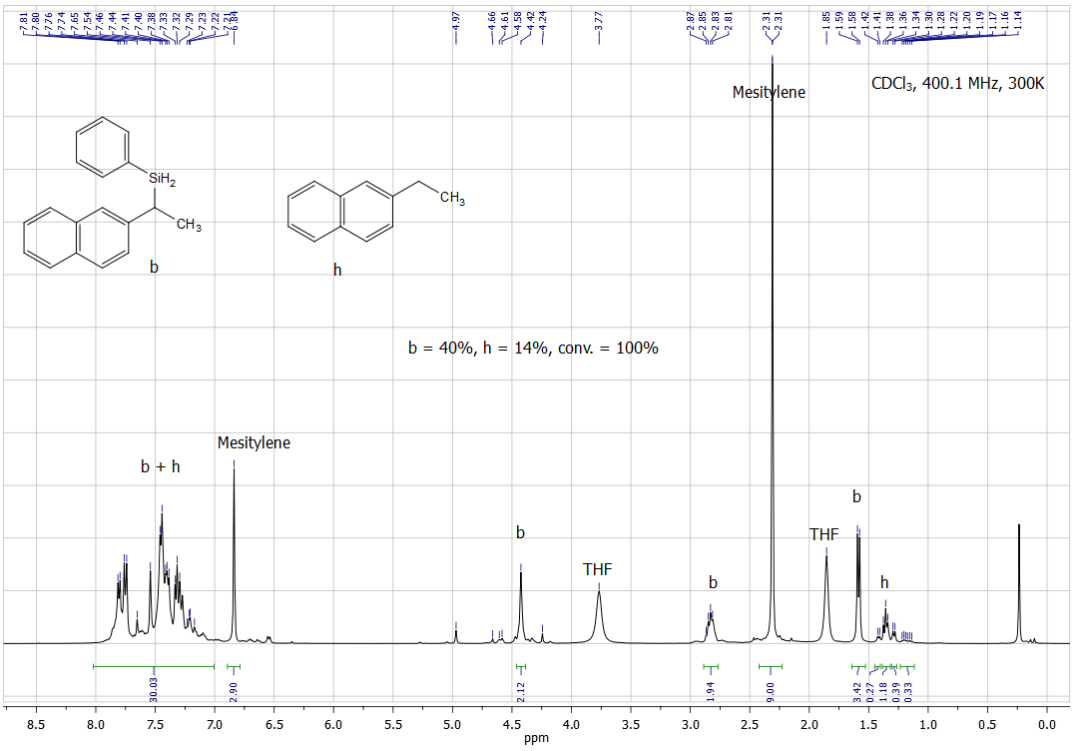

Figure 6.32. ^{1}H NMR spectrum of crude product mixture of hydrosilylation of 2-vinylnaphthalene. Conditions: THF, 60 °C, 68 h. Spectral data in accordance with the reports.[5][6]

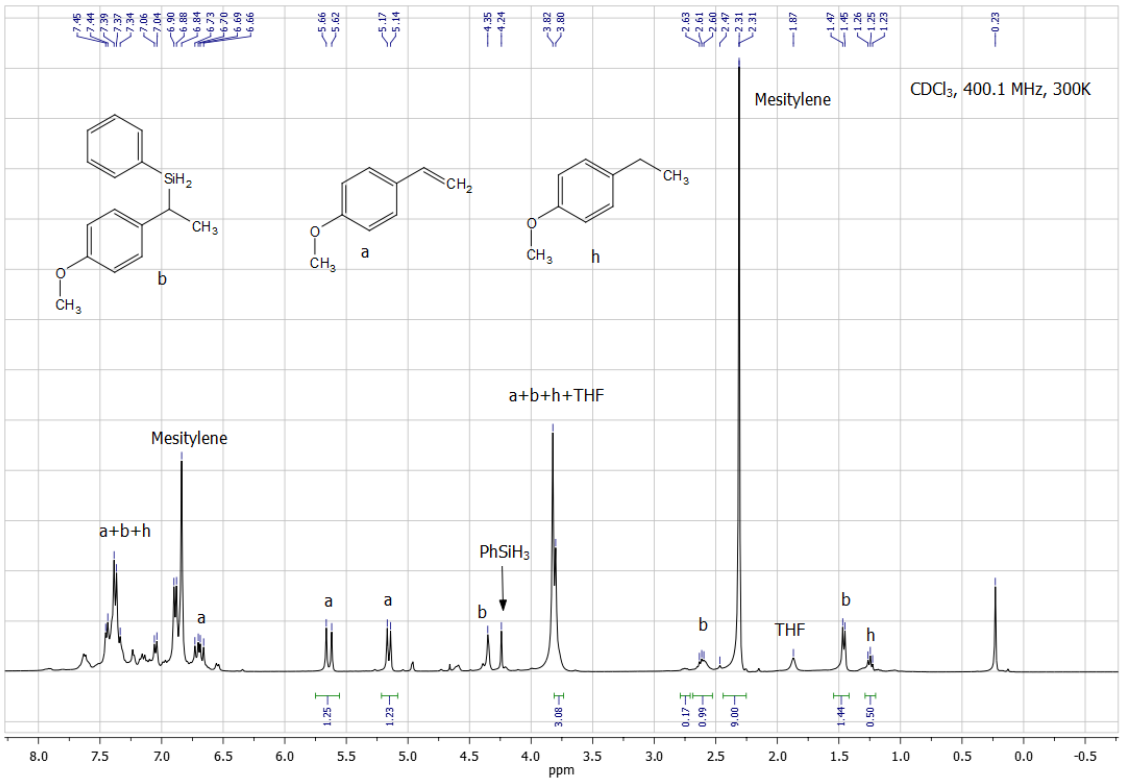

Figure 6.33. ^{1}H NMR spectrum of crude product mixture of hydrosilylation of 4-Vinylanisole. Conditions: THF, 60 °C, 68 h. Spectral data in accordance with reports.[5,6]

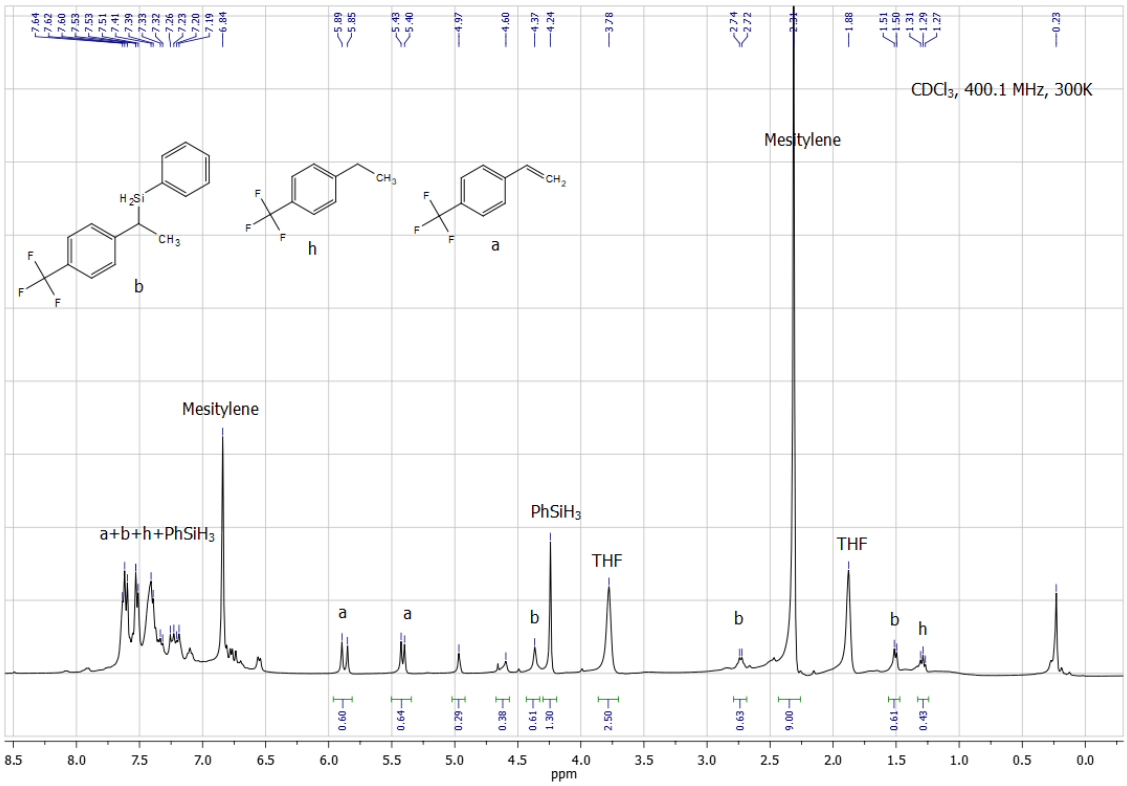

Figure 6.34. ^{1}H NMR spectrum of crude product mixture of hydrosilylation of 4-(Trifluoromethyl)styrene. Conditions: THF, 60 °C, 68 h. Spectral data in accordance with report. [5]

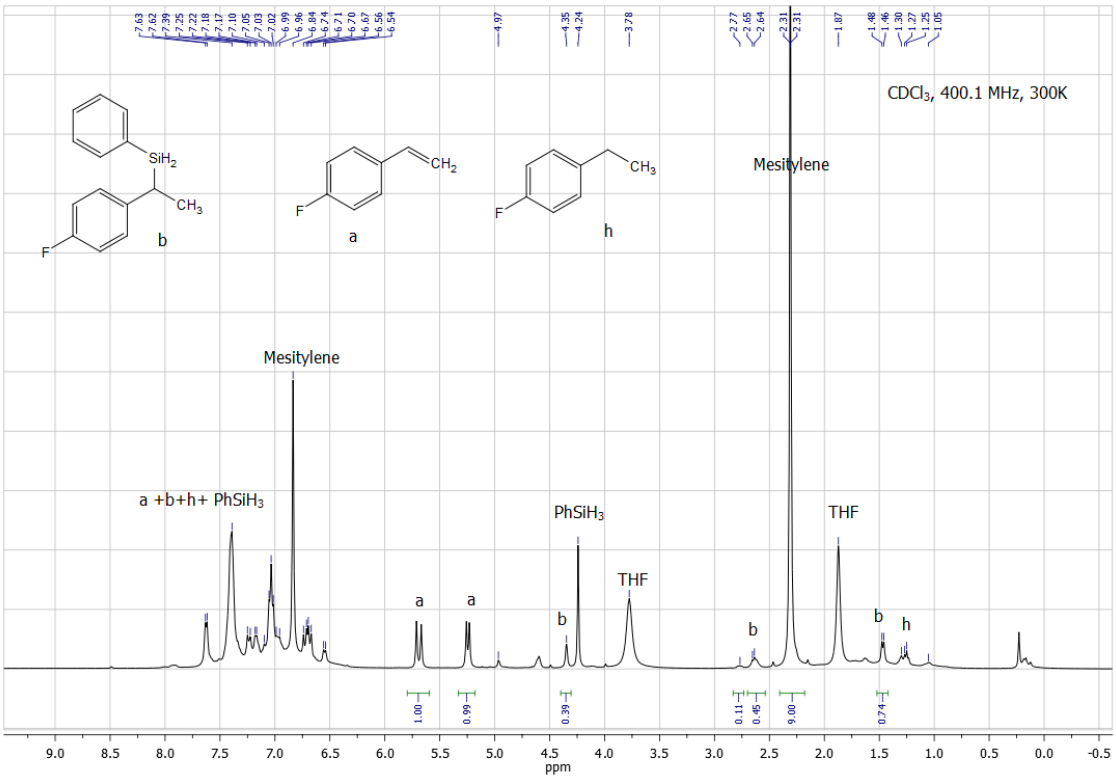

Figure 6.35. ^{1}H NMR spectrum of crude product mixture of hydrosilylation of 4-fluorostyrene. Conditions: THF, 60 °C, 68 h. Spectral data in accordance with reports. [5,6]

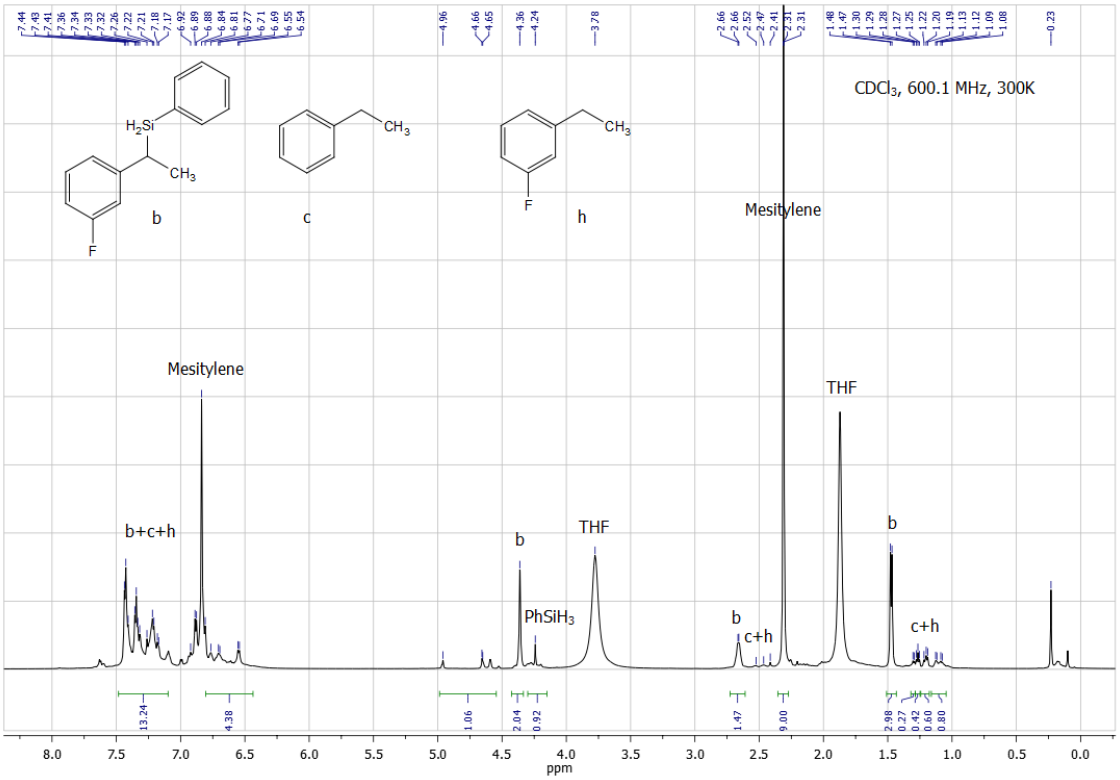

Figure 6.36. ^{1}H NMR spectrum of crude product mixture of hydrosilylation of 3-Fluorostyrene. Conditions: THF, 60 °C, 68 h. Spectral data in accordance with report.[6]

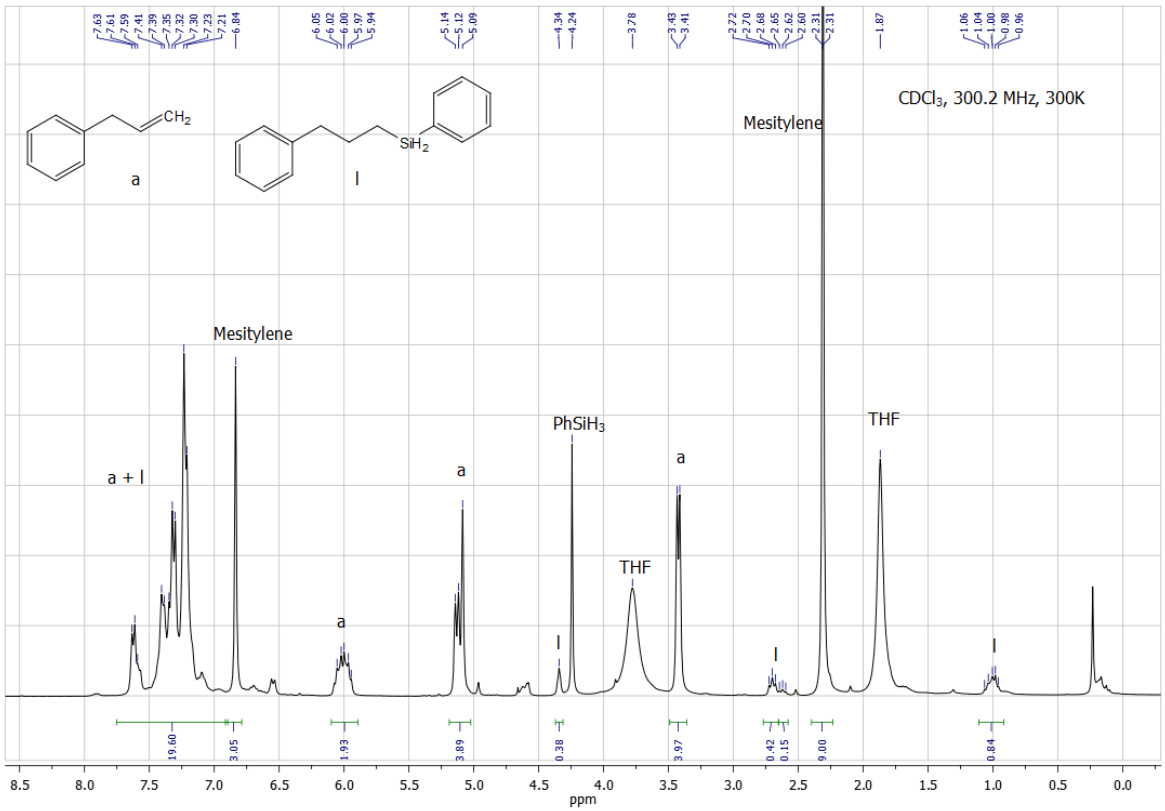

Figure 6.37. ^{1}H NMR spectrum of crude product mixture of hydrosilylation of allylbenzene. Conditions: THF, 60 °C, 24 h. Spectral data in accordance with report.[6]

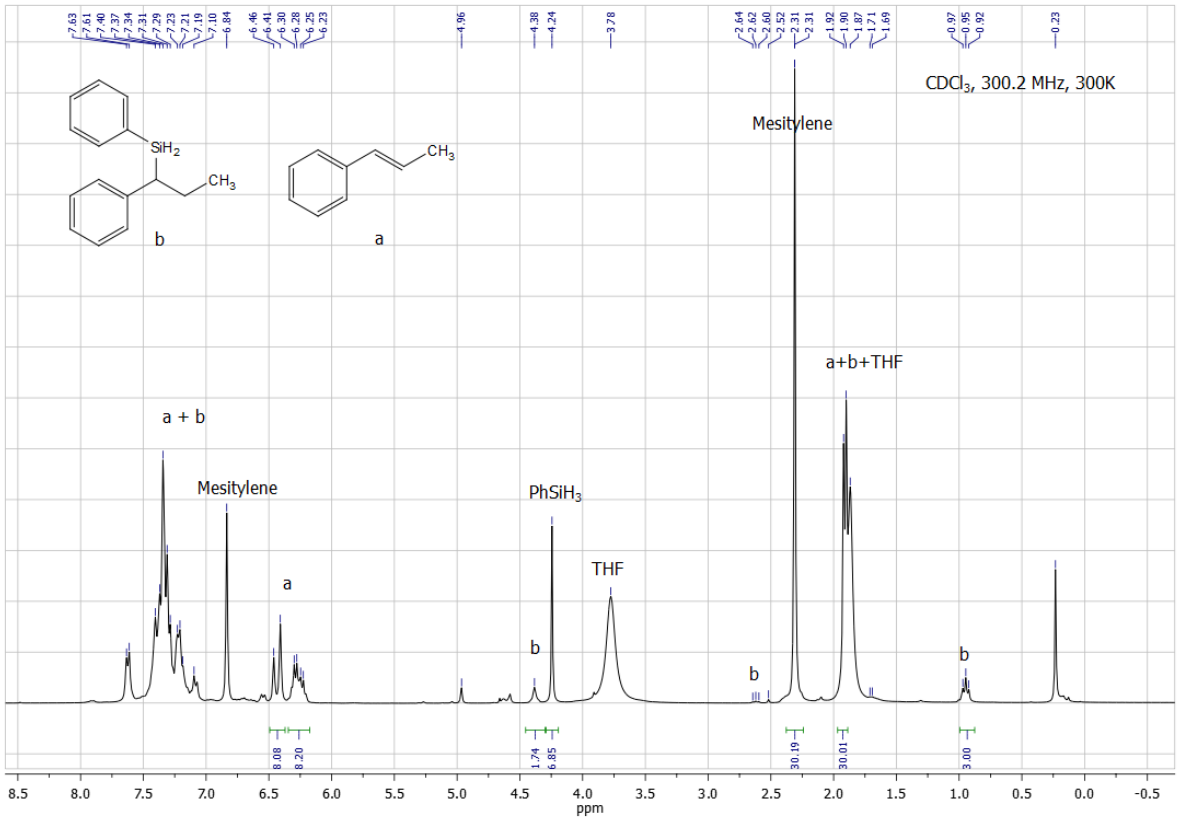

Figure 6.38. ^{1}H NMR spectrum of crude product mixture of hydrosilylation of *trans*-β-Methylstyrene. Conditions: THF, 60 °C, 24 h. Spectral data in accordance with report.[6]

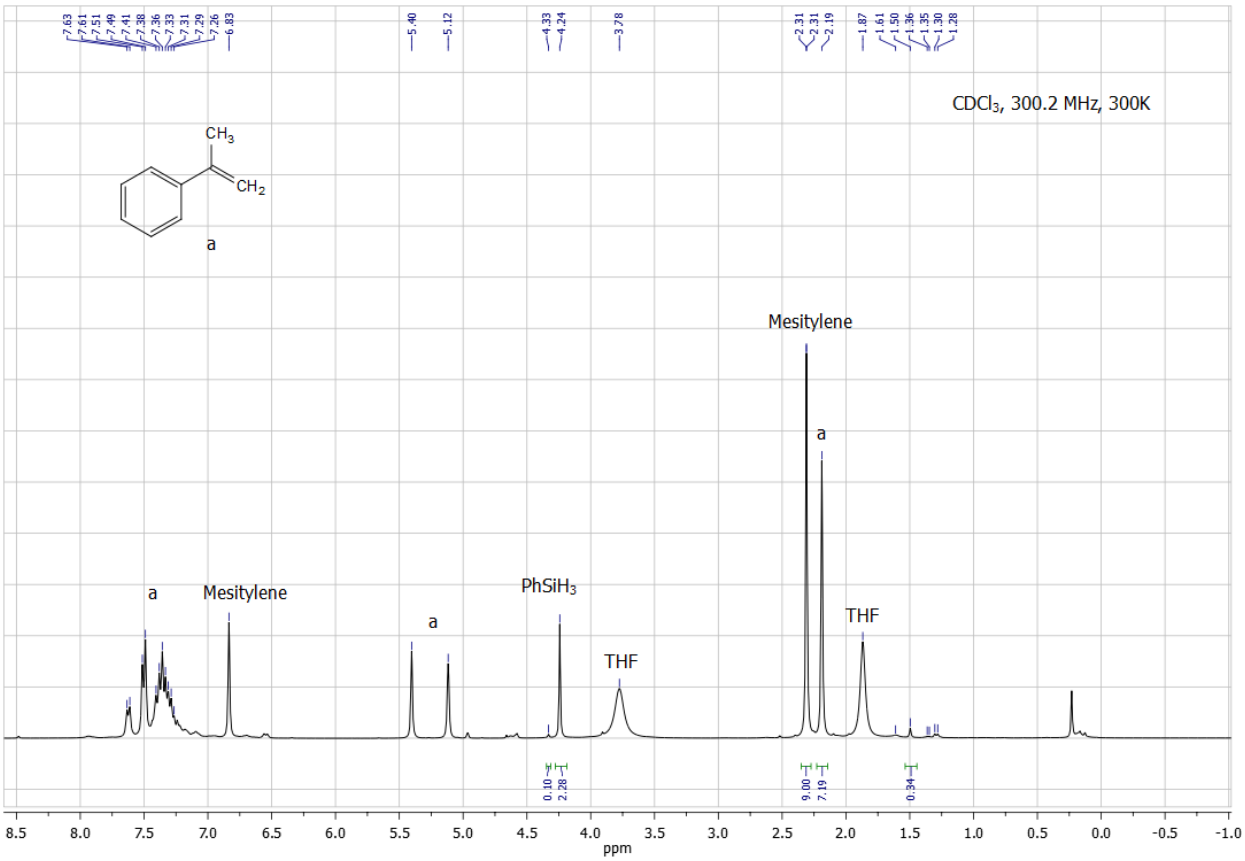

Figure 6.39. ^{1}H NMR spectrum of crude product mixture of hydrosilylation of α-methylstyrene. Conditions: THF, 60 °C, 24 h. Spectral data in accordance with report.[6]

6.5.6. Literature Overview of Catalysts in Hydrosilylaton of Alkenes

Table 6.3. Overview of Fe catalysts and reaction conditions in Markovnikov-selective hydrosilylations of alkenes.

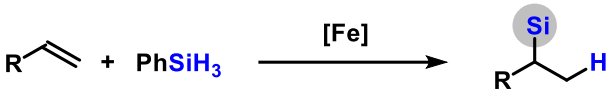

Entry	Catalyst	R	cat. (mol%)	Solvent	T °C	t, h	additives	scope	ref
1	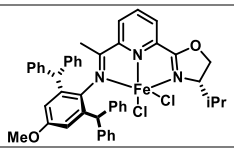	alkyl	5	THF	rt	2	NaO*t*Bu	30 examples; up to 97% yield	[7]
2	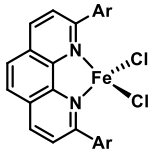 Ar = 3,5-(^{t}Bu)$_2$C$_6$H$_3$ 2,4,6-(^{i}Pr)$_3$C$_6$H$_2$	alkyl aryl	2-5	THF, PhMe or neat	30-35	10	EtMgBr	27 examples for styrenes: 88-95% yield r.r. >98/2	[6]
3*	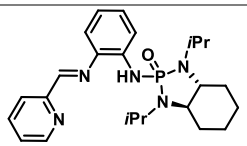 + $FeBr_2$	aryl	5	THF	40	24	NaO*t*Bu	17 examples; 30-99% yield; r.r. 19/1 to 99/1	[8]

* Ph_2SiH_2 silane was used

6.5.7. X-ray Crystallography

Single-crystal X-ray experiments were performed at 100 K using a SuperNova four-circle diffractometer in Kappa geometry with a 50 W Cu or Mo (Kα radiation) microfocus tube, an Atlas CCD detector (Rigaku Oxford Diffraction), and a Cryostream 700 Plus cooler (Oxford Cryosystems Ltd). Data collection, cell refinement, data reduction, and absorption correction were done using CrysAlisPro [9]. Intensities were measured using omega scans.

Single-crystal X-ray data was solved and refined as follows: The space group was determined either by using XPREP (Bruker AXS Inc. [10]) or CrysAlisPro and the phase problem was solved either (a) by structure-invariant direct methods with SHELXS [11], or (b) by using the dual-space algorithm implemented in SHELXT [12]. In every case, full-matrix least-squares refinement was done on F^2 using SHELXL [12].

Missing secondary atom sites were located from the difference Fourier map. If possible, non-hydrogen atoms were refined using individual, anisotropic displacement parameters. The fully refined data was reviewed using PLATON [13]. Carbon atom-bound hydrogen atoms were positioned geometrically and refined riding on their respective parent atoms. U_{iso}(H) was fixed at 1.5 (CH_3) or 1.2 (all other H atoms) of the parent atom's isotropic displacement parameter.

Table .6.4. Crystallographic data for compounds **1, 2, KFe(hmds)$_3$**

Identification code	***rac*-1•6C$_4$H$_8$O**	***meso-1*•C$_4$H$_{10}$O**
Empirical formula	$C_{56}H_{88}FeKN_3O_6Si_2$	$C_{36}H_{50}FeKN_3OSi_2$
Formula weight	1050.42	691.92
T/K	99.97(12)	99.9(3)
Crystal system	triclinic	monoclinic
Space group	P-1	$P2_1/n$
a/Å	16.5320(3)	12.8273(5)
b/Å	18.4489(3)	21.6003(5)
c/Å	19.5309(3)	13.8994(5)
α/°	90.1440(10)	90
β/°	90.378(2)	98.104(4)
γ/°	99.197(2)	90
Volume/Å^3	5880.13(17)	3812.7(2)
Z	4	4
ρ_{calc}g/cm^3	1.187	1.205
μ/mm^{-1}	3.454	4.976
Crystal size/mm^3	0.299 × 0.182 × 0.049	0.30 × 0.12 × 0.09
Radiation	Cu Kα (λ = 1.54184)	CuKα (λ = 1.54184)
2Θ range /°	6.624 to 152.278	7.618 to 152.296
Reflections collected	73371	38633
Independent reflections	24229 [R_{int} = 0.0561, R_{sigma} = 0.0546]	7869 [R_{int} = 0.0502, R_{sigma} = 0.0345]
Data/restraints /parameters	24229/1394/1307	7869/0/397
GoF	1.032	1.052
R ind. [I>=2σ (I)]R_1 (wR_2)	R_1 = 0.0673, wR_2 = 0.1682	R_1 = 0.0386, wR_2 = 0.0989
Final R ind. [all data] R_1 (wR_2)	R_1 = 0.0762, wR_2 = 0.1751	R_1 = 0.0498, wR_2 = 0.1063
Largest diff. peak/hole / e Å^{-3}	0.82/-0.67	0.35/-0.33

Identification code	**2a**•2C_4H_8O	**2b**•3C_4H_8O	**KFe(hmds)$_3$**•2$C_4H_{10}O$
Empirical formula	$C_{64}H_{72}Fe_2K_4N_8O_2$	$C_{96}H_{107}Fe_3K_6N_{12}O_3$	$C_{26}H_{74}FeKN_3O_2Si_6$
Formula weight	1253.39	1879.08	724.37
T/K	99.95(16)	99.94(18)	99.97(16)
Crystal system	trigonal	monoclinic	triclinic
Space group	R-3	$P2_1/n$	P-1
a/Å	45.1458(5)	21.6510(3)	11.9537(7)
b/Å	45.1458(5)	19.4063(2)	13.1469(13)
c/Å	17.2734(2)	25.2680(2)	15.1460(12)
α/°	90	90.0	78.987(7)
β/°	90	100.5538(11)	68.452(7)
γ/°	120	90.0	79.226(7)
Volume/Å^3	30488.8(8)	10437.2(2)	2155.3(3)
Z	18	4	2
ρ_{calc}g/cm^3	1.229	1.196	1.116
μ/mm^{-1}	5.986	5.829	5.450
Crystal size/mm^3	0.3 × 0.3 × 0.2	0.3 × 0.25 × 0.2	0.189 × 0.11 × 0.059
Radiation	Cu Kα (λ = 1.54184)	Cu Kα (λ = 1.54178)	Cu Kα (λ = 1.54184)
2Θ range /°	6.782 to 153.112	6.726 to 152.494	6.332 to 111.496
Reflections collected	74635	109568	11119
Independent reflections	14071 [R_{int} = 0.0536, R_{sigma} = 0.0345]	21700 [R_{int} = 0.0531, R_{sigma} = 0.0389]	5458 [R_{int} = 0.0371, R_{sigma} = 0.0599]
Data/restraints /parameters	14071/0/721	21700/0/1081	5458/93/392
GoF	1.035	1.040	1.027
R ind. [I>=2σ (I)]R_1 (wR_2)	R_1 = 0.0446, wR_2 = 0.1109	R_1 = 0.0395, wR_2 = 0.0920	R_1 = 0.0418, wR_2 = 0.0874
Final R ind. [all data] R_1 (wR_2)	R_1 = 0.0487, wR_2 = 0.1135	R_1 = 0.0529, wR_2 = 0.0978	R_1 = 0.0640, wR_2 = 0.0993
Largest diff. peak/hole / e Å^{-3}	0.39/-0.56	0.77/-0.39	0.30/-0.33

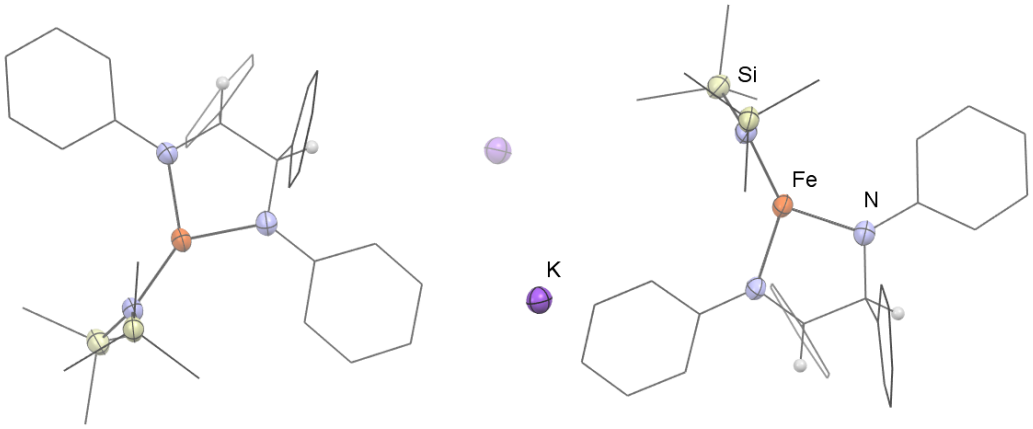

Figure 6.40. The asymmetric unit of complex *rac*-**1**. Each potassium ion is hexa-coordinated by THF molecules (omitted for clarity).

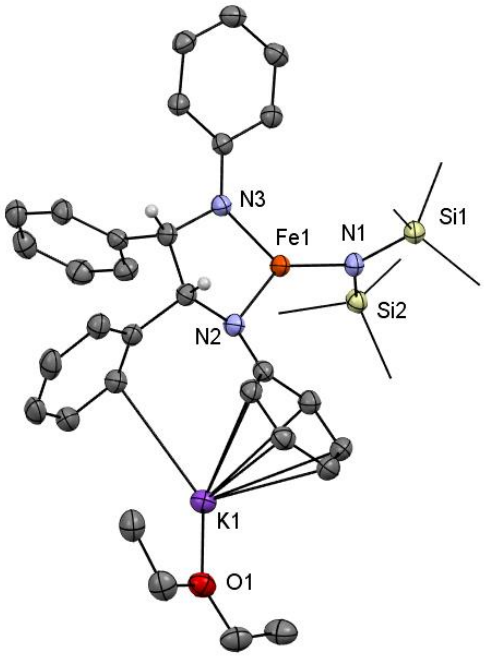

Figure 6.41. The asymmetric unit of complex *meso*-**1**.

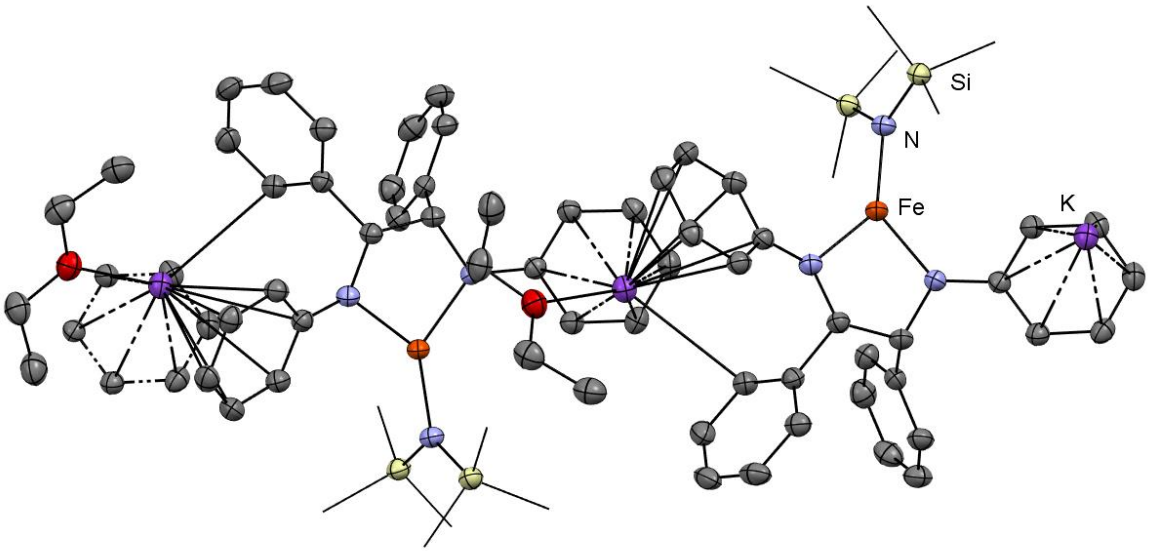

Figure 6.42. Section of the polymeric structure in crystalline *meso*-**1**.

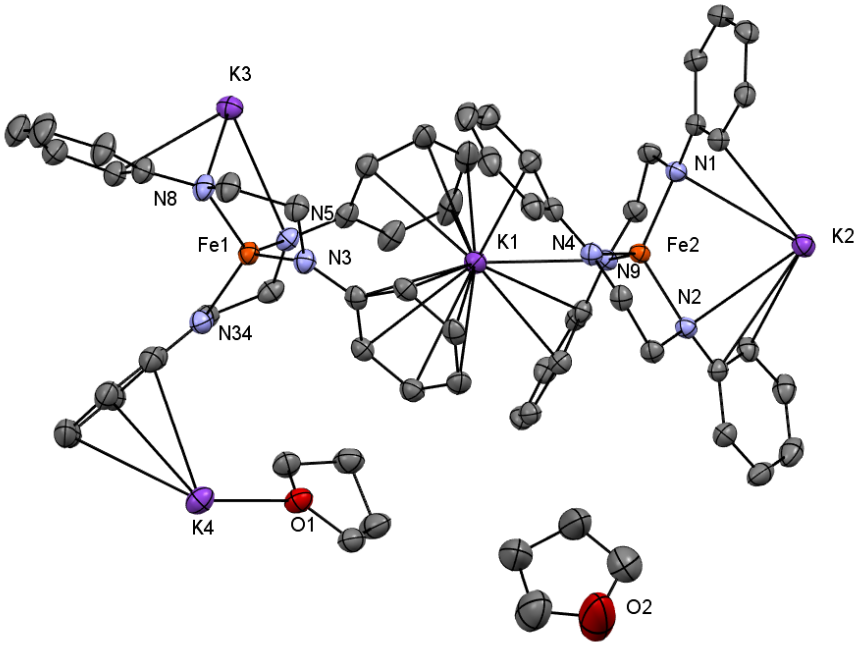

Figure 6.43. The asymmetric unit of complex **2a**.

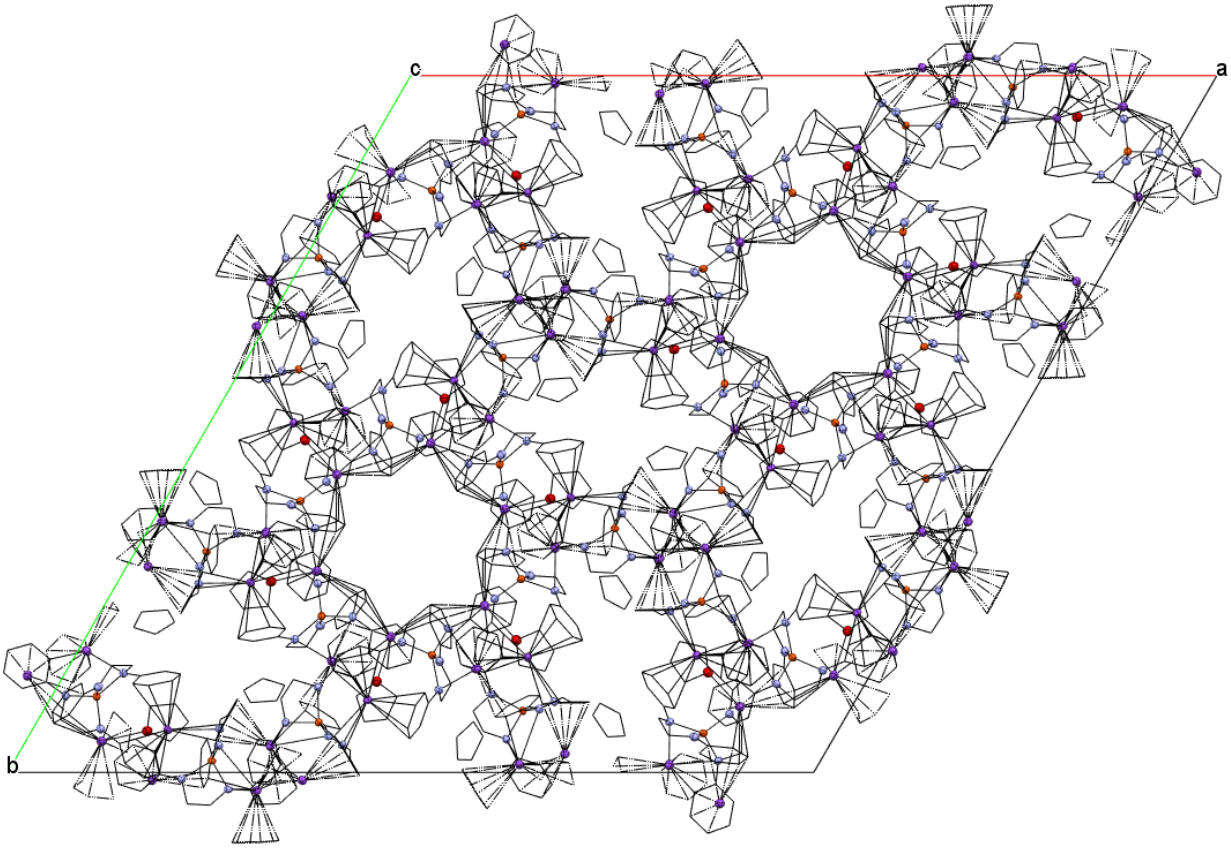

Figure 6.44. The packed unit cell of **2a** displaying the polymeric network.

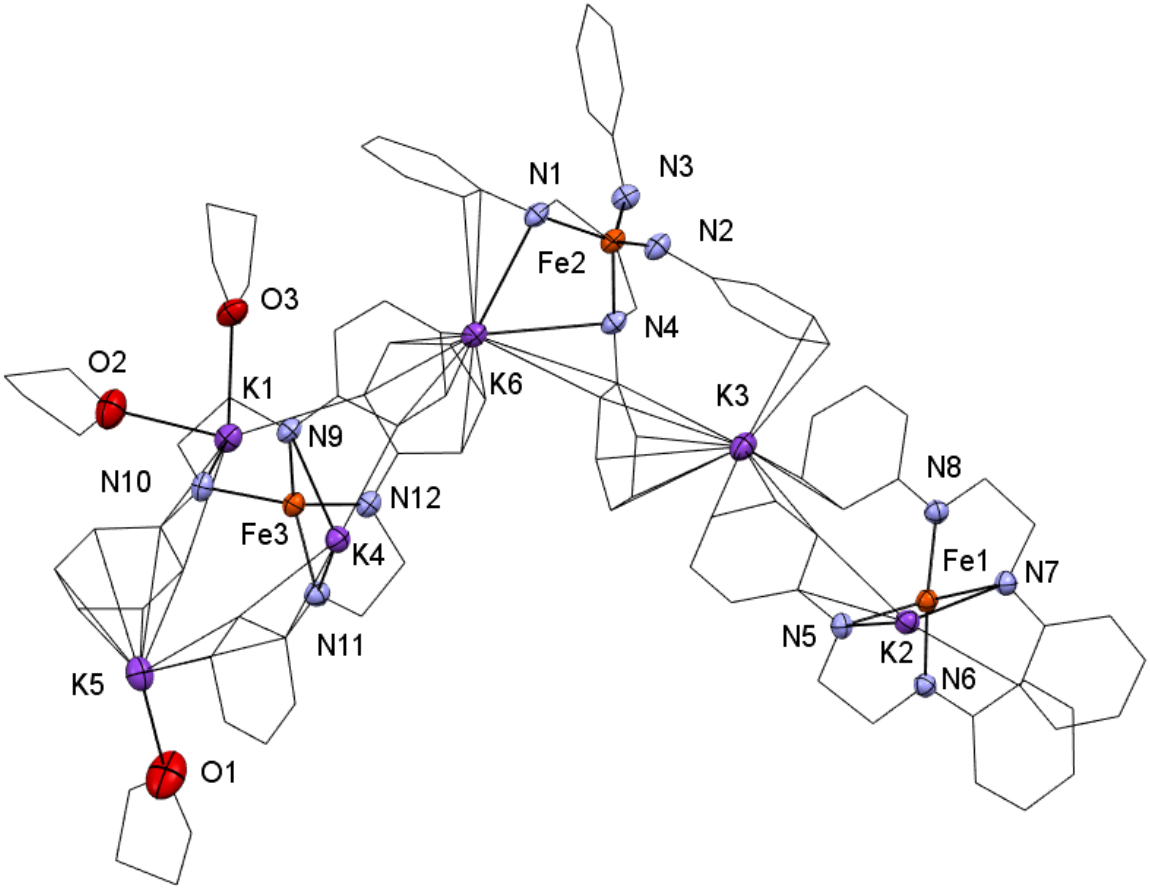

Figure 6.45. The asymmetric unit of complex **2b**.

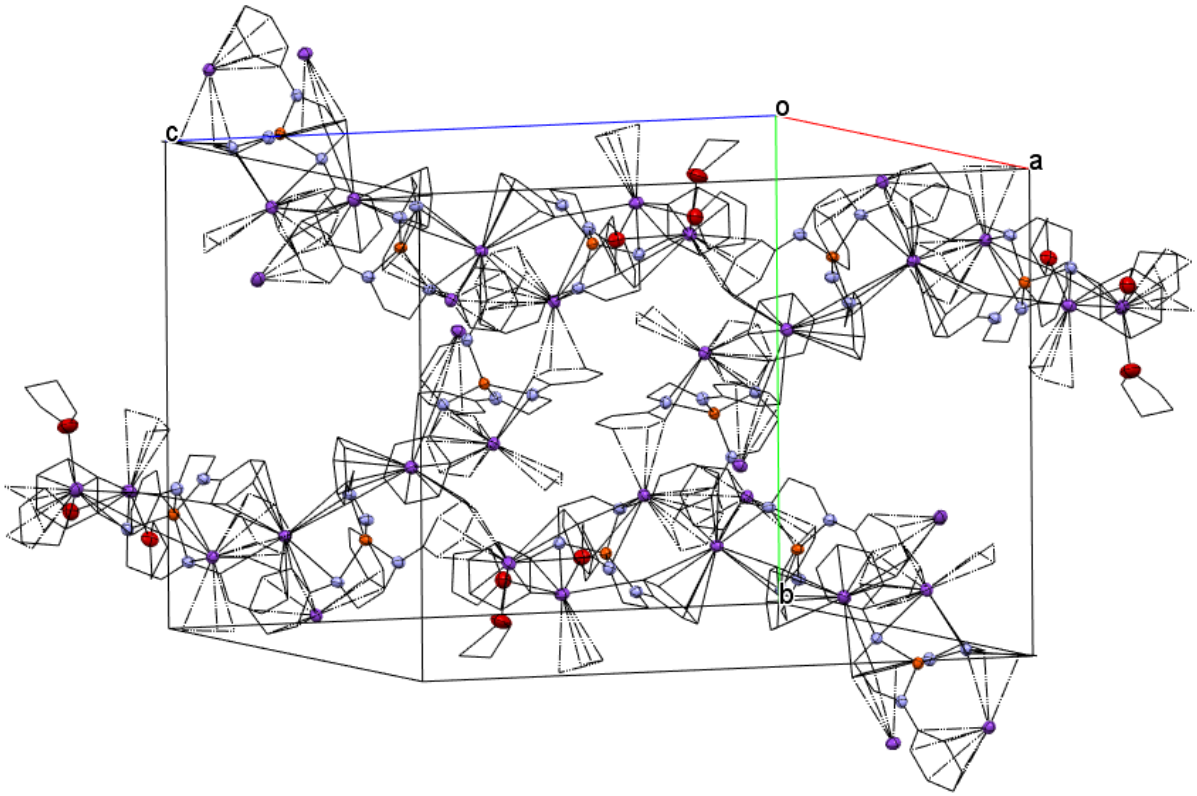

Figure 6.46. The packed unit cell of **2b** displaying the polymeric network.

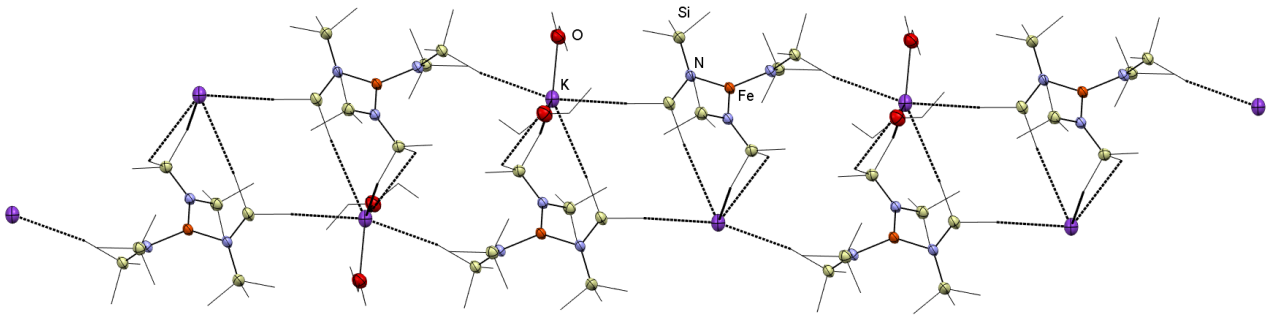

Figure 6.47. Section of the polymeric structure in the crystal of $KFe(hmds)_3$.

6.5.8. References

[1] D. L. J. Broere, I. Čorić, A. Brosnahan, P. L. Holland, *Inorg. Chem.* **2017**, *56*, 3140–3143.

[2] J. G. Smith, C. D. Veach, *Can. J. Chem.* **1966**, *44*, 2497–2502.

[3] S. K. Sur, *J. Magn. Reson.* **1989**, *82*, 169–173.

[4] M. P. Cibuzar, R. Waterman, *Organometallics* **2018**, *37*, 4395–4401.

[5] C. Wang, W. J. Teo, S. Ge, *ACS Catal.* **2017**, *7*, 855–863.

[6] M. Y. Hu, Q. He, S. J. Fan, Z. C. Wang, L. Y. Liu, Y. J. Mu, Q. Peng, S. F. Zhu, *Nat. Commun.* **2018**, *9*, 221.

[7] B. Cheng, W. Liu, Z. Lu, *J. Am. Chem. Soc.* **2018**, *140*, 5014–5017.

[8] S. Zhang, J. S. Liao, D. K. Unruh, G. Li, M. Findlater, *Org. Chem. Front.* **2021**, *8*, 2174–2181.

[9] Agilent Technologies Ltd, Yarnton, Oxfordshire, England, **2014**.

[10] Bruker AXS Inc., Madison, Wisconsin, USA, **2014**.

[11] G. M. Sheldrick, *Acta Cryst. A* **2008**, *64*, 112–122.

[12] G. M. Sheldrick, *Acta Cryst. A* **2015**, *71*, 3–8.

[13] A. L. Spek, *Acta Cryst. D* **2009**, *65*, 148–55.

7. Summary

2-pyridonates represent a versatile 1,3-*N,O* heterobidentate ligand platform that combines tunability, flexible binding modes (μ_n, κ^n), hemilability, and proton responsive character. These features enable the use of pyridonates as bridging ligands to assemble metal clusters and as chemically non-innocent ligands capable of cooperative bond cleavage and catalysis. Additional inspiration comes from nature: iron-pyridone complex is found in the active center of the [Fe]-hydrogenase metalloenzyme.

In the present thesis, a structurally diverse series of new Fe (II) and Co (II) pyridonate complexes have been investigated. Different types of binding modes, as well as evidence for hemilability and metal-ligand cooperativity are demonstrated.

Chapter 2 introduces the reader to the main features of 2-pyridonate ligands and an overview to the current state of research on 3d transition metal pyridonate complexes. Development of the catalytically relevant, biomimetic [Fe]-hydrogenase complexes shows an interesting trajectory starting from Fe(II) pyridonate/pyridinol complexes leading to the currently state of the art Mn(I) model complexes. Applications of the first-row transition metal pyridonates in homogeneous catalysis remains relatively scarce in comparison to their noble metal congeners. Nevertheless, there is a significantly growing amount of interest in the development of 3d metal over the previous decades. Mononuclear pyridonate complexes of Ti, V, Mn - Cu have been reviewed and their performances in different catalytic transformation were discussed. The critical roles of flexible coordination, hemilability and metal-ligand cooperation in catalysis were also highlighted.

Chapter 3 gives an overview on a convenient halide-free iron (II) complex: bis[bis(trimethylsilyl)amido]iron(II) ($Fe(hmds)_2$). Its open-shell electronic structure, lipophilicity, high Lewis acidity and facile protolytic ligand exchange make $Fe(hmds)_2$ a convenient precursor for low valent metal complexes. The broad applications of bis[bis(trimethylsilyl)amido]iron(II) for synthesis of molecular complexes, clusters and materials are demonstrated on multiple examples. Moreover, catalytic activity of $Fe(hmds)_2$ in hydrogenation, hydrosilylation, cyclotrimerization and other transformations were underlined.

Chapter 4 describes the utilization of pyridonates for the development of topologically unprecedented iron (II) clusters. These clusters were afforded via protolytic ligand exchange between the common precursor $Fe[N(SiMe_3)_2]_2$ and simple, commercially available 2-pyridone (L^HH) and 6-methyl-2-pyridone ($L^{Me}H$). The pentanuclear cluster $Fe_5(LH)_6[N(SiMe_3)_2]_4$ (Fe_5) exhibits a very rare diamondoid structure, featuring a $Fe@Fe_4$ tetrahedron core. The slightly bulkier 6-methyl-2-pyridonate afforded the tetranuclear $Fe_4(LMe)_6[N(SiMe_3)_2]_2$ (Fe_4), containing a planar butterfly Fe_4 rhomboid. The high-spin configuration of Fe(II) ions and different coordination environments in Fe_4 and Fe_5 are evident from ^{59}Fe Mössbauer spectroscopy. The SQUID magnetometry revealed that both clusters exhibit overall weak antiferromagnetic interactions. Moreover, the Fe_4 cluster constitutes a rare example of a field-induced single molecular magnet with U_{eff} = 38.5 K. Reactivity studies of the clusters toward protic reagents demonstrate both the stability of Fe_4 (retention of the tetranuclear metal

core) as well as the lability of Fe_5 (rearrangement of the tetranuclear metal core) clusters.

In contrast, **Chapter 5** discusses a *mononuclear* half-sandwich cobalt complex supported by phosphinopyridonate ligand. This complex was prepared in a one-pot synthesis from commercial 6-methyl-2-pyridone by deprotonation, phosphinylation, and substitution at $[Cp^*CoCl]_2$. Crystal structure revealed that the ligand binds to the cobalt center in κ^2-*P,N*-chelating mode with the 2-C=O moiety remaining uncoordinated. Cobalt pyridonate demonstrated remarkably high catalytic productivity (TON 1000, TOF 12.000 h^{-1}) in CO_2 hydroboration under mild conditions and low catalytic loading (25 °C, 0.1 mol%). Employing pinacolborane (HBpin) as a reductant, a near perfect chemoselectivity toward the formation of borylformate HCO_2Bpin was achieved. Mechanistic studies on potential catalytic intermediates suggest the borane-induced redox disproportion of Co (II) pre-catalyst as evident in NMR analysis and the isolation of Co^{III} hydrido species. The catalytic performance of the cobalt pyridonate system is attributed to the metal-ligand cooperative BH bond cleavage of the reagent and its potential hemilability. Future applications of cobalt pyridonate to the wide space of hydrofunctionalization and hydrogenation reactions are easily foreseeable.

Chapter 6 reports on the synthesis of a heteroleptic tri-coordinate amidoferrate $K[Fe(\kappa^2\text{-}N\frown N)N(SiMe_3)_2]$ ($N\frown N$ = 1,2-diphenylethylene-1,2-diamido), that displays high catalytic activity in the regioselective hydrosilylation of alkenes. The amidoferrate could be obtained via two different synthetic pathways: *(i)* one pot reductive dimerization of N-benzylideneaniline followed by co-complexation with $Fe(hmds)_2$; *(ii)* monodeprotonation – co-complexation of *rac*-tetraphenyl ethylenediamine ($^{Ph}LH_2$) via sequential addition of 1 equiv. K(hmds) and 1 equiv. $Fe(hmds)_2$. The highly regioselective hydrosilylation of alkenes using $PhSiH_3$ is demonstrated on the scope of 12 styrenes. Mechanistic studies suggest the initial silylative amide dissociation and the formation of a potential iron hydride species – a step that was significantly accelerated in the presence of styrenes.

8. Appendix

8.1. List of Abbreviations

9-BBN	9-borabicyclo[3.3.1]nonane	**HSQC**	heteronuclear Single Quantum Coherence
Ac	acetyl	**HYSCORE**	hyperfine sublevel correlation
ac	alternating current	**iPr**	iso-propyl
acac	acetylacetonate	**IR**	infrared spectroscopy
Ad	adamantyl	**LIFDI**	liquid injection field desorption/ ionization
ATR	attenuated total reflection	**m.p.**	melting point
BMS	borane dimethylsulfide	**Me**	methyl
Bn	benzyl	**Mes**	mesityl
bpy	2,2‘-bipyridine	**MLC**	metal-ligand cooperativity
btz	benzotriazolate	**MOF**	metal–organic frameworks
cat	catechol	**MPT**	methanopterin
Cy	cyclohexyl	**MS**	mass spectrometry
Cyp	cyclopentyl	**NHC**	N-heterocyclic carbene
DBU	1,8-Diazabicyclo[5.4.0]undec-7-ene	**NMR**	nuclear magnetic resonance
dc	direct current	**PCET**	proton coupled electron transfer
DCM	dichloromethane	**Ph**	phenyl
DEPT	distortionless enhancement by polarization transfer	**pin**	pinacol
DFT	density functional theory	**ppm**	parts per million
DIBAL-H	diisobutylaluminium hydride	**pyphos**	2-[2-(diphenylphosphanyl) ethyl]pyridine
DIPP	2,6-diisopropylphenyl	**QTM**	Quantum Tunneling of Magnetization
DMAP	dimethylaminopyridine	**R**	substituent
EPR	electron paramagnetic resonance	**rt**	room temperature

eq.	equation	**SMM**	single molecular magnet
equiv.	equivalent	**SQUID**	superconducting quantum interference device
ESI	electron spray ionization	**tBu**	tert-buthyl
Et	ethyl	**TCNQ**	7,7,8,8-tetracyano-p-quinodimethane
fac	facial	**THF**	tetrahydrofuran
FID	flame ionization detector	**TMS**	trimethylsilyl
GC	gas chromatography	**TOF**	turnover frequency
GMP	guanosine monophosphate	**TON**	turnover number
HA	hydroamination	**UV**	ultraviolet radiation
HAA	hydroaminoalkylation	**Vis**	visible radiation
hmds	hexamethyldisilazide	**XRD**	X-ray diffraction
HSAB	hard and soft acids and bases	**ZFS**	zero field splitting

8.2. List of Chemicals

Chemical **CAS** **Molecular formula**	**H-phrases** **P-phrases**	**GHS-symbols**
Diethylether 60-29-7 $C_4H_{10}O$	H224 - H302 - H336 P210 - P261	GHS02, GHS07
Ethanol 64-17-5 C_2H_6O	H225 - H319 P210 - P280 - P305 + P351 + P338 - P337 + P313 - P403 + P235	GHS02, GHS07
Methanol 67-56-1 CH_4O	H225 - H301 + H311 + H331 - H370 P210 - P233 - P280 - P301 + P310 - P303 + P361 + P353 - P304 + P340 + P311	GHS02, GHS06, GHS08
2-Propanol 67-63-0 C_3H_8O	H225 - H319 - H336 P210 - P233 - P240 - P241 - P242 - P305 + P351 + P338	GHS02, GHS07
Acetone 67-64-1 C_3H_6O	H225 - H319 - H336 P210 - P233 - P240 - P241 - P242 - P305 + P351 + P338	GHS02, GHS07
Acetonitrile 75-05-8 C_2H_3N	H225 - H302 + H312 - H319 - H331 P210 - P280 - P301 + P312 - P303 + P361 + P353 - P304 + P340 + P311 - P305 + P351 + P338	GHS02, GHS06
Dichloromethane 75-09-2 CH_2Cl_2	H315 - H319 - H336 - H351 P201 - P202 - P261 - P302 + P352 - P305 + P351 + P338 - P308 + P313	GHS07, GHS08
Acetophenone 98-86-2 C_8H_8O	H302 - H319 P264 - P270 - P280 - P301 + P312 - P305 + P351 + P338 - P337 + P313	GHS07
Styrene 100-42-5 C_8H_8	H226 - H315 - H319 - H332 - H361d - H372 P201 - P210 - P261 - P280 - P304 + P340 + P312 - P308 + P313	GHS02, GHS07, GHS08
Toluene 108-88-3 C_7H_8	H225 - H304 - H315 - H336 - H361d - H373 P210 - P240 - P301 + P310 + P330 - P302 +	GHS02, GHS07, GHS08

	P352 - P314 - P403 + P233	
Pentane 109-66-0 C_5H_{12}	H225 - H304 - H336 - H411 P210 - P273 - P301 + P310 + P331	GHS02, GHS07, GHS08, GHS09
n-Butyllithium (1.6 M in hexane) 109-72-8 C_4H_9Li	H225 - H250 - H261 - H304 - H314 - H336 - H361f - H373 - H411 P210 - P222 - P231 + P232 - P261 - P273 - P422	GHS02, GHS05, GHS07, GHS08, GHS09
Tetrahydrofuran 109-99-9 C_4H_8O	H225 - H302 - H319 - H335 - H336 - H351 P201 - P202 - P210 - P301 + P312 - P305 + P351 + P338 - P308 + P313	GHS02, GHS07, GHS08
Hexane 110-54-3 C_6H_{14}	H225 - H304 - H315 - H336 - H361f - H373 - H411 P201 - P210 - P273 - P301 + P310 + P331 - P302 + P352 - P308 + P313	GHS02, GHS07, GHS08, GHS09
Ethylacetate 141-78-6 $C_4H_8O_2$	H225 - H319 - H336P210 - P233 - P240 - P305 + P351 + P338 - P403 + P235	GHS02, GHS07
Sodiumhydrogencarbonat 144-55-8 $NaHCO_3$	Not available/applicable	
Sodiumcarbonat 497-19-8 Na_2CO_3	H319 P264 - P280 - P305 + P351 + P338 - P337 + P313	GHS07
Chloroform-d_1 865-49-6 $CDCl_3$	H302 - H315 - H319 - H331 - H351 - H361d - H372 P260 - P280 - P301 + P312 + P330 - P304 + P340 + P311 - P305 + P351 + P338 - P403 + P233	GHS06, GHS08
Benzene-d_6 1076-43-3 C_6D_6	H225 - H304 - H315 - H319 - H340 - H350 - H372 - H412 P201 - P210 - P273 - P301 + P310 + P331 - P302 + P352 - P308 + P313	GHS02, GHS07, GHS08
Tetrahydrofuran-d8 1693-74-9 C_4D_8O	H225 - H319 - H335 - H351	GHS02, GHS07, GHS08

	P202 - P210 - P233 - P240 - P305 + P351 + P338 - P308 + P313	
Toluene-d8 2037-26-5 $C_6D_5CD_3$	H225 - H304 - H315 - H336 - H361d - H373 P202 - P210 - P233 - P301 + P310 - P303 + P361 + P353 - P331	GHS02,GHS07, GHS08
Acetonitrile-d3 2206-26-0 CD_3CN	H226 - H302 + H312 + H332 - H319 P210 - P280 - P301 + P312 - P303 + P361 + P353 - P304 + P340 + P312 - P305 + P351 + P338	GHS02, GHS07
Potassium hydroxide 1310-58-3 KOH	H290 - H302 - H314 P234 - P260 - P280 - P301 + P312 - P303 + P361 + P353 - P305 + P351 + P338	GHS05, GHS07
Hydrogen 1333-74-0 H_2	H220 - H280 P20 - P377 - P381 - P403	GHS02, GHS04
1-Ethanone-4-(2-Phenylethynyl)-benzene 1942-31-0 $C_{16}H_{12}O$	Not available/applicable	
Magnesiumsulfate 7487-88-9 $MgSO_4$	Not available/applicable	
Silicagel 7631-86-9 SiO_2	Not available/applicable	
Sodium hydride 7646-69-7 NaH	H228 - H260 - H290 - H314 P210 - P231 + P232 - P260 - P280 - P303 + P361 + P353 - P305 + P351 + P338 + P310	GHS02, GHS05
Cobalt-(II)-chloride 7646-79-9 $CoCl_2$	H302 - H317 - H334 - H341 - H350i - H360 - H410 P273 - P280 - P301 + P312 - P302 + P352 - P304 + P340 + P312 - P308 + P313	GHS07, GHS08, GHS09
Hydrochloricacid 7647-01-0 HCl	H290 - H314 - H335 P234 - P261 - P271 - P280 - P303 + P361 + P353 - P305 + P351 + P338	GHS05, GHS07
Sodium chloride 7647-14-5 NaCl	Not available/applicable	
Sodiumsulfate	Not available/applicable	

7757-82-6 Na_2SO_4		
Iron-(II)-chloride 7758-94-3 $FeCl_2$	H302 - H318 P264 - P270 - P280 - P301 + P312 - P305 + P351 + P338 - P501	GHS05, GHS07
Ammonium chloride 12125-02-9 NH_4Cl	H302 - H319 P264 - P270 - P280 - P301 + P312 - P305 + P351 + P338 - P337 + P313	GHS07
N-benzylideneaniline 538-51-2 $C_{13}H_{11}N$	H315, H319, H335 P302+P352, P305+P351+P338	GHS07
Sodium 7440-23-5 Na	H260 - H314 P223 - P231 + P232 - P280 - P305 + P351 + P338 - P370 + P378 - P422	GHS02, GHS05
Potassium 7440-09-7 K	H260 - H314 P223 - P231 + P232 - P260 - P280 - P303 + P361 + P353 - P305 + P351 + P338	GHS02, GHS05
N,N′-Diphenylethylenediamine 150-61-8 $C_{14}H_{16}N$	H315 - H319 - H335 P261 - P264 - P271 - P280 - P302 + P352 - P305 + P351 + P338	GHS07
Styrene-d_3 3814-93-5 $C_8H_6D_3$	H226 - H315 - H319 - H332 - H361 - H372 P202 - P210 - P303 + P361 + P353 - P304 + P340 + P312 - P305 + P351 + P338 - P308 + P313	GHS02, GHS07, GHS08
Dichloro(phenyl)silane 1631-84-1 $C_6H_6Cl_2Si$	H226 – H314 P280 – P305 + P351 + P338 – P310	GHS02, GHS05
Phenylsilane 694-53-1 C_6H_8Si	H225 - H302 + H332 - H315 - H319 - H335 P210 - P301 + P312 + P330 - P302 + P352 - P304 + P340 + P312 - P305 + P351 + P338	GHS02, GHS07
3-Methylstyrene 100-80-1 C_9H_{10}	H226 - H304 - H315 - H319 - H332 - H335 P210 - P301 + P310 + P331 - P302 + P352 - P304 + P340 + P312 - P305 + P351 + P338	GHS02, GHS07, GHS08
4-Methylstyrene 622-97-9	H226 - H304 - H411	GHS02, GHS08, GHS09

C_9H_{10}	P210 - P273 - P301 + P310 + P331	
4-Vinylanisole 637-69-4 $C_9H_{10}O$	Not available/applicable	
3-Fluorostyrene 350-51-6 C_8H_7F	H226 - H319 P210 - P233 - P240 - P241 - P242 - P305 + P351 + P338	GHS02, GHS07
3-(Trifluoromethyl)styrene 402-24-4 C_9H_7F	H226 - H315 - H319 - H335 P210 - P233 - P240 - P241 - P303 + P361 + P353 - P305 + P351 + P338	GHS02, GHS07
2-Vinylnaphthalene 827-54-3 $C_{12}H_{10}$	H371 P308 + P311	GHS08
trans-β-Methylstyrene 873-66-5 C_9H_{10}	H226 - H304 - H315 - H318 - H334 - H335 P261 - P280 - P301 + P310 - P305 + P351 + P338 - P331 - P342 + P311	GHS02, GHS05, GHS07, GHS08
α-Methylstyrene 98-83-9 C_9H_{10}	H226 - H304 - H317 - H319 - H335 - H361fd - H411 P210 - P273 - P280 - P301 + P310 - P303 + P361 + P353 - P331	GHS02, GHS07, GHS08, GHS09
Allylbenzene 300-57-2 C_9H_{10}	H226 - H304 P210 - P301 + P310 + P331	GHS02, GHS08
1-Octene 111-66-0 C_8H_{16}	H225 - H304 - H410 P210 - P233 - P240 - P273 - P301 + P310 - P331	GHS02, GHS08, GHS09
Vinylcyclohexane 695-12-5 C_8H_{14}	H225 P210 - P233 - P303 + P361 + P353 - P370 + P378 - P403 + P235 - P501	GHS02
4-Vinylpyridine 100-43-6 C_7H_7N	H226 - H301 + H311 + H331 - H314 - H317 - H411 P210 - P273 - P280 - P303 + P361 + P353 - P304 + P340 + P310 - P305 + P351 + P338	GHS02, GHS05, GHS06, GHS09
2-Hydroxypyridine 142-08-5 C_5H_5NO	H301 P264 - P270 - P301 + P310 - P405 - P501	GHS06
2-Hydroxy-6-methylpyridine	H315 - H319 - H335	GHS07

3279-76-3 C_6H_7NO	P261 - P264 - P271 - P280 - P302 + P352 - P305 + P351 + P338	
Phenylacetylene 536-74-3 C_8H_6	H226 - H315 - H319 - H335 - H350 P202 - P210 - P233 - P303 + P361 + P353 - P305 + P351 + P338 - P308 + P313	GHS02, GHS07, GHS08
Ethyl benzoate 93-89-0 $C_9H_{10}O_2$	Not available/applicable	
N,N-Dimethylbenzamide 611-74-5 $C_9H_{11}NO$	H302 - H315 - H319 - H335 P261 - P264 - P270 - P301 + P312 - P302 + P352 - P305 + P351 + P338	GHS07
2,6-Di-tert-butyl-4-methylphenol 128-37-0 C15H24O	H410 P273 - P391 - P501	GHS09
Hydroquinone 123-31-9 $C_6H_6O_2$	H302 - H318 - H341 - H351 - H410 P202 - P273 - P280 - P301 + P312 - P305 + P351 + P338 - P308 + P313	GHS05, GHS07, GHS08, GHS09
1,4-Benzenedimethanol 589-29-7 $C_8H_{10}O_2$	H302 + H332 P301 + P312 – P304 + P340	GHS07
Terephthalic acid 100-21-0 $C_8H_6O_4$	Not available/applicable	
1,2,3,4,5-Pentamethylcyclopentadiene 4045-44-7 $C_{10}H_{16}$	H226	GHS02
Triphenyl borate 1095-03-0 $C_{18}H_{15}BO_3$	H301 + H311 + H331 - H318 P261 - P280 - P301 + P310 - P302 + P352 + P312 - P304 + P340 + P311 - P305 + P351 + P338	GH S05,GHS06
Chlorodiphenylphosphine 1079-66-9 $C_{12}H_{10}ClP$	H290 - H302 - H314 - H412 P234 - P273 - P280 - P301 + P312 - P303 + P361 + P353 - P305 + P351 + P338	GHS05, GHS07
Chlorodiisopropylphosphine 40244-90-4 $C_6H_{14}ClP$	H225 - H314 P210 - P233 - P240 - P280 - P303 + P361 + P353 - P305 + P351 + P338	GHS02, GHS05

Bis(pentamethylcyclopentadienyl)cobalt(II) 74507-62-3 $C_{20}H_{30}Co$	Not available/applicable	
4,4,5,5-Tetramethyl-1,3,2-dioxaborolane 25015-63-8 $C_6H_{13}BO_2$	H225 - H261 P210 - P231 + P232 - P233 - P280 - P302 + P335 + P334 - P370 + P378	GHS02
Catecholborane 274-07-7 $C_6H_5BO_2$	H225 - H314 P210 - P233 - P240 - P280 - P303 + P361 + P353 - P305 + P351 + P338	GHS02, GHS05
9-Borabicyclo[3.3.1]nonane (1.6 M in THF) 280-64-8 $C_8H_{15}B$	H225 - H260 - H302 - H319 - H335 - H336 - H351 P201 - P210 - P231 + P232 - P301 + P312 - P305 + P351 + P338 - P308 + P313	GHS02, GHS07, GHS08
Borane dimethyl sulfide complex 13292-87-0 $C_2H_6S.BH_3$	H225 - H260 - H301 + H311 - H318 - H360FD - H412 P210 - P231 + P232 - P273 - P280 - P301 + P310 - P305 + P351 + P338	GHS02, GHS05, GHS06, GHS08
Carbon dioxide 124-38-9 CO_2	H280 P410 + P403	GHS04

8.3. Acknowledgements

In this section I would like to thank all the people who supported me during my PhD journey.

Thank you, Axel, for giving me the opportunity to work in your group, in the beautiful, brand-new lab (hope, I did not scratch it too much…). I am very grateful for the freedom you provided for project selection and development. I am also very thankful for many research related discussions, guidance with manuscripts preparation and opportunities to participate international conferences.

I am very thankful to Dr. Uttam Chakraborty for supporting my first steps in the lab and introducing me to the magnificent world of metal clusters. Thank you, Dr. Pradip Ghosh, – for teaching me how to use glovebox, organize experiments and design projects. Special thanks to Dr. Dieter Schaarschmidt for the help and support in all aspects of lab life!

I would like to thank all the members from the AJvW group for warm welcome in Hamburg and great amount of fun and support during my four years here. Luana, Bernhard, Jenny, Robin, Jackie, Ursula, Ben, Thilo, TOK, Till, Roderich, Nils, Carl, Mattis, Christoph, Stephan, Lea, Guojiao, Mike, Josef, Javier, Michael, Chiara, Sofia, Charlotte, Isabelle, Finn - that was unforgettable time together – in the lab and outside!

I am very grateful to Prof. Dr. Franc Meyer, Dr. Sandeep Gupta and Isabelle Rüter for fruitful collaboration and warm welcome in Göttingen.

Last but not the least I want to thank my Family and my Friends.

8.4. Curriculum Vitae

Andrey Fedulin

22089, Hamburg, Germany
Wandsbeker Chaussee 220

+4917676712272
andrey.fedulin@chemie.uni-hamburg.de

Education

2018 – Present	University of Hamburg, Hamburg, Germany, Ph.D. student, Inorganic Chemistry and Catalysis
2011 – 2017	Lomonosov Moscow State University, Chemistry Department, Division of Organic chemistry, specialist (equivalent of M.Sc.) in organic/organometallic chemistry (GPA 4.7 of 5.0)

Research and Work Experience

2018 - present — University of Hamburg, Hamburg, Germany, research group of Prof. Jacobi von Wangelin

- Synthesis, characterization (XRD, SQUID, Mössbauer) and reactivity studies of topologically unprecedented iron(II) pyridonate clusters
- Design of 3d metal complexes supported by pyridonephosphine ligands capable for metal-ligand cooperative bond activation
- Development of reductive catalytic transformations mediated by pyridonate complexes: Co catalysed pyridine hydroboration, Mn catalysed CO_2 hydrogenation
- Synthesis of novel amidoferrate complexes bearing ethylenediamido ligands and their application in catalytic styrene hydrosilylations

2017 - 2018 — “Institute of Chemical Reagents and High Purity Chemical Substances” of National Research Center “Kurchatov Institute” Research fellow

- Synthesis of polyimides and composite materials, based on polyimides

2015 - 2017 — Lomonosov Moscow State University, Moscow, Russia, Diploma project (equivalent to M.Sc).

- Synthesis and catalytic applications of Al, Sn, Ge complexes supported by SNS pincer type ligands

Advisor: Dr. Kirill V. Zaitsev

2013 - 2015 — Course project in organic chemistry

- Multi-step synthesis of zirconocenes, substituted ferrocenes, titanium, magnesium and platinum complexes
- Exploration of catalytic hydrosilylation of olefins by Pt(II) complexes based on various diphosphinoferrocenes

Advisor: Prof. Dr I. Nifant'ev.

2011 - 2013 Course project in Inorganic Chemistry

- Development of new method of complex fluorides synthesis by decomposition of metal fluoroacetates in presence of β-cyclodextrin

Advisor: Dr. A. Fedorova

Teaching

2018 - present Supervisor in advanced undergraduate teaching laboratories "Integriertes Synthesepraktikum in Anorganischer und Organischer Chemie"
Mentor in undergraduate "Catalysis" internship

Competences and Skills

Laboratory skills: Synthetic organic/organometallic/coordination chemistry, column chromatography, inert techniques (Schlenk and Glovebox); X-ray quality single crystals growing, high pressure reactions (Parr autoclaves)

Analytical characterization: GC-MS, GC-FID, multinuclear NMR (including paramagnetic compounds), IR, UV-Vis, cyclic voltammetry, scXRD and powder diffraction, magnetic characterization: Evans NMR and SQUID (basics)

Software: ChemDraw, TopSpin, Diamond, Mercury, Origin, Olex2, MestreNova

Instrument maintenance: high pressure equipment (autoclaves and gas cylinders) and MBrown glovebox maintenance and repair

Publications

1. Chakraborty, U., Fedulin, A., Jacobi von Wangelin, A. Synthesis and Catalysis of Anionic Amido Iron(II) Complexes., *ChemCatChem*, **2022**, 14 (UC and AF contributed equally).

2. Andrey Fedulin, Sandeep K. Gupta, Isabelle Rüter, Franc Meyer, and Axel Jacobi von Wangelin. Polynuclear Iron(II) Pyridonates: Synthesis and Reactivity of Fe_4 and Fe_5 Clusters. *Inorganic Chemistry* **2022**, *61*, 6149-6159.

3. Fedulin, A.; Jacobi von Wangelin, A. Bis[bis(trimethylsilyl)amido]iron(II): Silanamine, 1,1,1-trimethyl-N-(trimethylsilyl)-, iron(2+) salt (2:1). In *Encyclopedia of Reagents for Organic Synthesis.*

4. Anna A. Fedorova, Andrey I. Fedulin, Igor V. Morozov. New method of beta-$NaYF_4$: Yb^{3+}, Er^{3+} synthesis by using beta-cyclodextrin. *J. Fluorine Chem.*, **2015**. V. 178. P. 173–177.

5. Andrey I. Fedulin, Yurii F. Oprunenko, Sergey S. Karlov, Galina S. Zaitseva, Kirill V. Zaitsev. Tetrylenes based on polydentate sulfur-containing ligands, *Mendeleev Communications*, **2021**, 850-852.

6. Andrey I. Fedulin, Andrei V. Churakov, Kirill V. Zaitsev, Methylaluminum complexes based on tridentate 2,6-bis(mercaptoalkyl)pyridine SNS-ligands, *Mendeleev Communications,* **2021**, 847-849.

Conferences

- Fedulin A.I., Fedorova A.A., Morozov I.V., Kuznetsov S.V, Fedorov P.P. Synthesis of $NaYF_4$ doped with Yb^{3+} and Er^{3+} ions using beta cyclodextrin. Abstracts of the 9th All-Russian Conference "Fluorine Chemistry", Moscow, 2012, October 20-25, Poster
- XX International Scientific Conference of Students, Graduate Students and Young Scientists «Lomonosov-2013». Synthesis of $NaYF_4$ doped with Yb^{3+} and Er^{3+} ions using beta cyclodextrin. Moscow 2013, Presentation
- 27th International Chugaev Conference on Coordination Chemistry 4th Conference-School for Young Researchers “Physicochemical Methods in Coordination Chemistry”, October 2-6, 2017, N. Novgorod, Russia «Tetrylenes stabilized by polydentate ligands: synthesis, structure, properties and application», Abstract
- International Conference “Organoelement Compounds and Polymers 2019” A.N. Nesmeyanov Institute of Organoelement Compounds (INEOS) Moscow, Russia, 18-22 November 2019, Poster
- 44th ICCC International Conference on Coordination Chemistry, Rimini (Italy), 28 August - 2 September 2022, Poster

Awards

- XX International Scientific Conference of Students, Graduate students and Young Scientists “Lomonosov 2013” – first place diploma
- LMSU Increased Scholarship for Scientific Researches (2014, 2016)

8.5. Eideststattliche Erklärung

„Hiermit versichere ich an Eides statt, die vorliegende Dissertation selbst verfasst und keine anderen als die angegebenen Hilfsmittel benutzt zu haben. Die eingereichte schriftliche Fassung entspricht der auf dem elektronischen Speichermedium. Ich versichere, dass diese Dissertation nicht in einem früheren Promotionsverfahren eingereicht wurde.“

Datum 08.02.2023

Unterschrift